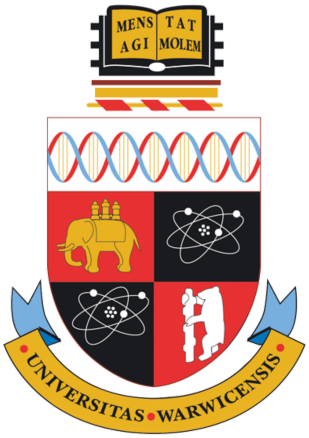

Probing the local and average structure of functional materials

Anna Herlihy

A Thesis presented for the degree of

Doctor of Philosophy in Chemistry

Chemistry Department

University of Warwick

UK

March 2022

Contents

*

List of Figures

List of Tables

Acknowledgments

I would first and foremost like to thank my supervisors Mark Senn and Nick Funnell for all the encouragement and support throughout my PhD. I genuinely could not have wished for better supervisors. Mark—thank you for imparting even a fraction of your knowledge of crystallography and irreps, and for championing a healthy work-life balance. Nick—thank you for your assiduous approach to all my stupid questions and anything requiring feedback, and also for always immediately spotting the errors in my FORTRAN code.

I have been very lucky to collaborate with a number of knowledgeable and helpful people throughout my PhD. So, thank you to the rest of the PEARL team; Craig Bull and Chris Ridley, not only for assistance with experiments and collecting data, but for instilling a deep understanding that 10 am and 3 pm is **coffee time**. Thank you to Andrew Goodwin, Harry Geddes and Gabrielle Sosso for their helpful discussions and contributions to the high-pressure total scattering work on correcting for a PTM. A big thanks also goes to David Keen and Wojciech Sławiński for answering questions on PDF normalisations and notation, and to Helen Playford for getting me started with *StoG*. Without the diffraction data collected by Wei-Tin Chen, much of the average structure work in Chapter 4 would not have been possible, so I am indebted to him for his generosity in sharing his beamtime.

My enthusiasm for central facilities stems from a placement year I did at

the I11 beamline, so I would really like to thank Stephen Thompson and Claire Murray for introducing me to this world. Steve—never have I ever related more to 'the more you know the more you realise you don't know' (it just keeps getting worse!).

A huge thanks goes to all the Senn group members for the fantastic group dynamic and providing such a nurturing environment in which to carry out a PhD. Thanks in particular to Tobie, Gabriel, and Jere for, respectively, your PDF/coding expertise, emotional support, and constructive criticism.

On a more personal note, I would like to thank my family and friends for the endless love and support you show me every day. I owe Mathwin, Charlotte, Beth, and Beth so much gratitude for being the most wonderful, caring friends. Thank you especially for the Taylor Swift therapy sessions and adventurous bike rides!

And finally, I would like to thank my family—Mum, Dad, Claire, Niall, Gma, Gpa, Mike, all of you—I could not have done it without you. I have been so lucky to have such a force of unwavering support and belief, which has seen me through the most challenging times. And last but definitely not least, to Jane—thank you for getting me here.

Declaration

This Thesis has been composed by myself except where indicated within the relevant Chapter, and has not been submitted for a degree at any other university. Parts of this Thesis have been published or submitted for publication:

- A. Herlihy, T. A. Bird, C. J. Ridley, C. L. Bull, N. P. Funnell and M. S. Senn, *PRB*, 2022, **105**, 094114.
- A. Herlihy, H. S. Geddes, G. C. Sosso, C. L. Bull, C. J. Ridley, A. L. Goodwin, M. S. Senn and N. P. Funnell, *J. Appl. Crystallogr.*, 2021, **54**, 1546–1554.
- T. A. Bird, A. Herlihy and M. S. Senn, *J. Appl. Crystallogr.*, 2021, **54**, 1514–1520.

Abstract

Studying the average structure of functional materials as a function of temperature or chemical substitution can provide insight into structure-property relationships. Pressure provides another external control parameter, now routinely used in conjunction with diffraction. Local symmetry-breaking, or order-disorder type behaviours sometimes must be considered, for example, using total scattering, however, this is challenging for high-pressure measurements. This Thesis adds insight into structure-property relationships using this conventional paradigm and develops high pressure total scattering techniques, demonstrating applicability to ferroelectric phase transitions in $BaTiO_3$.

Variable-pressure neutron total scattering is complicated by contaminant scattering from pressure-transmitting media. This Thesis details an approach to account for the presence of a methanol:ethanol medium in PDFs, measured on PEARL (ISIS). Proof-of-principle measurements are demonstrated with Ni and MgO, in addition to the first neutron local structure measurements and analysis of α-quartz under *hydrostatic* pressure.

The local structure of ferroelectric $BaTiO_3$ under hydrostatic pressure has been interrogated using neutron total scattering, across its tetragonal to cubic transition. Small-box modelling, using local rhombohedral, tetragonal, and cubic distortions, shows that rhombohedral-type distortions become suppressed with pressure. The transition in high-temperature $BaTiO_3$ is best described with an order—disorder model, whereas the high-pressure results indicate that the structure is better described by the harmonic approximation.

The average and local structures of the superconductor $La_{1.875}Ba_{0.125}CuO_4$ have been investigated using temperature, pressure, and chemical substitution of JT-inactive Mg^{2+} for JT-active Cu^{2+} cations. The anomalous suppression of superconductivity coincides with a transition to a low-temperature tetragonal phase. Increased Mg^{2+} concentration is found to stabilise this phase, but prevents its coexistence with a superconductivity-hindering low-temperature orthorhombic phase, observed in the parent LBCO compound. X-ray total scattering indicates dynamic rotation of the Cu/MgO_6 octahedra at 400 K, and average structure measurements show a transition to a 'high-temperature' tetragonal phase occurs almost immediately with applied pressure.

Abbreviations

BM	Birch-Murnaghan
DLS	Diamond Light Source
EoS	equation of state
EXAFS	extended X-ray absorption fine structure
HTT	high temperature tetragonal
JT	Jahn-Teller
LBCO	$La_{1.875}Ba_{0.125}CuO_4$
LSCO	$La_{2-x}Sr_xCuO_4$
LTT	low temperature tetragonal
LTO	low temperature orthorhombic
ME	methanol:ethanol
NMF	non-negative matrix factorisation
NMR	nuclear magnetic resonance
NTE	negative thermal expansion
OD	order-disorder
OP(D)	order parameter (direction)
PDF	pair distribution function
PE	Paris–Edinburgh
PSD	position sensitive detector
PTM	pressure transmitting medium
RMC	reverse Monte Carlo
RP	Ruddlesden–Popper
SAPA	symmetry-adapted PDF analysis
ToF	time-of-flight
TPS	Taiwan Photon Source
XANES	X-ray absorption near edge structure
XRD	X-ray diffraction
ZTA	zirconia-toughened alumina

Chapter 1

Introduction

1.1 Crystalline structures

Within solid-state chemistry there is a continual search for crystalline materials with enhanced functional properties which can be utilised in functional devices such as batteries,[1] solid oxide fuel cells,[2] and memory storage.[3] Such materials exhibit highly-correlated structure-property relationships which are central to materials science, and, understanding how structure can influence properties such as magnetism,[4] superconductivity[5] and thermal expansion[6] forms a large effort of the solid-state community.

The design of functional solid-state materials has been facilitated by the ability to efficiently describe the structure of said materials crystallographically.[7] Crystalline structures are usually described *via* a unit cell—a parallelepiped—and its contents, or, motif. When translational symmetry operators are applied, an infinite crystal structure is then propagated in three-dimensional space. The unit cell is typically defined as the smallest repeating unit which contains the full symmetry of the structure, although this definition is not a requirement; unit cells and their origins are often chosen to emphasise certain symmetries or to allow comparisons to other similar structures.

Mathematical descriptions of the symmetry of a crystal can be used to rationalise temperature- and pressure-induced phase transitions and even to predict physical properties of a crystal. For example, properties such as ferroelectricity depend on the material being able to develop a spontaneous polarisation (*e.g.*, generate a polar vector $[x,y,z]$). Its associated point group symmetry may not posses any collection of symmetry operators that that lead to its cancellation ($[-x,-y,-z]$). As such, a crystal with ferroelectric properties is incompatible with space group symmetry that inverts the structure.

The periodic, ordered arrangements of atoms in crystalline materials makes them suitable for analysis by diffraction techniques, used in a number of fields

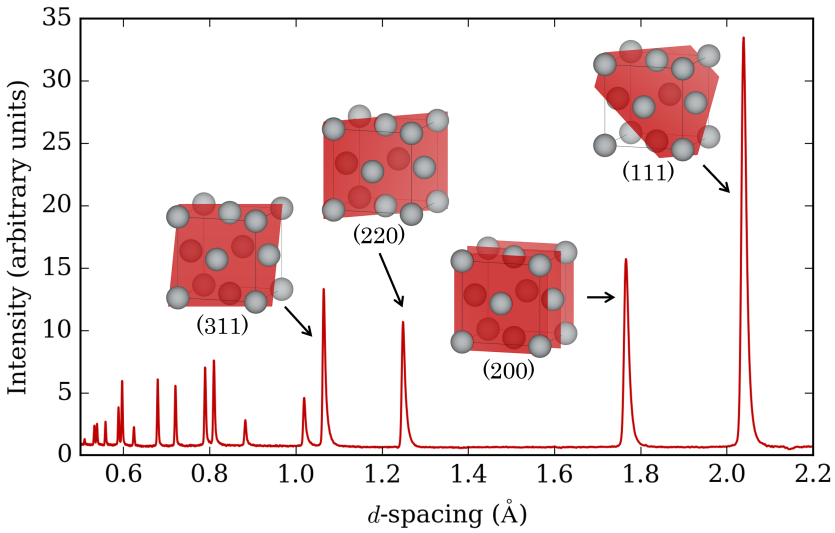

Figure 1.1: Diffraction pattern of a simple crystalline material with illustrations of representative Bragg planes.

to investigate average structures of single crystal and polycrystalline samples. Diffraction of X-rays by crystal structures was discovered a century ago by Max von Laue, with father and son W. H. and W. L. Bragg proposing the theory of diffraction from planes in the crystal in 1913.[7] Diffraction experiments using X-rays, neutrons or electrons result in strong Bragg reflections, or peaks for polycrystalline experiments (illustrated in Figure 1.1), providing information about the average crystal structure symmetry, unit cell dimensions and other key crystallographic properties. Such average structure determination has played an important role in understanding structure-property relationships.

There is however, an increasing awareness of the role that disorder plays in structure-property relationships of crystalline materials. This generates challenges for the crystallographic description which relies on long-range periodicity and the ability of the average structure to accurately describe the local structure. Deviations from the structure described by a relatively simple unit cell picture can obfuscate more complex local behaviour.

1.2 Deviations from crystallinity

Disorder within crystal structures presents itself in a number of different ways. Thermally-induced atomic displacement represents the most fundamental form of disorder. At temperatures above 0 K, thermal energy increasingly contributes to atomic vibrations, causing greater instantaneous deviations from the average symmetry (Figure 1.2(a)). Collective dynamic movements of atoms within the lattice can give rise to characteristic low energy vibrations called phonons with energies and populations that may in principle be calculated in the harmonic approximation. In this case, when averaging over time, the local symmetry will resemble an average symmetry.

Glassy materials such as silica (SiO_2) adopt a highly disordered structure composed of SiO_4 tetrahedra randomly orientated with shared corners (Figure 1.2(b)) or edges. The structure is well-defined over a few Ångströms, after which the periodicity is lost. A measured diffraction pattern would contain only diffuse scattering features and no strong Bragg reflections.

Other less extreme examples of disorder, are present in crystalline structures which exhibit, for example compositional or orientational disorder. Compositional disorder describes the situation where atomic positions are randomly occupied by certain atoms (Figure 1.2(c)) (or vacancies) such that the chemical composition remains unchanged. Materials with compositional disorder such as semiconducting and insulating alloys are used for applications such as thermoelectric converters where low thermal conductivity is a key property.[8] The alloy $Si_{0.5}Ge_{0.5}$ has been found to exhibit significantly reduced thermal conductivities compared to pure Si, largely on account of the disordered arrangement of Si and Ge atoms.[9,10]

Orientational disorder, such as the 'misorientation' of polyatomic units (SO_4) in potash alum ($KAl(SO_4)_2.12H_2O$) leads to anomalous materials properties such

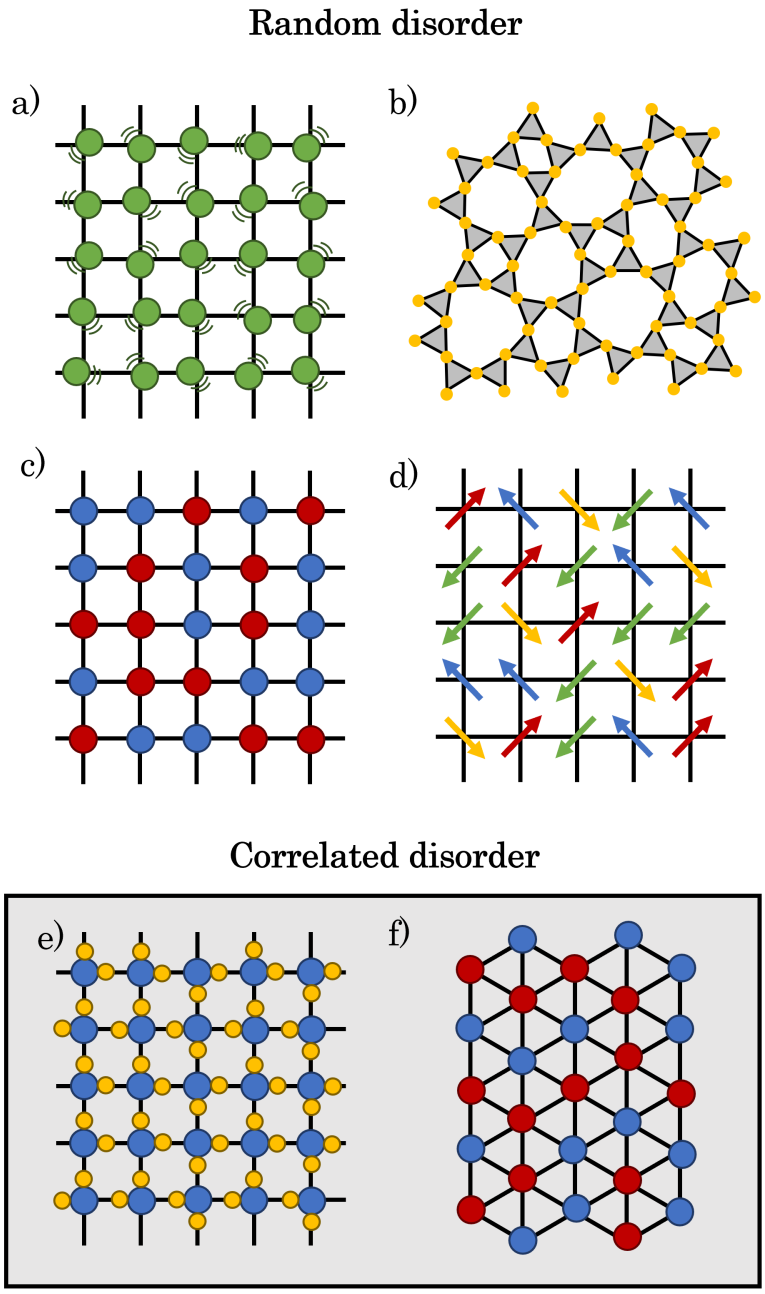

Figure 1.2: Illustration of different types of disorder, a) thermal disorder, b) structural, c) compositional and d) orientational. e) and f) are examples of correlated disorder arising in a hypothetical square ice structure and the Ising triangular lattice respectively. The former has correlated orientations of oxygen atoms (yellow circles) within rows and columns, and the later is a compromise of opposing spins (blue *versus* red circles) where on average, four nearest neighbour spins are in an opposite state, and the remaining two are aligned and forced to be 'frustrated'.

as reversible amorphisation under pressure. It is found that samples with a higher degree of disorder exhibit a reversible amorphisation whereas samples with low

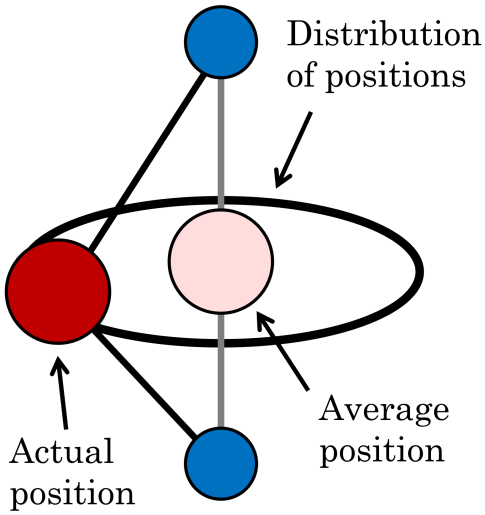

Figure 1.3: The apparent Si–O bond shortening observed of the average structure of β-cristobalite is due to an averaging of a distribution of bent O–Si–O configurations. The figure is recreated from Reference 13.

disorder exhibit a distinct phase transition to an ordered phase.[11]

In the examples above, there is a marked difference between the local and average symmetry of the system. The average structure—*i.e.*, the time- and space-averaged structure—will appear to have higher symmetry than the local structure and this can lead to an unphysical interpretation of local coordination environments of materials. For example, the average structure of β-cristobalite would apparently have linear O–Si–O bonds, which counter-intuitively shorten with increasing temperature. This atomic arrangement is known to be energetically unfavourable through simple valence shell electron pair repulsion theory, and experiments probing the local structure[12] have found that the O–Si–O bonds are in fact bent and the apparent linearity is due to averaging of the distribution of Si positions, shown in Figure 1.3.

Whilst disorder in crystalline materials is sometimes random; physical interactions between atoms can result instead in non-random, *correlated* disorder. Correlated disorder appears to arise *via* two scenarios—an underconstrained configuration with degenerate ground states, such that a unique ordering pattern

is not realised, or, an incompatibility between the interactions that govern the geometry of a lattice, also known as 'geometric frustration'.[14] Disorder arising from the former of these is illustrated by the example of hypothetical square ice (Figure 1.2(e)), as described by Keen and Goodwin.[14] Short-range interactions between O and H atoms means that, in this two-dimensional representation, there are ordered arrangements of O–H bonds along rows and columns but there is no requirement for order between them, hence there is correlated disorder.

Disorder arising from geometric frustration is illustrated by the Ising triangular antiferromagnet problem.[15] Ising spins (occupying one of two 'up', or 'down' states) arranged on a triangular lattice are frustrated where energy minimisation is driven by neighbouring spins occupying opposite states, but cannot be fully minimised due to the third spin necessarily aligning with another. Figure 1.2(f) represents a solution for opposing spins (depicted by blue and red circles) placed on a triangular lattice where on average four nearest neighbours are in an opposite spin state and two are forced to be frustrated. Although the long-range order is lost, the spin states are not random and are correlated.

In many functional materials, correlated deviation from perfect periodicity is found to play a significant role in governing functionality, for example in $BaTiO_3$, the subject of Chapter 3, which will be discussed later in detail.

1.2.1 Measuring disordered structures

There are a number of local structure probes useful for exploring solid-state structures. Spectroscopic techniques such as X-ray absorption near edge structure (XANES)[16] and extended X-ray absorption fine edge structure (EXAFS)[17,18] provide information about specific elements, oxidation states and the coordination geometry of a targeted site within a material. Nuclear magnetic resonance (NMR) spectroscopy[19] is used to study the local environments of specific nu-

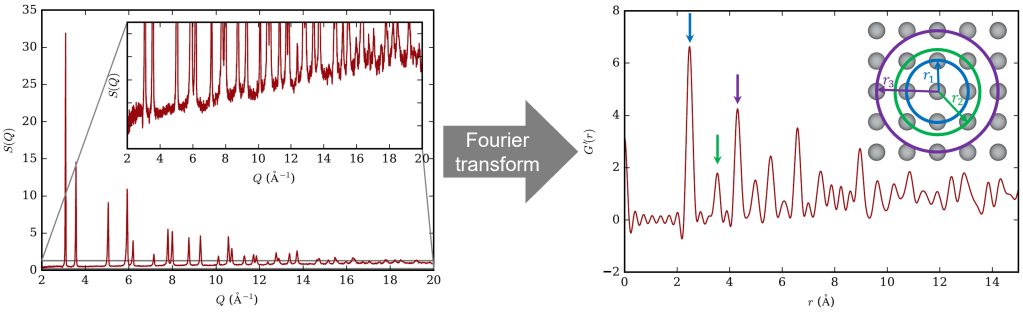

Figure 1.4: (a) The total scattering structure factor of Ni with an inset to highlight the region under which diffuse scattering is observed. (b) The corresponding PDF with an indication of specific atom–atom distances giving rise to the peak positions.

clei. Raman spectroscopy[20] also provides local structure information through the identification of vibrational modes—the number and character of which place constraints on the local symmetry. While the methods outlined above all have their individual strengths, they are limited, in that they can only identify very short-range structures (*i.e.*, first coordination spheres or individual molecules).

The technique of total scattering, however, probes all pair-wise interactions providing an instantaneous snapshot of all atom–atom distances within a material. Whilst in average-structure analysis, diffuse scattering is modelled, and discarded, as 'background', in total scattering, both the Bragg and diffuse scattering are considered together, as a 'total scattering' pattern (Figure 1.4(a)). Fourier transformation of a total scattering gives a pair distribution function (PDF) (Figure 1.4(b)) which can be defined as a weighted histogram of all the atom–atom distances within a material.

Following the definitions described by Keen[21] (and with respect to neutron scattering), the partial PDF, $g(r)$, describes the distances between two atom types i and j:

$$g_{ij}(r) = \frac{n_{ij}(r)}{4\pi r^2 dr \rho_j}, \tag{1.1}$$

where $n_{ij}(r)$ are the number of particles of type j between distances r and $r + \mathrm{d}r$

from a particle of type i, and ρ_j is the weighted number concentration of particle j ($\rho_j = c_j\rho_0$, where c_j is the proportion of species j).

Where there is more than one type of atom, the total radial distribution function, $G(r)$ describes all the distances within the material and is the weighted sum of the partial PDFs ($g_{ij}(r)$):

$$G(r) = \sum_{i,j=1}^{n} c_i c_j \bar{b}_i \bar{b}_j [g_{ij}(r) - 1], \tag{1.2}$$

where c_i is the proportion of species i, $\bar{b}_i$ is the scattering length of species, i.

A PDF, $G(r)$, is related to the average structure factor $F(Q)$ *via* a sine Fourier transformation as follows;

$$G(r) = \frac{1}{(2\pi)^3\rho_0} \int_0^\infty 4\pi Q^2 F(Q) \frac{\sin Qr}{Qr} \mathrm{d}Q. \tag{1.3}$$

There are a number of normalisation types used for total scattering patterns and PDFs, each with their own merit, for example, the $D(r)$ normalisation (defined below) progressively enhances the longer range structure.

Whilst $F(Q)$ has limiting values of $F(Q \to 0) = -\sum_{i=1}^{n} c_i \bar{b}_i^{-2} + \eta$ and $F(Q \to \infty) = 0$, the normalised total-scattering structure factor,

$$S(Q) = \frac{F(Q)}{(\sum_{i=1}^{n} c_i \bar{b}_i)^2} + 1, \tag{1.4}$$

has limiting values of $S(Q \to 0) = -\sum_{i=1}^{n} c_i \bar{b}_i^{-2} / (\sum_{i=1}^{n} c_i \bar{b}_i)^2 + \eta$ and $S(Q \to \infty) = 1$, where the lower limit is essentially zero.

PDF normalisations used in this Thesis are:

$$G'(r) = G(r) / (\sum_{i=1}^{n} c_i \bar{b}_i)^2 + 1 \tag{1.5}$$

and

$$D(r) = 4\pi r\rho_0 G(r), \tag{1.6}$$

and their limiting values are tabulated in Table 1.1. The $G'(r)$ normalisation means that for PDFs measured of solely positively scattering atoms (neutrons can be scattered negatively), the PDF is completely non-negative. This has been particularly significant for the work reported in Chapter 2, where treatment of data has required non-negative PDFs.

Table 1.1: Upper and lower limiting values for the alternative PDF normalisations used within this Thesis.

Notation	$(r < r^0)$	(r $\rightarrow \infty$)
$G(r)$	$-(\sum_{i=1}^{n} c_i b_i)^2$	0
$G'(r)$	0	1
$D(r)$	$-4\pi r\rho$	0

A good quality PDF, suitable for structural analysis is dependent on a number of requirements of the total scattering experiment; good signal to noise ratio, a reasonable dQ (diffraction resolution), accounting for any non-sample scattering, and a high maximum Q value ($Q = 4\pi\sin(\theta)/\lambda$), since the resolution (Δr) of a PDF is inversely related to the maximum Q value ($Q_{\max}$), $\Delta r = 2\pi/Q_{\max}$. A laboratory Ag-source diffractometer will provide a $Q_{\max}$ of 22 Å^{-1} at $2\theta = 90°$, although, data collection may take days to provide sufficient counting statistics. Synchrotron X-ray sources can provide intense, high energy X-rays, with $Q_{\max}$ values of up to 40 Å^{-1} and data collected in the order of seconds. Neutron time of flight (ToF) sources are often considered the 'gold standard' for PDF experiments due to the availability of short wavelength neutrons—providing $Q_{\max}$ values of up to 50 Å^{-1}—and the fact that neutrons continue to scatter strongly at high Q, whereas X-rays do not.

One of the strengths of total scattering is that the PDF can be used to perform quantitative analysis. Therefore, structural models can be compared with, and

refined against the measured PDF. Not only will the PDF provide short (to medium)-range local structure of a material (tens-to -hundreds of Ångströms[22]), but the ability to refine a structural model against both the PDF and Bragg data allows both local and average structure pictures to be reconciled, simultaneously.

The technique of total scattering has provided insight into a number of functional crystalline materials. Negative thermal expansion (NTE) is useful for many applications including for aerospace engineering, but the phenomenon whereby the volume of a material decreases on warming[23,24] is puzzling when observed with average structure techniques. The archetypal NTE material, ZrW_2O_8—when characterised with conventional X-ray diffraction—indicates that bond lengths unphysically shorten with increasing temperature.[25] Using PDF analysis, which is sensitive to correlated displacements of pairs of atoms, rather than individual atoms, it was found that the NTE behaviour was due to rotations of rigid units of ZrO_6 and WO_4 polyhedra.[26]

The $La_{1-x}Ca_xMnO_3$ series, studied for its colossal-magnetoresistance (CMR) property,[27] is another example of where total scattering has provided important structural information. Short-range correlated ordering of the Jahn-Teller (JT) distorted MnO_6 octahedra is only visible using local methods, and PDF experiments[28–30] have shown that whilst the average structure remains essentially unperturbed despite changes in the CMR behaviour, the local structure contains domains of ordered JT-distorted MnO_6 units.

Ongoing experimental development means that PDF measurements are increasingly used for *in operando*[31–34] and *in situ* studies.[35,36] For example, using *in operando* cell cycling, Hua *et al.* were able to measure the local structure of anode materials; Fe and Mn oxide, finding differences in the reaction mechanisms that had previously accepted within the field.[37]

1.3 Phase transitions

Temperature and pressure are common means of driving structural change through the addition or removal of thermal energy, or by minimising the free volume.[38–40] For example, the ZrW_2O_8 NTE[26,41] material previously mentioned not only exhibits temperature-induced functionality but also possesses useful pressure-related properties.[42,43] The disappearance of Bragg peaks indicates that under pressures of more than 1.5 GPa, the material goes through pressure-induced amorphisation.[44] Keen *et al.*[45] found through PDF measurements that new W–O–W bonds were formed on the application of pressure, and that the amorphisation mechanism was not unlike that found for the NTE behaviour, with correlated rotations and translations of the polyhedral units.[46]

Many of the property-inducing phase transitions of functional materials can be described as either displacive[47] or order-disorder (OD) type (depicted in Figure 1.5). The former involves concerted motions of atoms that change the symmetry of the crystal structure, for example, in $PbTiO_3$, Pb^{2+} and Ti^{4+} cations break inversion symmetry by moving along the [001] direction above the phase transi-

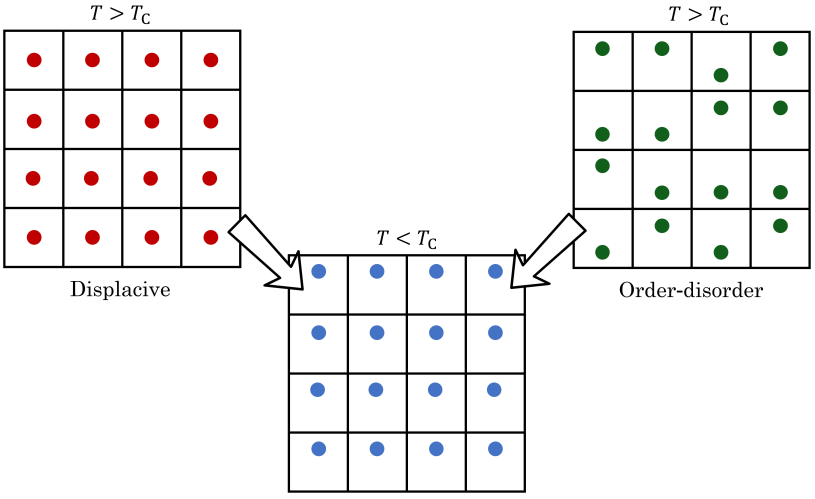

Figure 1.5: A schematic of displacive and order-disorder phase transitions showing the time-averaged positions of the atoms in the unit cells, where T_C is the phase transition temperature.

tion temperature.[48,49] After an OD phase transition, atoms that were in a disordered arrangement above the transition temperature become ordered on specific crystallographic sites below the transition temperature, resulting in a lowering of the crystallographic symmetry, whilst the local environments remain largely unchanged across the transition. This type of phase transition is exemplified by the calcite ($CaCO_3$) material, where a temperature-induced orientational OD phase transition is found due to temperature-induced ordering of CO_3^{2-} molecular ions in the [001] direction above 1260 K.[50,51]

Crystalline SiO_2 on heating, provides another example of displacive phase transitions.[12] At 573 °C a subtle phase transition from α-quartz to a β phase occurs, where the connectivity of SiO_4 tetrahedra remains the same and no bonds are formed or broken, although the tilting and symmetry of the system is altered. Above 870 °C, another phase transition occurs, to β-tridymite and again, at 1470 °C to β-cristobalite. The low-temperature α–to–β transition is an example of a displacive transitions where no bonds are formed or broken, whereas the higher-temperature phase transitions are reconstructive and involve a significant rearrangement of the structure where bonds can be formed and broken.

Ehrenfest classifications[52] may be used to classify a phase transition, based on how chemical potential (or Gibbs free energy, G) changes with the phase transition. Gibbs energy can be defined as:

$$G = U + PV - TS, \tag{1.7}$$

where U is the internal energy, P is the pressure, V is the volume, T is the temperature and S is the entropy. An abrupt change in both volume and entropy/enthalpy results in a discontinuity in the first derivative of Gibbs *versus* temperature or pressure - this defines a first order phase transition. First-order

transitions involve a latent heat and therefore hysteresis is often observed, with a difference in transition temperature on heating compared to cooling. Another characteristic of a first order phase transition is phase coexistence. A second order phase transition is where the volume, enthalpy and entropy do not change abruptly at the phase transition—there is a discontinuity in the second derivative of the free energy with respect to temperature or pressure.

Phase transitions can also be categorised as discontinuous or continuous, depending on definitions defined by Landau and Ginzburg.[47] Simple Landau models can be used to predict how the entropy will change across a phase transition assuming an order parameter (OP), η, that tends to zero at the phase transition temperature, T_C (on warming). This OP can be used to describe the distortion of the structure compared to the higher symmetry structure. For example, a phase transition in a perovskite ABO_3 might occur due to ordered tilting of BO_6 octahedra, in which case, the angle of the tilt may be used as the OP. The introduction of an OP for the description of phase transitions allows the link between thermodynamic properties and crystallographically OPs to be made.

The phenomenological Landau theory uses the assumption that the free energy of the system, $G(\eta)$, can be approximated as a function of η:

$$G(\eta) = G_0 + \frac{1}{2}A\eta^2 + \frac{1}{4}B\eta^4 + \frac{1}{6}C\eta^6 + ..., \tag{1.8}$$

where A, B and C are constants and G_0 is the free energy of the system when $\eta = 0$. For continuous phase transitions where there is only one OP, the free energy of a system can be expressed as a sum of only even powers (as shown in Equation 1.8), and often only terms up to the fourth power are found to be necessary. It is important to note that the relationship described by Equation 1.8 is only expected to accurately describe the free energy behaviour close to the

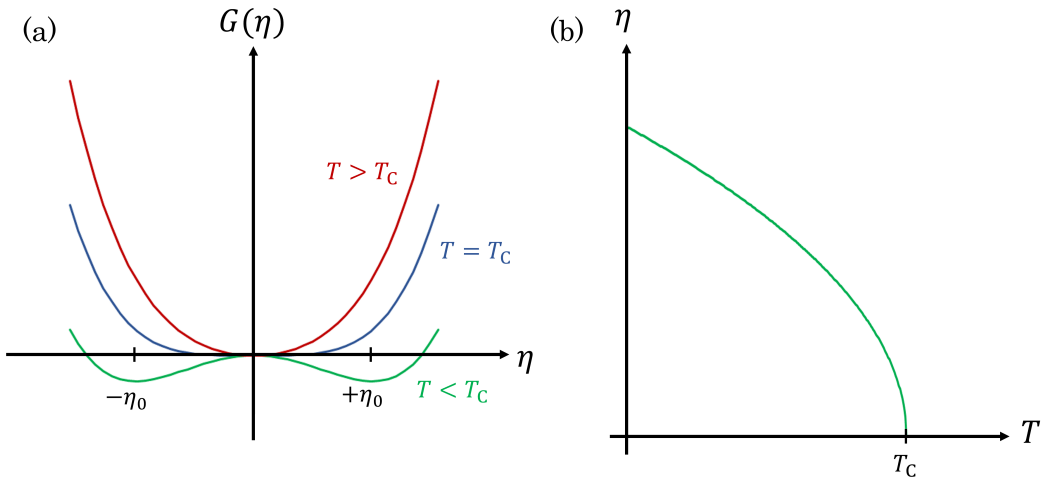

Figure 1.6: (a) Plot of Landau free energy curves for a system with OP, η showing that at $T<T_C$, the solution $\pm\eta_0$ minimises the free energy whereas at $T>T_C$, $\eta = 0$ is the only solution. (b) Plot of Equation 1.10 (provided in the text) of the evolution of parameter η with temperature.

phase transition.[47]

Figure 1.6(a) shows three free-energy curves for a second-order displacive phase transition. For $T>T_C$, the solution of the function is $\eta = 0$, and when $T<T_C$, $\eta = 0$ becomes a local maximum. Or in terms of the structural phase transition, for temperatures above the phase transition a free energy curve corresponds to a parabola centred at $\eta = 0$ which means that the undistorted structure is stable. Cooling through the phase transition temperature results in the minimum of the parabola shifting to a non-zero value of the OP, hence the distortion becomes energetically favourable.

In Landau theory it is generally assumed that a phase transition may be described by a temperature dependent coefficient of the second-order term of the OP,

$$A(T) = a(T - T_C), \tag{1.9}$$

and by substitution and subsequently solving $G(\eta)$, a solution is found for when

$T<T_C$. It can be shown that an expression for the variation of η with T is realised:

$$\eta = \eta_0(T_C - T)^{1/2}. \tag{1.10}$$

This relationship, plotted in Figure 1.6(b) can be used to predict the behaviour of a second-order phase transition when there is one OP driving the transition, and has been used in Chapter 4.

A more complex treatment of Landau theory can be used for discontinuous (first order) phase transitions and a full explanation can be found elsewhere.[53]

1.3.1 Representation analysis

Group theory is another useful mathematical tool for describing the relationship of symmetry elements in a crystal structure. Symmetry elements are grouped into types, or, 'conjugate' sets when $B = X^{-1}AX$, *i.e.*, A and B are conjugate. The operations of a symmetry element and the resulting change on a physical system can be expressed as a combination of vectors and matrices. This type of mathematical description is said to be a representation of a given group and the symmetry elements act as linear operators to result in specific representations of the group.

Character tables contain information about how specific distortions will break the symmetry of a point group, or, how the distortion transforms after the application of each symmetry operation of the group. Information about the retention or loss of symmetry is contained within the table and shows how many classes or, irreducible representations (irreps.) there are. An irrep. of a point group is then said to be a unique symmetry-breaking of an aristotype structure and cannot be broken down into smaller representations. Irreps. are orthogonal to each other which means that symmetry-breaking distortions described by OPs are orthogo-

nal to each other—this feature is exploited for analysing phase transitions using Landau theory.

The irreps of space groups are based on Bradley-Cracknell[54] notation, $K_n^{+/-}$, where K is the symbol for the high-symmetry points in reciprocal space, n is an identification number (with no other significance) and $+/-$ denotes a conservation $(+)$ or breaking $(-)$ of symmetry. For example the irrep. Γ_4^- of the parent group $Pm\bar{3}m$ describes a vector, **k** of [0,0,0] and the minus sign indicates that the irrep. breaks inversion symmetry. Additional information is provided by the order parameter direction (OPD) in the case of Γ_4^-, the general OPD is described by (a, b, c), indicating that it is a triply degenerate irrep. This can be understood by considering the correlated displacements along x, y and z, which can be transformed to be equivalent under the operators of $m\bar{3}m$. Although there is no symmetry-based constraint requiring the three dimensional basis that spans the triply degenerate irrep to coincide with lattice directions, the irrep matrices are usually chosen such that this is the case. Therefore, an OPD of (a,a,0) for example would describe a distortion acting in equal magnitude along the **a** and **b** lattice directions. It is important to realise that in general, irreps. and OPs can have dimensions exceeding three, and therefore there is not always a straightforward correspondence between the basis of the lattice vectors and the distortion-describing irrep.

There are a number of online tools such as the Bilbao Crystallographic Server,[55–57] designed to aid the routine representation analysis of crystal structures. Representation analysis is particularly useful for the study of displacive phase transitions, where a symmetry-breaking distortion can be described by a single or combination of 'irreps.', or for probing the local OPD to distinguish between OD and displacive transitions. The online tool ISODISTORT[58] has been used for mode decomposition and analysis throughout this Thesis.

1.4 Structure-property relationships of metal oxides

Solid oxide materials are ubiquitous in modern day technologies and are used in a multitude of functional devices such as solar cells,[59] fuel cells,[60] superconductors, to name a few. They exhibit a wide variety of physical properties due to their rich chemistry. Chapters 3 and 4 report the average and local structures of the perovskite material, $BaTiO_3$ and a A_2BO_4 Ruddlesden-Popper structure, respectively. Their structures and degrees of freedom relevant to this Thesis are discussed in this section. The perovskite structure is popular for exploring functionality in solid state materials due to its apparent chemical and structural flexibility. The most simple perovskite structure (Figure 1.7) has the chemical formula ABX_3 where A and B denote cations and X denotes an anion, most typically an O^{2-} ion and henceforth labelled as such. The A–site is generally occupied by larger alkali or rare-earth metals and coordinated by twelve O^{2-} ions, and the smaller B-site—usually occupied by transition metals—is octahedrally coordinated by six neighbouring O^{2-} ions with these octahedra joined at their corners, forming a network which plays a key role in the functionality of the

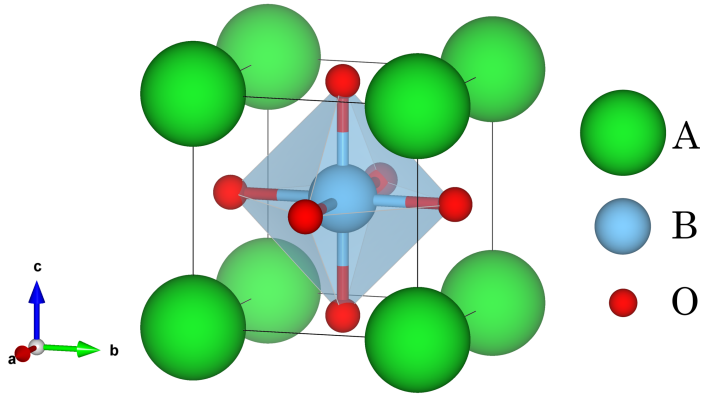

Figure 1.7: The highest-symmetry perovskite structure, where the B cation sits in exactly the centre of the unit cell, resulting in the highest symmetry cubic structure.

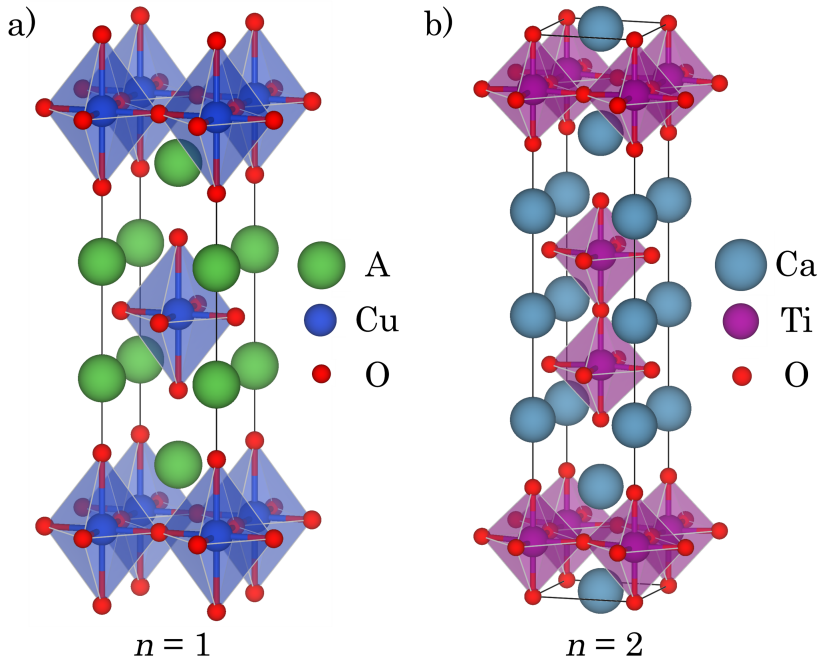

Figure 1.8: The crystal structures of Ruddlesden-Popper phases, (a) A_2CuO_4 ($n = 1$) and (b) $Ca_3Ti_2O_7$ ($n = 2$).

perovskite family.

Perovskite-related materials include Ruddlesden-Popper (RP) phases.[61,62] These structures consist of two-dimensional perovskite-type layers, interleaved with rock-salt layers. They have the general formula $A_{n+1}B_nX_{3n+1}$ where n corresponds to the number of octahedral layers. Notable examples of $n = 1$ and $n = 2$ RP phases (Figure 1.8) include A_2CuO_4 and $Ca_3Ti_2O_7$ respectively. The A_2CuO_4 material forms the basis of many high-temperature superconductor materials, with the A–site occupied by combinations of divalent (Ba, Sr, *etc*) and trivalent (La, Y, *etc*) atoms. $Ca_3Ti_2O_7$ (and $Ca_3Mn_2O_7$) has received recent attention due to the property of 'hybrid improper ferroelectricity', wherein two nonpolar distortions of the structure couple to a polar mode, generating an overall polar structure.[63]

The A– and B–sites of the perovskite and RP structures can accommodate a vast variety of elements, allowing the modification and design of specific mag-

netic, electronic and mechanical properties.[64,65] There are a number of ways the structure and property of a metal oxide can be influenced. Perhaps the simplest alterations can be made through size effects, where the chemical composition can be designed such that the ionic radii of the cations are slightly too large or too small.[66,67] This size mismatch for perovskites is often described and quantified by Goldschmidt's tolerance factor,[68]

$$t = \frac{r_{\mathrm{A}} + r_{\mathrm{O}}}{\sqrt{2}(r_{\mathrm{B}} + r_{\mathrm{O}})} \tag{1.11}$$

where r_{A}, r_{B} and r_{O} are the radii of the A, B and O ions respectively and a t value of 1 would describe an ideal undistorted (cubic) structure. Deviations from $t = 1$ result in a distortion of the perovskite structure through cation displacements, and—when t<1—flexibility *via* octahedral tilts and rotations often facilitate property-inducing phase transitions.

Where there are multiple atom-types occupying a single A- or B-site, ordering may occur–often described as rock salt, columnar or layered order.[69] If the two species are of similar charge and size, they are likely to be disordered. In the double perovskites, Sr_2FeMoO_6 and Pb_2ScTaO_6, disordering of the B-site cations is found to affect their physical properties of magneto-transport and dielectricity respectively.[70,71] Additionally, in the $AMnO_3$ material, the metal-insulator transition temperature is found to have a linear relationship with the A-site radius variance (where the average radii and charge is maintained).[64,65]

More complex effects such as orbital ordering can influence the physical properties and phase changes in solid metal oxides through orbital overlap and subsequent electronic effects. The orbitally-driven structural distortions of transition metals in octahedral geometries—ubiquitous in perovskite structures—are usually described by the Jahn-Teller (JT) distortion.

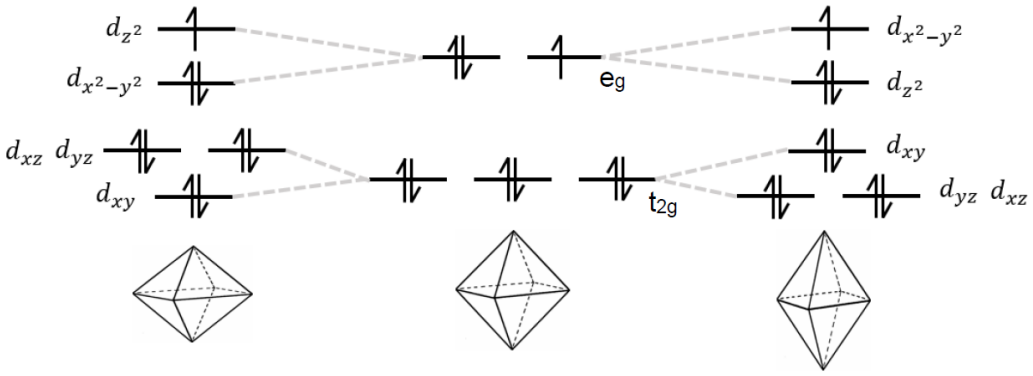

Figure 1.9: Diagram of the Jahn-Teller d-orbital splitting that occurs for a typical octahedral complex. The complex possesses a degenerate electronic ground state (middle), and distorts to remove the degeneracy, forming a lower energy system. Left, the z-ligands are compressed and right, the z-ligands are elongated.

The JT effect is a geometric distortion of a non-linear system and for octahedral complexes, the five d-electron orbitals are split into two degenerate states (labelled t_{2g} and e_g, shown in Figure 1.9). When the d-orbitals are filled asymmetrically, then JT effects occur where axial and equatorial bond lengths will lengthen or shorten to remove the degeneracy by distorting the octahedra. This acts to lower the overall free energy of the system *via* symmetry lowering. JT distortions often compete with other effects, including crystal strain, Coulombic repulsions and entropy, since at high temperatures, configurational degeneracy is favored. All of these factors can lead to a complex orbital ordering pattern of JT-elongated or compressed metal-oxygen bond lengths. Therefore, determining the average crystallographic structure reveals the orbital ordering of the structure to an extent, but deconvolution of the exact behaviour of the orbitals from any properties that arise from this effect is difficult. Understanding how the geometric JT effect couples with the crystal structure and functional phase transitions is one of the aims of this Thesis.

The second-order JT effect[72,73] (also known as the pseudo JT effect)—a key instability of the prototypical ferroelectric $BaTiO_3$—also results in distortions of the octahedral geometry. The second-order JT distortion is the result of interac-

tions between filled and empty molecular orbitals that are symmetry forbidden. Symmetry-breaking allows the highest-energy occupied orbitals to interact with lowest-energy unoccupied orbitals, and therefore an off-centre distortion of the central atom is favoured.

In perovskites, the second-order JT effect can arise either due to the presence of cations with a non-bonding lone pair or, the presence of d^0 metal ions. The latter is responsible for the ferroelectrically-significant off-centre displacement of the Ti^{4+} cation of the $BaTiO_3$ perovskite structure, where the hybridisation of empty Ti *d*-orbitals with filled O *p*-orbitals results in a near-degenerate state. JT distortion arising from non-bonding lone pairs is more common of heavier main-group elements (for example, $BiFeO_3$) and instead involves hybridisation of *s* and *p*-orbitals of the metal with the *p*-orbitals of the O anion.

1.5 Measuring average and local structure

1.5.1 Synchrotron X-ray sources

Although laboratory X-ray sources are useful in providing accessible X-rays, particle accelerators can produce brilliant, high flux light, with the ability to perform high-resolution measurements very quickly, allowing in-depth studies of the average and local structures of functional materials. Diamond Light Source (DLS) and the Taiwan Photon Source (TPS) were utilised for experiments presented in this Thesis. The two facilities are comparable, both being 3 GeV third-generation light sources, so-named because of the use of insertion devices—magnets designed to 'wiggle' or 'undulate' the electrons to produce intense sources of light. A synchrotron light source (schematically shown in Figure 1.10) produces 'synchrotron light' by using an electron gun to propel electrons down a linear accelerator (linac) into a booster ring where the electrons are accelerated to relativistic speeds. The

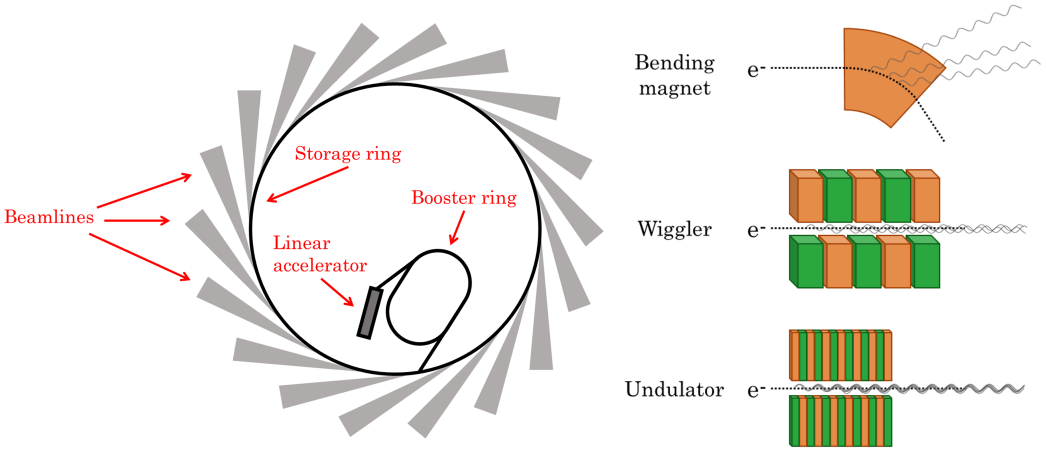

Figure 1.10: Left, a schematic of a synchrotron layout. Right, diagrams of synchrotron light being produced by a bending magnet, wiggler and undulator. The different colours of the magnetic devices indicate a change in magnetic pole.

electrons then enter the storage ring, where a series of bending magnets keep the beam focused and travelling around the ring. Synchrotron light is produced when the electrons change direction; either when they pass through bending magnets or insertion devices (Figure 1.10, right) the latter of which produce a more intense, tuneable light. The insertion device is either a wiggler—typically used where very high energies (up to 100 keV) are required—or an undulator, which produces a more intense beam with a much narrower radiation bandwidth. As the electrons change direction, they emit a beam of radiation which enters the optics hutch of the beamline, where the beam is focussed and collimated by optic devices such as monochromators and mirrors, before ultimately arriving at the sample position.

Two types of dedicated X-ray beamline were used for the work reported in this Thesis. The X-ray PDF beamline (I15-1, DLS) was used for local structure, total scattering experiments and high-resolution diffraction beamlines I11 (DLS), 09A and 19A (both at TPS) were used for variable-temperature average structure determination.

Pair distribution function beamline

The dedicated X-ray PDF beamline I15-1[74] at DLS was used for the local structure study reported in Chapter 4. The I15-1 beamline optics and end-station have been optimised to produce high energy X-rays, high flux and low background required for high quality PDFs. A wiggler device is used to produce high-energy X-rays and the combination of a Laue monochromator,[75] composed of three silicon crystals such that one of three energies can be chosen (40.0, 65.4 or 76.6 keV), with a focussing mirror[76] means that high energy X-rays and high flux are achieved. I15-1 utilises two large area detectors with one placed close to the sample at 45° to provide higher $Q_{\max}$ values (up to 40 Å^{-1} at 76.7 keV). A second detector is mounted further from the sample, allowing the simultaneous measurement of higher-resolution Bragg data.

The fact that X-ray scattering factors decrease as a function of diffraction angle means that the measured scattering factor must be divided by the square of the atomic form factor[77] in order to remove the scattering angle-dependency and to enhance the scattering at higher angles (high Q).[78] Often, the decay in intensity at high Q and resulting degradation of the signal-to-noise ratio means that PDFs generated from X-rays are, in practice, limited to a $Q_{\max}$ value below the theoretical experimental capability.

I15-1 is equipped with a Oxford Instruments Cryojet5 and a hot air blower, providing a combined temperature range of 85–1100 K, enabling investigation of local structure using non-ambient and variable temperature. Data reduction techniques must consider the changing sample environment, but otherwise remain the same.

High-resolution powder diffraction beamlines

Although a number of high-resolution powder diffraction beamlines (09A and 19A at the Taiwan Photon Source (TPS) and I11 (DLS)) were used for the work reported in Chapter 4, the experimental set-up and beamline design is essentially the same and the details for I11[79] are reported here.

The high flux afforded by synchtrotron light allows very high resolution diffraction data suitable for Rietveld analysis to be collected in a matter of seconds where data collection on laboratory diffractometers take on the order of hours. On I11, an undulator device is used to provide high-intensity X-rays, with energy tunable to a range of 5–25 keV (0.4–2.1 Å), along with a Si monochromator to select the specific energy. Position sensitive detectors (PSD) based on Si-strip modules are utilised for fast data collection and are particularly useful for *in situ* and *in operando* studies of functional materials under non-ambient conditions.

I11 is equipped with an Oxford Cryostream800+ and a hot air blower, with a combined temperature range of 100–1200 K. Beamlines 09A and 19A are capable of reaching temperatures down to 10 K through the use of an ESRF DynaFlow cryostat and therefore were vital for identifying the low temperature (<100 K) phase transitions reported in Chapter 4.

1.5.2 Time-of-flight neutron sources

Unlike X-rays, neutrons used for diffraction experiments cannot be produced in a laboratory and are instead generated at large-scale facilities either by nuclear fission at a reactor source (such as Institut Laue-Langevin, France), or spallation (at the Spallation Neutron Source, U.S.A. or ISIS Neutron and Muon Source, UK, for example). Neutrons produced by fission are high energy (MeV-region) and therefore must be moderated to wavelengths suitable for diffraction. Reactor sources are constant wavelength sources, whereas spallation, or, ToF flight

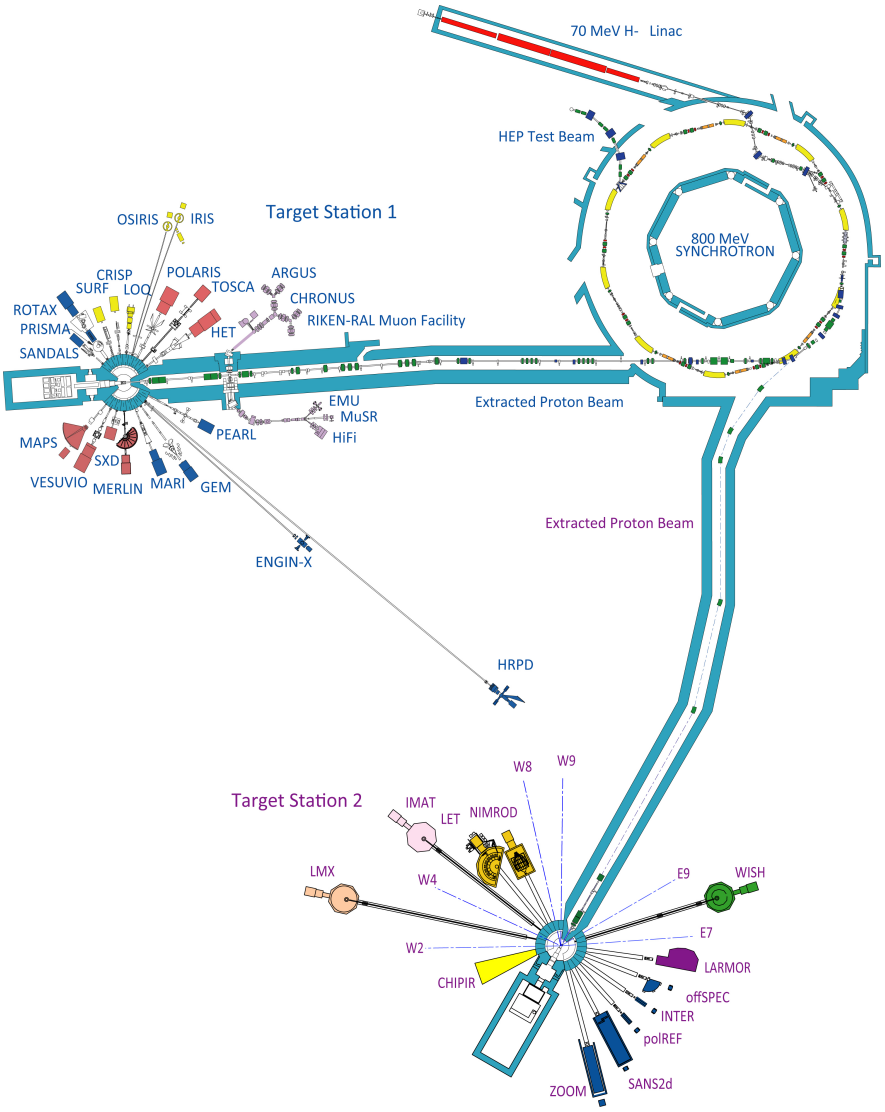

Figure 1.11: The layout of ISIS, the target stations and the instruments that surround each target.

sources use a range of neutron wavelengths, which is advantageous for particular experimental set ups, constrained to a 90° scattering geometry (*i.e.*, high pressure environments, discussed in detail below).

ISIS is a spallation facility and was the sole neutron source used for the work reported within this Thesis. Figure 1.11 shows the current layout of ISIS and its instruments. H^- ions are produced by an ion source (Cs vapour mixed with H_2 gas) using an electric discharge. The negative hydrogen ions are accelerated before being passed through a thin alumina foil which removes the electrons, leaving a beam of protons. The protons are accelerated further and then collided with a

tungsten target. As the tungsten target is bombarded with high energy protons, neutrons are released from the nuclei of the target atoms, a process called 'spallation'. This results in an intense neutron beam which is moderated by hydrogen, methane, or water moderators to slow the neutrons to useful wavelengths for experiments. ISIS is a pulsed ToF neutron source, and therefore the time taken for the neutron to reach the detectors from the moderator, t, is measured and related to d-spacing (d) and the flight path (L) by:

$$d = 1.9777 \times 10^{-3} t[Lsin\theta]^{-1}. \tag{1.12}$$

While X-rays are scattered by the electron cloud of each atom and suffer a fall-off in intensity at higher scattering angles (Figure 1.12), neutrons are scattered by the nuclei of atoms, which can be treated as point scatterers. Therefore, scattered neutrons do not suffer from decreasing scattering power as a function of scattering angle, so strong peaks are still obtained at high 2θ values, particularly for experiments carried out at low temperatures where smearing out of nuclear density due to thermal motion will be negligible. Another consequence of 'point

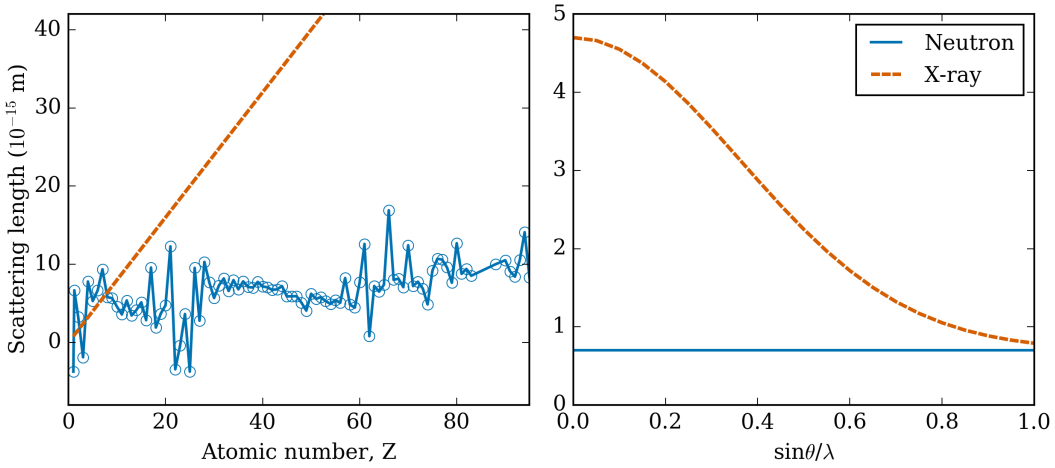

Figure 1.12: Left: Scattering lengths of X-rays and neutrons as a function of atomic number, Z. X-rays have a strong dependence on both Z and the scattering angle, θ, where neutrons do not. Right: The angular dependence of the X-ray and neutron scattering factors.

scattering' is that there is no dependence on Z values (shown in Figure 1.12), due to the fact the scattering is governed by nuclear rather than electromagnetic interactions. The nuclear interactions instead depend heavily on the makeup of the nuclei (number of protons, neutrons, *etc*). Unlike X-rays, there is no clear relationship between scattering power and nucleus composition. A fortunate consequence of this is that neutron diffraction is a useful technique for studying light atoms (particularly perovskite materials where often oxygen-containing octahedra play a key role in functionality), or materials with atoms of similar Z numbers which would not otherwise be distinguished using X-ray diffraction techniques. Neutron scattering lengths indicate how strongly elements and isotopes will scatter, and can be either positive or negative, for example the scattering length of Ti is -3.438×10^{-15} m and O is 5.803×10^{-15} m.

Scattering lengths can vary greatly between isotopes of the same element, and this isotope sensitivity is exploited by techniques such as selective labelling, to investigate localised environments in samples such as organic molecules.[80] Another useful property of neutrons is that they are highly penetrating and therefore there are generally less restrictive requirements of sample environment, compared with an analogous X-ray experiment. An unfortunate drawback of neutron scattering is that ^{1}H is an incoherent scatterer which leads to increased background and therefore most hydrogen-containing samples must be deuterated (substituted for ^{2}H), though this can be exploited for isotope substitution experiments.

As previously stated, ToF sources generally produce very good quality PDFs, where instruments such as GEM at ISIS achieve $Q_{\max}$ values of up to 50 Å^{-1}, resulting in a Δr of ca. 0.1 Å.

High-pressure neutron diffraction beamline

The dedicated high-pressure beamline PEARL was used to study the pressure-dependent local structure of $BaTiO_3$ (Chapter 3) and the average structure of Mg-substituted $La_{1.875}Ba_{0.125}CuO_4$ (Chapter 4). Chapter 2 is dedicated to the development of novel procedures to allow local structure techniques to be carried out more routinely, specifically using PEARL and measuring crystalline materials.

PEARL is a diffractometer (Figure 1.13) located on Target Station 1.[81] The instrument is supplied with neutrons *via* a liquid methane moderator set at 110 K, after which the beam is collimated using B_4C jaws which shape the beam to be 5×5 mm^2 at the sample position. Detector efficiency can be accounted for by normalising each detector by an incident beam scintillation monitor. Variation in flux with wavelength is normalised for by a vanadium measurement.

The instrument has been designed specifically to accommodate the Paris-Edinburgh (PE) press which is used to perform *in situ* high pressure measurements. The PE press is contained within an evacuated tank, 12.8 m from the methane detector, which can be translated along the beam path to ensure the

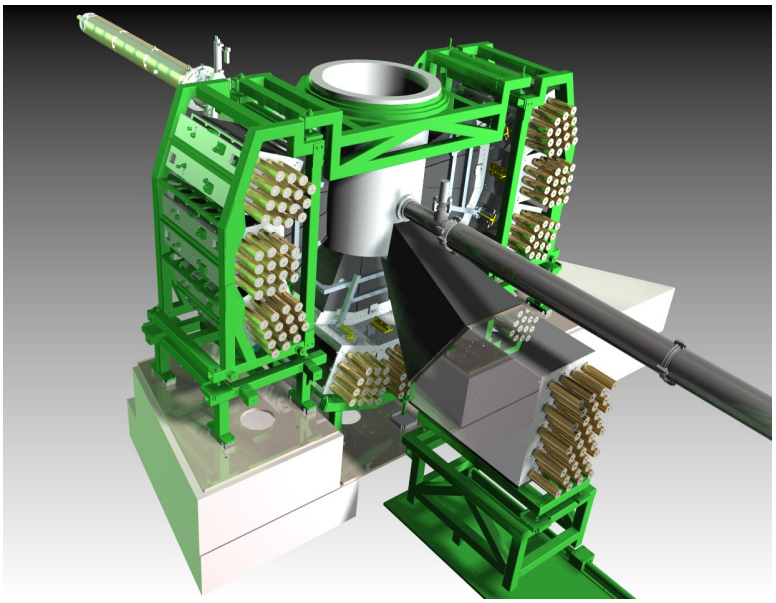

Figure 1.13: Schematic of the high-pressure instrument PEARL. The PE press sits in the beam and is surrounded by transverse detector banks.

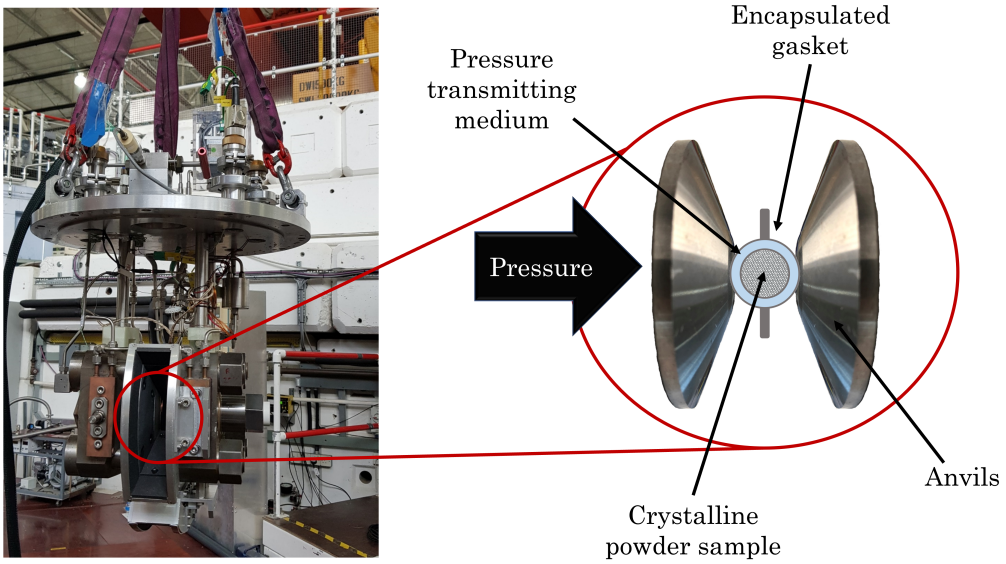

Figure 1.14: A PE press attached to the flange used to lower and seal the press into the evacuated sample tank. The ZTA anvil and gasket assembly is shown schematically on the right.

ToF path remains constant when pressure is increased. PEARL has nine transverse detectors which are normal to the incident beam, with a $81.2° \leq 2\theta \leq 98.8°$ diffracting angle range defined by the opening angle of the anvils used. The transverse detectors observe d-spacing in the range 0.3–4.1 Å corresponding to a Q-range of 1.5–20.3 Å.

In situ variable-pressure diffraction measurements are achieved using large-volume PE press (shown in Figure 1.14), with Bridgman-type opposed anvils with a toroidal profile.[82] Samples are typically loaded into a null-scattering TiZr (designed such that the negative and positive scattering lengths of Ti and Zr respectively, cancel out) gasket which sits in the centre of two opposing anvils, designed to have a geometry that accommodates the shape of the gasket. The anvils then sit inside the PE press, which is fitted with a boron nitride insert for collimation and boron-coated collimation 'ears' through which the scattered neutron beam will pass. The press is orientated towards the incident neutron beam, such that the neutron beam passes through the anvil and the scattered

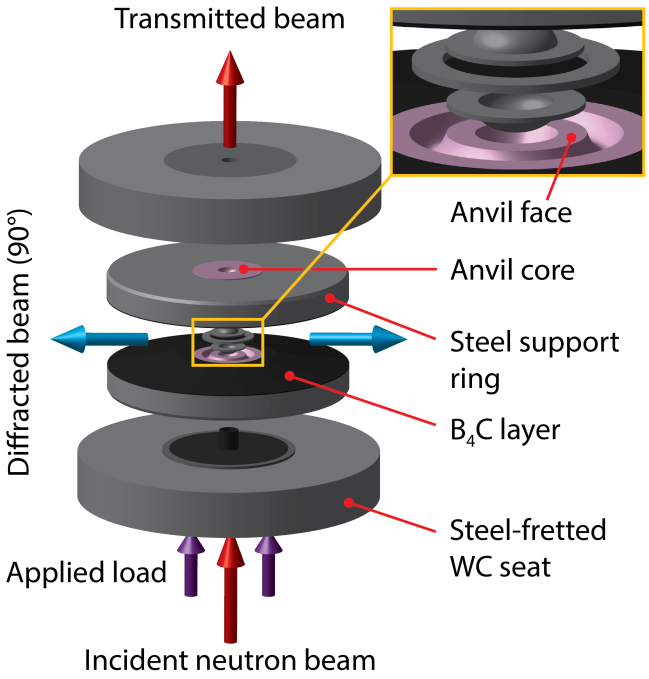

Figure 1.15: Schematic of the anvil and gasket assembly used on PEARL, with incident and diffracted beams indicated. The Figure is modified from Figure 3 in Reference 81.

beam is received by the 90° transverse detectors (shown in Figure 1.15). Load is applied to the gasket *via* an oil or pentane-driven piston towards one of the anvils. Due to the inverse relationship between volume and pressure, high pressure experiments notoriously require small sample volumes in order to achieve high pressure conditions, however, neutron experiments require sufficiently large sample volumes to negate the effect of weakly interacting neutrons and low flux compared to that of X-ray sources. Therefore there is a balance to be struck between counting statistics and attaining multi-GPa pressures. Standard sample volumes on PEARL are 66 mm^3, as per the design of the gasket and anvils which deliver high pressure.

The pressure applied to the sample is measured *via* known relationships between the pressure, temperature and volume of a measured material, or, an 'equation of state' (EoS). The Birch-Murnaghan (BM) EoS[83] is widely used by the high-pressure community and has been utilised in this Thesis both to determine experimental pressures and to derive the compressibility (bulk moduli values) of

materials with otherwise unknown EoS's. Where the EoS of a material is unknown, a pressure marker must be used. For neutron diffraction this is most commonly either a Pb pellet or NaCl powder.

The inclusion of a hydrostatic medium is important particularly for high-pressure measurements of crystalline materials, where non-hydrostatic conditions can result in sample strain, often evidenced by broadening Bragg peaks. Common hydrostatic media include methanol:ethanol mixtures, iso-*n*-pentanes and gases such as helium and argon.[84]

1.6 Thesis outline

Although total scattering techniques are now well established and used quite routinely, experimental requirements of respective (neutron) high-pressure and total scattering techniques means that, thus far, no such studies have been performed for crystalline materials under hydrostatic conditions. The inclusion of a PTM in order to afford hydrostatic pressure presents difficulties in that signal from the PTM will also be present in the measured PDF. The work reported in Chapter 2, is a facility development project, funded by the Science and Technology Facilities Council, and aims to address the difficulties of performing such an experiment. Simple crystalline materials Ni and MgO are first used as proof-of-principle examples and subsequent results derived from measurements of a more flexible crystalline material, α-quartz represent the first science-case of hydrostatic local structure high-pressure measurements on PEARL.

The type of significant structural insight available from high-pressure local structure experiments on PEARL is then illustrated by the study reported in Chapter 3, where the pressure-induced ferroelectric phase transition of $BaTiO_3$ has been investigated. Whilst the temperature-induced tetragonal-to-cubic phase

transition has been found to progress as an OD-type transition, experiments and analysis reported in this Thesis shows that the application of pressure recovers a more displacive behaviour. Careful modelling of local structure distortions over different ranges of the measured PDFs has allowed significant structural insight to be gained from relatively low resolution PDFs ($Q_{\max} = 20.32$ Å^{-1}).

The anomalous behaviour of the high-temperature superconductor material, $La_{1.875}Ba_{0.125}CuO_4$ (LBCO)—where there is a dip in the superconducting temperature for the specific '0.125' Ba doping—has been explored using and composition, temperature and pressure. The substitution of the JT-active Cu^{2+} cations with JT-inactive Mg^{2+} has enabled the role of the anisotropic JT distortion to be scrutinised. Variable-temperature high resolution XRD measurements have shown that a low temperature phase coexistence of tetragonal and orthorhombic phases, observed for LBCO, is removed when Mg^{2+} is substituted into the structure. Additionally, it is found that higher Mg-content increases the lower temperature first-order and higher temperature second-order phase transition temperatures. X-ray PDFs of the high temperature phase provide valuable insight into the nature of the high temperature local structure behaviour. Further average structure experiments using high-pressure neutron diffraction have allowed the pressure-induced phase transition to be explored and fundamental pressure-induced structural changes such as compressibility to be investigated.

1.7 References

[1] M. Pasta, D. Armstrong, Z. Brown, J. Bu, M. R. Castell, P. Chen, A. Cocks, S. A. Corr, E. J. Cussen, E. Darnbrough, V. Deshpande, C. Doerrer, M. S. Dyer, H. El-shinawi, N. Fleck, J. T. S. Irvine, H. J. Lee, G. Li, E. Liberti, I. Mcclelland, C. I. Thomas, S. J. Turrell, M. Vestli, C. K. Williams, Y. Zhou

and P. G. Bruce, *J. Phys. Energy.*, 2020, **2**, 032008.

[2] A. M. Abdalla, S. Hossain, P. M. I. Petra, M. Ghasemi and A. K. Azad, *Front. Energy*, 2020, **14(2)**, 359–382.

[3] J. F. Scott and C. A. Paz De Araujo, *Science*, 1989, **246**, 1400–1405.

[4] R. J. Harrison and A. Putnis, *Surv. Geophys.*, 1998, **19**, 461–520.

[5] C. N. R. Rao and K. Rao, *Phase Transitions in Solids: An Approach to the Study of Chemistry and the Physics of Solids*, McGraw-Hill, 1978.

[6] R. D. K. Roy and H. A. McKinstry, *Annu. Rev. Mater. Sci.*, 1989, **19**, 59–81.

[7] W. H. Bragg and W. L. Bragg, *Proc. R. Soc. Lond.*, 1913, **88**, 428–438.

[8] G. A. Slack and M. A. Hussain, *J. Appl. Phys.*, 1991, **70**, 2694–2718.

[9] J. Nie, R. Ranganathan, Z. Liang and P. Keblinski, *J. Appl. Phys.*, 2017, **122**, 045104.

[10] A. Giri, B. F. Donovan and P. E. Hopkins, *Phys. Rev. Mater.*, 2018, **2**, 056002.

[11] T. Sakuntala, A. K. Arora, N. V. Shekar and P. C. Sahu, *Europhys. Lett.*, 1998, **44**, 728–733.

[12] M. G. Tucker, M. T. Dove and D. A. Keen, *J. Phys. Condens. Matter*, 2000, **12**, L723–L730.

[13] M. T. Dove, M. G. Tucker and D. A. Keen, *Eur. J. Mineral.*, 2002, **14**, 331–348.

[14] D. A. Keen and A. L. Goodwin, *Nature*, 2015, **521**, 303–309.

[15] G. H. Wannier, *Phys. Rev.*, 1950, **79**, 357–364.

[16] G. S. Henderson, F. M. F. D. Groot and B. J. A. Moulton, *Rev. Mineral. Geochemistry*, 2014, **78**, 75–138.

[17] E. A. Stern, *Phys. Rev. B.*, 1974, **10**, 3027–3037.

[18] P. A. Lee and J. Pendry, *Phys. Rev. B.*, 1975, **11**, 2795–2811.

[19] S. E. Ashbrook, J. M. Griffin and K. E. Johnston, *Annu. Reports NMR Spectrosc.*, 2012, **11**, 485–508.

[20] L. A. Lyon, C. D. Keating, A. P. Fox, B. E. Baker, L. He, S. R. Nicewarner, S. P. Mulvaney and M. J. Natan, *Anal. Chem.*, 1998, **70**, 341–361.

[21] D. A. Keen, *J. Appl. Crystallogr.*, 2001, **34**, 172–177.

[22] D. Olds, C. N. Saunders, M. Peters, T. Proffen, J. Neuefeind and K. Page, *Acta. Cryst.*, 2018, **74**, 293–307.

[23] J. S. Evans, *J. Chem. Soc., Dalton trans.*, 1999, **19**, 3317–3326.

[24] G. D. Barrera, J. A. Bruno, T. H. Barron and N. L. Allan, *J. Phys. Condens. Matter*, 2005, **17**, R217–R252.

[25] K. W. Chapman, P. J. Chupas and C. J. Kepert, *J. Am. Chem. Soc.*, 2005, **127**, 15630–15636.

[26] M. G. Tucker, A. L. Goodwin, M. T. Dove, D. A. Keen, S. A. Wells and J. S. Evans, *Phys. Rev. Lett.*, 2005, **95**, 8–11.

[27] P. Radaelli, D. Cox and M. Marezio, *Phys. Rev. B*, 1997, **55**, 3015–3023.

[28] X. Qiu, T. Proffen, J. F. Mitchell and S. J. Billinge, *Phys. Rev. Lett.*, 2005, **94**, 1–4.

[29] E. S. Božin, X. Qiu, M. Schmidt, G. Paglia, J. F. Mitchell, P. G. Radaelli, T. Proffen and S. J. Billinge, *Phys. B Condens. Matter*, 2006, **385-386**, 110–112.

[30] T. Proffen and S. J. Billinge, *Appl. Phys. A.*, 2002, **74**, 1770–1772.

[31] M. Diaz-Lopez, G. L. Cutts, P. K. Allan, D. S. Keeble, A. Ross, V. Pralong, G. Spiekermann and P. A. Chatera, *J. Synchrotron. Rad.*, 2020, **27**, 1190–1199.

[32] K. Chapman, *MRS Bulletin*, 2016, **41**, 231–238.

[33] P. K. Allan, J. M. Griffin, A. Darwiche, O. J. Borkiewicz, K. M. Wiaderek, K. W. Chapman, A. J. Morris, P. J. Chupas, L. Monconduit and C. P. Grey, *J. Am. Chem. Soc.*, 2016, **138**, 2352–2365.

[34] J. K. Mathiesen, R. Väli, M. Härmas, E. Lust, J. F. von Bülow, K. M. Ø. Jensen and P. Norby, *J. Mater. Chem. A.*, 2019, **7**, 11709–11717.

[35] K. M. Ø. Jensen, H. L. Andersen, C. Tyrsted, E. D. Bøjesen, A. C. Dippel, N. Lock, S. J. Billinge, B. B. Iversen and M. Christensen, *ACS Nanoscale*, 2014, **8**, 10704–10714.

[36] D. Olds, K. Page, A. Paecklar, P. F. Peterson, J. Liu, G. Rucker, M. Ruiz-Rodriguez, M. Olsen, M. Pawel, S. H. Overbury and J. R. Neilson, *Rev. Sci. Instrum.*, 2017, **88**, 034101.

[37] X. Hua, P. K. Allan, C. Gong, P. A. Chater, E. M. Schmidt, H. S. Geddes, A. W. Robertson, P. G. Bruce and A. L. Goodwin, *Nat. Commun.*, 2021, **12**, 561.

[38] S. A. Moggach, W. G. Marshall and S. Parsons, *Acta Crystallogr. Sect. B*, 2006, **62**, 815–825.

[39] E. Eikeland, M. K. Thomsen, J. Overgaard, M. A. Spackman and B. B. Iversen, *Cryst. Growth Des.*, 2017, **17**, 3834–3846.

[40] P. A. Wood, R. S. Forgan, D. Henderson, S. Parsons, E. Pidcock, P. A. Tasker and J. E. Warren, *Acta Crystallogr. Sect. B*, 2006, **62**, 1099–1111.

[41] T. A. Mary, J. S. Evans, T. Vogt and A. W. Sleight, *Science*, 1996, **272**, 90–92.

[42] S. Kohara, K. Kato, S. Kimura, H. Tanaka, T. Usuki, K. Suzuya, H. Tanaka, Y. Moritomo, T. Matsunaga, N. Yamada, Y. Tanaka, H. Suematsu and M. Takata, *Appl. Phys. Lett.*, 2006, **89**, 201910.

[43] T. Matsunaga, J. Akola, S. Kohara, T. Honma, K. Kobayashi, E. Ikenaga, R. O. Jones, N. Yamada, M. Takata and R. Kojima, *Nat. Mater.*, 2011, **10**, 129–134.

[44] C. A. Perottoni and J. A. H. Jornada, *Science*, 1998, **280**, 886–890.

[45] D. A. Keen, A. L. Goodwin, M. G. Tucker, M. T. Dove, J. S. Evans, W. A. Crichton and M. Brunelli, *Phys. Rev. Lett.*, 2007, **98**, 6–9.

[46] R. J. Speedy, *J. Phys. Condens. Matter*, 1996, **8**, 10907–10918.

[47] M. T. Dove, *Am. Mineral.*, 1997, **82**, 213–244.

[48] G. Shirane, J. D. Axe, J. Harada and J. P. Remeika, *Phys. Rev. B*, 1970, **2**, 155–159.

[49] G. Burns and B. A. Scott, *Phys. Rev. Lett.*, 1970, **25**, 167–170.

[50] M. T. Dove and B. M. Powell, *Phys. Chem. Miner.*, 1989, **16**, 503–507.

[51] S. A. Redfern, E. Salje and A. Navrotsky, *Contrib. to Mineral. Petrol.*, 1989, **101**, 479–484.

[52] G. Jaeger, *Arch. Hist. Exact Sci.*, 1998, **53**, 51–81.

[53] P. M. Woodward, P. Karen, J. S. O. Evans and T. Vogt, *Solid State Materials Chemistry*, Cambridge University Press, 2021.

[54] C. Bradley and A. Cracknell, *Bradley, Christopher, and Arthur Cracknell. The mathematical theory of symmetry in solids: representation theory for point groups and space groups.*, Oxford University Press, 2010.

[55] M. I. Aroyo, J. M. Perez-Mato, D. Orobengoa, E. Tasci, G. De La Flor and A. Kirov, *Bulg. Chem. Commun.*, 2011, **43**, 183–197.

[56] M. I. Aroyo, A. Kirov, C. Capillas, J. M. Perez-Mato and H. Wondratschek, *Acta Crystallogr.*, 2006, **A62**, 115–128.

[57] M. I. Aroyo, J. M. Perez-Mato, C. Capillas, E. Kroumova, S. Ivantchev, G. Madariaga, A. Kirov and H. Wondratschek, *Z. Kristallogr. Cryst. Mater.*, 2006, **221**, 15–27.

[58] B. J. Campbell, H. T. Stokes, D. E. Tanner and D. M. Hatch, *J. Appl. Crystallogr.*, 2006, **39**, 607–614.

[59] J. Wang, Y. Liu, X. Chen, C. Chen, P. Chen, Z. Wang and Y. Duan, *Chemphyschem.*, 2019, **20**, 2580–2586.

[60] A. B. Stambouli and E. Traversa, *Renew. Sustain. Energy Rev.*, 2002, **6**, 433–455.

[61] S. N. Ruddlesden and P. Popper, *Acta Crystallogr.*, 1957, **10**, 538–539.

[62] S. N. Ruddlesden and P. Popper, *Acta Crystallogr.*, 1958, **11**, 54–55.

[63] N. A. Benedek and C. J. Fennie, *Phys. Rev. Lett.*, 2011, **106**, 107204.

[64] J. P. Attfield, *Chem. Mater.*, 1998, **10**, 3239–3248.

[65] J. P. Attfield, *Cryst. Eng.*, 2002, **5**, 427–438.

[66] S. Pang, J. Xu, Y. Su, G. Yang, M. Zhu, M. Cui, X. Shen and C. Chen, *Appl. Catal. B Environ.*, 2020, **270**, 118868.

[67] A. Sundaresan, A. Maignan and B. Raveau, *Phys. Rev. B*, 1997, **56**, 5092–5095.

[68] V. M. Goldschmidt, *Naturwissenschaften*, 1926, **14**, 477–485.

[69] G. King and P. M. Woodward, *J. Mater. Chem.*, 2010, **20**, 5785–5796.

[70] D. D. Sarma, *Curr. Opin. Solid State Mater. Sci.*, 2001, **5**, 261–268.

[71] V. I. Zinenko, N. G. Zamkova, E. G. Maksimov and S. N. Sofronova, *J. Exp. Theor. Phys.*, 2007, **105**, 617–625.

[72] U. Öpik and M. H. L. Pryce, *Proc. R. Soc. A*, 1957, **238**, 425–447.

[73] I. B. Bersuker, *Chem. Rev.*, 2013, **113**, 1351–1390.

[74] T. Connolley, C. M. Beavers and P. Chater, *Synchrotron Radiat. News*, 2020, **33**, 31–36.

[75] J. P. Sutter, P. A. Chater, M. R. Hillman, D. S. Keeble, M. G. Tucker and H. Wilhelm, *AIP Conf. Proc.*, 2016, **1741**, 040005.

[76] J. P. Sutter, P. A. Chater, R. Signorato, D. S. Keeble, M. R. Hillman, M. G. Tucker, S. G. Alcock, I. Nistea and H. Wilhelm, *Opt. Express*, 2019, **27**, 16121–16142 (2019).

[77] S. J. L. Billinge, *Phil. Trans. R. Soc. A.*, 2019, **377**, 20180413.

[78] D. A. Keen, *Crystallogr. Rev.*, 2020, **26**, 143–201.

[79] S. P. Thompson, J. E. Parker, J. Potter, T. P. Hill, A. Birt, T. M. Cobb, F. Yuan and C. C. Tang, *Rev. Sci. Instrum.*, 2009, **80**, 075107.

[80] G. Büldt, H. U. Gally, A. Seelid and G. Zaccai, *Nature*, 1978, **271**, 182–184.

[81] C. L. Bull, N. P. Funnell, M. G. Tucker, S. Hull, D. J. Francis and W. G. Marshall, *High Press. Res.*, 2016, **36**, 493–511.

[82] S. Klotz, J. M. Besson, G. Hamel, R. J. Nelmes, J. S. Loveday, W. G. Marshall and R. M. Wilson, *Appl. Phys. Lett.*, 1995, **66**, 1735–1737.

[83] F. Birch, *Phys. Rev.*, 1947, **71(11)**, 809.

[84] S. Klotz, J. C. Chervin, P. Munsch and G. Le Marchand, *J. Phys. D. Appl. Phys.*, 2009, **42**, 075413.

Chapter 2

Recovering local structure information from high-pressure total scattering

The work reported in this Chapter is published: A. Herlihy, H. S. Geddes, G. C. Sosso, C. L. Bull, C. J. Ridley, A. L. Goodwin, M. S. Senn and N. P. Funnell, *J. Appl. Crystallogr.*, 2021, **54**, 1546–1554.

2.1 Introduction

PDF analysis of crystalline materials offers a complementary view to the time-averaged structural information provided by more conventional diffraction experiments. In many instances, material properties can only be understood fully by considering local distortions that cannot be adequately described by an average-structure representation.[1] PDF analysis has proved crucial in fully characterising numerous functional materials, for example, oxide ion conductors,[2] negative thermal expansion compounds,[3] and the archetypal ferroelectric $BaTiO_3$.[4]

There are now a great number of facilities capable of making PDF measurements: instruments such as I15-1 (XPDF) at Diamond Light Source, UK, 11-ID-B at the Advanced Photon Source, USA, NOMAD at the Spallation Neutron Source, USA, and GEM and POLARIS at the ISIS Neutron and Muon Facility, UK[5–9] enable high-quality data collection, while also providing average structure measurements. The ability to measure both Bragg and diffuse scattering simultaneously means that both local and average information are encoded within the same scattering pattern, where reciprocal and real space information are straightforwardly related by Fourier transform. Thus, in principle, *in situ* experiments can be conducted for local structure measurements using the same methods as for routine powder diffraction. For the most part, this is indeed the case—variable temperature measurements are carried out in capillary mode with little change to the experimental set up and *in situ* experiments (for cell cycling, gas flow, *etc.*[10–12]) are designed such that non-sample scattering is reduced as much as possible. The only caveat is that, for generated PDFs to be physically meaningful, parasitic scattering arising from the sample environments must be accounted for by subtracting the scattering signature of the empty equipment.[13–15]

Crystalline materials are often probed by temperature or pressure, to explore their fundamental physical properties *via* observation of structural changes and

phase transitions. Pressure, in particular, can be varied to the extent that it can drive very pronounced structural changes, as crystal structures are forced to rearrange themselves to minimise volume, or avoid unfavourable interactions.[16–18] In general, high-pressure techniques are well-established[19,20] and are no longer the domain of specialist groups, but their use to obtain local structure information remains under-explored as significant technical challenges exist. Accessing the gigapascal regime requires very small sample volumes, jeopardising signal-to-noise; however, longer counting times and improved detector efficiencies can mitigate this. More problematic is the complication that arises from the use of a pressure-transmitting medium (PTM) to ensure hydrostatic compression—it has its own local structure signal that also changes with pressure. Common media include light organic materials such as methanol/ethanol, and pentane/isopentane mixtures.[21] This is not such an issue for X-ray experiments, where the scattering of the organic PTM is often negligible relative to that of the sample, and successful PDF measurements have been performed mostly using diamond anvil cells,[22,23] as well as the large-volume Paris–Edinburgh (PE) press—albeit over a very small pressure range.[24] For pressure measurements with neutrons, the PE press is more commonly used but, critically, the PTM must be deuterated to avoid incoherent scattering. The strong coherent scattering of deuterium by neutrons means the PTM contribution to the PDF cannot be ignored.

To date the only neutron total scattering experiments that have been carried out successfully are those that omit a PTM entirely—*i.e.*, experience non-hydrostatic compression—by using a PE press. Amorphous/glassy materials account for the bulk of these studies because these are not particularly susceptible to the effects of strain.[25,26] Recently, Playford *et al.*[27] showed, using the PEARL instrument at ISIS, that useable PDFs can be obtained for some simple crystalline systems. However, even some of these exhibited signs of strain broadening. Al-

though this will not impact the low-r region of the PDF where information about the shortest atom–atom distances is found, strain will affect the longer-range structure. Lack of hydrostaticity remains a significant obstacle to measuring local structure in crystalline materials at pressure, and the work reported in this Chapter aims to address precisely this limitation.

This Chapter presents a method for correcting PDFs of crystalline materials measured on the PEARL instrument for the presence of the most commonly used PTM: a 4:1 volume mixture of deuterated methanol and ethanol. The correction method involves applying an empirical correction based on a combination of molecular dynamics-informed PDFs and a non-negative matrix factorisation (NMF) approach to separating sample–PTM scattering contributions.[28,29] Simple crystalline materials—Ni and MgO are used as proof-of-principle, through comparing corrected PDFs to model PDFs where the assumption is made that the compressibilities and structural simplicity means that their local structures can be described by their known average crystalline structures. The method is then applied to α-quartz—an example of an apparently simple crystalline material with a local structure that is known to deviate from its average structure with temperature. This type of neutron PDF study has not previously been possible and these measurements represent an expansion of high-pressure local structure capabilities.

2.2 Experimental details

Crystalline samples of Ni, MgO and SiO_2, obtained commercially and used as received, were measured on the high-pressure instrument PEARL at the ISIS Neutron Facility.[30] Powdered samples were loaded into null-scattering TiZr single-toroid gaskets[31] with a 4:1 volume mixture of perdeuterated methanol:ethanol

(ME) PTM.[21] A PE press,[19] equipped with zirconia-toughened alumina (ZTA) anvils, was used to apply loads of 2, 25 and 50 tonnes to each sample; in each case the pressure was determined from the known equation of state for each material.[32–34] Neutron powder diffraction patterns were collected for a minimum of nine hours each. Analogous data collections were performed for a vanadium pellet and for a ME mixture on its own, also at loads of 2, 25 and 50 tonnes. It was difficult to quantify the mass of ME in each sample loading because it evaporates rapidly, meaning the gasket must be sealed by the PE press to prevent this happening. The gasket and sample were weighed prior to addition of the ME, to determine their respective masses. Following the experiment, the decompressed, now-sealed gasket assembly (*i.e.*, sample and ME) was weighed to obtain an estimate of the ME mass.

2.3 Data processing

Data collected by the main, transverse detector banks were reduced using the MANTID software package[35] over two different diffraction angle ranges—90±3.5° and 90±7° and Rietveld refinement was carried out using TOPAS Academic v6.[36] MANTID routines were also used for correcting for the effects of attenuation by the ZTA anvils and data were normalised by vanadium to account for flux profile and detector efficiencies. It was found that processing scattering data from a wider diffraction angle resulted in a greater contribution from the ZTA anvils relative to the sample scattering, evident by the change in peak intensities (shown for the lowest pressure MgO scattering data in Figure 2.1). All diffraction data were therefore focused from the reduced angle range to lessen the contribution from non-sample scattering.

Total scattering structure factors ($S(Q)$) of the sample with PTM were pro-

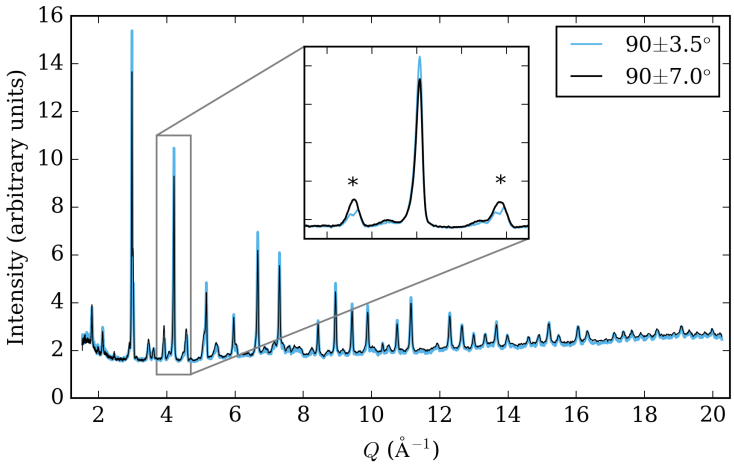

Figure 2.1: Neutron diffraction patterns of MgO measured in a PE press, with data focused from two different scattering angle ranges. Inset figure shows a representative range of data that best shows the difference in relative peak intensities of the sample (middle peak) and sample environment (indicated by asterisks).

duced by subtracting measurements of the sample environment (gasket and anvil assembly) scattering and applying a scale factor and y-offset ($S(Q)\times$scale + offset) such that $S(Q) \to 1$ at Q_{max}. The sample environment was accounted for by measuring a vanadium pellet at equivalent pressures to those of the sample measurements.[27] The aim of these measurements was to produce as-close-as-possible scattering geometries to those of the sample at each pressure, such that they can be subtracted as 'background' scattering. The resulting corrected $S(Q)$s were then Fourier transformed to produce PDFs, using the program StoG, distributed with the RMCProfile package.[37] A Fourier-filter was used, applying a minimum distance for the first real peak.

A slight offset between the sample environment Bragg peaks in the sample, and empty data, results in a spike in the difference curve after the subtraction is made. This is most notable in the highest pressure MgO data at low Q, shown in Figure 2.2, left. Artificial smoothing of these features was performed and the resulting PDF was found to be indistinguishable from the PDF produced from the uncorrected data (Figure 2.2, right).

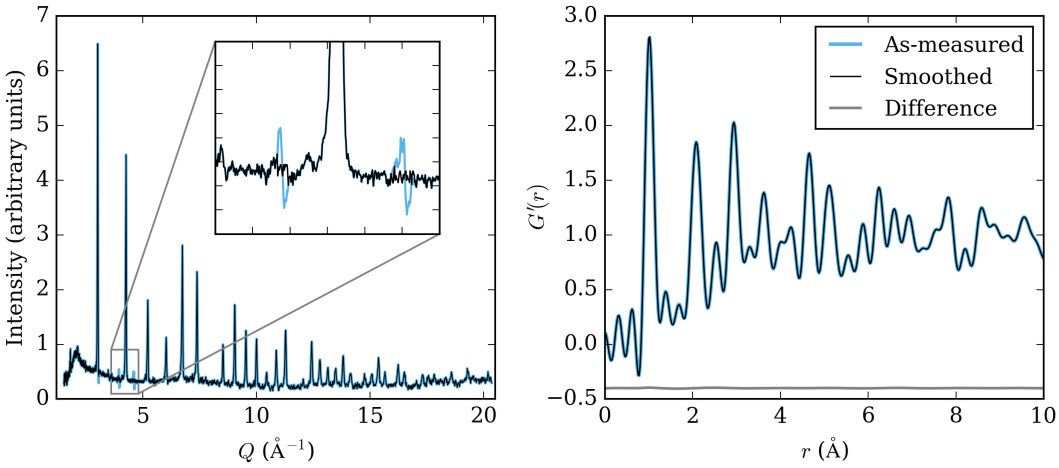

Figure 2.2: Left: Total scattering patterns of MgO at high pressure with and without artificial smoothing to remove features arising due the subtraction of slightly mismatched sample environment peaks. Right: PDFs produced from the smoothed and as-measured total scattering patterns. The essentially flat difference line shows that features due to the mismatch of ZTA Bragg peaks have a negligible effect on the resulting PDF.

For each sample, density and composition were estimated from the difference between the masses of the loaded gasket pre- and post-compression, and were used to normalise PDFs for subsequent treatment. As part of a simplified data treatment, and following established data reduction procedures,[27] inelasticity effects were not corrected for, as these were likely to be small for the relatively heavy sample materials, nor were corrections made for sample absorption since the attenuation due to the press would likely dominate over any sample effects. In justification of this assumption, absorption corrections were not required to obtain high-quality Rietveld fits.

PDF modelling was carried out using TOPAS Academic v6.[36] Simulated PDFs were convolved with a $\sin(Q_{\max}r/r)$ function where $Q_{\max} = 20.32$ Å^{-1}. To account for the instrumental characteristics, previously-measured near-ambient pressure Ni[27] (without a PTM) was used to determine a dQ damping factor of 0.045 Å^{-1}.

SiO_2 PDFs were analysed using 'large-box' modelling techniques *via* the RMCProfile software.[37] The refinements used a $5 \times 9 \times 8$ supercell of the Rietveld-refined unit cell, containing 6480 atoms, and near cubic-dimensions. Eleven in-

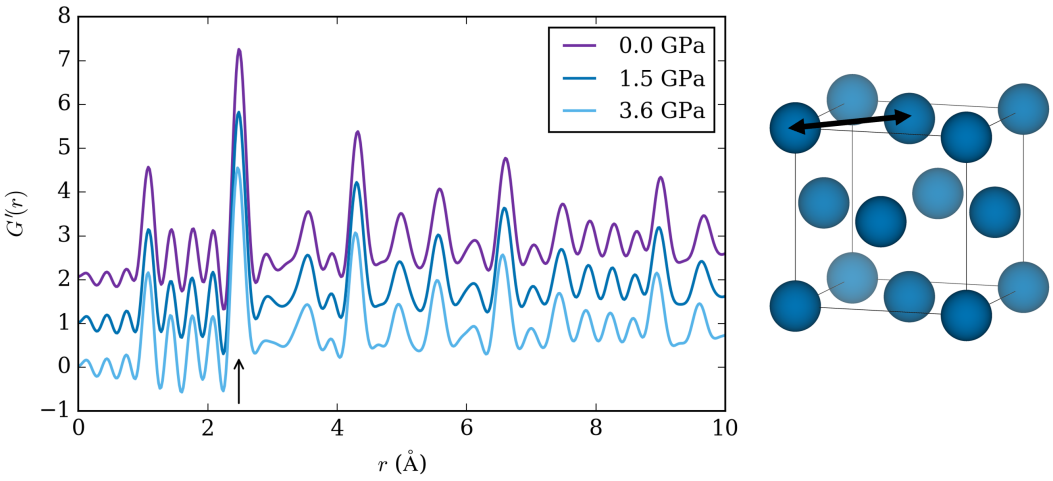

Figure 2.3: Variable pressure PDFs of Ni in ME, measured in the PE press. The black arrow indicates the peak due to the shortest atom–atom distance of crystalline Ni, as indicated on the right.

dependent refinements were carried out for each run to improve the statistical significance of subsequent structural analysis. Potentials-based restraints were applied to the Si–O nearest neighbour distances and O–Si–O angles to maintain tetrahedral geometry (see Appendix for details).

2.4 Average structure and uncorrected PDFs of Ni and MgO

The average crystal structures of Ni and MgO were confirmed *via* Rietveld analysis of the measured neutron diffraction patterns—Rietveld fits for all structures at each pressure measured are available in the Appendix. The known EoS's[32,38] were used to calculate sample pressures of 0.033(3), 1.49(9), and 3.6(2) GPa for Ni and 0.171(6), 1.84(1), and 3.849(19) GPa for MgO, though the errors on the pressure measurements are likely underestimated due to unaccounted-for errors in alignment of the PE press. Figure 2.3 shows the variable pressure Ni PDFs and Figure 2.4 shows the MgO PDFs. The PDFs exemplify the composite nature of the sample, with a prominent peak at ca. 1 Å arising from C–D and O–D pair

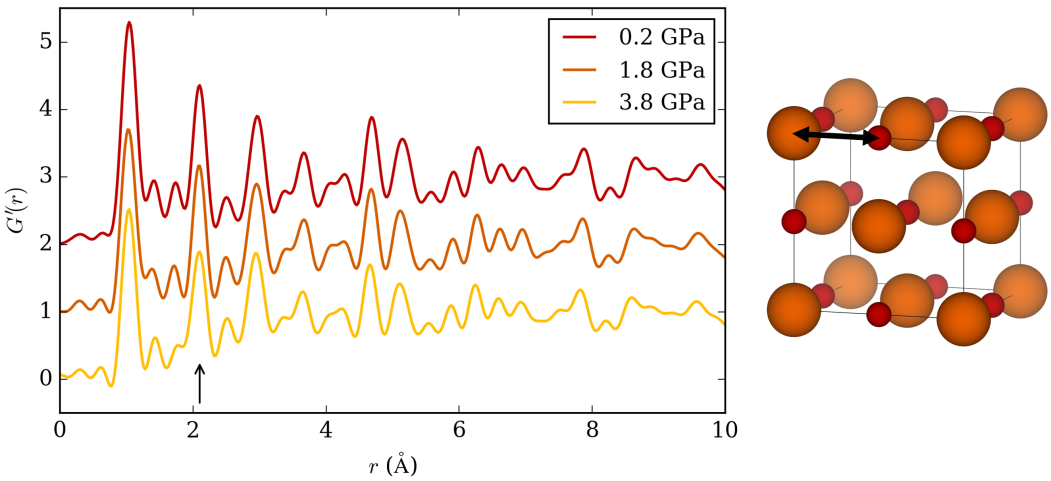

Figure 2.4: Variable pressure PDFs of MgO in ME measured in the PE press. The black arrow indicates the peak due to the shortest atom–atom distance of crystalline MgO, as indicated on the right.

correlations in the ME PTM in addition to underlying, unstructured correlations which contribute significantly up to ca. 3.5 Å. Prominent Fourier ripples at low r are also present due to the finite Q-range of the data. The $G'(r)$ normalisation is important for data treatment described later in this Chapter and therefore the PDFs are shown in this form. A comparison of the different PDF functions is reported in the Introduction of this Thesis and discussed in detail by Keen, 2001.[39]

2.5 Variable-pressure modelling of methanol/ethanol PDFs

Once scattering from the PE press is accounted for, the PDF resulting from a variable-pressure hydrostatic measurement (such as is shown in Figure 2.4) is comprised of three components: i) correlations in the bulk of the pure crystalline material, ii) correlations within the ME and iii) crystalline–ME pairwise interactions. The initial assumption is made that the last of these is in sufficiently low concentration that it can be ignored—this will later be shown to be the case. An-

other assumption is made that the structural behaviour of the ME is independent from the sample it is being used to compress. In this way, the ME PDF can be described using an analytically-derived function, calculable for any pressure between 0–10 GPa—the approximate hydrostatic range of ME seen experimentally.[21] A NMF approach is then used to assign relative weights to functions describing the ME and crystalline sample, such that they are straightforwardly separated.[28] This procedure is implemented in a Fortran90 routine (see Appendix), which takes variable-pressure, environment-corrected, PDFs and user-determined pressure as an input.

2.5.1 Generating methanol:ethanol PDFs from atomistic models

The following calculations were carried out by Dr Gabrielle Sosso, and subsequent analysis of the large-box simulations were performed by myself. Molecular dynamics (MD) simulations were performed using the GROMACS package (version 5.1.4, single precision).[40] The CHARMM36 (Nov18)[41] force field was used to model methanol/ethanol mixtures. The equations of motions were integrated using a leap-frog integrator, with a time step of 2 fs. The van der Waals (non-bonded) interactions were taken into account up to 10 Å, with a switching function bringing them to zero at 12 Å. The particle-mesh-Ewald framework was used to deal with electrostatic interactions.[42] To mimic the experimental conditions, the isobaric-isothermal NPT (constant pressure) ensemble was sampled: the stochastic velocity rescaling thermostat of Bussi-Donadio-Parrinello[43] was used to enforce room temperature conditions, *via* a weak coupling constant of 1 ps. The Berendsen barostat[44] was employed to apply isotropic pressure on the (cubic) simulation boxes, with a coupling constant of 2 ps. The P-LINCS algorithm[45] was used to constrain O–H bonds. The system (Figure 2.5) contained

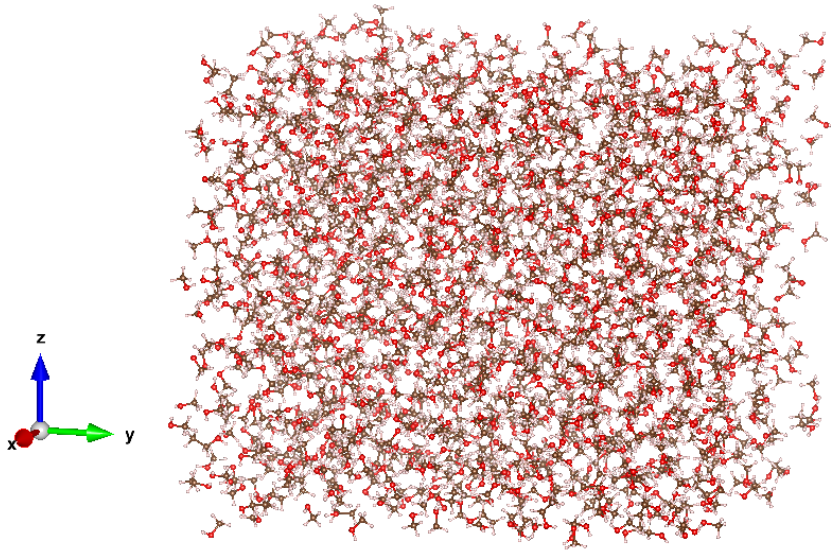

Figure 2.5: A representative 0 GPa MD simulation box, containing 1200 methanol molecules and 200 ethanol molecules.

1200 methanol molecules and 200 ethanol molecules (9000 atoms in total; molar ratio 6:1, corresponding to a volume ratio of 4.18:1) and was equilibrated at room temperature and 0 GPa for 20 ns. The pressure was subsequently increased in increments of 0.5 GPa up to 10 GPa (20 steps in total). At each step, the system was first equilibrated for 10 ns, with the following 10 ns then used to calculate PDFs of the resulting atomistic configuration.

A Fortran program was written to calculate all atom–atom distances (n_{ij}), using periodic boundary conditions, and applying the correct normalisations, as described by Keen,[39] to calculate the partial pair distributions, $g(r)$, as per Equation 4.28, reported in Chapter 1. The partial PDFs were then summed and normalised appropriately to give the $G'(r)$ PDF form according to;

$$G'(r) = \Big(\big(\sum_{i,j=1}^{n} c_i c_j \bar{b}_i \bar{b}_j [g_{ij}(r) - 1] \big) / \big(\sum_{i=1}^{n} c_i \bar{b}_i \big)^2 \Big) + 1, \tag{2.1}$$

where c_i is the proportion of species i and $\bar{b}_i$ is the coherent bound neutron scattering length of species i.

PDFs were generated from each ME simulation box, *i.e.*, in 0.5 GPa steps

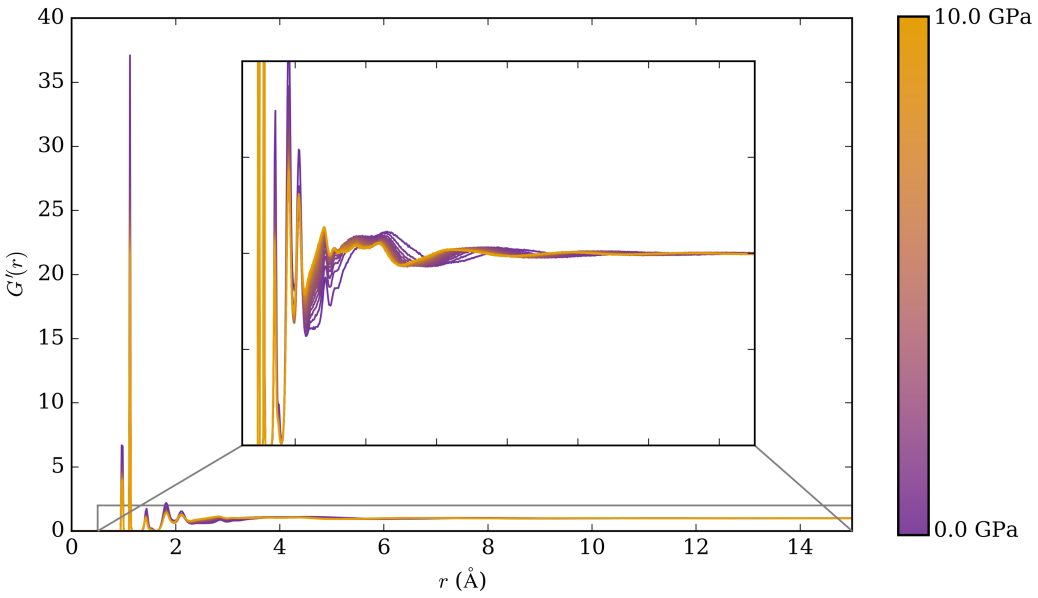

Figure 2.6: Calculated ME PDFs from each MD simulation at pressures from 0–10 GPa in steps of 0.5 GPa. The inset figure shows the subtle features between 2–4 Å more clearly. These PDFs are free of any instrumental effects—particularly peak broadening which arises due to the limited instrument Q_{max}.

between 0 and 10 GPa, and are shown in Figure 2.6. It is important to note that the relevant MD forcefield parametrisations for the methanol and ethanol molecules have been obtained at ambient pressure only. As such, one cannot assume *a priori* that the force field will yield sufficiently accurate results at the high-pressure conditions considered in this work. However, the corrected PDFs, presented later, are indicative of the adequacy of this computational setup.

A notable difference between the simulated and experimental PDFs is the substitution of ^{1}H with ^{2}H in the experimentally measured ME, in order to avoid the effects of incoherent scattering by neutrons. Whilst forcefields for isotopically-normal methanol and ethanol are readily available, the same cannot be said for the ^{2}H-versions of these molecules.[46] In light of the relatively low resolution of the PDF data, the difference in ^{1}H /^{2}H has been accounted for by shifting the O—H peak position at 0.97 Å (which remains constant across all pressures) by 0.03 Å, corresponding to the difference in H/D covalent bond distances identified by Soper

et al.[47] The C–H bonds were not adjusted, in accordance with observations by Kuchitsu & Bartell[48] and Allinger & Flanagan;[49] in any case the magnitude of the shifts involved is almost negligible, being nearly commensurate with the bin width of the PDFs (0.02 Å).

The PDFs generated thus far only describe ME at discrete pressure intervals of 0.5 GPa. It is however desirable that the ME PDFs should be calculable for any pressure between 0–10 GPa—the approximate hydrostatic range of ME seen experimentally.[21]

2.5.2 Modelling PDF pressure dependence

Initial attempts to model the variable-pressure ME PDF involved fitting a function that describes the compression of the PDF such that a canonical (lowest pressure) PDF was used to describe each PDF at any pressure up to 10 GPa. The ME PDF calculated at 0 GPa is described well by the sum of ten Gaussians and an additional function that accounts for the underlying shape of the $G'(r)$ normalisation (shown in Figure 2.7, and named 'analytical PDF' hereafter);

$$G'_{\mathrm{ME}}(r) = \sum_{i=1}^{10} a_i \exp\left[\frac{-(r-\mu_i)^2}{2\sigma_i^2}\right] + \left[1 - \exp\left(-\frac{r}{k}\right)^{\beta}\right]. \tag{2.2}$$

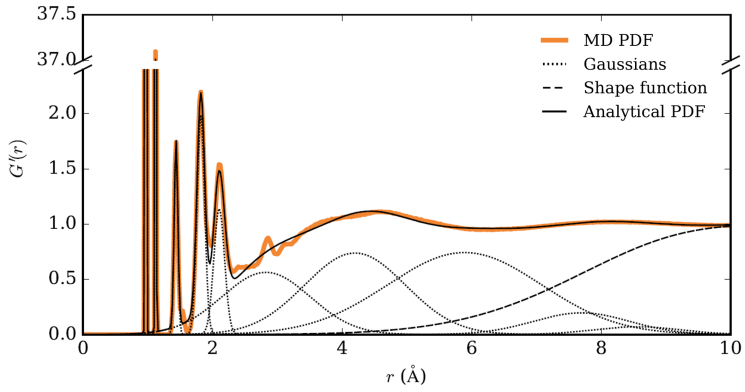

Figure 2.7: An MD PDF for ME at 0 GPa, calculatd from MD simulations, overlaid with the analytical PDF comprised of ten Gaussians and a shape function.

a_i, μ_i and σ_i are the parameters for the ith Gaussian, and k and β describe the underlying shape of the PDF. All parameters were determined *via* a least-squares fitting procedure implemented using TOPAS. The Gaussians do not have any physical significance—they are simply used as a means to recreate the PDF empirically.

When an organic, molecular system is compressed, the shortest atom–atom correlations, corresponding to covalent bonds, should not change, whereas longer, intermolecular atom–atom distances will decrease. In a PDF this is reflected in unchanging peaks at low r and peaks at high r shifting to lower r values.

The following function describes this type of change in peak position for variable pressure PDFs;

$$\alpha_{ij} = 1 + (\rho_j - 1)[erf(r_i/r_c)]^v, \tag{2.3}$$

where i refers to the ith Gaussian, j refers to the pressure, ρ_j is a pressure-dependent parameter describing the degree of peak shifting, and r_c and v globally describe the change in compression behaviour on moving between the regions corresponding to intra- and intermolecular interactions.

As shown in Figure 2.8 (for only the lowest and highest pressure PDFs for

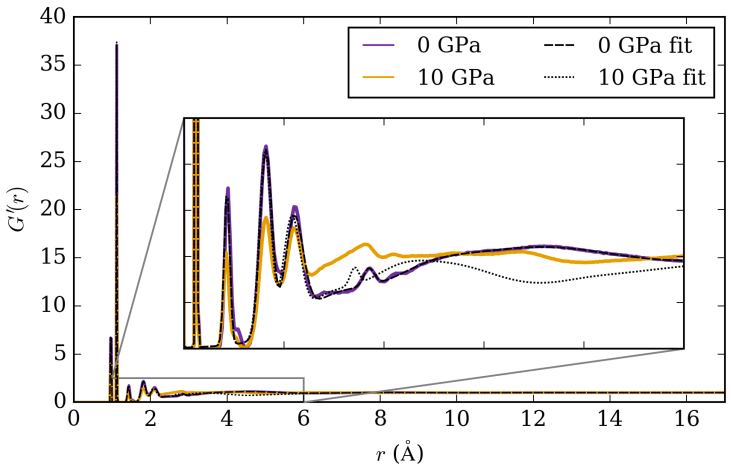

Figure 2.8: Gaussian fits to the MD simulated PDFs at 0 and 10 GPa using the function described by Equation 2.3.

clarity), although the stretch function does indeed result in a shift of the broader Gaussian peaks to lower r, the sum of Gaussians no longer describes the overall shape well. Additionally, there are decreases in intensity of the more defined peaks that cannot be accounted for by only altering peak positions and as such, applying a global pressure-dependence to all Gaussian peaks was found to be too simplistic.

Instead, the following approach was used to relate experimentally determined pressure to the form of the local structure scattering signature. Each MD PDF,

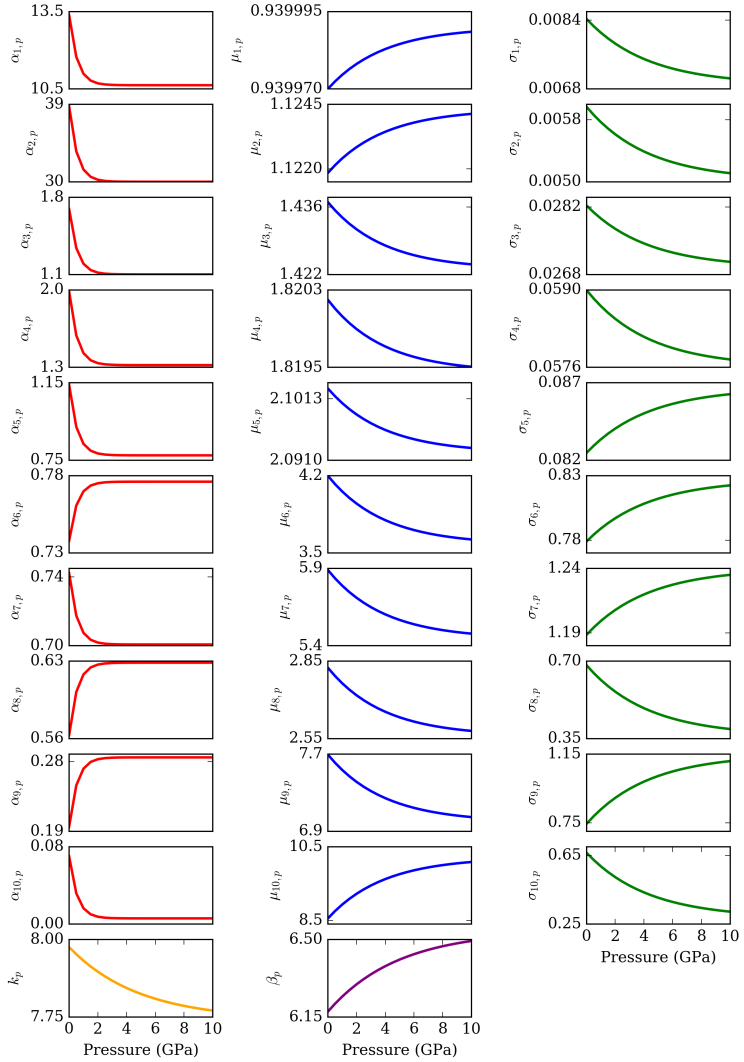

Figure 2.9: Gaussian and shape function parameters ($a_{i,p}$, $\mu_{i,p}$, $\sigma_{i,p}$, k_p and β_p) for the i^{th} Gaussian at pressure p, used to calculate the ME PDFs. Note the difference in y-axis scale between the plots.

at pressure p, is, as described before, approximated as the sum of ten Gaussians and an additional function that accounts for the underlying shape of the $G'(r)$ normalisation. When allowing the Gaussian parameters to vary freely on fitting, it was found that they displayed a pressure-dependence proportional to $\exp(-p)$. Therefore, the parameters were constrained to follow this form, as shown in Figure 2.9, in order to reduce the number of variables required to model the MD PDFs. Each Gaussian and shape function parameter (here x is used to denote a parameter ϵ $\{a_{i,p}$, $\mu_{i,p}$, $\sigma_{i,p}$, k_p and $\beta_p\}$) then has a pressure-dependence;

$$x(p) = x_{\max} + (x_0 - x_{\max})\exp\left(\frac{-p}{p_0}\right) \tag{2.4}$$

where x_0 and $x_{\max}$ are the parameter values at zero and maximum pressures (10 GPa), respectively, and p_0 captures the rate of change for these values. Values of x_0 and $x_{\max}$ for each parameter, and global p_0 values for $a_{i,p}$, $\mu_{i,p}$, $\sigma_{i,p}$, k_p and β_p values (a total of 68 parameters), were determined by carrying out a simultaneous least-squares refinement in TOPAS against the series of MD PDFs.

Representative examples of the analytical PDFs are shown in Figure 2.10 for

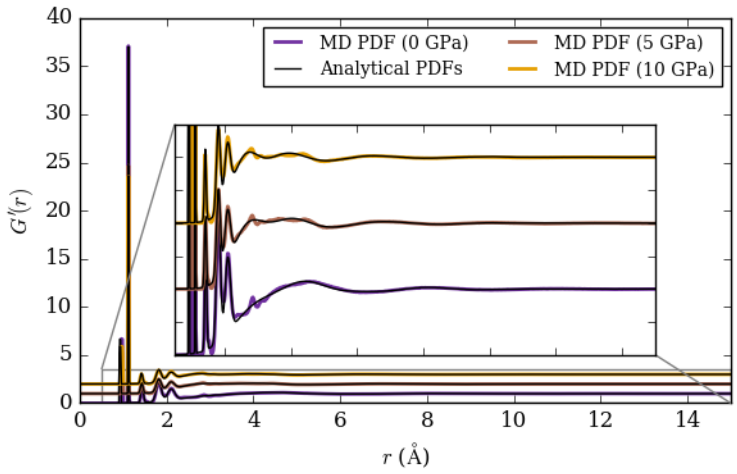

Figure 2.10: Calculated ME PDFs from the 0, 5, and 10 GPa MD simulation and corresponding analytical PDFs, composed of 10 Gaussian peaks and an underlying shape function, offset in the y-direction.

0, 5 and 10 GPa against to the corresponding MD PDFs (see Appendix for the full data range). Compared to Figure 2.8, the analytical PDFs describe the MD PDFs much better and the broader features and peak intensities of the more defined peaks are well described by the 10 Gaussian functions.

Thus, with this approach, an end user need only specify a pressure to generate the relevant ME PDF. Finally, the ME PDF is degraded to account for the finite Q limit encountered experimentally by convolving with a user-defined $\sin(Q_{\mathrm{max}}r)/r$ term (where $Q_{\mathrm{max}} = 20.32$ Å^{-1} for the examples presented here). The resulting function then more closely matches what is actually measured in the diffraction experiment. The purely empirical nature of the function to describe the ME means that, in principle, it could straightforwardly be adapted to other pressure-transmitting media, or MD simulations using alternative forcefields.

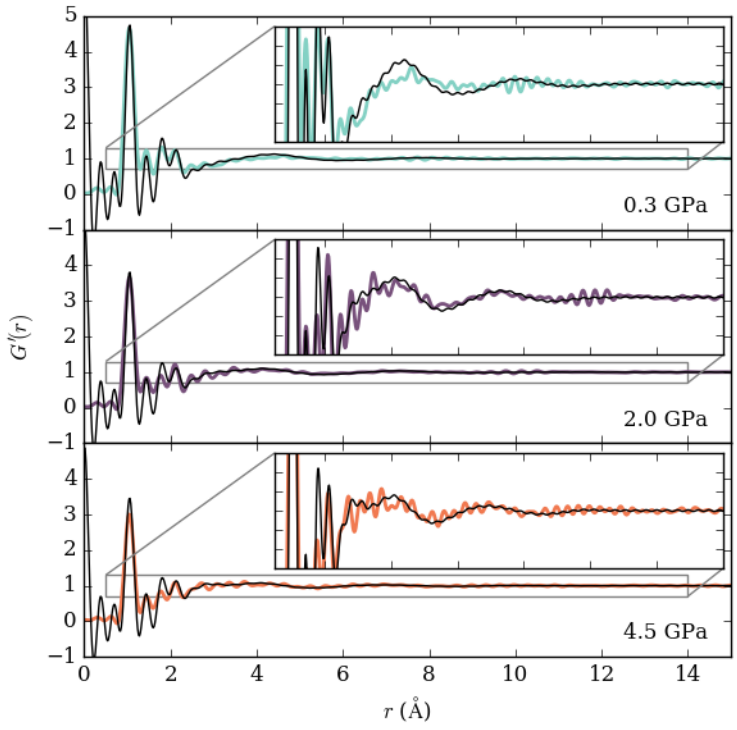

Figure 2.11: Measured variable-pressure ME PDFs (colours) compared to the analytical ME PDFs (black). Determining the pressure from an equation of state is not possible with ME and therefore corresponding modelled PDFs were chosen by comparing the 1–6 Å region and selecting the PDF with the best fit.

As an assessment of how closely the analytical PDFs represent the local structure of ME, they are compared to the PDFs of ME experimentally measured on PEARL (Figure 2.11). The convolved analytical PDFs were generated for estimated pressures of 0.3, 3.0 and 4.5 GPa, as a pressure marker was not used and only the applied loads of 2, 25, and 50 tonnes were known. There is very good agreement between the measured and modelled PDFs—peak positions and intensities in the low r region are well-replicated, as are broader features at longer length-scales. Intensity mismatches in low r are due the application of a Fourier-filter to the experimental data, and at high r, these differences are likely within error of each other.

Although the analytical function does not reproduce subtle features of the MD model in the 2–4 Å region, convolution with $\sin(Q_{\mathrm{max}}r)/r$, blurs this fine detail, and comparisons of convolved MD with convolved analytical PDFs shown in Figure 2.12 confirm this. If neutron instruments with significantly larger Q_{max} values were used such that these details were more clearly resolved, this might necessitate additional Gaussian functions to adequately model the PDF.

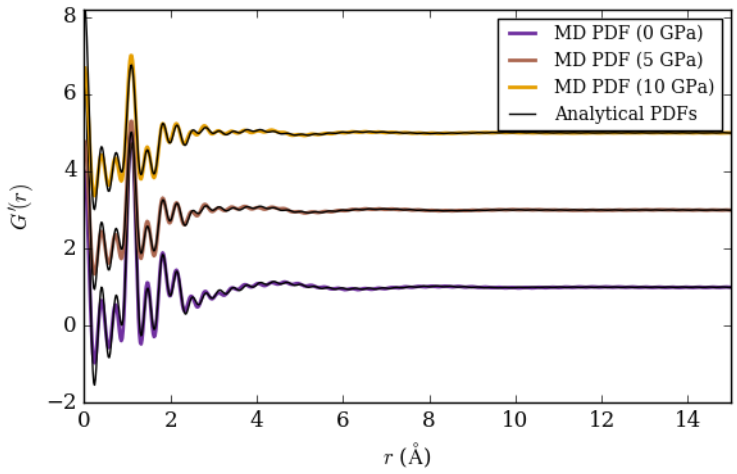

Figure 2.12: MD PDFs and analytical PDFs, convolved with $\sin(Q_{\mathrm{max}}/r)$, where $Q_{\mathrm{max}} = 20.32$ Å^{-1}. PDFs at 0, 5, and 10 GPa are shown, offset in the y-direction. The comparisons of peak positions and intensities show excellent agreement between calculated MD PDFs and analytical PDFs.

2.6 Extracting the sample PDF *via* non-negative matrix factorisation

Now that the ME PDF can be described at any pressure between 0–10 GPa, a NMF approach can then be used to assign relative weights to functions describing the ME and crystalline sample, such that they are straightforwardly separated.[28] This procedure has been implemented in a Fortran90 routine (see Appendix), which takes variable-pressure, environment-corrected, PDFs and a user-determined pressure as an input. The procedural steps are outlined in more detail below.

PDFs of composite systems such as amorphous solid dispersions and battery materials have been successfully separated into their constituent components using NMF methods.[28,29] Ordinarily, this approach recovers the relative scattering contributions of individual components to a series of composite PDFs, with continually-evolving relative concentrations. The key difference with these measured variable-pressure PDFs is that the form of the individual PDFs changes with pressure. A modified version of the NMF approach outlined by Geddes *et al.*[28] (and described below) has been used to extract scattering from the sample. Very simple materials (Ni and MgO) with relatively large bulk moduli (K_0 = 177 and 180 GPa, respectively[50,51]) have been measured, where there should be little deviation between the local and average structures, and therefore the extracted PDFs can be verified by comparing to 'small-box' models generated by the average crystallographic structures, completely independent of any refinement procedures.

Once the pressure-dependent ME PDF has been defined (as described above), the next step of the correction procedure is to determine the relative weighting of ME and sample component PDFs for each measured PDF individually. $|G'_{\mathrm{calc}}(r) - G'_{\mathrm{exp}}(r)|^2$ is minimised where

$$G'_{\mathrm{calc}}(r) = G'_{\mathrm{C}}(r)w + G'_{\mathrm{ME}}(r)(1-w), \tag{2.5}$$

$G'_{\mathrm{exp}}(r)$ is the experimentally-observed PDF, $G'_{\mathrm{C}}(r)$ is the unknown crystalline sample PDF, and w is the weight of the crystalline component. The sum of weights is constrained to unity so that the $G'(r \to \infty) = 1$ limiting value is maintained and $G'_{\mathrm{ME}}(r)$ is fixed as the ME PDF calculated *via* the method outlined above. A non-negative constraint is also applied to both the $G'_{\mathrm{C}}(r)$ and w parameters. Minimisation of $|G'_{\mathrm{calc}}(r) - G'_{\mathrm{exp}}(r)|^2$ is achieved by a Metropolis Monte Carlo procedure, randomly selecting $G'_{\mathrm{C}}(r)$ and w values at each iteration of the refinement. Simulated annealing is used,[52] where acceptance criteria become increasingly strict until convergence occurs and a best fit to data is realised. When performing the fit, the intensity assigned to the unknown crystalline component is completely unconstrained and so, without guidance, the optimal fit will always results in the unknown crystalline material accounting for the entire PDF. The strongest signature of the ME PDF is found at ca. 1 Å, corresponding to C–D and O–D pair correlations. Neither the Ni nor MgO test cases have correlations in this region, so the $G'_{\mathrm{C}}(r)$ components were only fitted above the shortest atom–atom distance r_{min} expected for the sample, and $G'_{\mathrm{ME}}(r)$ was fitted over the full data range. This highlights a couple of limitations: i) this approach is unlikely to work well for any sample with a significant number of covalently-bound deuterium (or hydrogen) atoms, and ii) knowledge of the immediate bonding environment in the sample is needed in advance, though this a reasonable assumption for most experiments covering the 0–10 GPa range.

By design, the refinement preserves a constant sample:ME ratio across a pressure series, though the ability to recover this trend directly was examined. When the weights are allowed to refine independently of other pressure points, they do show reasonable consistency across the pressure series: 0.55, 0.55 and 0.51 for

the Ni sample; and 0.29, 0.30 and 0.29 for MgO. These deviations, though small, are at odds with the experiment – namely that the sample concentration cannot change over the course of compression. The benefit of using the NMF approach to fit to all pressure points simultaneously lies in ensuring that a single, optimal, sample concentration is determined.

Once a best fit has been achieved, and $G'_{\mathrm{C}}(r)$ and w have been refined, the as-measured PDF can be corrected for the PTM contribution. The calculated ME PDF, weighted by the refined $(1 - w)$ value is subtracted from the as-measured PDF, and then corrected by multiplying by $1/w$. All the steps above are performed by a Fortran90 routine which has been made available through publication.[53]

2.7 Correction and validation of Ni and MgO PDFs

There is no means of straightforwardly validating the corrected PDFs – there are no hydrostatic measurements to compare directly against and therefore materials have been chosen such that their local structures can be anticipated (free of any interference from ME) as their local structures are known to be highly similar to their average structures. Corrected and simulated PDFs should be similar if the effects of ME have been properly removed and therefore the performance of the correction method can be bench-marked against the simulated PDF from average structure.

Figures 2.13 and 2.14 show the corrected variable-pressure Ni and MgO PDFs respectively, plotted against fits generated using 'small-box' modelling and average crystallographic structures for Ni and MgO ($Fm\bar{3}m$). The low r regions for both samples are particularly noisy. This arises because the sample contribution

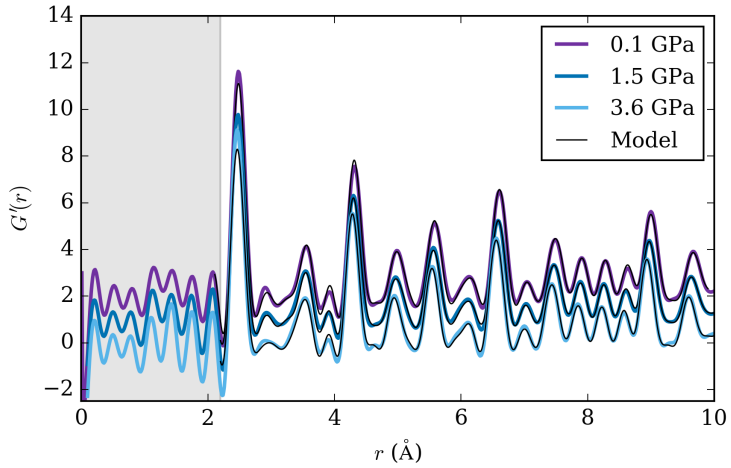

Figure 2.13: Corrected Ni PDFs (colours) compared with small-box simulated model PDFs (black) derived from average structure starting models. The grey low-r region indicates where sample peaks are not expected and the PDFs have not been modelled.

to the PDF has not been fitted below r_{min} and therefore any naturally-occurring Fourier ripples have been exaggerated in the corrected PDF and, additionally, the ME PDF imposes large Fourier ripples due to convolution by the $\sin(Q_{\text{max}}r)/r$ function. Since the method requires that there should be no sample peak overlap with the ca. 1 Å ME peak, any features in the region $r < r_{\text{min}}$ are accepted as unrelated to the sample and are ignored.

In both cases, the level of agreement between the simulated and corrected-

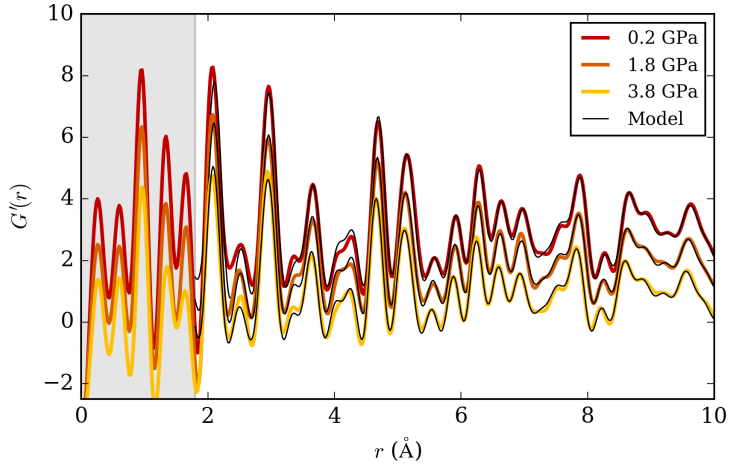

Figure 2.14: Corrected MgO PDFs (colours) compared with small-box simulated model PDFs (black) derived from average structure starting models. The grey low-r region indicates where sample peaks are not expected and the PDFs have not been modelled.

experiment PDFs is good and shows that physically sensible PDFs can be recovered for simple crystalline materials. This shows immediately that for these simple test cases, the following assumptions hold true: first, that the measured PDF can be treated as two, independent components; there are no significant sample–ME correlations present and these can be safely ignored; and, second, the empirical relationship between the form of the ME PDF and pressure is appropriate.

2.8 Extracting pressure from local structure

To investigate the sensitivity of the PDFs to the user-defined pressure and therefore modelled ME PDF, the correction procedure described above was performed on the MgO PDFs using ME PDFs generated for a number of pressures. For the lowest pressure PDF measured at 0.171(6) GPa, ME PDFs were generated at pressures from 0.021–0.421 GPa in steps of 0.05 GPa. The calculated difference between the minimised $|G'_{\mathrm{calc}}(r) - G'_{\mathrm{exp}}(r)|^2$ value for each tested ME PDF and that found for a ME PDF generated at the known pressure of 0.171(6) GPa and is denoted ΔE, where a negative value shows an improvement, or, a better fit of weighted $G'_{\mathrm{C}}(r)$ and $G'_{\mathrm{ME}}(r)$. The left-hand panel of Figure 2.15 shows the ΔE for the lowest pressure PDF and initially suggests an interesting sensitivity of the correction procedure to the modelled PTM. A negative ΔE value at 0.121 GPa is physically reasonable—this value is realistically within error of the experimental pressure 0.171 GPa—where the errors of these calculated pressures are underestimated. The quadratic form of the ΔE values suggests that an exact pressure could be calculated solely from the fitting of a ME PDF component, rather than having to first determine an EoS by performing an additional average structure experiment with a pressure marker.

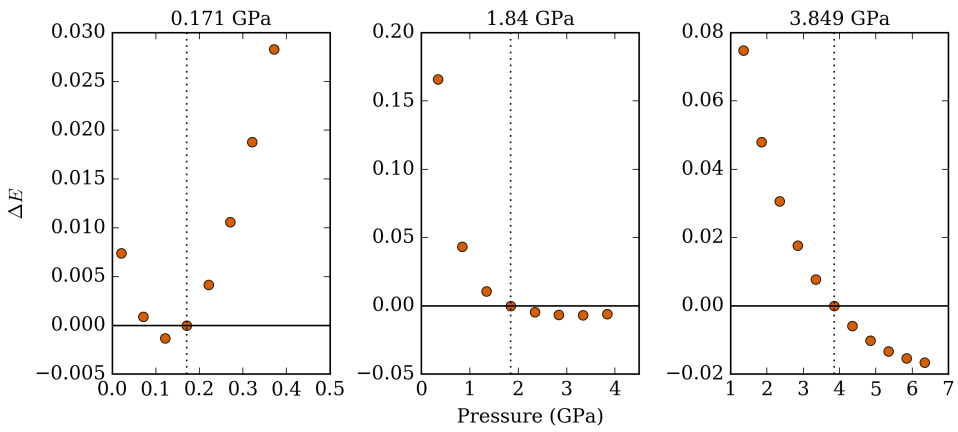

Figure 2.15: Calculated differences (ΔE) in minimised $|G'_{\mathrm{calc}}(r) - G'_{\mathrm{exp}}(r)|^2$ between the value found for the experimentally determined pressure of MgO measurements and the 'tested' pressure indicated by the x-axis.

However, the results for the intermediate and highest pressure refinements shown in Figure 2.15 are less convincing. For the PDF measured at 1.84(1) GPa, ME PDFs were generated at pressures of 0.34–4.34 GPa in steps of 0.5 GPa and for the measurement at 3.849(19) GPa, ME PDFs were generated at 1.349–6.349 GPa, also in steps of 0.5 GPa. At the highest pressure, modelling the ME PDF up to 6.3 GPa resulted in a better fit, as shown by the negative ΔE value, but a pressure 2 GPa higher than that calculated using the MgO EoS are well beyond those expected for loads of 50 tonnes and are not within error of the experimentally determined pressure of 3.8 GPa.

The results for the lower pressure measurement suggest that there may be a sensitivity to the pressure-dependent modelled ME PDFs that could be exploited for low pressure PDF measurements where the EoS of a material is unknown, however, this work is ongoing.

2.9 Local structure of α-quartz under pressure

Having confirmed the validity of the correction approach using simple crystalline materials, the next step is to test a more flexible system and one for which local

structure is perhaps not as well described by the average structure. α-Quartz is such a system with a much smaller bulk modulus ($K_0 = 37$ GPa)[54] than Ni and MgO. It has been widely studied using variable-temperature total-scattering owing to the fact that the conventional crystallographic analysis presents a geometry and Si–O bond distance that does not accurately describe the true silicate structure.[55,56] Instead, local structure methods have been used in conjunction with 'big-box' RMC modelling methods to reveal the structural changes and phase transitions driven by temperature changes.[55] Local structure measurements under pressure have until now been inaccessible and therefore the correction described above was applied to α-quartz. The sample was measured on PEARL using the same procedure as for Ni and MgO. Rietveld analysis of the diffraction patterns confirmed the $P3_121$ crystal structure[57] at all three pressures (plots provided in the Appendix).

The absence of pronounced Bragg peak broadening (*i.e.*, strain) in the diffraction patterns confirms hydrostatic compression of the sample, in contrast to measurements of α-quartz without a PTM.[27] This is further supported by the strong structural correlations observed in the PDFs shown in Figure 2.16(a), at high r, whereas these are damped for samples experiencing strain. Sample pressures at the three applied loads were found to be 0.0766(11), 1.337(2) and 3.757(4) GPa using the refined lattice parameters and EoS.[34] The first PDF peak at ca. 1.6 Å, corresponding to the Si—O distance, is sufficiently distinct from the 1 Å ME peak. Corrected PDFs of α-quartz were generated using the NMF approach described above, and are shown in Figure 2.16(b) and more clearly in (c) for the r-range 1–4 Å. The change in the relative intensities of the strong sample peaks at ca. 1.60 and 2.62 Å upon subtracting the PTM scattering, shown in Figure 2.16(d) illustrates the effect of the more subtle, underlying ME correlations.

RMC modelling, using the RMCProfile program,[37] yielded satisfactory fits

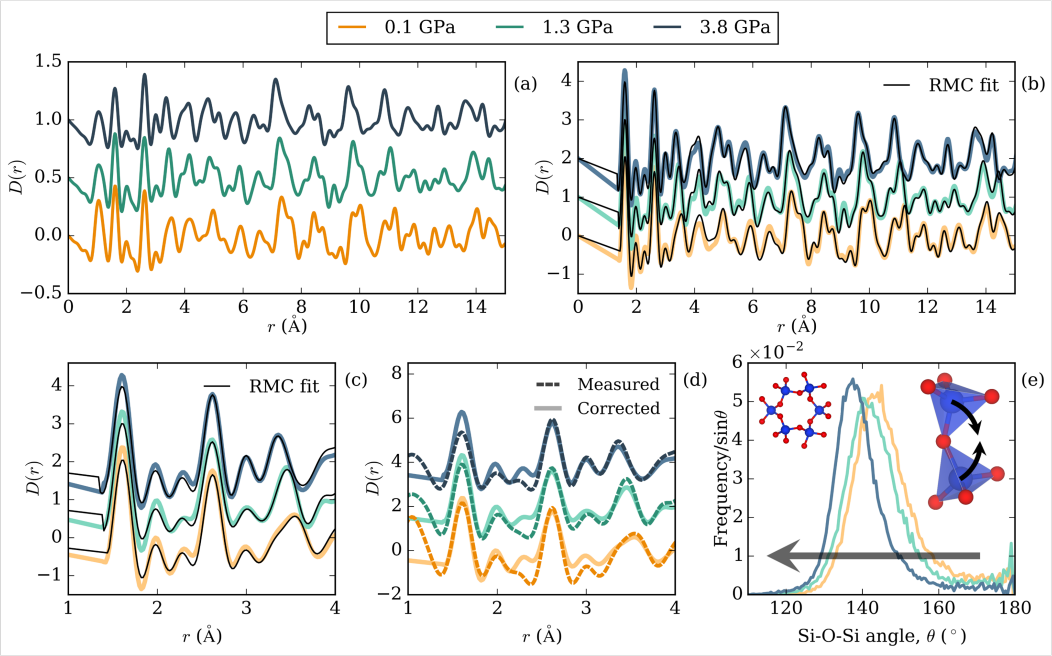

Figure 2.16: (a) As-measured PDFs of α-quartz, offset with increasing pressure. (b) Corrected PDFs and their corresponding RMC fits (black line). Fourier ripples are present and modelled between the first two sample peaks at 1.60 and 2.62 Å. (c) Expanded region of (b) showing the 1–4 Å region more clearly. (d) Comparisons of the as-measured and corrected 1.60 and 2.62 Å PDF peaks, highlighting the effect of ME on the relative peak intensities. The as-measured PDFs have been scaled to aid visual comparison. (e) Si–O–Si bond angle distributions from RMC models, corresponding to deformation of the α-quartz structure, with the horizontal arrow indicating angle distribution progression with increasing pressure. The left-hand inset shows the crystal structure connectivity of the SiO_4 units, and the right-hand inset shows an approximate mode of deformation.

to the corrected PDFs. Though some intensity mismatch is evident, particularly in the 0–1.5 Å region, this is a consequence of refining an overall scaling parameter which helps mitigate against the difficulties in performing an exact normalisation of the data at each pressure point. The rigidity of the individual SiO_4 units is well-known and these have been restrained accordingly; the accurate reproduction of all r-dependent features in the fits is a strong indication that the corrected PDFs are indeed fit for purpose. Interrogation of inter-tetrahedral angle distributions (>46900 angles, Figure 2.16(e)), extracted from RMC-refined configurations, shows a contraction of the Si–O–Si angle that appears consistent with the angle compressibility seen in the average structure; 0.012 and 0.011 GPa^{-1},

respectively. These represent the first experimental measurements of the α-quartz local structure under hydrostatic pressure. Quartz is one of the most well-studied materials in the solid-state community but, until now, analysis of its local structure under pressure has been restricted to computational studies or experimental measurements that are accompanied by strain-induced broadening. Though the RMC models suggest a minimal difference between the local and average angle compressibilities in this instance, the viability of exploring local structure in other hydrostatically-compressed, flexible, crystalline systems is exciting.

2.10 Conclusions

Local structure analysis has previously proven crucial in properly identifying structural features/distortions that underpin material behaviour in a wide variety of systems, be it determining local structure mechanisms of battery materials,[15,58] defects in metal-organic frameworks[59,60] or the nature of phase transitions in multiferroic materials.[61] Thus far, analogous experiments have not been possible for hydrostatic high-pressure neutron experiments, restricting exploration of local structure in crystalline materials to near-ambient pressure. The approach described in this Chapter mitigates against the PTM limitation where ME signal contributes to the PDF and it is hoped that this correction procedure might now make high-pressure PDF measurement of a multitude of crystalline systems viable. An obvious extension of this work would be to explore transferability of the analytical ME function to more complex, flexible materials, *e.g.*, frameworks, where the sample PDF would change more rapidly as a function of pressure, than seen for the relatively-simple systems here. For example, the NTE material ScF_3,[62,63] where the application of pressure could provide insight into its complex expansion behaviour would be an ideal candidate. The focus on the 4:1 deuterated

ME mixture here reflects its common usage, but this method could in principle be applied to other PTMs if their pressure dependence can be straightforwardly expressed as an empirical function.

2.11 References

[1] D. A. Keen, *Crystallogr. Rev.*, 2020, **26**, 143–201.

[2] M. Scavini, M. Coduri, M. Allieta, M. Brunelli and C. Ferrero, *Chem. Mater.*, 2012, **24**, 1338–1345.

[3] K. W. Chapman, P. J. Chupas and C. J. Kepert, *J. Am. Chem. Soc.*, 2005, **127**, 15630–15636.

[4] M. S. Senn, D. A. Keen, T. C. Lucas, J. A. Hriljac and A. L. Goodwin, *Phys. Rev. Lett.*, 2016, **116**, 207602.

[5] U. Ruett, J. Almer, P. Kenesei, J. S. Park, R. Osborn, Y. Ren, D. Robinson, M. Krogstad, S. Rosenkranz, X. Zhang, M. Li and K. M. Wiaderek, *Synchrotron Radiat. News*, 2020, **33**, 44–50.

[6] J. Neuefeind, M. Feygenson, J. Carruth, R. Hoffmann and K. K. Chipley, *Nucl. Instruments Methods Phys. Res. Sect. B Beam Interact. with Mater. Atoms*, 2012, **287**, 68–75.

[7] A. C. Hannon, *Nucl. Instruments Methods Phys. Res. Sect. A Accel. Spectrometers, Detect. Assoc. Equip.*, 2005, **551**, 88–107.

[8] R. I. Smith, S. Hull, M. G. Tucker, H. Y. Playford, D. J. McPhail, S. P. Waller and S. T. Norberg, *Rev. Sci. Instrum.*, 2019, **90**, 115101.

[9] T. Connolley, C. M. Beavers and P. Chater, *Synchrotron Radiat. News*, 2020, **33**, 31–36.

[10] J. K. Mathiesen, R. Väli, M. Härmas, E. Lust, J. F. von Bülow, K. M. Ø. Jensen and P. Norby, *J. Mater. Chem. A*, 2019, **7**, 11709–11717.

[11] K. M. Ø. Jensen, H. L. Andersen, C. Tyrsted, E. D. Bøjesen, A. C. Dippel, N. Lock, S. J. Billinge, B. B. Iversen and M. Christensen, *ACS Nano*, 2014, **8**, 10704–10714.

[12] D. Olds, K. Page, A. Paecklar, P. F. Peterson, J. Liu, G. Rucker, M. Ruiz-Rodriguez, M. Olsen, M. Pawel, S. H. Overbury and J. R. Neilson, *Rev. Sci. Instrum.*, 2017, **88**, 034101.

[13] D. Saha, E. D. Bøjesen, K. M. Ø. Jensen, A. C. Dippel and B. B. Iversen, *J. Phys. Chem. C*, 2015, **119**, 13357–13362.

[14] W. A. Sławinski, *J. Appl. Crystallogr.*, 2018, **51**, 919–923.

[15] M. Diaz-Lopez, G. L. Cutts, P. K. Allan, D. S. Keeble, A. Ross, V. Pralong, G. Spiekermann and P. A. Chatera, *J. Synchrotron Radiat.*, 2020, **27**, 1190–1199.

[16] S. A. Moggach, W. G. Marshall and S. Parsons, *Acta Crystallogr. Sect. B*, 2006, **62**, 815–825.

[17] E. Eikeland, M. K. Thomsen, J. Overgaard, M. A. Spackman and B. B. Iversen, *Cryst. Growth Des.*, 2017, **17**, 3834–3846.

[18] P. A. Wood, R. S. Forgan, D. Henderson, S. Parsons, E. Pidcock, P. A. Tasker and J. E. Warren, *Acta Crystallogr. Sect. B*, 2006, **62**, 1099–1111.

[19] J. M. Besson, R. J. Nelmes, G. Hamel, J. S. Loveday, G. Weill and S. Hull, *Phys. B Condens. Matter*, 1992, **180-181**, 907–910.

[20] S. Klotz, J. M. Besson, G. Hamel, R. J. Nelmes, J. S. Loveday, W. G. Marshall and R. M. Wilson, *Appl. Phys. Lett.*, 1995, **66**, 1735–1737.

[21] S. Klotz, J. C. Chervin, P. Munsch and G. Le Marchand, *J. Phys. D. Appl. Phys.*, 2009, **42**, 075413.

[22] K. W. Chapman, P. J. Chupas, G. J. Halder, J. A. Hriljac, C. Kurtz, B. K. Greve, C. J. Ruschman and A. P. Wilkinson, *J. Appl. Crystallogr.*, 2010, **43**, 297–307.

[23] L. Wang, W. Yang, Y. Ding, Y. Ren, S. Xiao, B. Liu, S. V. Sinogeikin, Y. Meng, D. J. Gosztola, G. Shen, R. J. Hemley, W. L. Mao and H.-k. Mao, *Phys. Rev. Lett.*, 2010, **105**, 095701.

[24] K. W. Chapman, P. J. Chupas, C. A. Kurtz, D. R. Locke, J. B. Parise and J. A. Hriljac, *J. Appl. Crystallogr.*, 2007, **40**, 196–198.

[25] P. S. Salmon, J. W. Drewitt, D. A. Whittaker, A. Zeidler, K. Wezka, C. L. Bull, M. G. Tucker, M. C. Wilding, M. Guthrie and D. Marrocchelli, *J. Phys. Condens. Matter*, 2012, **24**, 415102.

[26] A. Zeidler, K. Wezka, D. A. Whittaker, P. S. Salmon, A. Baroni, S. Klotz, H. E. Fischer, M. C. Wilding, C. L. Bull, M. G. Tucker, M. Salanne, G. Ferlat and M. Micoulaut, *Phys. Rev. B*, 2014, **90**, 024206.

[27] H. Y. Playford, M. G. Tucker and C. L. Bull, *J. Appl. Crystallogr.*, 2017, **50**, 87–95.

[28] H. S. Geddes, H. Blade, J. F. McCabe, L. P. Hughes and A. L. Goodwin, *Chem. Commun.*, 2019, **55**, 13346–13349.

[29] X. Hua, P. K. Allan, C. Gong, P. A. Chater, E. M. Schmidt, H. S. Geddes, A. W. Robertson, P. G. Bruce and A. L. Goodwin, *Nat. Commun.*, 2021, **12**, 561.

[30] C. L. Bull, N. P. Funnell, M. G. Tucker, S. Hull, D. J. Francis and W. G. Marshall, *High Press. Res.*, 2016, **36**, 493–511.

[31] W. G. Marshall and D. J. Francis, *J. Appl. Crystallogr.*, 2002, **35**, 122–125.

[32] B. Chen, D. Penwell and M. B. Kruger, *Solid State Commun.*, 2000, **115**, 191–194.

[33] M. H. G. Jacobs and H. A. J. Oonk, *Phys. Chem. Chem. Phys.*, 2000, **2**, 2641–2646.

[34] R. J. Angel and D. R. Allan, *J. Appl. Crystallogr.*, 1997, **30**, 461–466.

[35] O. Arnold, J. C. Bilheux, J. M. Borreguero, A. Buts, S. I. Campbell, L. Chapon, M. Doucet, N. Draper, R. Ferraz Leal, M. A. Gigg, V. E. Lynch, A. Markvardsen, D. J. Mikkelson, R. L. Mikkelson, R. Miller, K. Palmen, P. Parker, G. Passos, T. G. Perring, P. F. Peterson, S. Ren, M. A. Reuter, A. T. Savici, J. W. Taylor, R. J. Taylor, R. Tolchenov, W. Zhou and J. Zikovsky, *Nucl. Instruments Methods Phys. Res. Sect. A Accel. Spectrometers, Detect. Assoc. Equip.*, 2014, **764**, 156–166.

[36] A. A. Coelho, *J. Appl. Crystallogr.*, 2018, **51**, 210–218.

[37] M. G. Tucker, D. A. Keen, M. T. Dove, A. L. Goodwin and Q. Hui, *J. Phys. Condens. Matter*, 2007, **19**, 335218.

[38] B. Li, K. Woody and J. Kung, *J. Geophys. Res. Solid Earth.*, 2006, **111**, 11206.

[39] D. A. Keen, *J. Appl. Crystallogr.*, 2001, **34**, 172–177.

[40] M. J. Abraham, T. Murtola, R. Schulz, S. Páll, J. C. Smith, B. Hess and E. Lindah, *SoftwareX*, 2015, **1-2**, 19–25.

[41] J. Huang, S. Rauscher, G. Nawrocki, T. Ran, M. Feig, B. L. De Groot, H. Grubmüller and A. D. MacKerell, *Nat. Methods*, 2016, **14**, 71–73.

[42] B. A. Luty, M. E. Davis, I. G. Tironi and W. F. Van Gunsteren, *Mol. Simul.*, 1994, **14**, 11–20.

[43] G. Bussi, D. Donadio and M. Parrinello, *J. Chem. Phys.*, 2007, **126**, 014101.

[44] H. J. C. Berendsen, J. P. M. Postma, W. F. van Gunsteren, A. DiNola and J. R. Haak, *J. Chem. Phys.*, 1984, **81**, 3684–3690.

[45] B. Hess, *J. Chem. Theory Comput.*, 2008, **4**, 116–122.

[46] R. Agarwal, M. D. Smith and J. C. Smith, *J. Chem. Theory Comput.*, 2020, **16**, 2529–2540.

[47] A. K. Soper and C. J. Benmore, *Phys. Rev. Lett.*, 2008, **101**, 065502.

[48] K. Kuchitsu and L. S. Bartell, *J. Chem. Phys.*, 1962, **36**, 2470–2481.

[49] N. L. Allinger and H. L. Flanagan, *J. Comput. Chem.*, 1983, **4**, 399–403.

[50] J. Zhang, Y. Zhao and B. Palosz, *Appl. Phys. Lett.*, 2007, **90**, 043112.

[51] S. S. Kushwah and J. Shanker, *Phys. B Condens. Matter*, 1998, **253**, 90–95.

[52] S. Kirkpatrick, C. C. Gelatt and M. P. Vecchi, *Science*, 1983, **220**, 671–680.

[53] A. Herlihy, H. S. Geddes, G. C. Sosso, C. L. Bull, C. J. Ridley, A. L. Goodwin, M. S. Senn and N. P. Funnell, *J. Appl. Crystallogr.*, 2021, **54**, 1546–1554.

[54] L.-G. Liu, *Mech. Mater.*, 1993, **14**, 283–290.

[55] M. T. Dove, M. G. Tucker and D. A. Keen, *Eur. J. Mineral.*, 2002, **14**, 331–348.

[56] M. G. Tucker, M. T. Dove and D. A. Keen, *J. Phys. Condens. Matter*, 2000, **12**, L723–L730.

[57] V. P. Prakapenka, G. Shen, L. S. Dubrovinsky, M. L. Rivers and S. R. Sutton, *J. Phys. Chem. Solids.*, 2004, **65**, 1537–1545.

[58] L. Malavasi, *Dalt. Trans.*, 2011, **40**, 3777–3788.

[59] M. J. Cliffe, W. Wan, X. Zou, P. A. Chater, A. K. Kleppe, M. G. Tucker, H. Wilhelm, N. P. Funnell, F. X. Coudert and A. L. Goodwin, *Nat. Commun.*, 2014, **5**, 4176.

[60] F. X. Coudert, *Chem. Mater.*, 2015, **27**, 1905–1916.

[61] E. Gilioli and L. Ehm, *IUCrJ*, 2014, **1**, 590–603.

[62] B. K. Greve, K. L. Martin, P. L. Lee, P. J. Chupas, K. W. Chapman and A. P. Wilkinson, *J. Am. Chem. Soc.*, 2010, **132**, 15496–15498.

[63] T. A. Bird, J. Woodland-Scott, L. Hu, M. T. Wharmby, J. Chen, A. L. Goodwin and M. S. Senn, *Phys. Rev. B*, 2020, **101**, 064306.

Chapter 3

Recovery of harmonic–like behaviour of the polar mode in $BaTiO_3$ at high pressures

The work reported in this Chapter is published: A. Herlihy, T. A. Bird, C. J. Ridley, C. L. Bull, N. P. Funnell and M. S. Senn, *PRB*, 2022, **105**, 094114.

3.1 Introduction

$BaTiO_3$ is often presented as a classic example of a 'proper ferroelectric' where, due to the second-order Jahn-Teller effect, an off-centring of the Ti^{4+} cation from the centre of the octahedron results in a net polarisation.[1] The resulting ferroelectric properties and high dielectric constant make $BaTiO_3$ a very attractive material for use in devices such as capacitors,[2] and the perovskite-structured material has become the 'prototypical' ferroelectric; intensively studied to understand the link between ferroelectricity and crystal structure.[3] Above its Curie temperature (T_C), $BaTiO_3$ adopts a cubic structure. Below T_C, the average structure is reduced to a tetragonal symmetry and on decreasing temperature further, $BaTiO_3$ transforms to orthorhombic and, finally, rhombohedral structures.[3–6]

Despite many decades of study, there remains an ongoing debate about the nature of the ferroelectric phase transition. A popular theory, suggested by Cochran[5] in 1960 describes a displacive model whereby Ti^{4+} cations are displaced along $\langle 100 \rangle$, $\langle 110 \rangle$, and $\langle 111 \rangle$ directions for the tetragonal, orthorhombic and rhombohedral phases respectively. This model, however, fails to address key

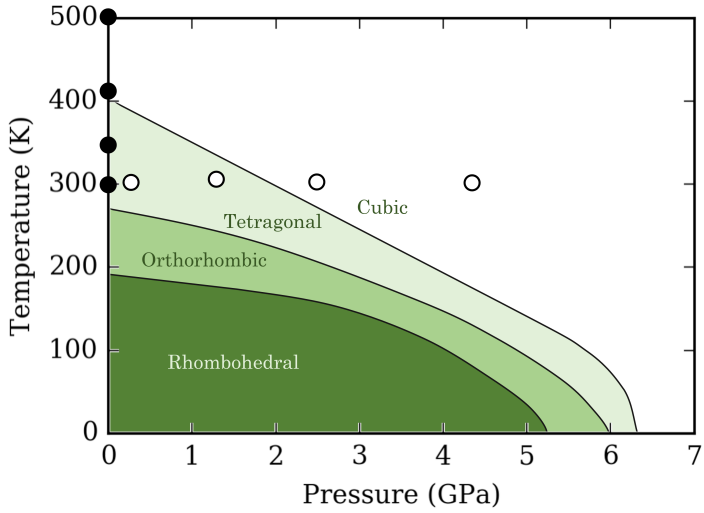

Figure 3.1: The phase diagram of the average structure of $BaTiO_3$, recreated from the work of Ishidate *et al.*[7] Open circles represent the pressures at which $BaTiO_3$ was measured for this local structure study and filled circles represent previously measured ambient pressure data.

observations such as the strong diffuse X-ray scattering which is present in all but the rhombohedral phase[8–10] and the presence of first-order Raman excitations in the cubic phase.[11] The displacive model also does not account for the orthorhombic and rhombohedral phase transitions, which do not follow a group-subgroup relationship which is otherwise present for this type of transition. In 1968, Comés *et al.*[8] proposed an order-disorder (OD) model, also commonly referred to as the 'eight-site' model, where the crystallographically-rich phase diagram of $BaTiO_3$ (Figure 3.1) is rationalised due to correlations of local Ti displacements along the eight $\langle 111 \rangle$ directions. The displacement of Ti from the centre of its TiO_6 coordination environment is locally favoured due to the second-order Jahn-Teller effect. Correlated $\langle 111 \rangle$ displacements of the Ti atom in successive $\langle 100 \rangle$ directions give rise to the observed average symmetry, and it is this underlying disorder that appears to simultaneously reconcile the perceived average symmetry with the anomalous experimental results. However, the observation of heavily-damped modes[12–14] appears at odds with an OD model, and supports the soft-mode explanation. Furthermore, there is not yet consensus—within the OD interpretation—on the exact nature of the disordered local arrangements of Ti cations, where some reports (*via* solid state NMR[15]) suggest a local tetragonal distortion and others support a rhombohedral[16,17] distortion.

Since the first proposal of these two contending models, a multitude of experimental and computational studies have favoured either one of these two possible scenarios. Local probes tend to support an OD model.[15,16,18] Such studies include a variable temperature neutron total scattering study, performed on GEM at ISIS.[19] High quality PDFs (Q_{max} = 40 Å) measured at 15, 150, 210, 250, 293, 350, 410 and 500 K (Figure 3.2) were analysed using a symmetry-motivated approach, showing that the Ti displacements are rhombohedral-like at every measured temperature.

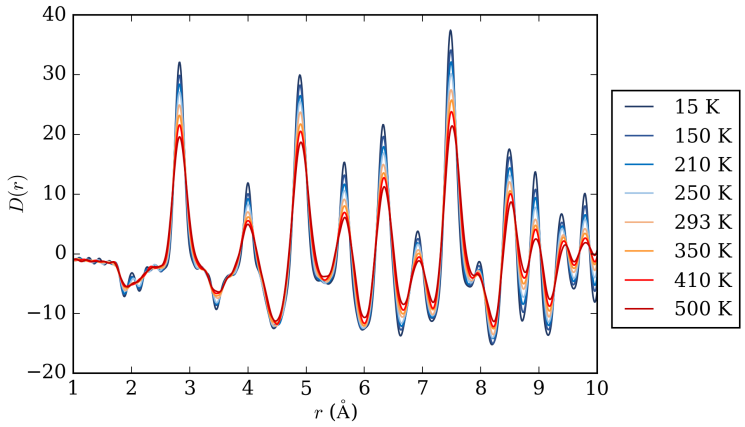

Figure 3.2: Variable temperature PDFs of $BaTiO_3$ measured on GEM, analysed and published by Senn *et al.*[19] in support of the order-disorder model.

More recently, additional work has come out in support of the soft mode model,[10] where diffuse scattering is attributed to the overdamped anharmonic soft phonon branch. This results in a local probability distribution for the Ti atoms that has a minimum coinciding with the average crystallographic position and a maximum along ⟨111⟩ directions with an average magnitude of ca. 0.15 Å. It seems that a wealth of experimental and computational observations can either be explained by invoking an OD scenario or considering highly over-damped, anharmonic, soft phonon modes that imply the Ti atoms spend a substantial amount of time off-centre. Consideration of the long range ordering of dynamic ⟨111⟩ Ti displacements projected onto the ⟨100⟩ directions as 'chains' of correlated local rhombohedral Ti displacements (shown in Figure 3.3) appears to reconcile these two models.[19] Regardless of the perspective adopted, it is clear that the local symmetry deviates substantially from the average crystallographic symmetry over short length scales and long time periods,[20] indicating a significant departure from the harmonic soft mode/displacive picture.

Clearly, the investigation of the temperature-induced phase transitions of $BaTiO_3$ has been extensive, and a wide range of techniques have been utilised to investigate the average and local structure of the perovskite structure.[21] Investi-

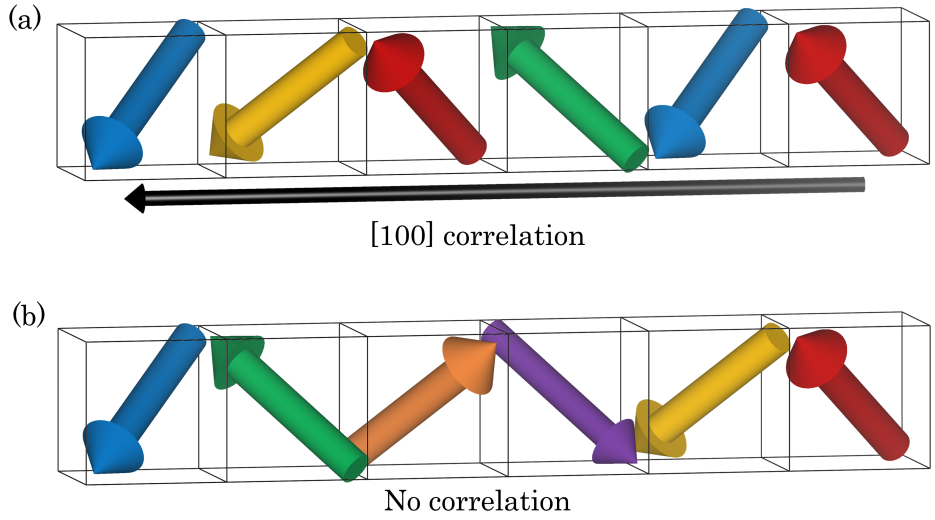

Figure 3.3: Arrows representing the local ⟨111⟩ Ti displacements correlated along a [100] direction (a) and uncorrelated (b), with no common distortion direction.

gation of the pressure-induced phase transition is important too as the application of pressure is known to induce phase transitions in perovskites[22] and therefore can be used to tune functionality. However, challenges associated with *in situ* high pressure measurements—outlined in Chapter 2—have perhaps limited investigation of the local structure of $BaTiO_3$ in other regions of the phase diagram.

Modest hydrostatic pressure will initially act to suppress ferroelectric distortions in ABO_3 perovskites due to the increasing influence of short-range electronic repulsions over long-range Coulomb ionic interactions which favour polar distortions.[23] The well-established average structure phase diagram (Figure 3.1) of $BaTiO_3$ indicates that at ambient temperature, there is a tetragonal-to-cubic phase transition at ca. 2 GPa.[6,7,24] High-pressure Raman studies show evidence for persistent disorder within the cubic phase, with the suggestion that this disorder results from off-centre Ti atoms and grain boundary/intergrain stress.[25] X-ray absorption spectroscopy (XAS) of the Ti K edge also suggests that Ti remains displaced until 10 GPa, above which the Ti is centred and local and average symmetries are reconciled.[26] Together, these results might imply that the high

temperature and high pressure behaviour mimic each other. However, neither of these studies appear to have allowed for robust refinement of competing models against the local probe data.

PDFs generated from total scattering experiments and their sensitivity to short-range atom–atom correlations are well suited to this kind of modelling and therefore interrogation of the local structure behaviour of $BaTiO_3$. Thus, this Chapter reports the first analysis of neutron total scattering measurements of $BaTiO_3$ at pressures up to 4.2 GPa, in order to directly investigate the nature of the pressure-induced tetragonal-to-cubic phase transition of $BaTiO_3$ over a range of length scales.

Building on the newly developed symmetry adapted PDF analysis (SAPA)[27] technique, whereby distortion modes grouped by irreducible representation are refined against local structure measurements, the high-pressure PDF data have been analysed, revealing pressure-induced suppression of the local Ti displacements. The same modelling approach is applied to previously-published variable temperature PDFs[19] in order to determine how the departure of local from average symmetry compares for pressure *versus* temperature. This analysis of ambient temperature, variable-pressure PDFs points toward a gradual pressure-induced suppression of the anharmonic potential implicit in describing the OD behaviour of $BaTiO_3$, towards a more harmonic-like soft-mode picture.

3.2 Experimental details

Polycrystalline $BaTiO_3$ (also used for the variable-temperature study carried out using the GEM instrument) was measured on the high-pressure instrument PEARL,[28] at the ISIS Neutron and Muon Facility. An argon gas pressure transmitting medium (PTM) was chosen as argon is a relatively weak neutron scatterer

(with a neutron scattering length of 1.909×10^{-15} m compared to 5.803×10^{-15} m of oxygen). $BaTiO_3$ was loaded into a null-scattering TiZr gasket[29] which was placed between ZTA anvils inside a clamp device, designed for use with gas loading apparatus.[30] The clamp was left unsealed, and placed in the loader which was then filled with argon gas and compressed to ca. 2 kbar. The clamp was sealed shut, removed from the gas loader, and placed into the oil-driven PE press with which loads of 3, 25, 40 and 50 tonnes were applied to the sample. Stacked vanadium discs were loaded in the same way, with an argon PTM. Ideally the same ZTA anvils would have been used for the vanadium measurement however experimental restrictions of the gas-loader meant that the gaskets had to be loaded and sealed by their respective anvil assemblies before the experiment.

Applying the same loads to different gasket assemblies (*i.e.*, $BaTiO_3$ powder and vanadium discs) does not necessarily realise the same pressure as gasket packing will vary between loading. Normally a pressure marker or sample with a known EoS would be used to determine the pressure, as is the case with the $BaTiO_3$ measurements, however, including a pressure marker to the vanadium would only complicate correction procedures for generating PDFs, for the same reasons detailed in Chapter 2.

Instead, the load applied to the vanadium discs was incrementally increased and the diffraction pattern measured for sufficient time to determine peak positions and approximate background levels. The diffraction pattern of the vanadium measurement was compared to the $BaTiO_3$ measurement and the load was increased until the positions of the ZTA anvil Bragg peaks matched, as shown in Figure 6.12 for the lowest pressure data collection (analogous figures for the three higher pressure data collections are provided in the Appendix). The vanadium was subsequently measured under loads of 8, 20, 30, 45 tonnes, corresponding to pressures roughly equivalent to those of the measured $BaTiO_3$ data.

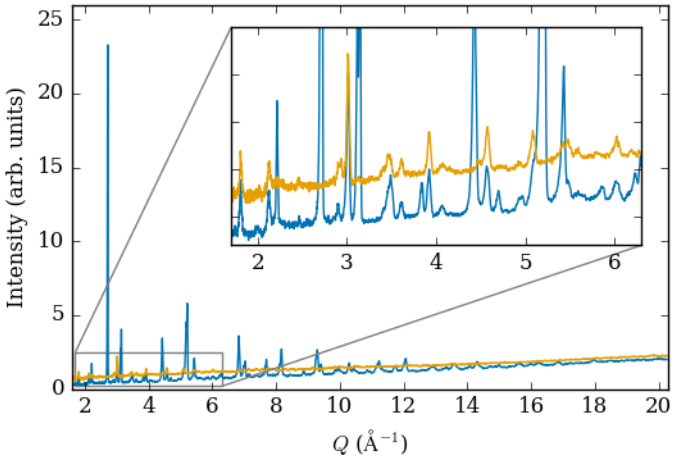

Figure 3.4: Neutron diffraction patterns of $BaTiO_3$ (blue) and vanadium (yellow) measured on PEARL at three and eight tonnes respectively. The inset plot shows a comparison of the two diffraction patterns and the Bragg scattering from the ZTA anvils more clearly.

Neutron powder diffraction patterns were collected for a minimum of 11 hours each to ensure sufficient signal-to-noise ratio at high Q. Data were reduced using the MANTID software package[31] to correct for the effects of attenuation by the ZTA anvils and normalised against a vanadium sphere measurement, performed at the start of each cycle, to account for flux profile. Small-box PDF modelling and Rietveld refinements were carried out using TOPAS Academic v6.[32] Si and CeO_2 standards, also measured at the start of the cycle, were used to refine diffractometer constants and peak shape parameters, respectively.

3.3 High-pressure average structure

Neutron diffraction patterns indicated that the measured average structures of $BaTiO_3$ at high pressures were consistent with previous literature.[6,24,33] The neutron diffraction patterns (Figure 3.5) at 0.24 and 1.19 GPa exhibited peak splitting, clearly observed at a d-spacing of ca. 2.0 Å, corresponding to the (200)/(002) peaks. This is indicative of tetragonal symmetry, and Rietveld refinements confirmed a $P4mm$ average crystal structure. Above 2 GPa, $BaTiO_3$ transforms to

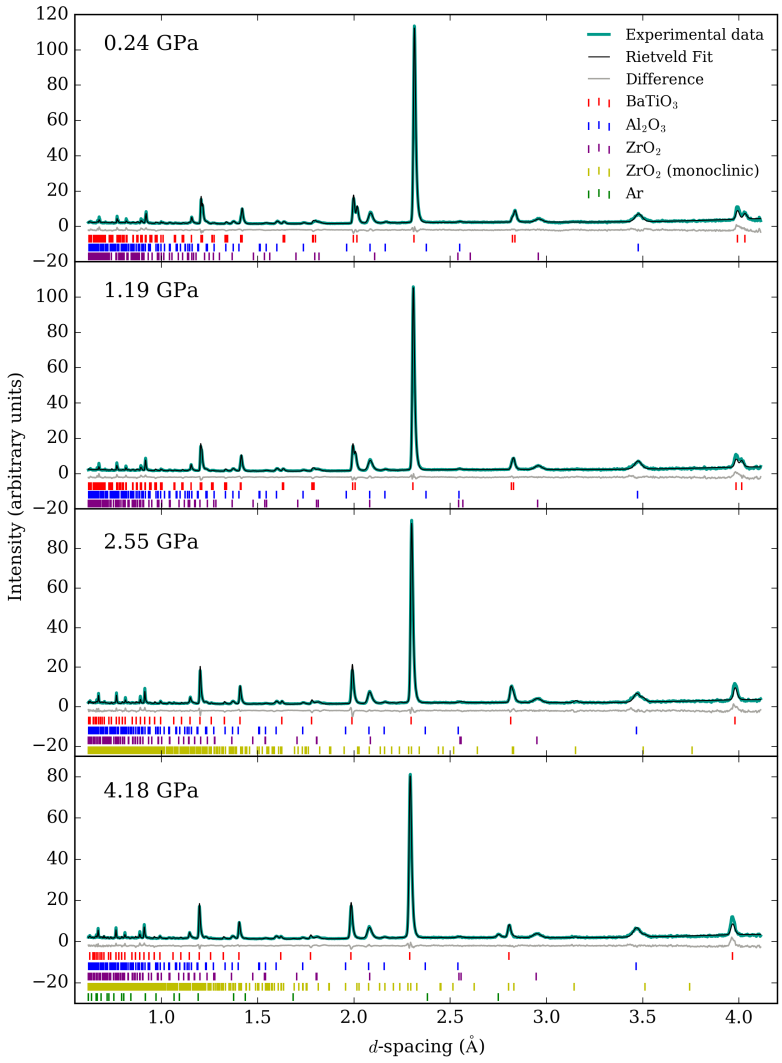

Figure 3.5: Rietveld fits of as-measured neutron diffraction patterns of $BaTiO_3$ at increasing pressure.

an average cubic symmetry ($Pm\bar{3}m$), confirmed again by Rietveld refinement at 2.55 and 4.18 GPa, and accompanied by an absence of 'tetragonal' peak splitting. At 4.18 GPa an additional reflection is observed at a d-spacing of ca. 2.7 Å. This was tentatively assigned to the most intense reflection (111) of cubic ($Fm\bar{3}m$) argon, although it is important to note that the absence of any significant peak broadening in the diffraction pattern confirmed that the sample remained under hydrostatic conditions throughout the experiment.

3.4 Generating and modelling PDFs

Total scattering data were collected and treated using largely the same procedure described by Playford *et al.*[34] and in Chapter 2, and summarised again here for completeness. The total scattering pattern ($S(Q)$) was produced by subtracting the scattering pattern of the vanadium measurement from the $BaTiO_3$ measurement to account for scattering from the gasket and anvil assembly, and the subsequent scattering pattern was corrected by applying a scale factor and an offset value such that the resulting $S(Q)\rightarrow 1$ at Q_{max}. PDFs (Figure 3.6) were obtained *via* Fourier transform of the $S(Q)$ function using the program StoG, distributed with the RMCProfile package.[35]

There was no evidence of an argon contribution to the PDF. A cubic crystal structure would result in a shortest atom–atom correlation of ca. 3.4 Å at 4.18 GPa and above the level of Fourier artefacts there are no such peaks and later small-box modelling revealed no misfitting around this r region. In each PDF, r-dependent broadening that arises from correlated thermal motion was modelled using a simple quadratic, *i.e.*, $b_r = b_i + \alpha r + \beta r^2$, where α and β are constant across all atomic sites and b_i is element dependent. For this work,

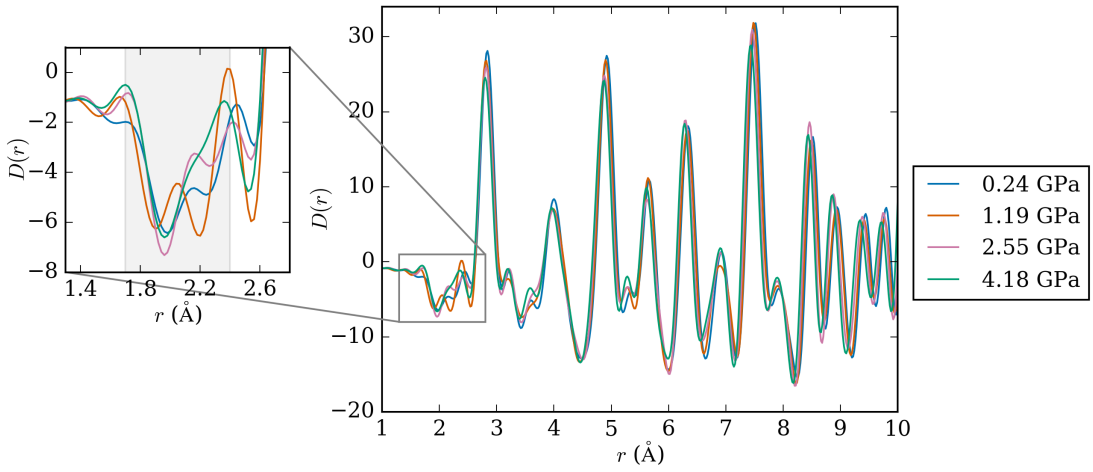

Figure 3.6: Variable-pressure PDFs measured on PEARL, with a zoomed section and grey region highlighting the negative peak due to the Ti–O correlation.

β was fixed at zero as it is found to refine to negligible values.[36] Damping of the PDF intensity at high r—due to Q resolution (dQ) was accounted for with dQ = 0.045 Å^{-1}. The lattice parameters of $BaTiO_3$ were determined from Rietveld refinement against the Bragg data and the known equation of state reported by Bull *et al.*[24] was used to calculate sample pressures of 0.24(2), 1.19(2), 2.55(6) and 4.18(8) GPa—corresponding to two lower pressure measurements in the average tetragonal regime, and two high pressure measurements in the average cubic regime.

The effect of the finite and limited Q-range of PEARL on the resulting PDFs is apparent in Figure 3.6. Below 4 Å there are clear Fourier termination ripples either side of the negative Ba–Ti peak at ca. 3.3 Å and although the 'key' negative Ti–O peak (zoomed plot in Figure 3.6) displays some very pronounced differences, the features appear affected by the Fourier artefacts.

3.5 Validation of PDF sensitivity

The lack of high pressure neutron PDF studies of $BaTiO_3$, and of crystalline materials more generally can be attributed to the often opposing requirements of high pressure and PDF experiments. It is only relatively recently that high-pressure neutron PDF measurements have been achieved for crystalline materials,[34,37] therefore the study reported within this Chapter represents an emerging capability of high-pressure neutron total scattering, and exemplifies the types of local structure information that an experiment on PEARL may provide.

Requirements of high-quality PDF experiments include minimisation (and/or subtraction) of any non-sample scattering and a large Q_{max} where the resolution of a PDF is inversely related to the maximum experimental Q value ($\Delta r = 2\pi/Q_{max}$). PEARL has a limited Q_{max} (20.32 Å^{-1}), due to a combi-

nation of instrument characteristics and PE press geometry—where scattering is constrained to 90°—compared to instruments typically used to measure local structure on such materials, where Q_{max} values are more commonly in the range 40–50 Å^{-1}. Therefore it is first necessary to establish whether the data with reduced Q_{max} have sufficient r-resolution to allow investigation of the ferroelectric modes of $BaTiO_3$.

In order to evaluate the sensitivity of the symmetry-adapted small-box modelling approach to limited Q_{max} values, PDFs were processed from room temperature $S(Q)$s measured on GEM (previously published by Senn *et al.*[19]) with artificially reduced Q_{max} values of 10–40 Å^{-1} in steps of 5 Å^{-1}, as shown in Figure 3.7. Even with a low Q_{max} of 15 Å^{-1}, the PDF is remarkably similar to that of the highest resolution PDF, however there are clear and substantial differences at low r, particularly of the Ti–O peak shown inset in Figure 3.7. The position of the peak minimum remains constant at 1.90 Å within the histogram bin size (0.02 Å) of the PDF between 40–25 Å^{-1}. The peak minimum shifts by 0.04 Å at 20 Å^{-1} and by 0.12 Å at 15 Å^{-1}. This gives confidence that the PDFs mea-

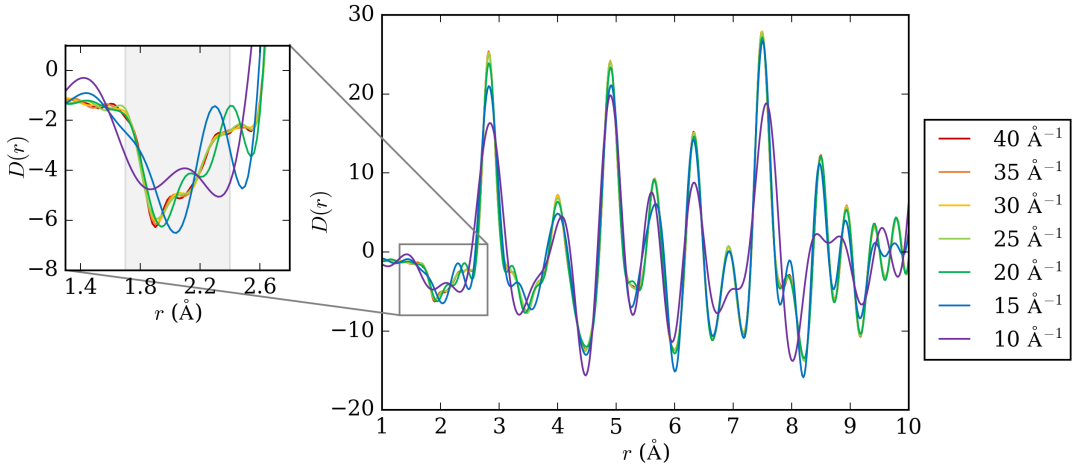

Figure 3.7: $BaTiO_3$ PDFs produced from the total scattering data measured on GEM at 293 K[19] with artificially reduced maximum Q_{max} values indicated by the legend. The zoomed section and grey region highlights the negative peak due to the Ti–O correlation. Note that the PDFs generated with a Q_{max} of 35 Å^{-1} and 40 Å^{-1} are not clearly visible as there is only a marginal change.

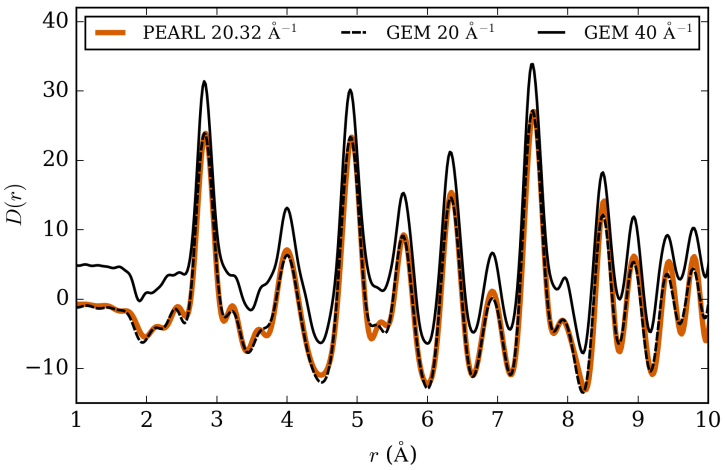

Figure 3.8: PDFs of $BaTiO_3$ measured on PEARL at 0.24 GPa, processed with a Q_{max} of 20.32 Å^{-1}, and on GEM at ambient pressure and temperature, processed with Q_{max} values of 20 and 40 Å^{-1} (the latter is offset in the y-direction for clarity).

sured on PEARL with $Q_{max} = 20.32$ Å^{-1} are not significantly impacted by the relatively low Q.

Figure 3.8 shows that PDFs measured on GEM and PEARL (*i.e.*, in a vanadium can and PE press respectively) and processed with the same Q_{max} very closely agree, again, validating the high-pressure data.

To further test the validity of the PDF, the models were refined following previously published work, where previous analysis by Senn *et al.*[19] of the variable temperature GEM PDFs showed that the Γ_4^- irrep. (which essentially describes the displacement of the Ti atom) could be identified as the best fitting irrep. at all temperatures compared to all other symmetry-lowering distortion modes. Therefore, in order to test the sensitivity of the variable-Q_{max} PDFs to the known Γ_4^- distortion (*i.e.*, whether Γ_4^- is still identified as the best fitting irrep.), a 'symmetry-adapted pair distribution function analysis' (SAPA)[27] was performed.

The SAPA approach, developed within the Senn group,[27] is a symmetry-motivated small box modelling method whereby symmetry-based constraints are used in order to probe specific distortions within a material. A parent cell is

chosen that exhibits the highest symmetry that structural class can crystallise in—for a perovskite this is $Pm\bar{3}m$. The potential symmetry lowering distortions are then described by considering an expanded $P1$ supercell. The online tool ISODISTORT[38] is then used to describe the various symmetry lowering required to reach this supercell in terms of distortion modes transforming as irreps. of the parent $Pm\bar{3}m$ structure. These irreps. are then in turn either fixed to zero or allowed to refine against the PDF data, with initial amplitudes randomised and refinements repeated many times (100–500 cycles) in order to ensure the local minima is reached. Analysis of fitting statistics and refined mode amplitudes enable a robust evaluation of lattice dynamics and local distortions. For analysis of the $BaTiO_3$ PDFs, using the same approach previously applied to the ambient pressure GEM PDFs, the distortion modes were generated using a $2 \times 2 \times 2$ high symmetry supercell $Pm\bar{3}m$ structure and the lattice parameters were constrained to those of the average tetragonal structure of $BaTiO_3$ at 293 K. The irreps. listed in Figure 3.9 were refined against the PDFs with 500 cycles at each $Q_{\max}$ value, where at the start of each cycle the mode amplitudes defined for the irrep. are randomised (within the range -0.05 to 0.05), in order to ensure the

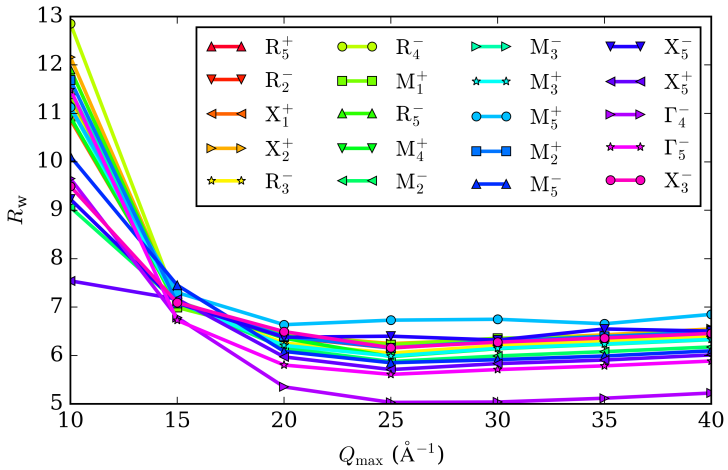

Figure 3.9: Fitting statistics (R_w) for irreps. tested against PDFs of $BaTiO_3$ as a function of $Q_{\max}$ value.

global minimum had been reached.

Figure 3.9 shows the fitting statistics R_w for the 20 irreps. tested against the variable-Q_{max} PDFs. It is unsurprising that the Γ_4^- irrep. results in the best fit, as indicated by a lower R_w value, for the higher resolution PDFs. At $Q_{max} = 20$ Å^{-1} the Γ_4^- irrep. reassuringly still results in the best fit, indicating sufficient PDF peak resolution for this type of mode analysis. By $Q_{max} = 15$ Å^{-1}, the Γ_4^- and Γ_5^- irreps. result in equally good fits and by $Q_{max} = 10$ Å^{-1}, the X_5^+ apparently fits the best and sensitivity to the ferroelectric mode is evidently lost. The key finding here is that $Q_{max} = 20$ Å^{-1} is sufficient for recovering the known OP, Γ_4^-.

In order to ascertain the OPD and nature of the local Ti displacements—the main goal of this work—a more directed modelling approach can be taken. To ensure that the PEARL PDFs were sensitive to the OPD, further analysis was performed. The local structure was modelled using a $P1$ unit cell, with only polar distortion modes associated with Ti and O (transforming as the Γ_4^- irrep.) refined, and Ba modes set to zero to fix the floating origin of the unit cell. The most general OPD associated with this irrep is three dimensional (a, b, c). The Ti(T_{1u}), O(A_{2u}) and O(E_u) modes, that form a basis of this irrep, thus have three branches each, where particular constraints on the branched mode amplitudes correspond to higher symmetry OPDs. Since ambient pressure $BaTiO_3$ has been shown to exhibit a local rhombohedral-type distortion, the OPDs of the modes can be constrained to (a, a, a) rhombohedral symmetry.

The rhombohedral model was fitted to this contiguous series of variable-Q_{max} PDFs, over the r-range 1.2–10 Å, with lattice parameters fixed to those determined by Rietveld refinement. The resulting mode amplitude values for Ti are shown in Figure 3.10. They again show notable consistency over the Q-range 20–40 Å^{-1}, and—since a 293 K total scattering measurement of $BaTiO_3$ on the GEM instrument is the closest comparison to the lowest pressure (0.24(2) GPa),

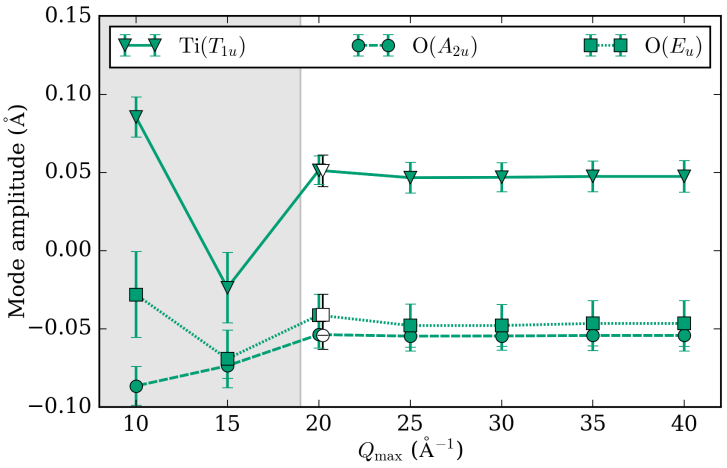

Figure 3.10: Refined mode amplitude values for rhombohedrally constrained Ti and O distortions for a room temperature $BaTiO_3$ PDF measured on GEM and processed with Q_{max} values ranging from 10–40 Å^{-1} in steps of 5 Å^{-1} (filled markers). The unfilled markers represent the mode amplitude values for the lowest pressure (0.24(2) GPa), ambient temperature measurement of $BaTiO_3$ on PEARL. The grey section represents the Q_{max} region for which refined mode distortions behave unphysically.

ambient temperature PEARL measurement—the PEARL data can be directly compared. Crucially, it is found that the modes refined against the 0.24 GPa PEARL data with $Q_{max} = 20.32$ Å^{-1} (open symbols in Figure 3.10) are in excellent agreement with the 20 Å^{-1} GEM results, falling well within error of each other. As found with the full SAPA analysis, at $Q_{max} = 15$ Å^{-1} the values become inconsistent with those found for higher resolution PDFs.

These specific (a, a, a) OPD results establish the lower limit in Q_{max} with respect to extracting physically meaningful displacements in this study and validate the sensitivity of the high pressure PDFs with respect to the local OPs that are key in this local structure investigation.

3.6 Constrained small box modelling

A significant strength of total scattering is the ability to investigate the structure over a range of length-scales and as a function of r. A PDF can be generated

with very large r_{max} values, dependent on the sample and instrumental effects. In order to explore the information contained, as a function of correlation distance, within the PDF, different r-ranges of PDF were investigated. Variable-range modelling[21,39] has been used whereby the minimum of the fitting range (r_{min}) is kept constant and the maximum (r_{max}) is increased sequentially. A similar technique is so-called 'box-car' fitting[40,41] where the fitting range is held constant and shifted along the PDF, resulting in the progressively reduced influence of the immediate local structure on the refined small-box model—results from this type of analysis have been reported in the Appendix.

Small-box variable range PDF refinements were performed with an r_{min} of 1.2 Å and an r_{max} increasing from 4 to 30 Å in steps of 1 Å. Therefore, the overall fitting range was varied between 2.8 and 28.8 Å, such that progressively large length-scale atom–atom correlations were probed as $r_{max} \rightarrow 30$ Å.

Lattice parameters—determined from Rietveld refinements of the diffraction patterns—were fixed for all subsequent small-box PDF refinements, constraining the metric symmetries to those known from the average structures. Rather than allowing the distortion modes to refine freely, the OPD was constrained to be consistent with cubic $(0,0,0)$, tetragonal $(a,0,0)$ or rhombohedral (a,a,a) sym-

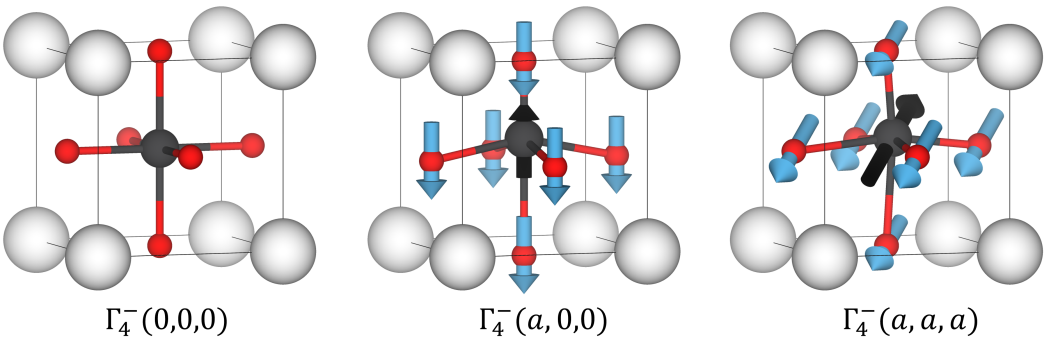

Figure 3.11: Behaviour of the modes belonging to the Γ_4^- irrep. in the indicated OPD. The black arrows indicate the atom displacement arising from the Ti(T_{1u}) mode and the blue arrows correspond to the combination of the O(A_{2u}) and O(E_u) modes. White spheres are Ba atoms.

metries in order to test these three specific local distortion behaviours, shown in Figure 3.11. Other OPDs such as $(a, a, 0)$, $(a, b, 0)$ or (a, a, b) were not considered as the aim of this work was to resolve the OD behaviour of $BaTiO_3$ at the tetragonal to cubic phase transition.

3.6.1 Ti and O distortion modes

Figure 3.12 shows the R_{w} and mode amplitude values for $(0, 0, 0)$, $(a, 0, 0)$ and (a, a, a) modes refined against the variable-pressure PDFs. The atomic displacement parameters described by the simple quadratic function were fixed to values as discussed in the next section. The fitting statistics indicate that a rhombohedral model provides a consistently improved fit over all r_{max} values at the two lower pressures, however, the individual mode amplitudes behave unphysically for some pressures and fitting ranges. At 0.24 GPa, the mode amplitudes of the Ti(T_{1u}) mode are consistently positive and the amplitudes of the O(A_{2u}) and O(E_u) modes are either negative, or within error of, negative values. This $+--$ coupling of the Ti and O atoms must be maintained in order to correctly describe the relative displacements of the atoms (*e.g.*, as in Figure 3.11). The necessary coupling is progressively lost with higher pressure PDF refinements, particularly for those measured at 2.55 and 4.18 GPa, where for r_{max}>10 Å, Ti and O atoms refined to displace in the same, rather than opposite, directions.

In order to maintain the correct relative displacements associated with the modes, the ratio describing relative Ti(T_{1u}):O(A_{2u}):O(E_u) displacements was constrained. A rhombohedral (a, a, a) model was refined against high quality diffraction data measured at 15 and 293 K on GEM and the Ti(T_{1u}):O(A_{2u}):O(E_u) ratios were found to be 1:−1.46:−1.10 and 1:−1.74:−1.43. These values were simplified to a combined representative ratio; 1:−1.6:−1.3, which was subsequently used to constrain the modes in order to test against the correct and as-described local

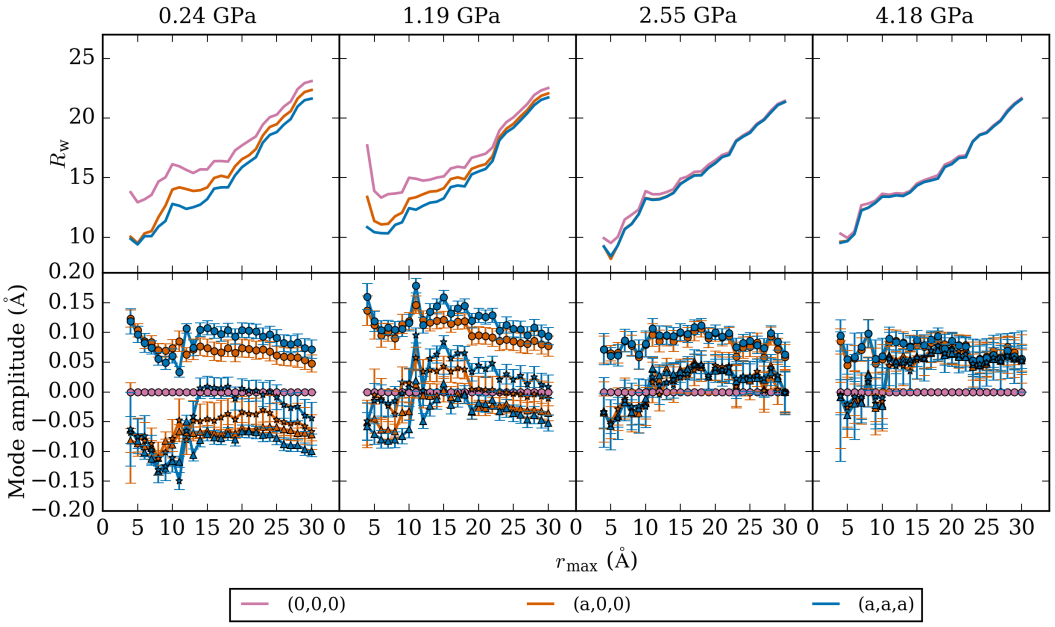

Figure 3.12: Fitting statistics (R_w) and refined Γ_4^- mode amplitudes against high pressure PDFs for Ti(T_{1u}) (circles), O(A_{2u}) (triangles) and O(E_u) (stars) modes, where the displacements related to the Ti and O atoms are unconstrained. Constrained order parameter directions are indicated by the legend. R_w values for tetragonal and rhombohedral modes at 2.55 and 4.18 GPa are almost exactly coincident, and cannot be visually distinguished.

structure distortions. Although the refined $|Q(\Gamma_4^-)|$ values differ slightly depending on the precise ratio used, it was found that the relative values and fitting statistics of each refinement remain essentially constant. Rather than reporting the refined mode amplitudes for each of the constrained Ti(T_{1u}), O(A_{2u}) and O(E_u) distortions, the mode amplitude values reported herein refer to the overall A_P values defined in ISODISTORT,[38] as the parent-cell-normalized amplitude, and are assigned the notation $|Q(\Gamma_4^-)|$.

3.6.2 Atomic displacement parameters

Figure 3.13 shows the R_w, $|Q(\Gamma_4^-)|$ and isotropic displacement parameters from variable-range refinements against the PEARL PDFs. For these refinements, the ratios between the Ti(T_{1u}):O(A_{2u}):O(E_u) displacements were fixed as described previously and the displacement parameters describing each atom individually (B_{iso}) and globally (α) were allowed to refine. Particularly for the lower pres-

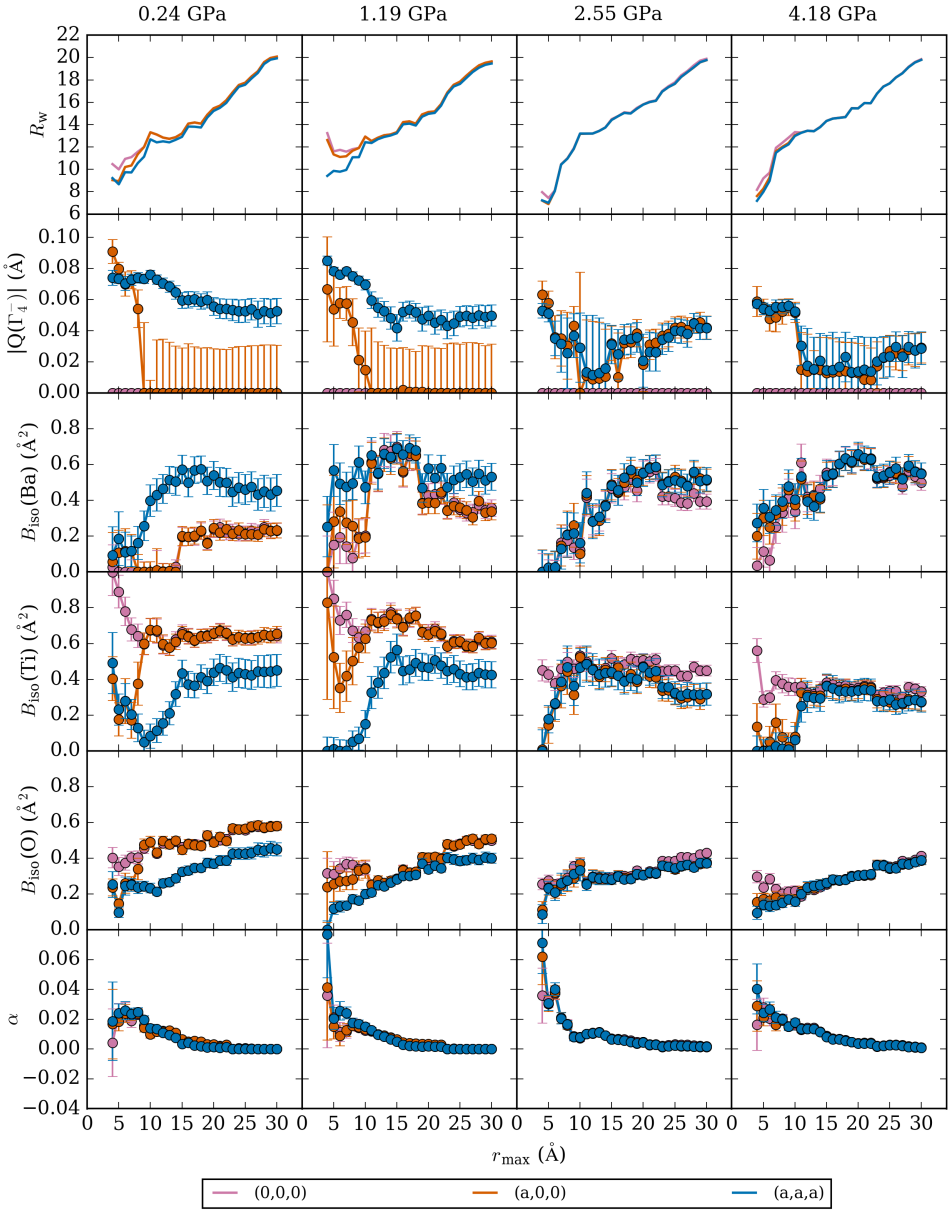

Figure 3.13: Fitting statistics (R_w), $|Q(\Gamma_4^-)|$ values, and atomic displacement parameters (B_{iso} and α) for mode-constrained, variable-range refinements against high-pressure $BaTiO_3$ PDFs. R_w values for tetragonal and rhombohedral modes at 2.55 and 4.18 GPa are almost exactly coincident, and cannot be visually distinguished.

sure PDFs, it seems that atomic displacement parameters compensate for when $|Q(\Gamma_4^-)|$ has an apparently over-constrained OPD. This is perhaps expected for the $(0,0,0)$ model, where at 0.24 GPa, the local structure is known to adopt a rhombohedral local symmetry and therefore artificially larger displacement parameters compensate for the over-constrained symmetry. Less convincing though,

are the higher Ti B_{iso} values for the $(a, 0, 0)$ model at 0.24 and 1.19 GPa where the $|Q(\Gamma_4^-)|$ values tend toward zero with increasing r. Other erroneous behaviour is observed at low r_{max} values, where a Ti B_{iso} of zero (as seen in the (a, a, a) models) is unphysical.

In order to avoid the influence of erratic B_{iso} values on the refined models, seven models with different fixed B_{iso} values, summarised in Table 3.1 were tested. The α value was fixed at 0.01 for all seven models. Although the following constraints produce less erratic trends, the conclusions described in Section 3.7 are consistent with those derived from models using unconstrained B_{iso} values.

Table 3.1: Atomic displacement parameters (B_{iso}) used to model correlated thermal motion. B_{iso} values were fixed for seven models and tested against variable pressure PDFs (α was fixed to 0.01 and the r^2 coefficient was fixed at zero).

	B_{iso} (Å^2)		
Model	Ba	Ti	O
1	0.1	0.2	0.2
2	0.2	0.3	0.2
3	0.5	0.5	0.4
4	0.4	0.3	0.3
5	0.3	0.3	0.3
6	0.3	0.2	0.3
7	0.3	0.4	0.3

In order to evaluate the seven models, variable-range fitting was carried out in the same way as previously reported, with fixed mode ratios and lattice parameters fixed to those refined by Rietveld analysis of the average structure. Figure 3.14 shows the R_w values for each atomic displacement parameter model, applied to the three $(0, 0, 0)$, $(a, 0, 0)$ and (a, a, a) local symmetry models, and tested against each variable-pressure PDF. Models 1, 2 and 3 mostly result in worse fits, suggesting over– (models 1 and 2) or under– (model 3) constrained displacement parameters.

Figure 3.15 shows the $|Q(\Gamma_4^-)|$ values refined against each variable pressure PDF and described by either an $(a, 0, 0)$ or (a, a, a) OPD. Fitting statistics have

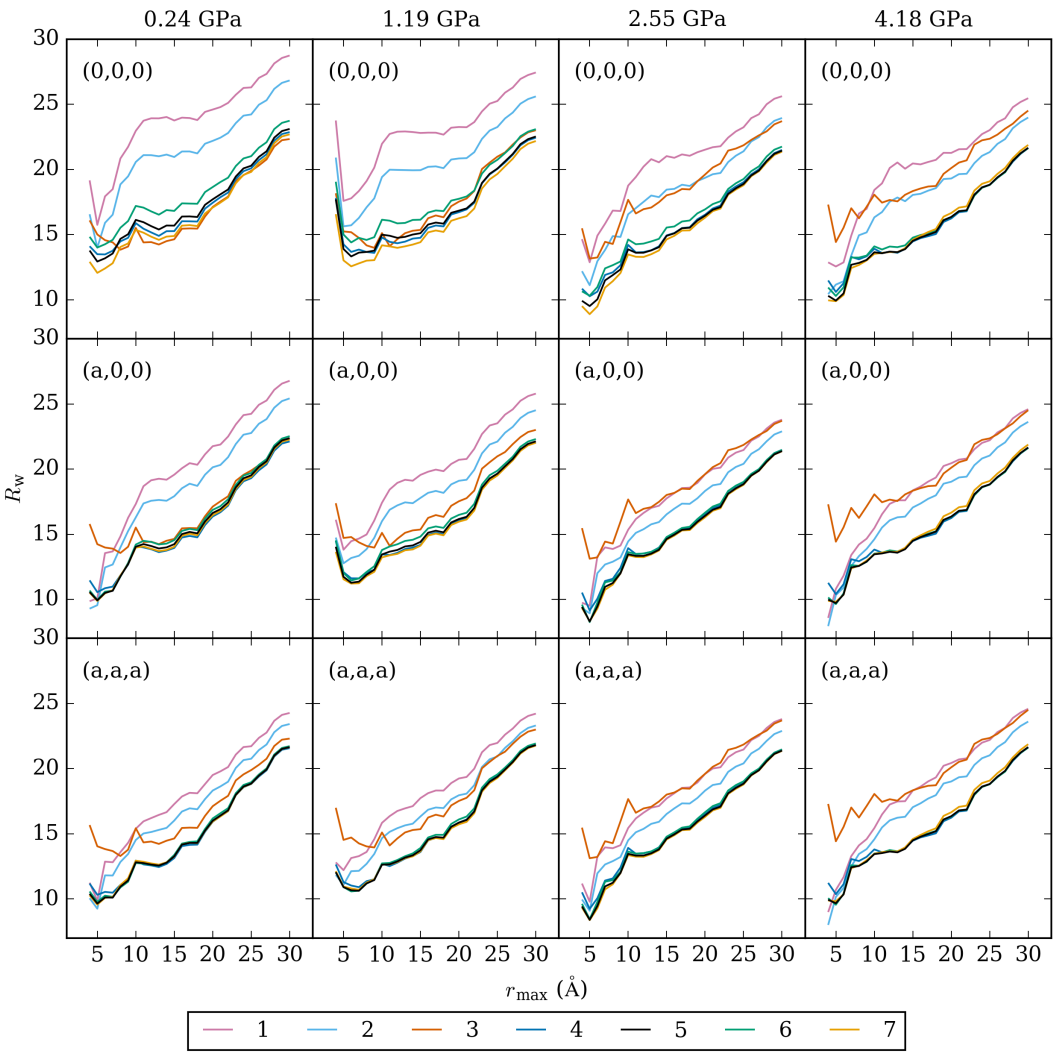

Figure 3.14: R_w for each of the seven atomic displacement models, tested against each variable-pressure PDF, modelling constrained (0,0,0), $(a,0,0)$ and (a,a,a) OPDs. For models 4–7, in some plots R_w values are almost exactly coincident, and cannot be visually distinguished.

already indicated that models 1–3 produce worse fits, and the $|Q(\Gamma_4^-)|$ values show that these models result in maximum and minimum $|Q(\Gamma_4^-)|$ ranges for each PDF and local symmetry. Models 4–7 result in very similar $|Q(\Gamma_4^-)|$ values at 0.24 and 1.19 GPa, but at 2.55 and 4.18 GPa there is a larger discrepancy between them, with model 5 representing an approximate average of the refined values from models 4–7. At these higher pressures, the fitting statistics indicate that model 5 best describes the atomic displacement parameters for $(a,0,0)$ and (a,a,a) local symmetries. Model 5, corresponding to B_{iso} parameters of 0.3 for

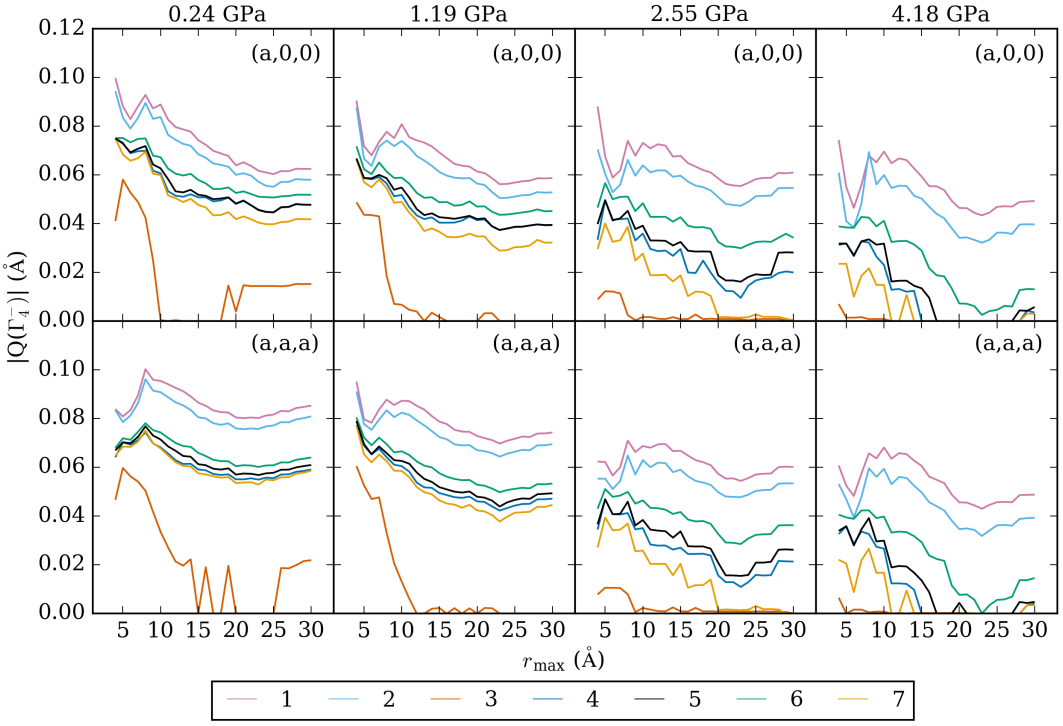

Figure 3.15: Refined $|Q(\Gamma_4^-)|$ values for each of the seven atomic displacement models, tested against each variable pressure PDF, modelling constrained $(a, 0, 0)$ and (a, a, a) OPDs. For models 4–7, in some plots R_w values are almost exactly coincident, and cannot be visually distinguished.

Ba, Ti and O atoms, was therefore chosen to model the atomic displacement parameters at all pressures.

3.7 Modelling the local structure of $BaTiO_3$

Having established constraints on the mode and B_{iso} parameters, models of cubic, tetragonal and rhombohedral local symmetries were fitted to the variable pressure PDFs. Refined models for the local structure of $BaTiO_3$ at high pressure were compared to analogous results for the thermally-induced phase transition, where the average structure of $BaTiO_3$ is known to be tetragonal at 293 and 350 K and cubic at 410 and 500 K, inviting a comparison of the local structure of $BaTiO_3$ at high pressure and high temperature. The same modelling approach was therefore applied to PDFs measured at 293, 350, 410 and 500 K using the

GEM instrument at ISIS (which were processed with $Q_{max} = 20$ Å^{-1} for a fairer comparison), and previously published in support of persistent OD behaviour at high temperature.[19] Atomic displacement parameters were allowed to refine against the GEM data as these were found to behave more stably than those found for the PEARL data. Refined displacement parameters (provided in the Appendix) are found to increase with higher applied temperature and if they were to be held fixed (as has been done with the PEARL data), the models would have to be more complex to compensate for this reduction in parameter space.

3.7.1 Variable-range modelling

Refining small-box models over an increasing range of r (Å) of the PDF provides information on the correlation length scale. This is particularly relevant for materials with OD behaviour such as $BaTiO_3$ where a local rhombohedral distortion may be observed over a short length scale—for example one unit cell—however, longer length scales will increasingly tend towards the average structure. Comparisons of fitting statistics (R_w) and $|Q(\Gamma_4^-)|$ values for cubic, tetragonal and rhombohedral models, refined against variable pressure (PEARL) and variable temperature (GEM) PDFs are shown in Figure 3.16. The results show the evolution of local displacements of Ti and O atoms as a function of pressure and temperature.

At 0.24 and 1.19 GPa, consistent improvements in R_w over all r_{max} indicate that the local and medium-range structure of $BaTiO_3$ is best described by a rhombohedral displacement of the Ti atom. The refined $|Q(\Gamma_4^-)|$ values for an $(a, 0, 0)$ OPD are approximately $\sqrt{3}/2$ smaller than those of an (a, a, a) OPD suggesting that the $(a, 0, 0)$ model is essentially resolving a projection of the [111] type displacement onto the [100] direction.

The results for the local structure of $BaTiO_3$ at 1.19 GPa are very similar to

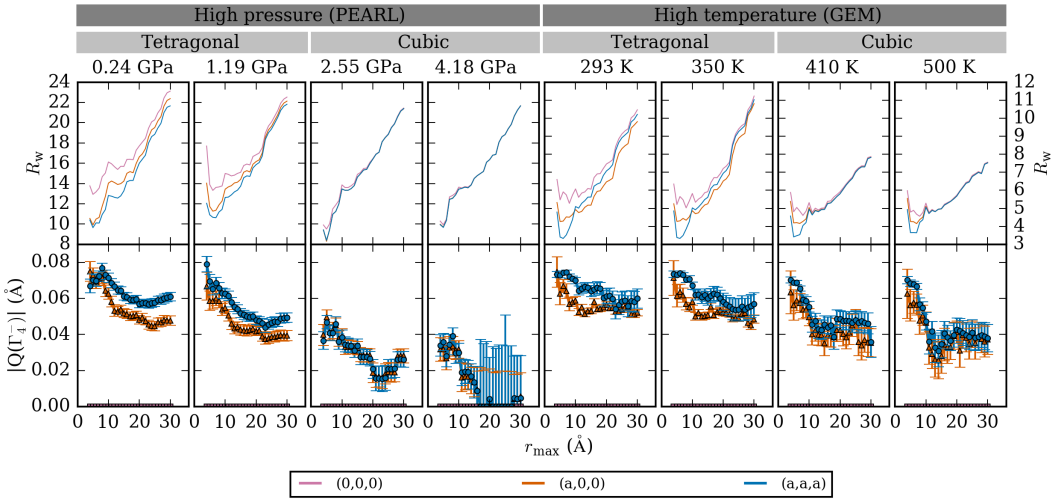

Figure 3.16: R_w and $|Q(\Gamma_4^-)|$ values for variable-range refinements for cubic (0,0,0), tetragonal $(a,0,0)$ and rhombohedral (a,a,a) OPDs against variable pressure (left) and temperature (right) PDFs. R_w values for tetragonal and rhombohedral modes in the high pressure cubic data are almost exactly coincident, and cannot be visually distinguished.

those found for the structure at 0.24 GPa and a decrease in $|Q(\Gamma_4^-)|$ of ca. 15% points towards a small pressure-induced hardening of the local potential describing the off-centre displacements. These results are in line with those of the variable temperature PDFs, measured at 293 and 350 K. R_w values at 293 and 350 K again favour rhombohedral-type displacements up to $r_{max} = 10$ Å, above which, fitting statistics favour the tetragonal model, indicating sensitivity of the PDF to the average, long-range structure. $|Q(\Gamma_4^-)|$ values are in good agreement with the variable pressure results. Again, relative $|Q(\Gamma_4^-)|$ values for $(a,0,0)$ compared to (a,a,a) OPDs suggest the resolution of the [111] type displacement onto the [100] direction.

However, this analysis reveals a clear divergence of the local structure at higher pressures from those observed at lower pressures and indeed, higher temperatures where the average structure has the same symmetry. At 2.55 and 4.18 GPa, $|Q(\Gamma_4^-)|$ at $r_{max} = 4$ Å becomes suppressed by ca. 50% (cf. 0.24 GPa) and the magnitudes of $|Q(\Gamma_4^-)|$ with OPD $(a,0,0)$ and (a,a,a) are approximately equal. Over all r_{max} there is negligible difference between the R_w values for mod-

els of tetragonal and rhombohedral Ti displacements. At 2.55 GPa the difference between cubic models and models with off-centre displacements decreases approximately linearly until r_{max} = 20 Å, after which the difference in R_w falls below significance, whereas at 4.18 GPa this occurs at r_{max} = 10 Å. At 4.18 GPa, by 16 Å, $|Q(\Gamma_4^-)|$ refines to zero, suggesting that the correlation length of the Ti displacements is below four unit cell lengths, although this correlation length is affected by the sensitivity of the PDF to all directions and not only the [100] correlation, as discussed in further detail below. Nevertheless, the suppression of $|Q(\Gamma_4^-)|$, isotropy of the displacement with respect to the different OPD, and the relative reduction in correlation lengths are all consistent with the ferroelectric instability in $BaTiO_3$ being well-described by the harmonic approximation at elevated pressures.

Conversely, previously-published results[19] for high temperature PDF data at 410 and 500 K clearly favour an (a, a, a) OPD, consistent with the model of chains of rhombohedrally displaced Ti, which retain substantial correlations along $\langle 100 \rangle$ directions. Refined $|Q(\Gamma_4^-)|$ values over r_{max} = 4–10 Å are similar to those observed at lower temperatures (at r_{max} = 4 Å, $|Q(\Gamma_4^-)|$ at 293 K = 0.094 Å, 350 K = 0.074 Å, 410 K = 0.071 Å, 500 K = 0.071 Å), but fall to values that are ca. 2/3 of those observed over longer r_{max}. The persisting sensitivity to displacements in the high temperature cubic regime is consistent with the model of correlated chains of [111] displacements projected along the [100] axis and lends further support to the OD model for the temperature-induced phase transition.

3.7.2 Comparison with literature

The high pressure trends found here agree with the work of Ravy *et al.*[9] who report diminishing diffuse scattering lines at high pressure and broadening of the diffuse features, indicative of a decrease in correlation length of Ti chains, which

they discuss in the wider context of pressure-induced Ti-centring. Correlation lengths of ca. six unit cell lengths (24 Å) implied by the breadth of diffuse features at ca. 4 GPa are also in good agreement with our results. Where structured diffuse scattering is sensitive to chain correlations, the PDF method will average chain and non-chain interactions resulting in apparently shorter correlation lengths. Furthermore, observed correlation lengths arising from this high pressure neutron PDF work, broadly agree with domain sizes determined from high pressure X-ray PDFs[42] measured up to 6.85 GPa. Whilst these PDFs were presented in support of tetragonal domains, it is likely that the insensitivity of X-rays to the lighter oxygen atoms means that it is more challenging to resolve the level of atomic positional accuracy that neutron radiation provides. Although XAS measurements[26] suggest continual off-centre Ti displacements up to 10 GPa, the sensitivity of the technique is limited to the immediate local environment of the probe atom, extending as far as the next-nearest neighbour only. This makes it difficult to judge how these results differ from those expected from the root mean square displacement of a harmonic oscillator—estimated to be 0.05 Å at 4.18 GPa from the $r_{\max} = 4$ Å variable-range refinements.

It is perhaps interesting to speculate on the differing local structure behaviour of high temperature and high pressure $BaTiO_3$. Given that polar distortions are in general coupled to the expansion of the lattice, it is understandable that the application of pressure will act to reduce the magnitude of the Ti and O displacements until they are consistent with those expected within the harmonic approximation, in which, displacements along [111], [100], or indeed any other lattice direction, necessarily carry the same energy penalty. On the other hand, above the tetragonal to cubic phase transition positive thermal lattice expansion dominates and no resulting hardening of the anharmonic potential that describes the Ti off-centring is observed.

3.8 Conclusions and further work

These results not only lend weight to the narrative that the OD behaviour of $BaTiO_3$ is suppressed at high pressure, but also adds to an emerging research direction on neutron local structure measurements of crystalline materials under hydrostatic pressure,[34,37] where local structure analysis approaches such as the simplified SAPA method can be applied. Such experiments would likely provide fundamental insight into the pressure-induced phase behaviour of framework materials such as Prussian blue analogues.[43,44]

Although it might be tempting to conclude from the average structures that the high temperature and high pressure tetragonal and cubic phases behave in an analogous manner, in terms of the local structure, this high pressure PDF study shows that this is not the case. The SAPA method of interrogating the local structure of $BaTiO_3$ reveals that at high pressure, the OD model provides a less satisfactory description. Significant suppression of the mode over short $r_{\max}$, isotropy of the OPD, and loss of sensitivity to correlated Ti displacements at high pressure all point towards more harmonic character, which contrasts the high temperature behaviour.

3.9 References

[1] I. B. Bersuker, *Phys. Lett.*, 1966, **20**, 589–590.

[2] M. Acosta, N. Novak, V. Rojas, S. Patel, R. Vaish, J. Koruza, G. A. Rossetti and J. Rödel, *Appl. Phys. Rev.*, 2017, **4**, 041305.

[3] A. V. Hippel, R. G. Breckenridge, F. G. Chesley and L. Tisza, *Ind. Eng. Chem.*, 1946, **38**, 1097–1109.

[4] H. D. Megaw, *Proc. R. Soc. London*, 1947, **189**, 261–283.

[5] W. Cochran, *Adv. Phys.*, 1960, **9**, 387–423.

[6] S. A. Hayward and E. K. H. Salje, *J. Phys. Condens. Matter*, 2002, **14**, L599–L604.

[7] T. Ishidate and S. Abe, *Phys. Rev. Lett.*, 1997, **78**, 2397–2400.

[8] R. Comés, M. Lambert and A. Guinier, *Solid State Commun.*, 1968, **6**, 715–719.

[9] S. Ravy, J.-P. Itié, A. Polian and M. Hanfland, *Phys. Rev. Lett.*, 2007, **99(11)**, 117601.

[10] M. Paściak, T. R. Welberry, J. Kulda, S. Leoni and J. Hlinka, *Phys. Rev. Lett.*, 2018, **120**, 167601.

[11] A. M. Quittet and M. Lambert, *Solid State Commun.*, 1973, **12**, 1053–1055.

[12] Y. Luspin, J. L. Servoin and F. Gervais, *J. Phys. C Solid State Phys.*, 1980, **13**, 3761–3773.

[13] J. Harada, J. D. Axe and G. Shirane, *Phys. Rev. B*, 1971, **4**, 155–162.

[14] Y. Yamada, G. Shirane and A. Linz, *Phys. Rev.*, 1969, **177**, 848–857.

[15] B. Zalar, V. V. Laguta and R. Blinc, *Phys. Rev. Lett.*, 2003, **90**, 037601.

[16] B. Ravel, E. A. Stern, R. I. Vedrinskii and V. Kraizman, *Ferroelectrics.*, 1998, **206-207**, 407–430.

[17] E. A. Stern, *Phys. Rev. Lett.*, 2004, **93**, 037601.

[18] C. Laulhé, F. Hippert, R. Bellissent, A. Simon and G. J. Cuello, *Phys. Rev. B*, 2009, **79**, 064104.

[19] M. S. Senn, D. A. Keen, T. C. Lucas, J. A. Hriljac and A. L. Goodwin, *Phys. Rev. Lett.*, 2016, **116**, 207602.

[20] M. Paściak, S. E. Boulfelfel and S. Leoni, *J. Phys. Chem. B.*, 2010, **114**, 16465–16470.

[21] C. M. Culbertson, A. T. Flak, M. Yatskin, P. H. Cheong, D. P. Cann and M. R. Dolgos, *Sci. Rep.*, 2020, **10**, 3729.

[22] G. A. Samara, T. Sakudo and K. Yoshimitsu, *Phys. Rev. Lett.*, 1975, **35**, 1767–1769.

[23] I. A. Kornev, L. Bellaiche, P. Bouvier, P. E. Janolin, B. Dkhil and J. Kreisel, *Phys. Rev. Lett.*, 2005, **95**, 196804.

[24] C. L. Bull, C. J. Ridley, K. S. Knight, N. P. Funnell and A. S. Gibbs, *Mater. Adv.*, 2021, **2**, 6094–6103.

[25] U. D. Venkateswaran, V. M. Naik and R. Naik, *Phys. Rev. B - Condens. Matter Mater. Phys.*, 1998, **58**, 14256–14260.

[26] J. P. Itié, B. Couzinet, A. Polian, A. M. Flank and P. Lagarde, *Europhys. Lett.*, 2006, **74**, 706–711.

[27] T. A. Bird, A. Herlihy and M. S. Senn, *J. Appl. Crystallogr.*, 2021, **54**, 1514–1520.

[28] C. L. Bull, N. P. Funnell, M. G. Tucker, S. Hull, D. J. Francis and W. G. Marshall, *High Press. Res.*, 2016, **36**, 493–511.

[29] W. G. Marshall and D. J. Francis, *J. Appl. Crystallogr.*, 2002, **35**, 122–125.

[30] S. Klotz, J. Philippe, C. L. Bull, J. S. Loveday and R. J. Nelmes, *High Press. Res.*, 2013, **33**, 214–220.

[31] O. Arnold, J. C. Bilheux, J. M. Borreguero, A. Buts, S. I. Campbell, L. Chapon, M. Doucet, N. Draper, R. Ferraz Leal, M. A. Gigg, V. E. Lynch, A. Markvardsen, D. J. Mikkelson, R. L. Mikkelson, R. Miller, K. Palmen, P. Parker, G. Passos, T. G. Perring, P. F. Peterson, S. Ren, M. A. Reuter, A. T. Savici, J. W. Taylor, R. J. Taylor, R. Tolchenov, W. Zhou and J. Zikovsky, *Nucl. Instruments Methods Phys. Res. Sect. A Accel. Spectrometers, Detect. Assoc. Equip.*, 2014, **764**, 156–166.

[32] A. A. Coelho, *J. Appl. Crystallogr.*, 2018, **51**, 210–218.

[33] P. Pruzan, D. Gourdain, J. C. Chervin, B. Canny, B. Couzinet and M. Hanfland, *Solid State Commun.*, 2002, **123**, 21–26.

[34] H. Y. Playford, M. G. Tucker and C. L. Bull, *J. Appl. Crystallogr.*, 2017, **50**, 87–95.

[35] M. G. Tucker, D. A. Keen, M. T. Dove, A. L. Goodwin and Q. Hui, *J. Phys. Condens. Matter*, 2007, **19**, 335218.

[36] T. A. Bird, J. Woodland-Scott, L. Hu, M. T. Wharmby, J. Chen, A. L. Goodwin and M. S. Senn, *Phys. Rev. B*, 2020, **101**, 064306.

[37] A. Herlihy, H. S. Geddes, G. C. Sosso, C. L. Bull, C. J. Ridley, A. L. Goodwin, M. S. Senn and N. P. Funnell, *J. Appl. Crystallogr.*, 2021, **54**, 1546–1554.

[38] B. J. Campbell, H. T. Stokes, D. E. Tanner and D. M. Hatch, *J. Appl. Crystallogr.*, 2006, **39**, 607–614.

[39] M. B. Smith, K. Page, T. Siegrist, P. L. Redmond, E. C. Walter, R. Seshadri, L. E. Brus and M. L. Steigerwald, *J. Am. Chem. Soc.*, 2008, **130**, 6955–6963.

[40] T.-M. Usher, T. Iamsasri and J. S. Forrester, *J. Appl. Phys.*, 2016, **120**, 184102.

[41] D. Hou, C. Zhao, A. R. Paterson, S. Li and J. L. Jones, *J. Eur. Ceram. Soc.*, 2018, **38**, 971–987.

[42] L. Ehm, L. A. Borkowski, J. B. Parise, S. Ghose and Z. Chen, *Appl. Phys. Lett.*, 2011, **98**, 021901.

[43] K. W. Chapman, P. J. Chupas, R. Maxey and J. W. Richardson, *Chem. Commun.*, 2006, **38**, 4013–4015.

[44] H. L. B. Boström, I. E. Collings, D. Daisenberger, C. J. Ridley, N. P. Funnell and A. B. Cairns, *J. Am. Chem. Soc.*, 2021, **143**, 3544–3554.

Chapter 4

The average and local structure of Mg-substituted $La_{1.875}Ba_{0.125}CuO_4$

4.1 Introduction

A property of key interest arising in solid oxide materials is superconductivity. A superconducting material shows no electrical resistance and expulsion of magnetic fields when cooled below a characteristic critical temperature, T_C. The phenomenon was discovered in 1911 by Heike Kamerlingh Onnes who found that the resistance of a mercury wire dropped to zero at T_C 4.2 K.[1]

A significant breakthrough was made in 1986 when Georg Bednorz and Alex Müller discovered that $La_{5-x}Ba_xCu_5O_{5(3-y)}$ exhibited superconductivity at 28 K.[2] Shortly after, $La_{1.85}Ba_{0.15}CuO_4$ was identified with $T_C = 30$ K, $La_{1.85}Sr_{0.15}CuO_4$ with $T_C = 38$ K,[3] $YBa_2Cu_3O_7$ with $T_C = 93$ K[4] and $HgBa_2Ca_2Cu_3O_8$ with a remarkable $T_C = 134$ K.[5] Superconductors with T_C >77.2 K are particularly useful as they can be cooled using liquid nitrogen and therefore have applications for devices such as magnetic resonance imaging scanners, nuclear magnetic resonance spectrometers and potentially future fusion reactor tokamaks.[6–8]

Despite the technological importance of higher T_C materials, significant attention has remained focused on the lower T_C cuprate materials due to a poor understanding of the origin and mechanism of superconductivity, and the anomalous behaviour of the Ba-doped cuprate, $La_{2-x}Ba_xCuO_4$. Where isostructural $La_{2-x}Sr_xCuO_4$ exhibits superconductivity in the compositional region $x = 0-0.2$, with a maximum at ca. 0.15, $La_{2-x}Ba_xCuO_4$, is found to have a suppressed T_C at $x = 0.125$, commonly referred to as the '$1/8^{th}$ anomaly'[9] (shown in Figure 4.1). It appears that a low temperature tetragonal (LTT) structural phase is coincident with the suppression of superconductivity, and much of the research on the high-T_C cuprates material remains focused on the potential coupling of this additional phase transition to electronic phenomena such as charge-density waves (CDW) and spin-ordered states.[10–12] Despite significant research, the relationship between such electronic and structural behaviours is still not well understood.

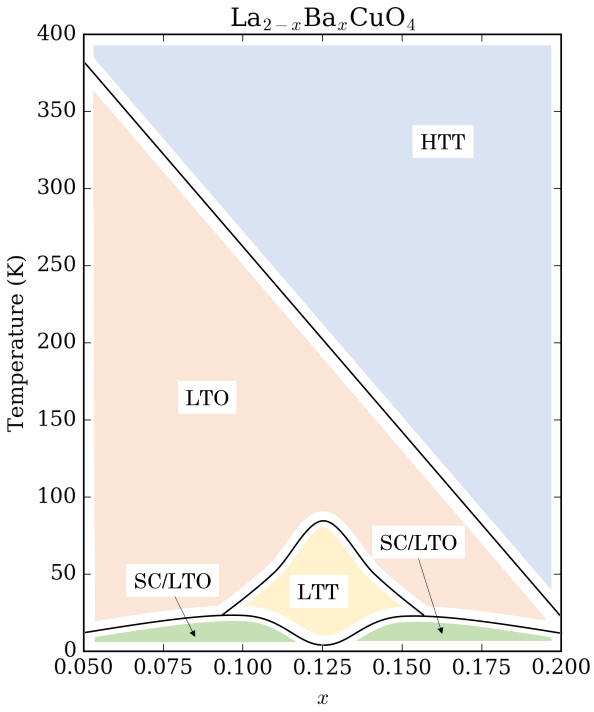

Figure 4.1: The temperature *versus* Ba-doping phase diagram of LBCO. The blue, orange and yellow regions show the HTT, LTO and anomalous LTT average structures respectively and the green regions show the temperatures and Ba-doping levels for which superconductivity (SC) arises.

Understanding the origin of the anomalous behaviour of LBCO will provide significant insight into the origin of superconductivity in these high-T_C cuprates, and will aid the design of future high-T_C superconductors.

The average structure symmetries of $La_{2-x}Ba_xCuO_4$ with $x = 0.125$ (hereafter referred to as LBCO) and the corresponding temperature-dependent phase transitions are well known.[13] Above ca. 240 K,[14,15] LBCO adopts a 'high temperature tetragonal' (HTT) $I4/mmm$ phase (Figure 4.2(a)) where the CuO_6 octahedra are arranged in staggered layers stacked along the c-axis of the Ruddlesden-Popper (RP) structure. On cooling below 240 K, LBCO goes through a second order phase transition to a 'low temperature orthorhombic' (LTO) phase. The CuO_6 octahedra rotate alternately about the [110] direction (with respect to the HTT structure), as shown in Figure 4.2(b), resulting in $Bmab$ symme-

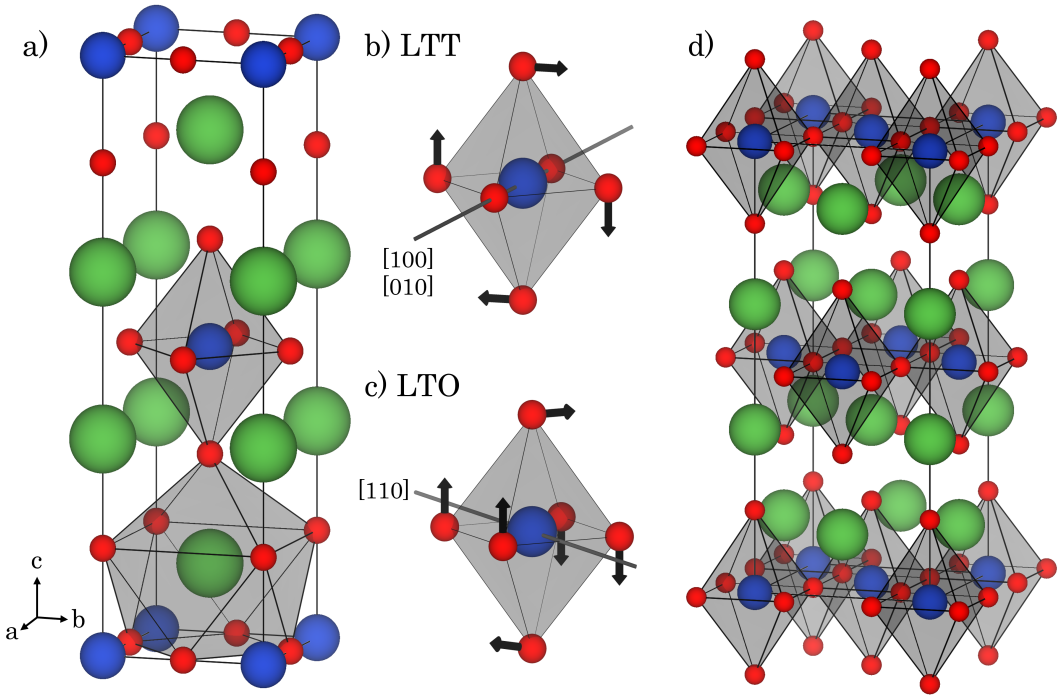

Figure 4.2: The crystal structure of LBCO, where La/Ba atoms are shown as green spheres, Cu atoms as blue spheres and O atoms as red spheres. (a) Unit cell in the HTT phase ($I4/mmm$), with CuO_6 octahedra and 9-coordinate La/BaO_9 polyhedra highlighted. Rotation directions of the CuO_6 octahedra in (b) the LTO phase ($Bmab$) and (c) the LTT phase $P4_2/ncm$, with respect to the HTT cell. (d) The unit cell of the LTO and LTT phases.

try. This $Bmab$ structure is a supercell with respect to HTT, with a basis of $[\mathbf{a}_{\mathrm{HTT}} + \mathbf{b}_{\mathrm{HTT}}]$,$[-\mathbf{a}_{\mathrm{HTT}} + \mathbf{b}_{\mathrm{HTT}}]$,$[\mathbf{c}_{\mathrm{HTT}}]$ and no change of origin (shown in Figure 4.2(d)). The rotation of the CuO_6 octahedra can be described by the X_3^+ irrep. of $I4/mmm$ with an OPD, $(a, 0)$. The distortion results in a buckling of the CuO_2 planes which is reportedly coupled with the superconductivity that arises at specific doping levels of the cuprate materials.

Below ca. 80 K, LBCO goes through a second phase transition from LTO to the LTT phase described in the space group $P4_2/ncm$, with the same basis as LTO with respect to HTT. In this phase the octahedra instead rotate along the [100] and [010] directions (with respect to the HTT structure) with alternate CuO_2 layers rotating in opposite directions, preserving tetragonal symmetry. The rotation is described again by the X_3^+ irrep, but now with an OPD of (a, a) that describes an equal rotation magnitude about **a** and **b**. Since there is no group-

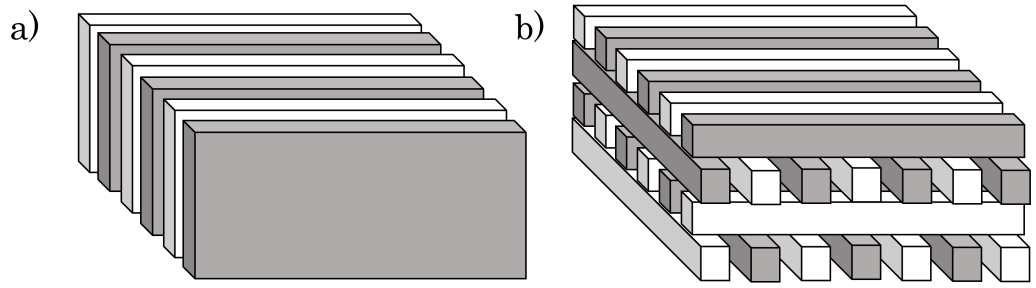

Figure 4.3: Schematic diagram of CDW stripe order within the LTO (left) and LTT (right) phases.

subgroup relationship between the LTT and LTO phases, the phase transition is necessarily first order, displaying a coexistence of phases over a finite temperature range.[16]

A large focus of investigation into the $1/8^{th}$ suppression of superconductivity has centred around the appearance of CDW ordering—observed by both neutron and X-ray scattering[17] which reportedly competes with the superconductivity of the system. The fact that CDW formation temperature is coincident with the LTT phase transition has attracted significant attention. The structural anisotropy, and related rotation of the CuO_6 octahedra is thought to pin charge stripes.[17,18] The theory is that whilst an aligned stripe orientation allows superconductivity within the CuO_2 planes in LTO, the structural anisotropy of the LTT phase induces a 90° rotation of the charge stripes in alternating CuO_2 layers (shown in Figure 4.3), disrupting Josephson coupling and therefore suppressing the superconducting properties.[19,20]

Unpublished work carried out within the Senn group has shown through single-crystal and high-resolution powder XRD studies that there is a pronounced coexistence of the LTT and LTO phases at low temperature. Fitting the data with a two-phase model indicated that there is an increased rotation of the CuO_6 octahedra in the LTT phase, resulting in larger buckling of the CuO_2 planes and presumably reduced band gaps. This finding suggests that the low temper-

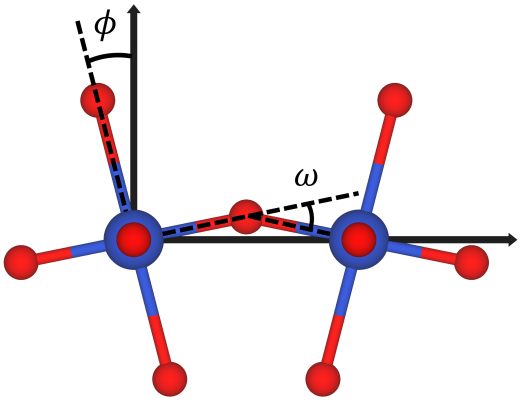

Figure 4.4: Diagram of two corner-sharing CuO_6 octahedra, showing the ϕ and ω angles used to characterise the magnitude of the octahedral tilt.

ature behaviour of LBCO and the relationship between superconductivity and electronic effects such as charge pinning must be revisited.

Work on the local structure of LSCO using single-crystal neutron scattering experiments, points towards a displacive phase transition of LTO to a HTT phase with weakly-ordered rotations (ϕ, shown in Figure 4.4) of ca. 0.4°—determined *via* the analysis of diffuse scattering reflections.[21] Similar analyses of the diffuse scattering arising from an XRD experiment on LBCO found a local rotation magnitude of ca. 0.25° in the HTT phase.[22]

The use of direct local structure probes indicate slightly larger rotation magnitudes. A PDF study on LSCO reported that local LTO-type rotation angles of ca. 1.5° persist in the 10 K HTT phase[23] (above $x = 0.2$) and for LBCO, studies using neutron PDF and XAFS techniques suggested that in all three average LTT, LTO and HTT phases, the CuO_6 octahedra continue to rotate locally in an LTT-like manner, ordered over ca. 10 Å.[24,25] This would suggest that the HTT→LTO and LTO→LTT phase transitions are better described as being order-disorder, although this interpretation contradicts the displacive behaviour evident through average structure techniques.[16,26]

Pressure, rather than temperature, is another important variable that can be

used to drive structural changes and phase transitions, therefore tuning properties of superconducting materials.[27–29] Shortly after the discovery of superconductivity in the $Ba_xLa_{5-x}Cu_5O_{5(3-y)}$ ceramic, Chu *et al.*[30] found that T_C could be increased from 30 to 40 K through the application of modest pressure (1.3 GPa).

Pressure suppresses the LTO phase in LSCO, where the change in T_C is highly correlated to the stabilisation of the HTT phase and flattening of the CuO_2 planes.[31] The same pressure-dependent phase behaviour is found for LBCO, where the application of hydrostatic pressure results in the suppression of the LTT and LTO phase transitions completely by 1.85 GPa,[22] although the recovery of T_C is slow and remains at low at ca. 10 K for $x = 0.125$.[10,31]

Despite the significant amount of work on the LBCO system, there is much left to discover about the structure-property relationships and in particular the nature of the anomalous LTT phase. Thus far, the role of the A-site cation has been thoroughly studied,[32,33] but there is surprisingly little investigation into the role of the B-site Cu ion. Charge balancing at the $x = 0.125$ doping level requires that 87.5% of the Cu ions have the 2+ the oxidation state, and the remaining 12.5% are 3+. The population of JT-active cations may be altered by adjusting the Ba-content, although this will also have a significant affect on the hole doping levels. Substituting Cu^{2+} with Mg^{2+} provides a way of directly investigating the influence of the JT distortion associated with the Cu^{2+} cation on the observed structural symmetries of LBCO, as Mg^{2+} has almost the same ionic radius as Cu^{2+} (0.72 Å *versus* 0.73 Å[34]) and therefore differs only in the lack of JT activity.

The aim of this Chapter is to investigate the link between the JT activity of the Cu^{2+} cation and structural symmetry by preparing a series of Mg-substituted LBCO ($La_{1.875}Ba_{0.125}(Cu_{1-y}Mg_y)_{0.875}Cu_{0.125}O_4$) samples. Variable-temperature PXRD studies on the Mg-substituted series, reported in this Chapter, have shown

than the transition temperatures of the LTT and LTO phases are strongly coupled to the local anisotropy of the Cu^{2+} state, proving that there is an interplay between doping and structural symmetry beyond tolerance factor effects. Furthermore, this work has found that Mg substitution completely suppresses the LTO–LTT phase coexistence at lower temperatures, suggesting that it is a by-product of the competition between electronic instabilities (such as CDW and superconductivity) that are only expected to be present in the pristine LBCO system. Further structural investigations were carried out through a high temperature total scattering experiment, performed on the I15-1 beamline—probing the local structure of the HTT phases of Mg-substituted LBCO—and a high-pressure neutron diffraction experiment, to understand the effects of hydrostatic pressure on a Mg-substituted LBCO.

4.2 Experimental

4.2.1 Solid-state synthesis of Mg-substituted $La_{1.875}Ba_{0.125}CuO_4$

$La_{1.875}Ba_{0.125}(Cu_{1-y}Mg_y)_{0.875}Cu_{0.125}O_4$ ($y = 0 - 0.7$, in 0.1 steps) was synthesised by mixing predried La_2O_3 (99.99%, Sigma Aldrich), $BaCO_3$ (99.95%, Alfa Aesar), CuO (99.999%, Sigma Aldrich) and MgO (99.99%, Sigma Aldrich) in the stoichiometric ratios detailed in Table 4.1. Powders were ground into a homogenous mixture and then pressed into pellets using a Specac 10 tonne die press. Pellets were placed into a zirconia crucible and calcined in air at 900°C for 20 hours. Three heating cycles were then carried out, at 1050°C for 15 hours, 1100°C for 20 hours and 1200°C for 20 hours, with pellets cooled to room temperature, ground and re-pressed between each cycle. The error of the Mg-content y arising from weighing of the reactants was calculated to be ± 0.002.

Table 4.1: Reactants and their stoichiometric y-dependent ratios.

Reactant	Ratio
La_2O_3	0.9375
$BaCO_3$	0.125
CuO	$0.875(1-y)$+0.125
MgO	$0.875y$

4.2.2 Variable-temperature XRD

Variable-temperature powder diffraction patterns of the Mg-LBCO series were measured using high-resolution XRD beamlines at DLS and TPS, with different experimental details for each sample. Data from TPS was collected by Dr Wei-Tin Chen. All variable temperature measurements were performed on warming. All data were collected using a MYTHEN detector. All wavelengths and instrument-dependent parameters (peak shapes and axial divergence) were determined *via* Rietveld refinements of a Si NIST standard.

$y = 0.0$

Low temperature data were collected using beamline 09A (TPS), using an energy of 20 keV (0.62059 Å). The sample was loaded into a 0.2 mm diameter quartz capillary and the temperature controlled using an ESRF DynaFlow cryostat, with data measured at temperatures from 10–130 K in steps of 10 K (ramp rate of 1.67 K/min).

Further data were obtained from 90–300 K in 10 K steps, also using beamline 09A, with an energy of 20 keV (0.61990 Å). The sample was loaded into a 0.1 mm diameter Lindemann glass capillary and the temperature was controlled using an Oxford Cryostream 800+ with a ramp rate of 2.5 K/min.

High temperature data were collected from 300–400 K in steps of 10 K using beamline I11 (DLS). An energy of 15 keV (0.82686 Å) was used and an Oxford Cryostream+ used to control the temperature with a ramp rate of 6 K/min.

$y = 0.1$

Data were collected using beamline I11 (DLS) with an energy of 15 keV (0.82686 Å). The sample was loaded into a 0.3 mm diameter borosilicate glass capillary and data were collected from 100–400 K in 10 K steps. The temperature was controlled using an Oxford Cryostream Plus.

$y = 0.2$

Low temperature data were collected using beamline 09A (TPS), using an energy of 20 keV (0.61993 Å). The sample was loaded into a 0.3 mm diameter quartz capillary and the temperature controlled using an ESRF DynaFlow cryostat, with data measured at temperatures from 10–120 K in steps of 10 K (ramp rate of 1.67 K/min).

Higher temperature data were collected from 90–400 K in steps of 10 K also using beamline 09A. The sample was loaded into a 0.1 mm Lindemann glass capillary. An energy of 12 keV (1.03342 Å) was used and an Oxford Cryostream800+ used to control the temperature with a ramp rate of 2.5 K/min.

$y = 0.3$

Low temperature data were collected using beamline 19A (TPS), using an energy of 20 keV (0.61990 Å). The sample was loaded into a 0.3 mm diameter quartz capillary and the temperature controlled using an ESRF DynaFlow cryostat, with data measured at temperatures from 20–110 K in steps of 10 K (ramp rate of 1.67 K/min).

Higher temperature data were collected from 90–400 K in steps of 10 K using beamline 09A. The sample was loaded into a 0.1 mm Lindemann glass capillary. An energy of 12 keV (1.03342 Å) was used and an Oxford Cryostream800+ used to control the temperature with a ramp rate of 2.5 K/min.

y = 0.4 and 0.5

Data were collected from 90–400 K in steps of 10 K using beamline 09A. The samples were loaded into 0.1 mm Lindemann glass capillaries. An energy of 12 keV (1.03342 Å) was used and an Oxford Cryostream800+ used to control the temperature with a ramp rate of 2.5 K/min.

y = 0.6 and 0.7

Ambient temperature diffraction patterns were measured using I11 (DLS), with an energy of 15 keV (0.82686 Å). The samples were loaded into 0.3 mm diameter borosilicate glass capillaries.

4.2.3 Total scattering

Total-scattering measurements were carried out using the I15-1 (XPDF) beamline at DLS. Powdered samples of $La_{1.875}Ba_{0.125}(Cu_{1-y}Mg_y)_{0.875}Cu_{0.125}O_4$ ($y = 0-0.5$, in steps of 0.1) were loaded in borosilicate capillaries which were mounted on an XY sample stage and spun at 10 Hz. X-rays with an energy of 76.6 keV (0.1617 Å) and PerkinElmer XRD 16611 CP3 and PerkinElmer XRD 4343 CT detectors were used to collect data corresponding to the local, and average, crystal structure simultaneously. An empty capillary was measured to account for non-sample scattering contributions. All samples were measured at 400 K using a hot air blower. The total scattering data were Fourier transformed using a Q_{max} of 25 $Å^{-1}$ with GUDRUNX.[35] Rietveld refinements of the XRD data were carried out using TOPAS, and small and big-box modelling were performed using TOPAS Academic v6[36] and RMCProfile[37] respectively.

4.2.4 High-pressure neutron diffraction

High-pressure neutron diffraction patterns of $La_{1.875}Ba_{0.125}(Cu_{1-y}Mg_y)_{0.875}Cu_{0.125}O_4$ with $y = 0.0$ (LBCO) and 0.5 were collected using the PEARL beamline at ISIS.[38] Powdered samples were loaded into an encapsulated null-scattering TiZr gasket,[39] which was placed into a PE press, equipped with ZTA anvils. Hydrostatic compression was achieved by using a 4:1 deuterated methanol:ethanol mixture[40] and a lead pellet was included as a pressure calibrant *via* the known EoS. Data were reduced using the MANTID software package[41] to correct for the effects of attenuation by the ZTA anvils and normalised by a vanadium standard to account for flux profile. Rietveld refinements were carried out using TOPAS Academic v6,[36] and Si and CeO_2 standards, measured at the start of the cycle, were used to refine diffractometer constants and peak shape parameters, respectively.

For the LBCO ($y = 0.0$) sample, data were collected at the following applied loads: 5.5 tonnes, then 9.5–27.5 in steps of 2 tonnes, and finally, 30–60 in steps of 5 tonnes. The corresponding calculated pressures shown in Figure 4.5 indicated

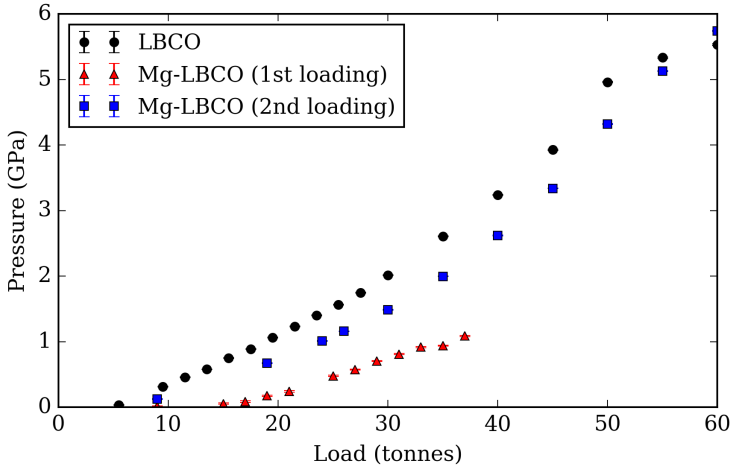

Figure 4.5: Pressure-load relationships for LBCO and the two loadings of Mg-LBCO, where the second loading showed an improvement in the pressure-load curve over the first loading. Error bars are shown but are smaller than the symbols.

that at 60 tonnes an upper pressure of 5.53(1) GPa was achieved. The plateauing observed for the last three load increments is characteristic of the upper limit of the load capabilities of the ZTA anvils.

For $La_{1.875}Ba_{0.125}(Cu_{1-y}Mg_y)_{0.875}Cu_{0.125}O_4$ $y = 0.5$, data were collected at 9 tonnes, then from 15–37 tonnes in steps of 2 tonnes. The pressure-load curve, shown in Figure 4.5, indicated poor pressure performance for the first loading; this was attributed to an under-packed gasket. A second compression was carried out with another instance of the sample, which showed much improved performance. For the second loading, data were collected at 9, 19, 24, 26 tonnes and then 30–60 tonnes in steps of 5 tonnes. The resulting pressure-load curve was much improved and an upper pressure of 5.752(7) GPa was achieved.

4.2.5 Refinement protocol

Structure modelling for Rietveld refinements against the variable-temperature XRD data and small-box modelling of X-ray PDFs was carried out using the approach outlined below unless stated otherwise, using TOPAS Academic v6.[36]

A symmetry-adapted approach was used whereby for all LTT, LTO and HTT phases, refinements were performed using a common subgroup, *Pccn* with appropriate symmetry constraints on atom displacements and lattice parameters. This means that all phases were modelled using the supercell structure depicted in Figure 4.2(d) so that refined parameters of the HTT structure—which conventionally would be described by a smaller unit cell—can be directly compared. The OP associated with the previously-described octahedral rotation is described by the irrep. X_3^+ with an OPD (a, b). For the HTT phase, the OPD is (0,0)—where there is no rotation in the average structure, for the LTO phase, the OPD is $(a, 0)$, and for LTT the OPD is (a, a), corresponding to the rotations shown in Figure 4.2. A second distortion is active within all HTT, LTO and LTT phases—the Γ_1^+ mode

Table 4.2: Ratio between the La/Ba, O1 (apical) and O2 (equatorial) distortion modes described by the X_3^+ and Γ_1^+ irreps.

Irrep	La/Ba	O1	O2
X_3^+	1	-3.0232	1.3905
Γ_1^+	1	-1.1026	n/a

(with OPD (a))—which describes a symmetry-conserving distortion where La/Ba and apical O atoms displace with a combined stretching motion along the c-axis.

In each model, two distortion parameters were refined, one describing the La/Ba X_3^+ distortion, and another describing the La/Ba Γ_1^+ distortion. All other modes transforming as the same irrep, acting on the oxygen atoms, were fixed to a ratio which was based on values determined from previous, unpublished single crystal studies (carried out within the Senn group) of isostructural $La_{1.675}Eu_{0.2}Sr_{0.125}CuO_4$ (LESCO) and reported in Table 4.2. The X_3^+ distortion acts on two distinct oxygen positions; the apical oxygen denoted 'O1', and the equatorial oxygen, denoted 'O2', whereas the Γ_1^+ distortion acts only on the apical O1 oxygen position.

Constraining oxygen distortions to the La distortions was vital for maintaining the octahedral geometry since freely refined modes resulted in incorrect coupling of the individual components due to the insensitivity of X-rays to the lighter oxygen atoms. The reported X_3^+ mode amplitudes are the parent-cell-normalized amplitudes (A_P values) defined by ISODISTORT.[42]

The atomic displacement parameters of the equatorial oxygen atoms were constrained to be equal, regardless of the phase symmetry and those describing the apical oxygen atoms were constrained to be 1.8× of the equatorial oxygen atoms (again, informed by single crystal LESCO data). Atomic displacement parameters for the remaining atom site types (A and B site atoms) were allowed to refine freely with no further constraints. Modelling of anisotropic peak broadening was carried out using the symmetry-dependent Stephens strain model[43] for each

phase in all samples.

4.3 Mg concentration limit in $La_{1.875}Ba_{0.125}CuO_4$

Rietveld analysis of the $La_{1.875}Ba_{0.125}(Cu_{1-y}Mg_y)_{0.875}Cu_{0.125}O_4$ ($y = 0.0 - 0.7$) samples showed that the solid-state synthesis yielded pure (greater than 99%) polycrystalline samples for y values up to 0.5. Samples synthesised with $y = 0.6$ and 0.7 (Rietveld fits are shown in Figure 4.6) yielded purities of 93.88% and 83.72% respectively, with impurity phases identified as $La(OH)_3$, La_2O_3 and MgO, which meant that the synthesised Mg-LBCO sample was non-stoichiometric. The $La(OH)_3$ impurity found for $y = 0.6$ is a result of unreacted La_2O_3 decomposing in air to the hydroxide form. Efforts to synthesise pure samples by increasing heating

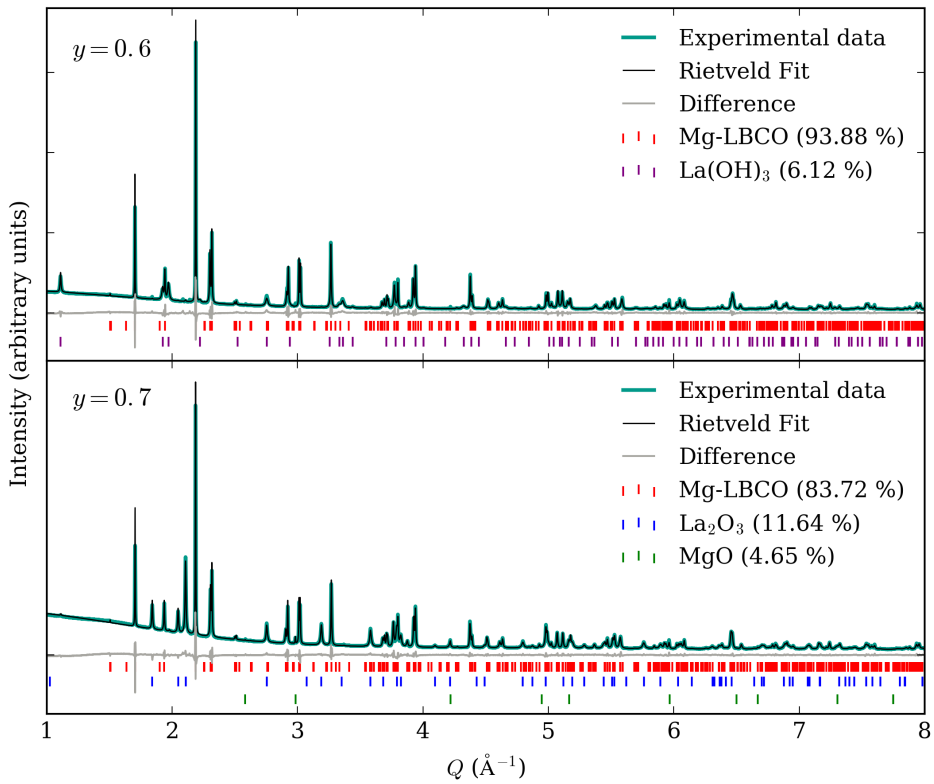

Figure 4.6: Rietveld fits of $La_{1.875}Ba_{0.125}(Cu_{1-y}Mg_y)_{0.875}Cu_{0.125}O_4$, $y = 0.6$ and $y = 0.7$, showing the impurity phases of $La(OH)_3$, La_2O_3 and MgO present in samples with increasingly large Mg content.

cycle times and temperatures were unsuccessful, and persisting impurities for the attempted synthesis of high Mg-content LBCO indicated a Mg concentration limit of $y = 0.5$ using conventional solid-state methods.

4.4 Variable temperature Mg-substituted $La_{1.875}Ba_{0.125}CuO_4$

An in-depth structural analysis was performed on the Mg-LBCO samples with y values up to 0.5. Rietveld analysis performed on the XRD patterns of the pure samples (shown in Figure 4.7) indicated that at 300 K the un-substituted sample, $y = 0$ (LBCO) adopted a HTT $I4/mmm$ phase, as expected from previous literature.[16] This was evidenced by the absence of any splitting of the (200) reflection, shown inset in Figure 4.7. This (200) reflection will be used to illustrate phase transition evolution regularly throughout this Chapter. Diffraction patterns and Rietveld refinements of the Mg-substituted LBCO samples showed that for $y = 0.1$ and 0.2, the structures were also in the HTT phase at 300 K,

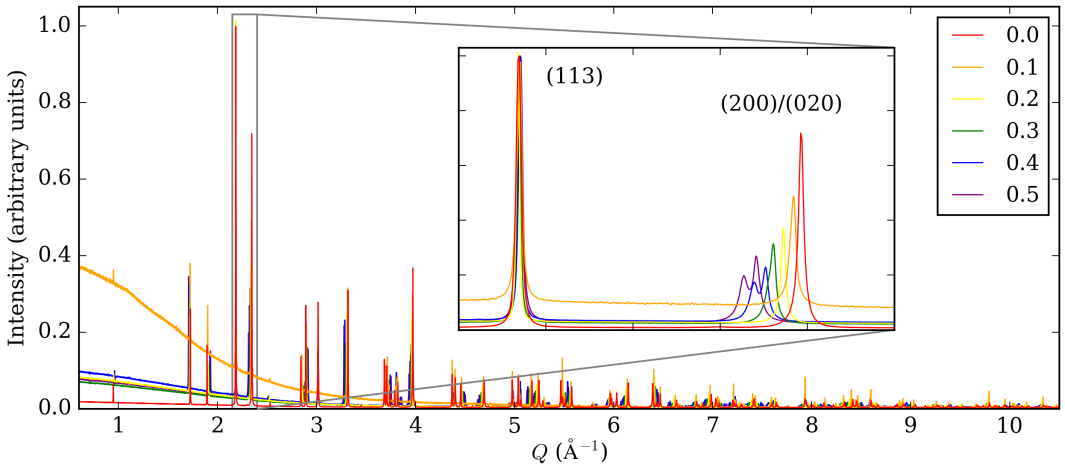

Figure 4.7: Diffraction patterns of $La_{1.875}Ba_{0.125}(Cu_{1-y}Mg_y)_{0.875}Cu_{0.125}O_4$ measured at 300 K. Inset figure shows the (113) and (200)/(020) peaks and the legend indicates the y values. Differences in observed background scattering are due to differences in capillary packing fraction. All peaks are indexed with respect to the *Pccn* supercell.

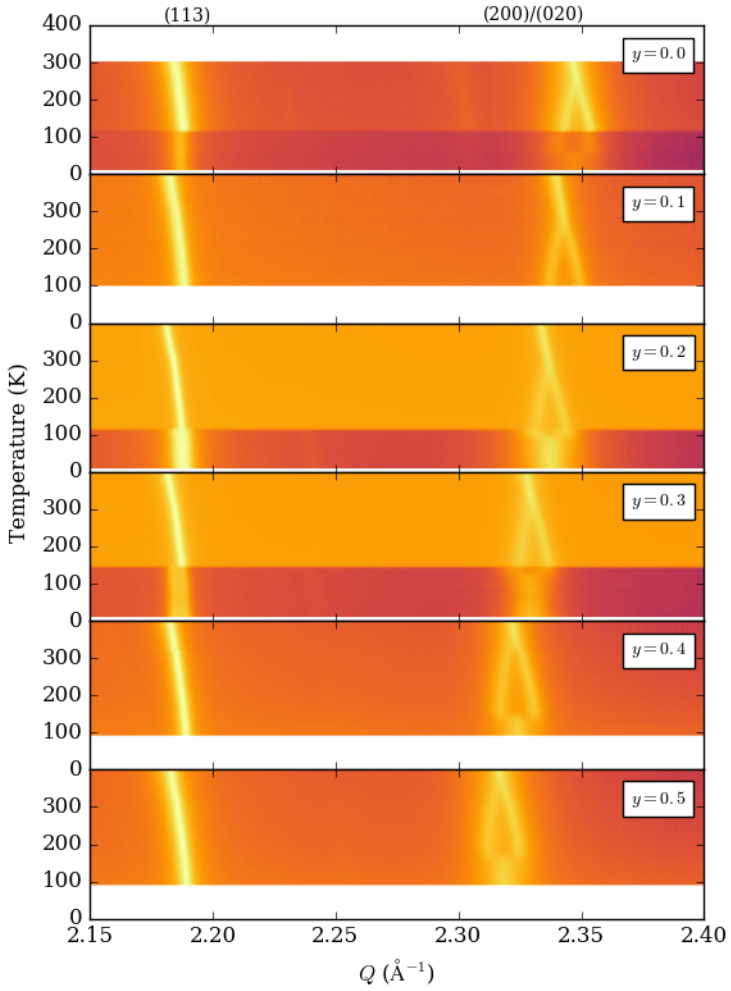

Figure 4.8: An X-ray intensity heat map of the evolution of the (113) and (200/020) Bragg peaks of $La_{1.875}Ba_{0.125}(Cu_{1-y}Mg_y)_{0.875}Cu_{0.125}O_4$ with temperature. White sections reflect temperatures at which data were not collected and changes in contrast between low and high temperatures are a result of different scattering intensities between data collected from different experiments.

whereas the samples with $y = 0.3$, 0.4 and 0.5 adopted the LTO *Bmab* phase—shown clearly for the $y = 0.5$ sample by the splitting of the (200) peak (where the HTT structure is indexed with respect to the *Pccn* cell) to a (200)/(020) peak in Figure 4.7.

The apparent influence of Mg-substitution on the phase of the LBCO structure, was then investigated *via* an in-depth variable-temperature powder XRD study. The heat maps of Figure 4.8 shows the temperatures that were investigated for each sample. The Figure shows the evolution of the (113) and (200)

Bragg peaks, the latter of which, for all samples, shows a clear discontinuous jump, and splitting, at low temperatures, followed by a continuous evolution to convergence again at high temperatures. These trends are indicative of a low-temperature first-order phase transition and a high-temperature second order phase transition, as reported in the literature for LBCO ($y = 0$).

Rietveld refinements against data of all samples at 400 K confirmed a HTT structure. For all samples, sequential refinement against data from decreasing temperatures continued to provide a good fit to the HTT structure, until peak splitting due to the second-order phase transition occurred, and an LTO model was used where lattice parameters were constrained to orthorhombic symmetry and the constrained X_3^+ distortion with OP $(a, 0)$ was refined. The phase transition temperature was found to vary between compositions and is discussed further below. On further temperature decrease, the orthorhombic splitting of the LTO structure increased until a second phase was observed and the diffraction patterns required a two phase model to produce a good fit to the data. Again, this lower temperature phase transition did not occur at the same temperature across the different Mg-substitution levels. Large increases in R_{wp} values were used to identify the onset of the LTO→LTT phase transition, and the temperatures at which a two phase regime was first observed is reported in Table 4.3 for the corresponding y values.

Table 4.3: The highest measured temperatures at which a two phase regime was observed for $La_{1.875}Ba_{0.125}(Cu_{1-y}Mg_y)_{0.875}Cu_{0.125}O_4$.

Mg-content (y)	T (K)
0.0	70
0.2	100
0.3	120
0.4	150
0.5	170

4.4.1 The second-order low temperature orthorhombic to high temperature tetragonal phase transition

The following section is focused on the single phase LTO and HTT regime, which precedes the first order phase transition to the LTT phase.

The occurrence of a second-order LTO→HTT phase transition in the Mg substituted cuprates is further evidenced by trends in the unit cell lattice parameters. The gradual convergence of the refined a and b lattice parameters of the LTO phase to a single value in the HTT phase can be described by an 'orthorhombicity' parameter η,

$$\eta = \left| \frac{2(a-b)}{(a+b)} \right|, \tag{4.1}$$

where an increasingly large value corresponds to a more orthorhombic structure and a value of zero corresponds to a tetragonal structure.

The η values plotted in Figure 4.9 indicate that the continuous, second order phase transition from LTO to HTT persists for all levels of Mg substitution. The shifts of the orthorhombicity 'curves' to higher temperatures shows an increase

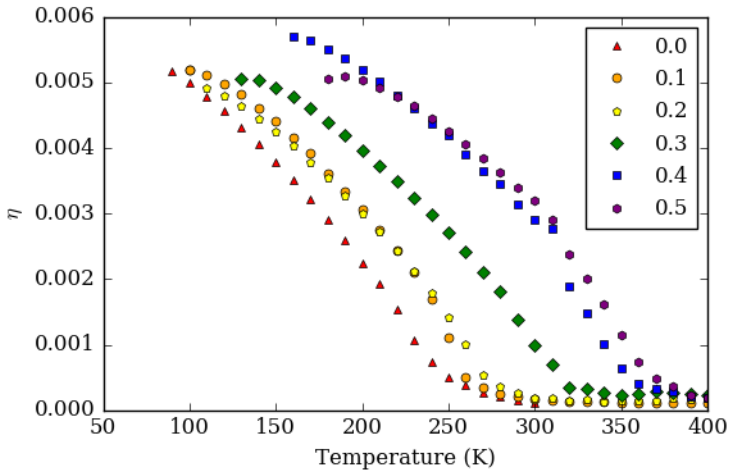

Figure 4.9: Temperature evolution of the lattice orthorhombicity (η) for $La_{1.875}Ba_{0.125}(Cu_{1-y}Mg_y)_{0.875}Cu_{0.125}O_4$, where the legend indicates y.

in the LTO→HTT phase transition temperature. The orthorhombic strain at the lower temperature limit immediately preceding the LTO→LTT phase transition temperature does not show any clear relationship with Mg-content, suggesting that the phase transition is not induced by a specific orthorhombic strain.

In order to determine the phase transition temperature more precisely than otherwise allowed by the minimum temperature step used in the experiment (10 K), Landau theory has been used.[44] The X_3^+ mode is known to be the OP driving the second-order phase transition and its temperature-dependent evolution in the vicinity of the second-order transition temperature (T_C) can be approximated as:

$$|X_3^+(T)| = |X_3^+|_{t=0}\left[\frac{T_C - T}{T_C}\right]^{1/2}, \tag{4.2}$$

where $|X_3^+|_{t=0}$ is the saturation value of X_3^+. In theory, this relationship may be used and refined against variable temperature, experimentally determined OP values in order to determine T_C.

The refined X_3^+ AP values for LBCO and the Mg-substituted samples are shown in Figure 4.10. Whereas mode amplitudes refined for LBCO tended towards zero on approaching the phase transition—in agreement with Landau the-

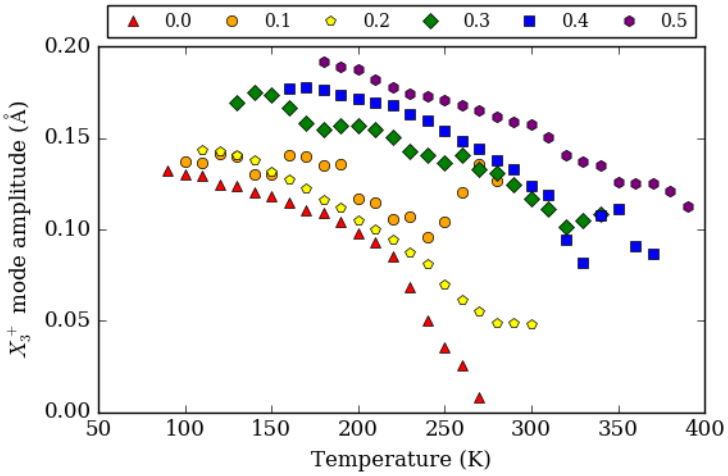

Figure 4.10: The X_3^+ mode amplitude of $La_{1.875}Ba_{0.125}(Cu_{1-y}Mg_y)_{0.875}Cu_{0.125}O_4$ (with y values indicated in the legend) in the LTO phase, as a function of temperature.

ory for a second order phase transition—the modes refined for the Mg-substituted samples do not. This could be due to insensitivity of the XRD technique to the mode, resulting in a non-zero amplitude at temperatures above the phase transition. This means that it is challenging to extract meaningful information from the X_3^+ mode amplitudes of the Mg-LBCO sample.

Instead, the secondary order parameter, strain (η) may be used:

$$\eta(T) = \eta_{t=0}\left[\frac{T_C - T}{T_C}\right], \tag{4.3}$$

where η is the previously defined strain. This was tested against the refined parameters for the LBCO ($y = 0.0$) sample where simultaneous fits to X_3^+ and η were carried out, and are shown in Figure 4.11. Least squares fitting was performed using TOPAS between 180–250 K *i.e.*, a finite range close to the apparent phase transition temperature, in accordance with Landau theory. The refined phase transition temperature of 254(1) K is slightly higher than the commonly-reported literature value for LBCO (240 K[14,15]) but is still in good agreement.

After confirming that fitting a linear relationship to the secondary OP η is

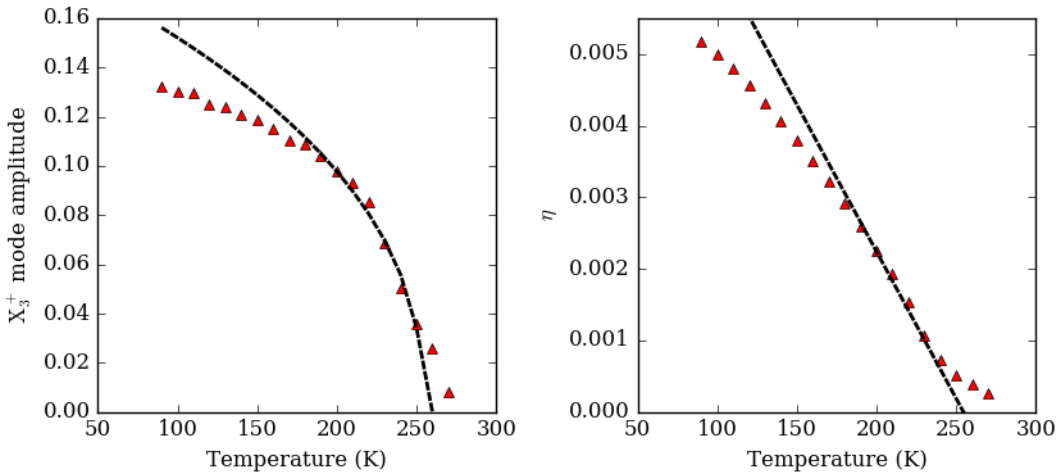

Figure 4.11: Plots of refined X_3^+ mode amplitudes (left) and orthorhombicity, η (right) for LBCO, represented by red triangles and the fits of relevant Landau relationships (dashed lines) as described in the text.

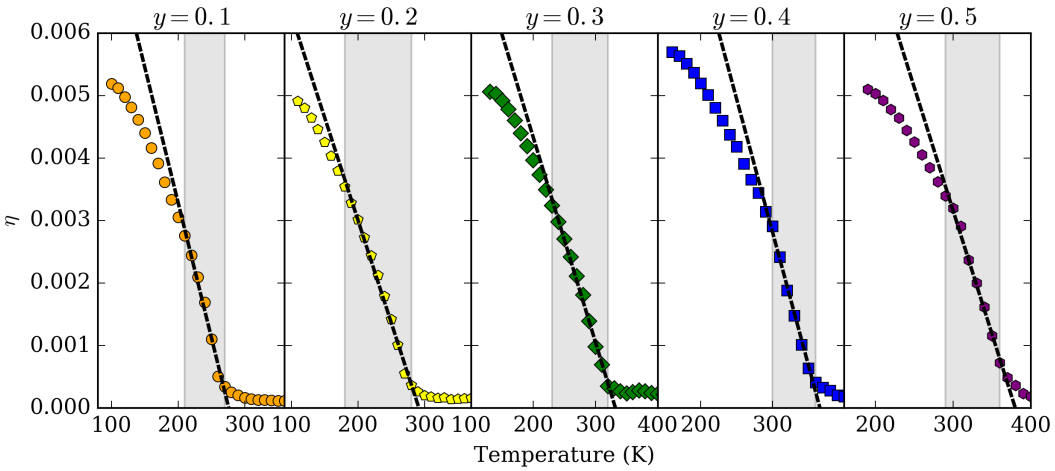

Figure 4.12: Plots of the orthorhombicity, η, of $La_{1.875}Ba_{0.125}(Cu_{1-y}Mg_y)_{0.875}Cu_{0.125}O_4$ (with y values indicated above each graph) and the fitted linear Landau relationship (dashed line) for each sample, described by Equation 4.3. Grey boxes show the finite temperature range used for the linear fit.

a valid approach for identifying the phase transition temperature, the same refinements were carried out for the Mg-substituted LBCO samples, using only the orthorhombicity parameter as a proxy for the true OP. The resulting fits are shown in Figure 4.12 and the resulting refined phase transition temperatures are reported in Table 4.4 and plotted in Figure 4.13. The reported errors of between 1–2 K are likely underestimated as the fitting procedure did not account for errors in the temperature or refined lattice parameters. The values show an approximately linear change in phase transition temperature with Mg-content, where the fit suggests a T_C increase of 26.7 K as a progression through the series.

Table 4.4: The LTO phase transition temperatures (T_C) of $La_{1.875}Ba_{0.125}(Cu_{1-y}Mg_y)_{0.875}Cu_{0.125}O_4$.

Mg-content (y)	T_C (K)
0.0	254(1)
0.1	276(1)
0.2	291(2)
0.3	332(2)
0.4	366(2)
0.5	380(2)

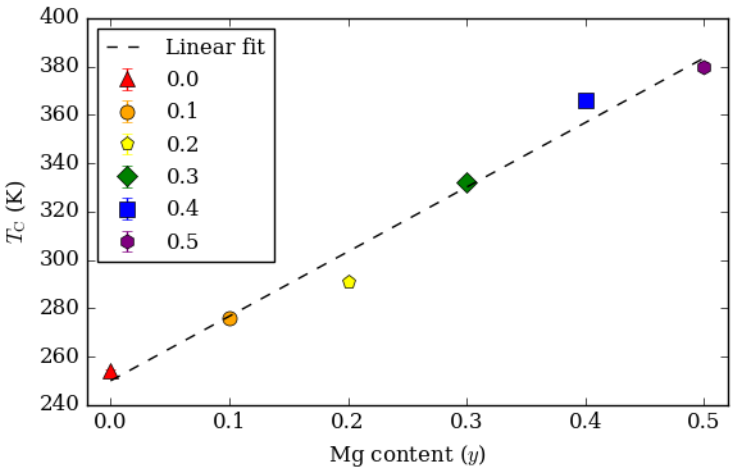

Figure 4.13: Refined LTO-to-HTT phase transition temperatures (T_C) for $La_{1.875}Ba_{0.125}(Cu_{1-y}Mg_y)_{0.875}Cu_{0.125}O_4$, where the legend corresponds to the y value and the error bars are smaller than the data points.

Octahedral rotation in the low temperature orthorhombic regime

The functionally-important octahedral rotations of the Cu/MgO_6 have also been investigated. The angle ϕ describes the rotation of the octahedra away from the [001] direction and ω describes the buckling of the bridging Cu–O–Cu bonds. The rotation angles have been calculated from the refined atomic positions, and the ϕ angles refined for the LTO structures shown in Figure 4.14.

Since the X_3^+ irrep. describes the rotational distortion, the angle magnitudes

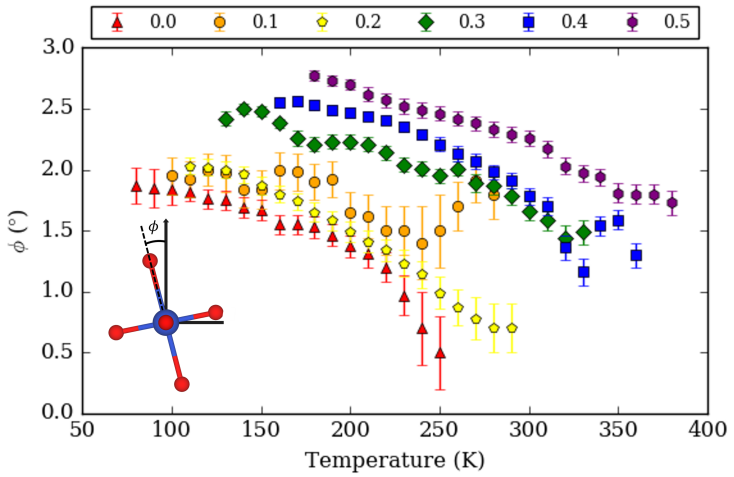

Figure 4.14: Plot of the temperature-dependence of the octahedral rotation magnitude ϕ for $La_{1.875}Ba_{0.125}(Cu_{1-y}Mg_y)_{0.875}Cu_{0.125}O_4$, where the legend corresponds to y.

follow exactly the same temperature and sample dependent trends as the mode amplitudes shown in Figure 4.10. It is important to note that the X_3^+ distortion is highly constrained with respect to the La/Ba atom positions, and therefore refined oxygen positions and octahedral rotations are inferred from the La/Ba positions, rather than freely-refined. Nevertheless, analysis of these constrained distortions provides useful insight into the average crystallographic structure. At the lower temperature LTO limit (chosen such that structural parameters are comparable between phases), the ϕ angle of LBCO is 1.87(15)°. The rotation magnitudes reported in the literature for the LTO phase are typically ca. 3.5°[45] and determined using neutron techniques. The discrepancies between the angle magnitudes could be due to X-rays being less sensitive to the oxygen positions. The ϕ angles found for the Mg-substituted LBCO show a positive trend, where an increase in Mg content results in an increase in the rotation magnitude and the same is found for the ω buckling angle.

Table 4.5: The octahedral rotation magnitude angle, ϕ, and buckling angle, ω, of Mg-LBCO at the lowest temperature at which there is a single phase of LTO for each sample.

Mg-content (y)	Temperature (K)	ϕ(°)	ω(°)
0.0	80	1.87(15)	2.16(18)
0.1	100	1.95(15)	2.23(16)
0.2	110	2.03(7)	2.34(8)
0.3	130	2.42(6)	2.74(6)
0.4	160	2.55(4)	2.82(6)
0.5	180	2.77(4)	3.04(6)

Reduced Jahn-Teller distortion

Since Rietveld analysis of the measured XRD patterns provides an average structure, where there are partial occupancies, only averaged atomic positions and bond lengths can be determined. Therefore, increased Mg^{2+} content should, on average, reduce the apparent JT distortion of the Cu/MgO_6 octahedra. First-

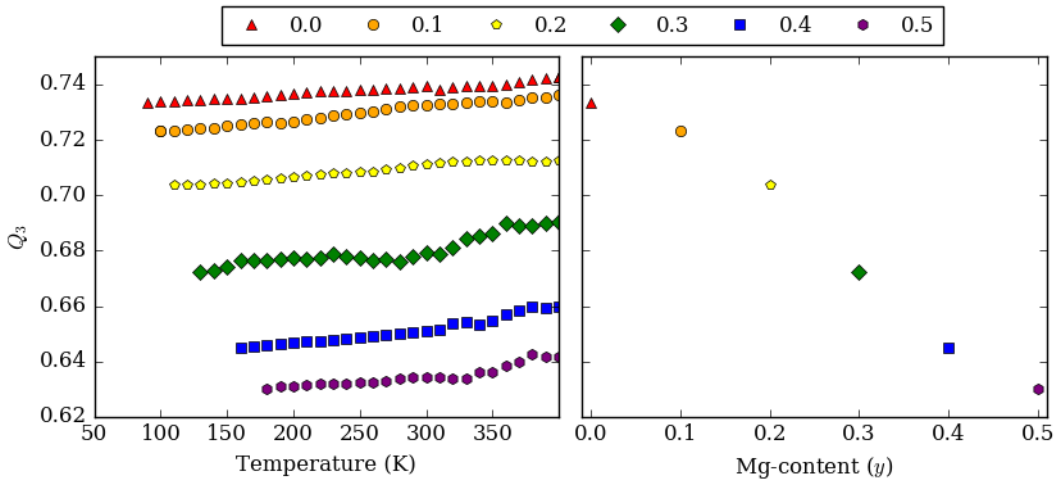

Figure 4.15: Left: JT distortion modes, Q_3, of $La_{1.875}Ba_{0.125}(Cu_{1-y}Mg_y)_{0.875}Cu_{0.125}O_4$. with temperature. Right: The distortion modes of the lowest temperature LTO phase for each sample. The legend corresponds to y.

order JT distortions can be described by the Q_3 mode.[46] The mode describes the JT instability related to a tetragonal-like distortion which is present in the LTO and HTT phases of LBCO:

$$Q_3 = \frac{2(l-s)}{\sqrt{2}}, \tag{4.4}$$

where l and s refer to long and short Cu–O bond lengths, respectively.

The Q_3 modes calculated for the LTO and HTT phases of Mg-substituted LBCO are shown in Figure 4.15 and comparisons of the Q_3 modes of the lowest temperature LTO structure for each sample, indicates that there is a near linear suppression of the JT distortion with increasing substitution with Mg. Extrapolation of the mode at the LTO limit to $y = 1.0$ reveals a distortion magnitude of ca. 0.52 which suggests that the RP structure has a mismatch between the La/BaO rock salt layers and the perovskite Cu/MgO_6 layers which can only be accommodated by an elongation of the Cu/MgO_6 octahedra. It therefore appears that a large proportion of the Q_3 in the $y = 0.0$ sample is due to the structural effects rather than the JT distortion.

4.4.2 The first-order low temperature tetragonal to low temperature orthorhombic phase transition

A study previously carried out by the Senn group has shown using high-resolution powder XRD that there is a pronounced and persisting phase coexistence of LTT and LTO in LBCO to at least 10 K. It was found that there is a ca. 57% LTO phase fraction, determined by Rietveld analysis, at 10 K. Phase coexistence has also been reported elsewhere within the literature although with much lower LTO levels of ca. 10%.[24,47]

The pronounced phase coexistence in the substituted LBCO sample was interrogated as part of this structural study. As previously stated, the phase coexistence was first observed at 70 K, *i.e.*, below 80 K—the widely reported LTO→LTT phase transition temperature (T_{LTT}). The diffraction patterns measured below 80 K were modelled with separate LTT and LTO phases, and the resulting fits to the (200)/(020) peaks for three representative temperatures are shown in Figure 4.16. The refined percentage of LTO at 10 K was 44.47%, determined by Rietveld analysis, and in good agreement with the aforementioned findings carried out within the Senn group.

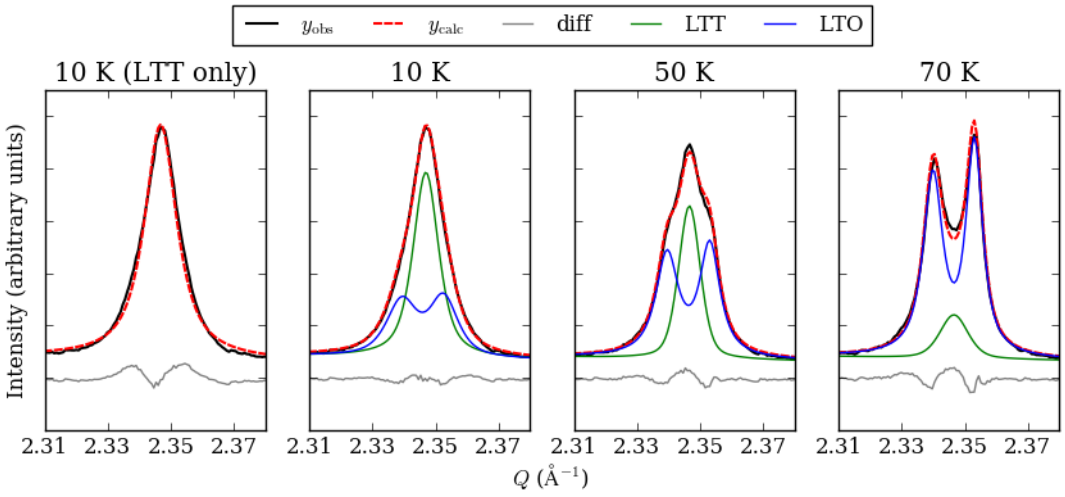

Figure 4.16: Plots of Rietveld fits of a two-phase, LTT and LTO model to the (200)/(020) peak of LBCO ($y = 0.0$) at the temperatures indicated.

Disappearance of the low temperature phase coexistence in Mg-substituted $La_{1.875}Ba_{0.125}CuO_4$

The same two-phase modelling approach was applied to the diffraction patterns measured of Mg-LBCO; plots of the (200)/(020) peaks are shown in Figure 4.17. Initially, refined phase fractions for all measured Mg-substituted samples suggest that the pronounced two-phase region is not unique to the LBCO structure. However, increasingly broadened LTO diffraction peaks and lattice parameter discontinuities when LTO was no longer the majority phase, were indicative of a system with a strain component—for example between misaligned LTT domains—rather than a distinct LTO phase.

The left-hand panel of Figure 4.18 shows the (200) peak fitting of the $y = 0.4$ Mg-LBCO (chosen as a representative sample) measured at 90 K. The diffraction pattern is fitted to a single phase of LTT and although the experiment peak is generally well-described by the model, there is a misfitted shoulder at high Q. Fitting to a two phase model of LTT and LTO improves the fitting (shown in the

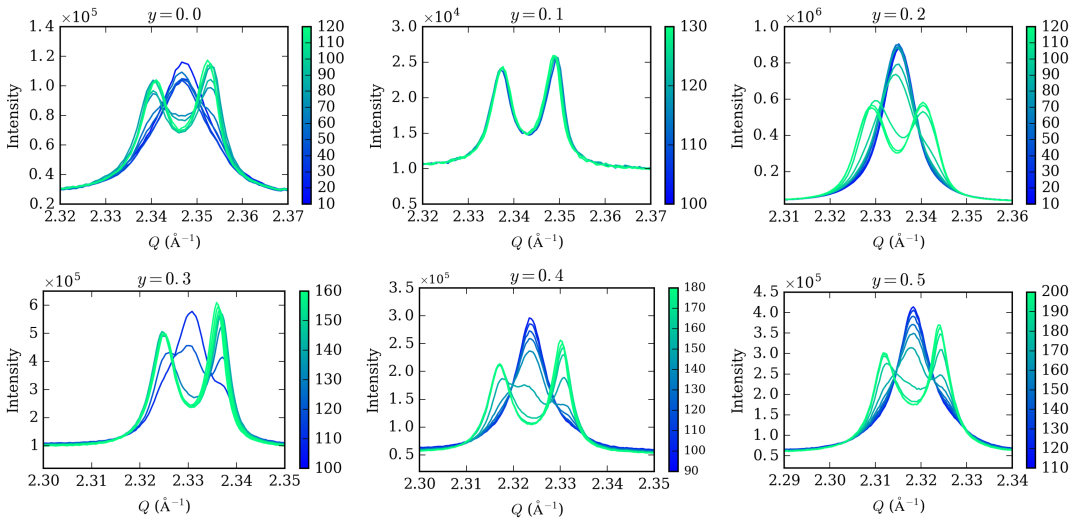

Figure 4.17: Plots of the (200)/(020) peaks from the lowest temperature diffraction patterns measured of $La_{1.875}Ba_{0.125}(Cu_{1-y}Mg_y)_{0.875}Cu_{0.125}O_4$. The LTO→LTT phase transition temperature is evident *via* an additional peak appearing with a decrease in temperature. The $y = 0.1$ sample was not measured at temperatures low enough to observe the phase transition.

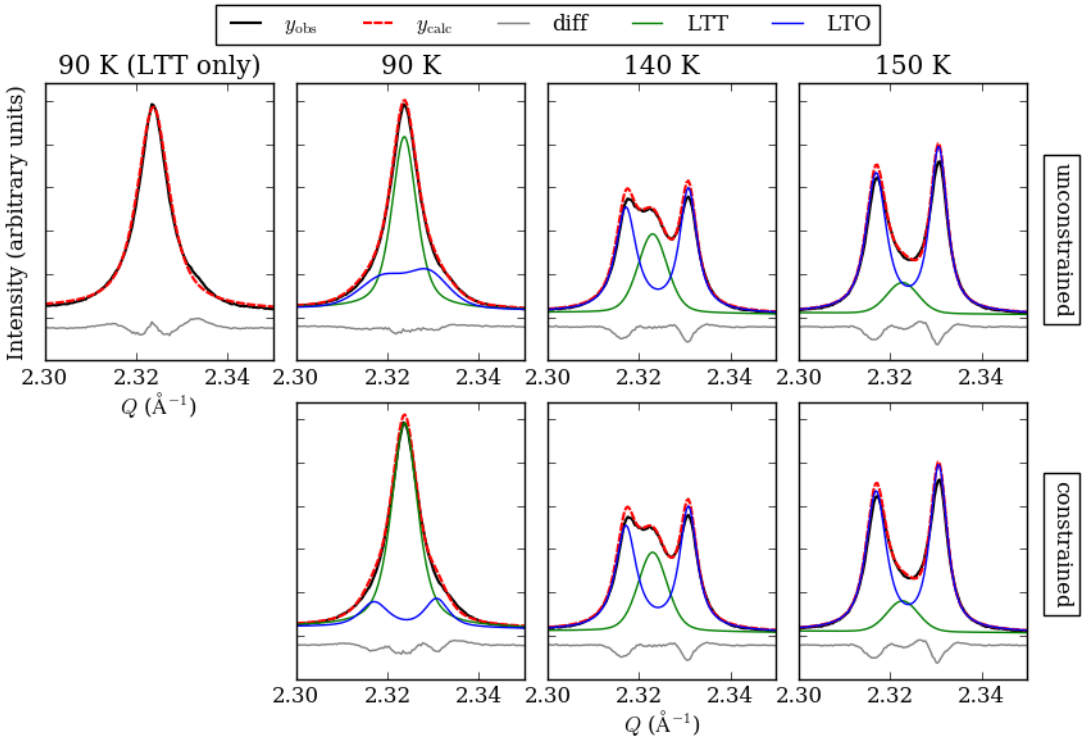

Figure 4.18: Plots of Rietveld fits of a two-phase, LTT and LTO model to the (200)/(020) peak of a representative Mg-LBCO sample ($y = 0.4$) at the temperatures indicated.

top panels for 90, 140 and 150 K), where the lattice parameters and anisotropic strain are refined freely. However, the LTO peak shapes at 90 K are significantly broadened and to a greater degree than those of the LBCO two-phase fit shown in Figure 4.16.

Therefore the following question arises—is the low temperature phase coexistence of Mg-substituted LBCO the same as the un-substituted LBCO material, *i.e.*, are the LTT and LTO structures comparable at the point of phase coexistence between LBCO and Mg-LBCO samples? To investigate the low temperature phase coexistence further, four two-phase models were tested against the low temperature diffraction patterns of all measured LBCO and Mg-LBCO samples:

1. LTT+LTO - the previously-described model, where refined lattice parameters and microstrain are allowed to refine freely.

2. LTT+LTO (fixed a:b) - a and b lattice parameters of the LTO phase were

constrained such that the orthorhombicity (a:b ratio) was fixed to the value determined by the LTT+LTO refinement prior to the LTO% falling below 50%.

3. LTT+LTO (fixed strain) - the anisotropic strain parameters for LTO were fixed to the values found from the LTT+LTO refinement prior to the LTO% falling below 50%.

4. LTT+LTO (fixed a:b and strain) - both the LTO a and b lattice parameters and the anisotropic strain parameters were constrained as previously described.

Figure 4.19 shows the fitting statistics (R_{wp}) and refined phase fraction of the LTO phase for the four models at temperatures below T_{LTT}. The R_{wp} values for a single phase LTT model are also shown for comparison. The results for LBCO

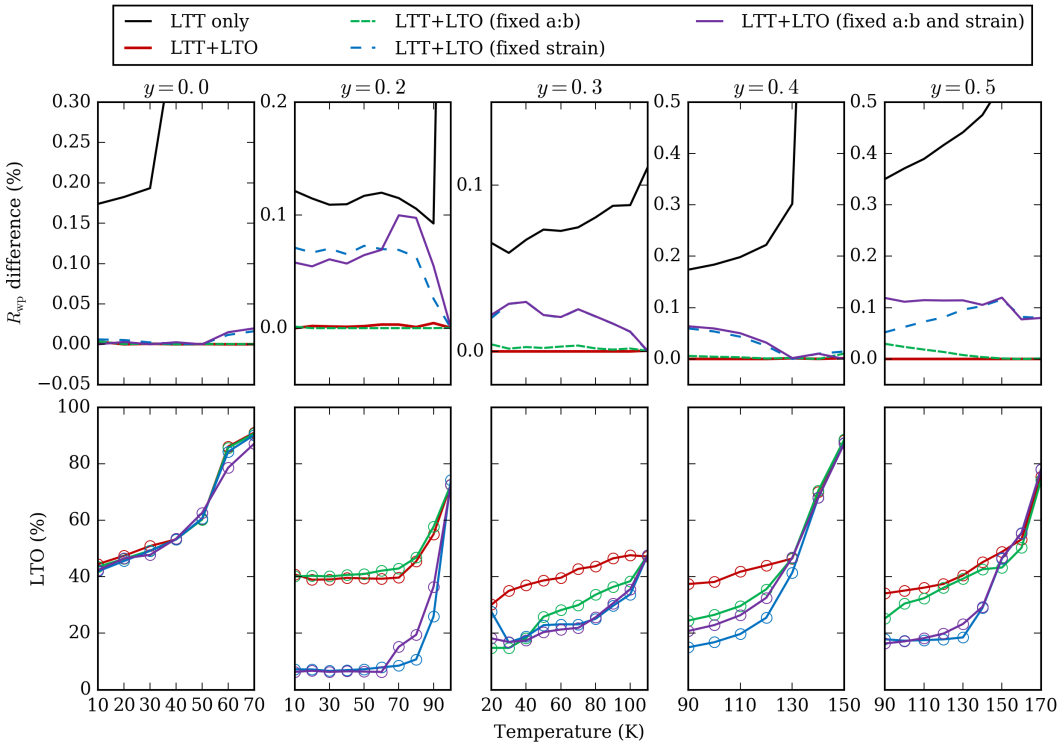

Figure 4.19: Top, percentage difference in fitting statistics, R_{wp} relative to the best R_{wp} value and bottom, refined percentage of the LTO phase for the four two-phase models as described in the text.

($y = 0.0$) show that the low temperature two-phase region is well described by the most constrained LTT+LTO (fixed a:b and strain) model, where R_{wp} between the less, and more constrained models, are very comparable. The refined LTO% is stable between the tested models, and has lattice and anistropic strain parameters that are consistent with those observed in the single-phase LTO regime.

The Mg-LBCO samples ($y = 0.1$–0.5) exhibit different trends compared to LBCO, although within themselves, the behaviour is consistent. The unconstrained LTT+LTO models provide better fitting statistics, unsurprisingly, and might lead one to conclude that there is a persisting phase coexistence of ca. 40% at the lowest measured temperatures for each sample. Constraining the a:b ratio results in R_{wp} values comparable to the unconstrained two-phase model and, on average, a reduction in the LTO phase fraction. Applying constraints to the strain parameter generally results in higher R_{wp} values which are accompanied by a decrease in LTO%, by up to 30%, and the most constrained model (a:b and strain) follows similar trends.

The differences in R_{wp} and LTO% found for LBCO compared to Mg-substituted LBCO using models where the strain is constrained confirms that any phase coexistence behaviour, once Mg is substituted into the structure, is distinctly different from that of LBCO. Although the refined LTO% values for Mg-LBCO at low temperature do not to refine to zero, it seems probable that the residual phase fractions for $y \geq 0.2$ observed in the most constrained LTT and LTO model are simply accounting for complex microstrain rather than an intrinsic phase coexistence. A ca. 30 K region of coexistence can therefore be identified for Mg-LBCO samples, where for $y = 0.2$, 0.3, 0.4 and 0.5, the phase transition to LTT is complete by 60, 80, 110 and 130 K, respectively.

The disappearance of the intrinsic phase existence for Mg-substituted LBCO suggests that the two-phase behaviour of LBCO is likely a direct result of the

competition between electronic phenomena (CDW and superconductivity), neither of which are expected for a Mg-substituted structure. This suggests that suppression of the phase segregation (macroscopic disorder) found in LBCO below 70 K, results in an LTO-favoured state and an increased T_C.

While octahedral rotation angles could not be extracted from the two phase models due to unstable refinement of the X_3^+ distortion, rotation angles from the single LTT phase for Mg-LBCO provide insight into the low temperature behaviour. Octahedral rotation (ϕ) and B–O–B buckling (ω) angles found for single phase LTT 70 K below the low temperature phase transition of each sample are reported in Table 4.6. The angles are calculated from refined oxygen positions, which have be constrained to the La/Ba distortion, and therefore any conclusions must be treated with caution. Nevertheless, the angles show an increase in magnitude with increasing Mg content, as observed with the LTO phase, but are smaller than those found for LBCO at 10 K ($\phi = 3.9°$ and $\omega = 7.8°$). The increase in magnitude across the series is likely due to shorter apical Mg–O bonds accommodating greater buckling of the La/BaO rock salt layer, where the shorter axial Cu/Mg–O bond length can cause a Cu/MgO_6 rotation of a larger angle whilst effecting the buckling less than a longer axial Cu/Mg–O bond.

Table 4.6: The octahedral rotation, ϕ, angles and buckling, ω, angles of LTT Mg-LBCO at 70 K below the LTO→LTT phase transition temperature.

Mg-content (y)	Temperature (K)	ϕ (°)	ω (°)
0.2	40	2.68(4)	4.33(9)
0.3	60	2.75(6)	4.40(12)
0.4	90	3.06(3)	4.80(7)
0.5	110	3.07(4)	4.78(8)

4.5 The local structure of high temperature tetragonal Mg-substituted $La_{1.875}Ba_{0.125}CuO_4$

The local structure of Mg-substituted LBCO has been investigated using X-ray PDF, where the HTT structures have been interrogated with the aim of understanding the effect of increased Mg content on the short-range atom–atom distances, and how the local structure of the HTT phase is altered by the substitution with JT-inactive Mg^{2+} cations.

The PDFs of $La_{1.875}Ba_{0.125}(Cu_{1-y}Mg_y)_{0.875}Cu_{0.125}O_4$ (y = 0.0–0.5 in steps of 0.1) measured at 400 K (where all samples are in the HTT phase) are shown in Figure 4.20. The bottom panel shows a calculated PDF of LBCO ($y = 0$), using an $I4/mmm$ space group where lattice parameters were determined *via* Rietveld refinement of the average structure. Visual comparison of the calculated and measured PDFs shows that PDF peak positions and intensities are, in general, reproduced by the average HTT structure. At higher r (>6 Å), gradual changes in the measured PDF peak positions and intensities as a function of increasing Mg content are consistent with increasing a- and decreasing c-lattice parameters, observed in the average structure. A noticeable difference between the modelled and measured PDFs however, lies in the 2.1–3.0 Å region, highlighted by the grey box in Figure 4.20.

One difficulty of analysing PDFs is peak overlap arising from different atom–atom correlations. Within the r region highlighted by the grey box in Figure 4.20 there are apparently two distinct PDF peaks in the calculated PDF. There is a smaller peak at ca. 2.4 Å which arises due to the apical Cu–O distance of the JT-distorted octahedra and the shortest (apical) La/Ba–O distance. The more

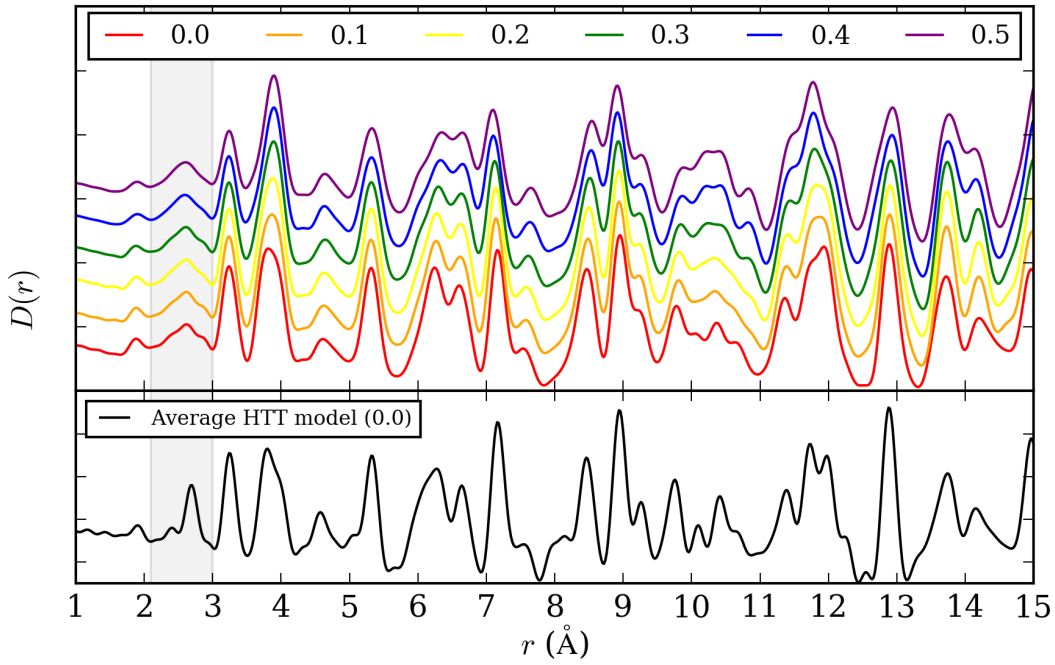

Figure 4.20: Top: X-ray PDFs of $La_{1.875}Ba_{0.125}(Cu_{1-y}Mg_y)_{0.875}Cu_{0.125}O_4$ measured at 400 K with increasing Mg content, where the legend indicates the y values, offset vertically for clarity. Bottom: A calculated X-ray PDF of $y = 0$ LBCO using the average HTT structure. The grey section spanning 2.1–3.0 Å highlights the most prominent differences between the experimental and calculated PDFs.

intense peak at ca. 2.7 Å is due to the eight longer La/Ba–O distances, which are constrained by symmetry to two crystallographically-inequivalent bonds, whereas in the LTT structure, the reduction in symmetry results in six inequivalent bond lengths. The feature at 2.7 Å, observed across the measured PDFs, is significantly broadened compared to the HTT PDF model and requires investigation *via* structural modelling. The substitution of Cu results in additional pairwise correlations, which should manifest most strongly at low r. The JT-distorted Cu–O bonds are split into two long (ca. 2.4 Å) and four short (ca. 1.9 Å) distances, whereas the two axial and four equatorial Mg–O distances are expected to be more similar to each other producing a single peak. However, the relatively poor scattering of the Mg and O atoms, combined with the reduced occurrence of this correlation means that this intermediate peak is not clearly visible in the data.

4.5.1 Small box analysis

To investigate the local symmetry-lowering distortions—and whether the measured X-ray PDFs are sensitive to the known X_3^+ irrep.—expected to be a soft phonon mode in the HTT phase—SAPA analysis[48] (as described in Chapter 3) was performed. Distortion modes were generated that lower the symmetry for the high-symmetry $I4/mmm$ structure to a $P1$ structure with basis $[\mathbf{a}_{\mathrm{HTT}} + \mathbf{b}_{\mathrm{HTT}}]$,$[-\mathbf{a}_{\mathrm{HTT}} + \mathbf{b}_{\mathrm{HTT}}]$,$[\mathbf{c}_{\mathrm{HTT}}]$, such that the symmetry-breaking distortions of the lower temperature $Bmab$ and $P4_2/ncm$ phases were contained within the decomposed modes. Lattice parameters were constrained to preserve the average tetragonal symmetry. The Γ_1^+ modes—corresponding to inherent apical displacements of La/Ba and O atoms—were refined against the high resolution average structure data (collected at TPS and I11, DLS) and the refined values then held fixed for all SAPA refinements. The remaining 16 irreps. listed in the legend of Figure 4.21 were refined, in turn, against the variable Mg-content PDFs over a fitting range of 1.0–15 Å such that the PDF contained all atom–atom distances described by the small-box model. To account for correlated thermal motion, and the resulting r-dependent broadening, the simple quadratic relationship was used, as described in Chapter 3. Atomic displacement parameters (B_{iso}) for La and Ba atoms were constrained to be equal, as were the parameters for Cu and Mg. The displacement parameters for apical (O1) and equatorial (O2) oxygen atoms were allowed to refine independently.

Figure 4.21 shows the difference in R_{w} compared to the worst fitting irrep. for each composition such that a more negative value corresponds to a better-fitting irrep. The results indicate that the M_5^-, X_2^+, X_1^+ and Γ_5^- irreps. consistently provide an improved fit across the compositional series. These irreps. point toward a different local symmetry than that described by the known X_3^+ distortion. The X_2^+, X_1^+, and Γ_5^- irreps. result in highly distorted Cu/MgO_6 octahedra shown in

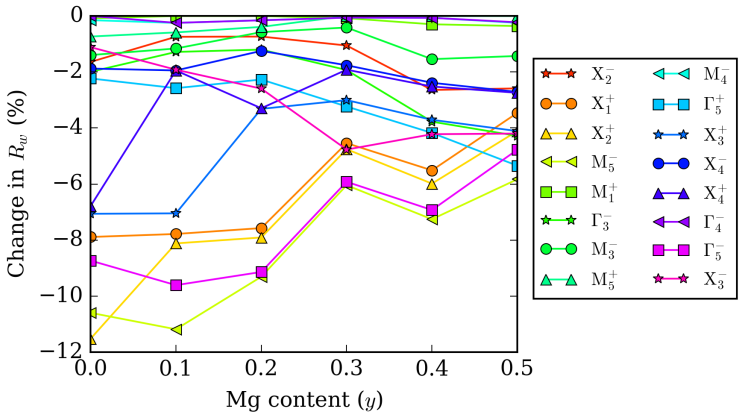

Figure 4.21: Percentage change in fitting statistics of each irrep. as a function of Mg-content, y. The change in R_w is calculated with respect to the worst-fitting irrep. for each y value such that a more negative value represents a better fit.

Figure 4.22.

The improved fits from the above distortion modes might lead one to conclude that the Cu/MgO_6 octahedra are highly distorted in the HTT phases of LBCO and Mg-LBCO, however, it may be that there is an occupancy disorder that happens to be modelled well by these distortions. This perhaps highlights a limitation of the small-box SAPA approach when considering the local structure,

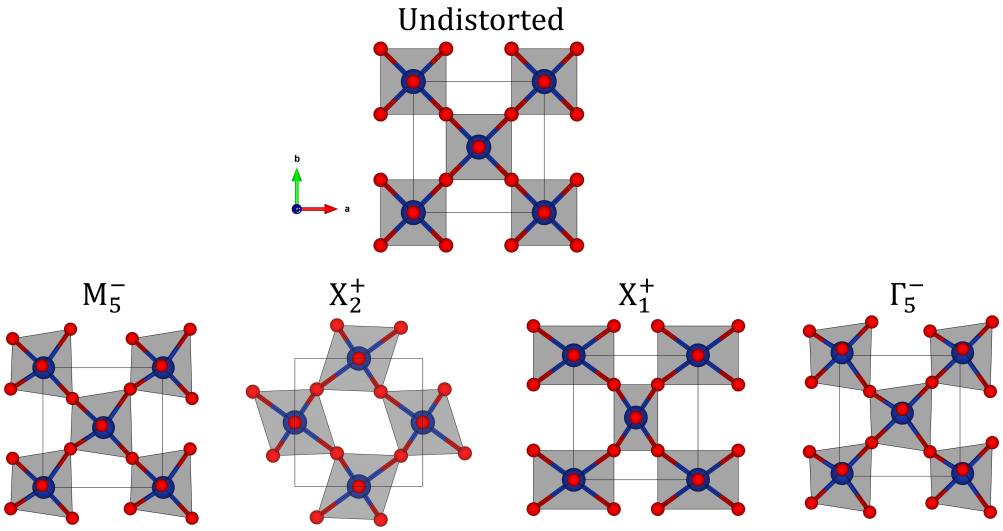

Figure 4.22: Representative structural distortions of the first layer of Cu/MgO_6 octahedra in the RP structure arising from the refined modes described by the M_5^-, X_2^+, X_1^+ and Γ_5^- irreps. For clarity the intermediate layer of octahedra are shown for the distortion described by the X_2^+ irrep. Cu/Mg atoms are shown as blue spheres and O atoms as red spheres.

particularly where the crystal structure has partially-occupied sites, by different atoms.

None-the-less, it is promising that the X_3^+ modes are consistently pulled out as the ca. fifth best fitting irrep, and therefore small-box modelling was performed to investigate the local structure using the constrained X_3^+ and Γ_1^+ distortions used for the average structure XRD study. Refinements were carried out using the *Pccn* space group and constraints appropriate to the LTT, LTO, and HTT models, as described in Section 4.2.5. Atomic displacement parameters were constrained in the same way as for the SAPA analysis and initial r-range of 1.0–15 Å was chosen such that it encompassed the longest atom–atom distance within the unit cell.

Fitting of the X-ray PDFs to LTT, LTO and HTT models shows to what extent the structures deviate over local length scales, with respect to the long-

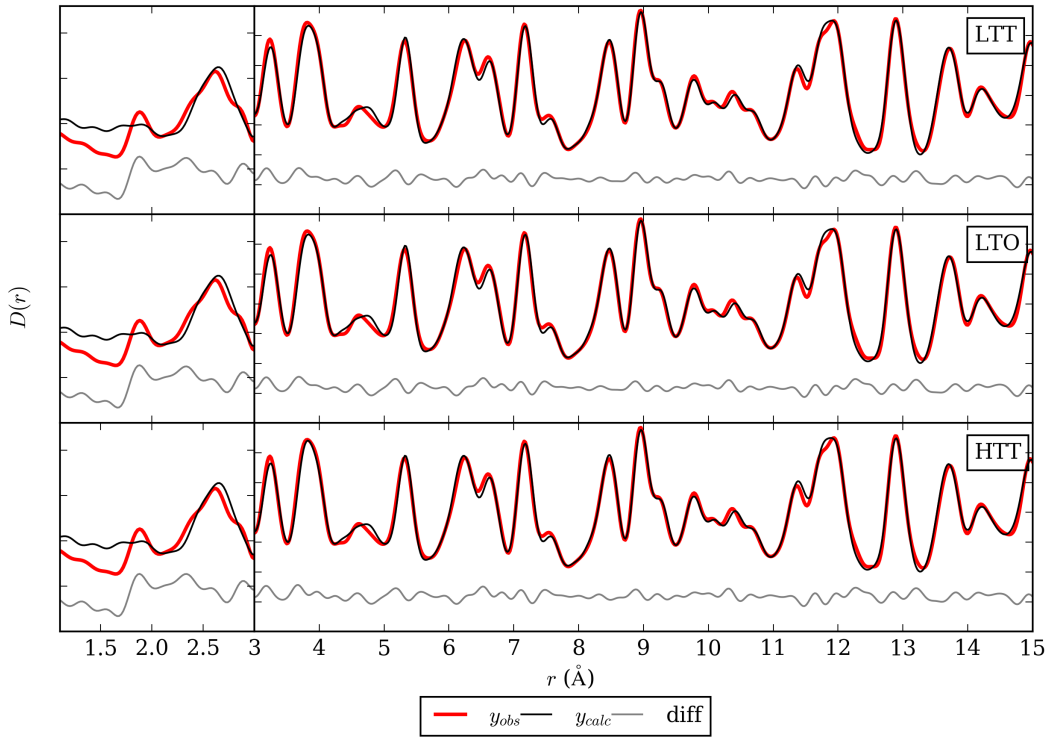

Figure 4.23: Small box fits to the X-ray PDF of LBCO ($La_{1.875}Ba_{0.125}(Cu_{1-y}Mg_y)_{0.875}Cu_{0.125}O_4$, $y = 0$), using LTT, LTO and HTT models. The low r-range is plotted with a separate y-axis for clarity.

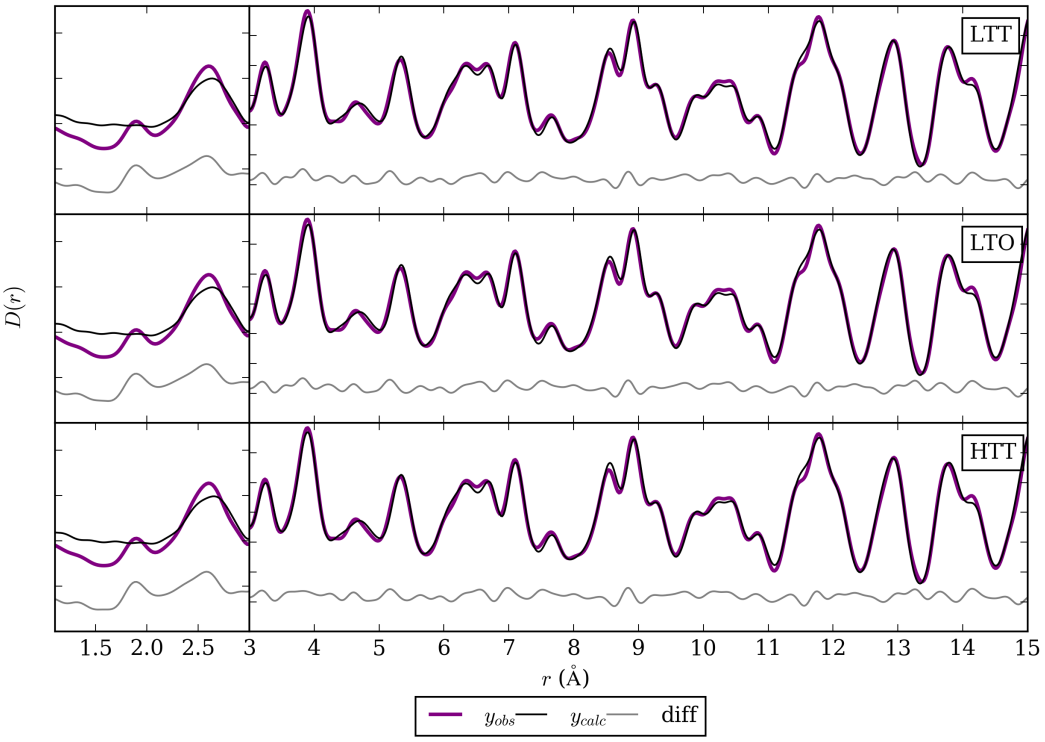

Figure 4.24: Small box fits to the X-ray PDF of $La_{1.875}Ba_{0.125}(Cu_{1-y}Mg_y)_{0.875}Cu_{0.125}O_4$, $y = 0.5$, using LTT, LTO and HTT models. The low r-range is plotted with a separate y-axis for clarity.

range average structure. Figures 4.23 and 4.24 show the fits of the LTT, LTO and HTT models to the $y = 0$ and 0.5 compositions, respectively (fits for the intermediate compositions are available in the Appendix). The small-box models all appear to describe the local structure well, however, it is particularly evident that the peaks below 3.0 Å are not well described by any of the three models, with the smallest peak corresponding to the shortest Cu–O distance at ca. 1.9 Å being almost undetectable in the model PDFs.

Visually, there is almost no difference between the fits of the three models against the PDF data and this is reflected in the fitting statistic (R_w) values, reported in Table 4.7. The very small differences in R_w would suggest that the X_3^+ distortion describing the Cu/MgO_6 octahedral rotation in the LTT and LTO structures does not improve the local structure model compared to the undistorted HTT structure. However, there are informative trends in atomic

displacement parameters and rotation angle magnitudes refined for the models with higher degrees of freedom.

Table 4.7: Fitting statistics (R_w), displacement parameters (B_{iso} with units of Å^2, and α) and octahedral rotation angles ϕ and ω from LTT, LTO and HTT model small-box refinements over 1.0–15 Å against X-ray PDFs of $La_{1.875}Ba_{0.125}(Cu_{1-y}Mg_y)_{0.875}Cu_{0.125}O_4$ measured at 400 K.

	y	R_w	B_{iso}(A)	B_{iso}(B)	B_{iso}(O1)	B_{iso}(O2)	α	ϕ (°)	ω (°)
LTT	0.0	11.717	0.25(2)	0.45(3)	3.5(2)	1.8(1)	0.031(2)	1.77(18)	3.0(5)
	0.1	11.655	0.24(2)	0.44(3)	3.4(2)	2.0(2)	0.033(2)	1.93(18)	3.2(4)
	0.2	11.388	0.25(2)	0.44(3)	3.4(2)	2.2(2)	0.033(2)	2.04(19)	3.3(3)
	0.3	11.352	0.24(2)	0.46(3)	3.5(2)	2.7(2)	0.034(2)	2.14(17)	3.5(4)
	0.4	11.823	0.24(2)	0.47(3)	3.8(2)	3.0(2)	0.035(3)	2.21(18)	3.5(4)
	0.5	11.379	0.28(2)	0.50(3)	4.1(3)	3.2(2)	0.033(3)	2.27(19)	3.6(3)
LTO	0.0	11.700	0.26(2)	0.45(3)	3.6(2)	1.7(1)	0.031(2)	1.7(3)	2.0(4)
	0.1	11.637	0.24(2)	0.45(3)	3.4(2)	2.0(2)	0.033(2)	1.8(3)	2.1(3)
	0.2	11.370	0.25(2)	0.44(3)	3.4(2)	2.3(2)	0.032(2)	1.8(3)	2.1(3)
	0.3	11.356	0.25(2)	0.45(3)	3.5(2)	2.8(2)	0.034(2)	1.9(2)	2.1(3)
	0.4	11.825	0.24(2)	0.47(3)	3.9(2)	3.0(3)	0.035(3)	2.2(3)	2.4(4)
	0.5	11.370	0.28(2)	0.50(3)	4.2(3)	3.2(2)	0.033(3)	2.2(2)	2.5(3)
HTT	0.0	11.828	0.27(2)	0.44(3)	3.6(2)	1.7(1)	0.030(2)	0	0
	0.1	11.790	0.26(2)	0.43(2)	3.5(2)	2.0(2)	0.032(2)	0	0
	0.2	11.510	0.26(2)	0.43(2)	3.5(2)	2.3(2)	0.032(2)	0	0
	0.3	11.557	0.26(2)	0.45(3)	3.6(2)	2.8(2)	0.034(2)	0	0
	0.4	12.083	0.26(3)	0.46(3)	3.9(2)	3.4(3)	0.034(2)	0	0
	0.5	11.596	0.29(2)	0.48(3)	4.2(2)	3.6(3)	0.034(3)	0	0

Table 4.7 shows the B_{iso} values for the A (La/Ba)- and B (Cu/Mg)-site cations, which fall within the range 0.25–0.48 Å^2, whereas the values for the oxygen atoms are more than twice as large. The larger refined thermal displacement parameters of the oxygen atoms are indicative of disorder within the Cu/MgO_6 octahedra and La/BaO_9 cluster and explain the broadening of the measured low r PDF peaks, especially the lowest r peak which is broadened almost below detection. The refined octahedral rotation (ϕ) and buckling (ω) angles (see Table 4.7) are consistent between the LTT and LTO models and show a near linear positive trend with increased Mg content. Note that all measurements were performed at 400 K, and therefore the samples have been measured at varying degrees of proximity to the LTO-to-HTT phase transition temperature, with $y = 0.5$ being in closest proximity to the phase transition with $T_C = 380$ K, and $y = 0.0$ being furthest away with $T_C = 254$ K. The apparent rotation of Cu/MgO_6 octahedra in

the local structure and the increase in angle magnitude found from the constrained small-box models could be due to dynamic rotation distortions, which are larger in the $y = 0.5$ sample due to the associated phonon mode being softer in energy.

Refining the LTT, LTO and HTT models over a limited r-range (1.6–3.1 Å) such that only the shortest La/Ba–Cu/Mg and Cu/Mg–O atom–atom distances are considered results in an improved fit (Figures 4.25 and 4.26, Figures for intermediate compositions are available in the Appendix) and smaller displacement parameter values for the oxygen atoms. The O1 and O2 B_{iso} values reported Table 4.8 are smaller than those reported in Table 4.7 and, are consistent with values expected for a high temperature refinement.[49]

Whilst the fitting statistics for the small-box modelled over a larger r-range of 1.0–15 Å show very little improvement between the LTT, LTO and HTT models, the R_w values for the smaller r-range (1.6–3.1 Å) consistently support a local LTO-type rotation of the Cu/MgO_6 octahedra. The representative fits of the

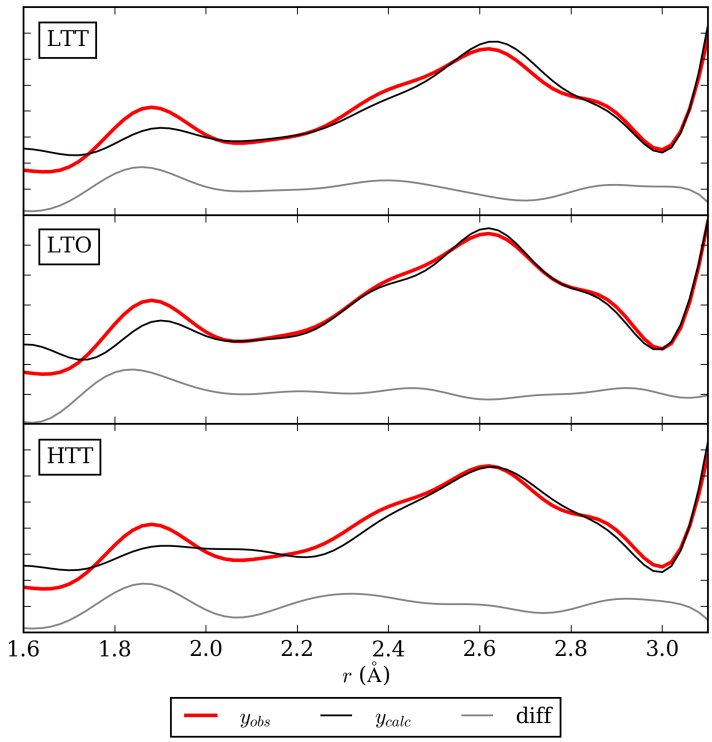

Figure 4.25: Small box fits to the X-ray PDF of $La_{1.875}Ba_{0.125}(Cu_{1-y}Mg_y)_{0.875}Cu_{0.125}O_4$, $y = 0.0$, using LTT, LTO and HTT models, over a short r-range of 1.6–3.1 Å.

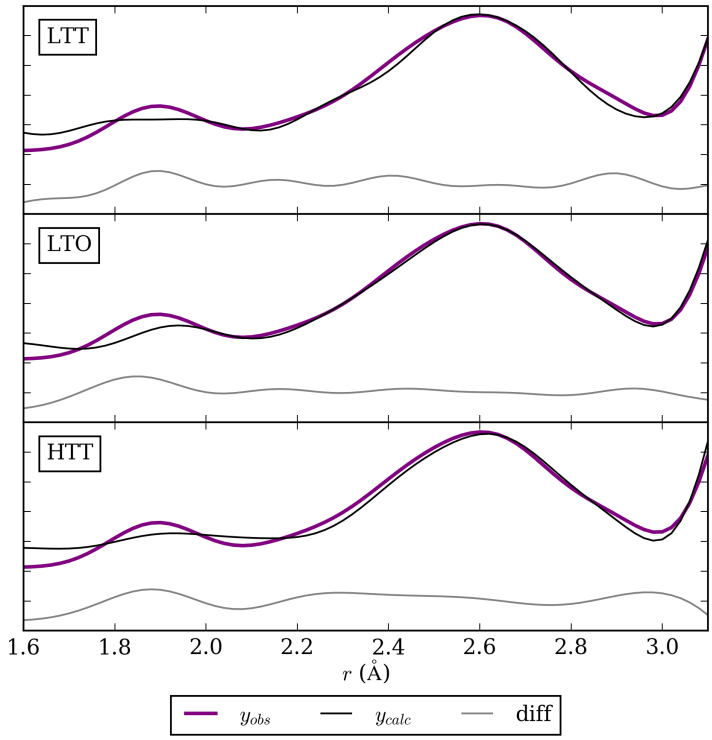

Figure 4.26: Small box fits to the X-ray PDF of $La_{1.875}Ba_{0.125}(Cu_{1-y}Mg_y)_{0.875}Cu_{0.125}O_4$, $y = 0.5$, using LTT, LTO and HTT models, over a short r-range of 1.6–3.1 Å.

$y = 0.0$ and $y = 0.5$ samples (Figures 4.25 and 4.26) show that the short-range modelling results in a much improved fit of the feature spanning 2.2–3.0 Å. The peak at ca. 1.9 Å is still poorly fitted although the intensity is best reproduced by the LTO models in both samples.

The refined rotation (ϕ) and buckling (ω) parameters also increase significantly compared to their values when refined against a larger r-range. An increase in Cu/MgO_6 rotation magnitude is also observed over the series observed over the shorter r-range.

Refining the local structure over variable length scales has been shown to provide important insight into the true local structure of solid-state materials.[50,51] In this case, it would appear that considering only the shortest atom–atom distances, resolves a local LTO-type structure in the average HTT phase of LBCO and Mg-LBCO. One might conclude that this is indicative of an anharmonic mode—describing dynamic rotations of the Cu/MgO_6 octahedra—a theory which

Table 4.8: Fitting statistics (R_w), displacement parameters (B_{iso} with units of $Å^2$, and α) and octahedral rotation, ϕ, and buckling, ω, angles from LTT, LTO and HTT small-box refinements over 1.6–3.1 Å against X-ray PDFs of $La_{1.875}Ba_{0.125}(Cu_{1-y}Mg_y)_{0.875}Cu_{0.125}O_4$ measured at 400 K.

	y	R_w	B_{iso}(A)	B_{iso}(B)	B_{iso}(O1)	B_{iso}(O2)	α	ϕ (°)	ω (°)
LTT	0.0	15.367	0.63(2)	0.002(10)	0.6(3)	1.3(2)	0.000(9)	3.23(19)	4.3(4)
	0.1	11.821	0.65(1)	0.002(7)	0.9(2)	1.4(1)	0.000(5)	3.67(16)	5.0(3)
	0.2	10.733	0.71(4)	0.000(22)	1.1(2)	1.5(1)	0.002(12)	3.96(17)	5.6(3)
	0.3	10.403	0.67(1)	0.001(3)	1.1(2)	1.6(1)	0.000(2)	3.85(16)	5.3(3)
	0.4	9.8864	0.77(3)	0.002(13)	1.3(3)	1.6(1)	0.000(8)	4.13(18)	5.8(4)
	0.5	10.270	0.78(7)	0.001(27)	0.90(4)	1.5(1)	0.012(364)	4.44(18)	6.7(4)
LTO	0.0	14.388	0.82(3)	0.001(1)	0.5(2)	1.2(1)	0.000(1)	4.7(3)	4.6(3)
	0.1	10.772	0.67(1)	0.000(1)	0.4(1)	1.2(1)	0.001(1)	4.4(3)	4.2(3)
	0.2	8.5244	0.74(2)	0.000(1)	0.5(1)	1.2(1)	0.000(1)	4.9(2)	4.8(3)
	0.3	9.5775	0.76(1)	0.000(1)	0.6(1)	1.2(1)	0.000(1)	4.9(3)	4.8(3)
	0.4	9.7642	0.95(2)	0.006(9)	0.6(2)	1.1(1)	0.000(84)	5.5(3)	5.4(3)
	0.5	10.063	0.96(1)	0.002(7)	0.6(2)	1.1(1)	0.000(6)	5.5(3)	5.5(3)
HTT	0.0	16.300	0.72(1)	0.001(5)	2.5(4)	1.7(2)	0.000(4)	0	0
	0.1	12.798	0.73(39)	0.000(181)	3.4(5)	1.9(2)	0.005(153)	0	0
	0.2	11.139	0.64(51)	0.00(294)	3.5(4)	1.9(2)	0.023(189)	0	0
	0.3	11.045	0.80(20)	0.000(136)	3.7(5)	2.0(2)	0.003(73)	0	0
	0.4	10.731	0.82(39)	0.026(148)	4.3(7)	2.1(2)	0.000(163)	0	0
	0.5	10.992	0.73(66)	0.001(311)	4.4(7)	2.0(2)	0.026(305)	0	0

is supported by the apparent softening of the mode reflected in the increase in rotation magnitude at closer proximity to the phase transition. Another interpretation is that the local structure of the HTT phases is of the order-disorder type, with harmonic LTT and LTO-type dynamic distortions, with equal magnitude. This interpretation is supported by the degeneracy of small box models over longer r-ranges—which will contain atom–atom distances arising due to correlations of octahedral rotations. These results must be treated tentatively though, as the small-box models are highly constrained and the refined distortions are based on the La/Ba atom positions. Further work including modelling the structure using a larger configuration (supercell) might provide a way of investigating potential disordered arrangements of LTT or LTO local structures.

4.5.2 Big box modelling

While there is essentially no contrast between the X-ray form factors of La compared to Ba, it may be possible to distinguish between the lighter Mg and Cu atoms. Small-box modelling treats the A and B sites as averaged La/Ba and

Cu/Mg atoms, with variable occupancies, and therefore cannot provide information about specific Mg and Cu atom–atom distances. Big box modelling provides a means of accounting for structures with long-range and/or more complex disorder and multiple A/B-site occupancies. As such, refinements were performed using the RMCProfile software[37] with the aim of obtaining information about distinct Mg and Cu environments. The refinements used a $8 \times 8 \times 4$ supercell (producing near-cubic supercell dimensions) of the HTT Rietveld-refined unit cell for each Mg-substituted LBCO sample and atomistic configurations were generated by randomly replacing La and Cu atoms with Ba and Mg, respectively, according to their occupancies. Minimum and maximum distance restraints were applied to the A–O and B–O atom–atom distances to prevent unphysical bond distances (details provided in the Appendix) and simultaneous fitting to reciprocal ($F(Q)$) space data was carried out in order to constrain average-structure characteristics.[37]

Figure 4.27(a) shows representative RMC fits to the LBCO ($y = 0.0$) and Mg-LBCO ($y = 0.5$) PDFs (fits for the intermediate compositions are presented in

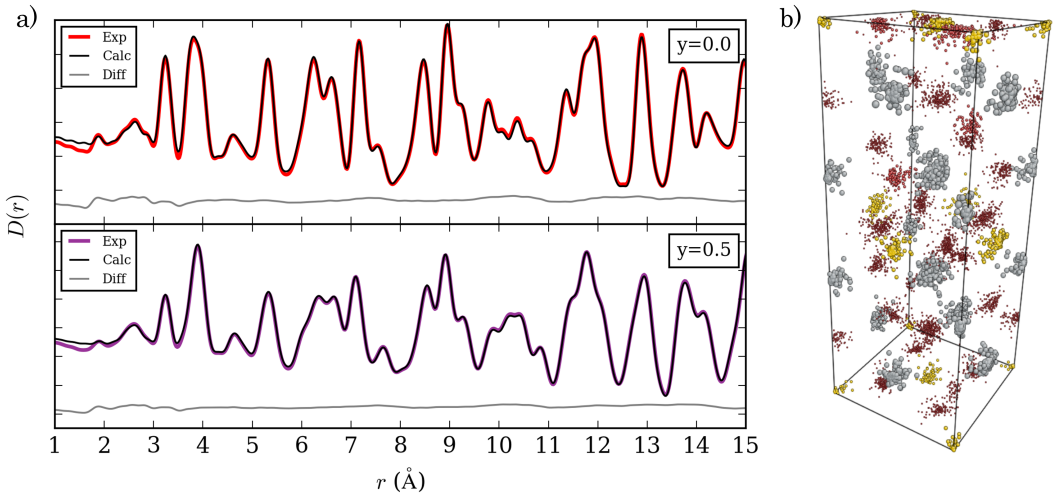

Figure 4.27: a) RMC fits of $La_{1.875}Ba_{0.125}(Cu_{1-y}Mg_y)_{0.875}Cu_{0.125}O_4$, $y = 0$ and $y = 0.5$ X-ray PDFs measured at 400 K. b) The collapsed unit cell of the final configuration refined for the $y = 0$ sample showing a significant degree of disorder within the cuprate structure. Grey atoms represent La and Ba, yellow atoms represent Cu and represent O atoms.

the Appendix). The fits, overall, are excellent, and the misfit of the low r slope—which predominantly affects the first PDF peak at ca. 2 Å—can be attributed to difficulties in putting the X-ray total scattering data on an absolute scale. The collapsed unit cell of the refined atomic positions for LBCO shows a structure with a significant amount of disorder, as observed by the small-box modelling.

Figure 4.28 shows the partial PDFs $g(r)$ of the Cu–O and Mg–O correlations calculated from the RMC configurations for all samples. The distribution of Mg–O atom distances is apparently greater than the distribution of Cu–O distances, however, it is expected that there should be distinct Mg–O distances where a MgO_6 octahedron is expected to have six equivalent bond lengths rather than four short and two long bond lengths, as with CuO_6. It is apparent that the shortest atom–atom distances cannot be resolved using this approach, and this big-box modelling method would benefit from a neutron total scattering experiment which would be more sensitive to the light atom positions.

The X-ray PDF study of Mg-substituted LBCO reported in this Chapter

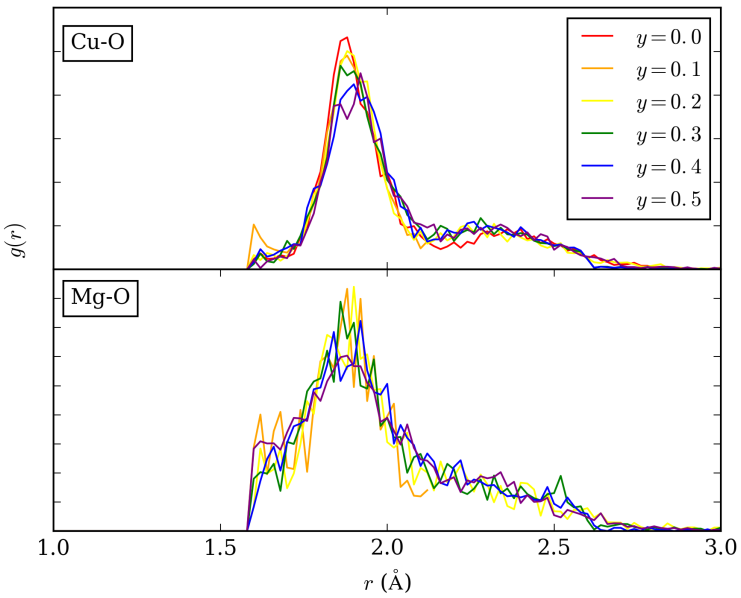

Figure 4.28: Partial Cu–O and Mg–O PDFs, $g(r)$ for $La_{1.875}Ba_{0.125}(Cu_{1-y}Mg_y)_{0.875}Cu_{0.125}O_4$.

tentatively indicates a preference for a HTT structure with Cu/MgO_6 octahedra rotations persisting above the LTO phase transition temperature. A preference for an LTT- or LTO-type distortion could not be definitively resolved from this work, although refined atomic displacement parameters derived from different modelled length scales might suggest dynamic distortions, with a softening of an anharmonic mode. Further work is required using other local structure techniques such as EXAFS to directly probe the Cu *versus* Mg atom–atom distances, and particularly neutron total scattering in order to explore the extent of oxygen displacement more thoroughly.

4.6 High-pressure neutron diffraction

As a continuation of the previous finding that the substitution of Cu has a significant effect on the LTT and LTO phase transition temperatures, two samples, $La_{1.875}Ba_{0.125}(Cu_{1-y}Mg_y)_{0.875}Cu_{0.125}O_4$ with $y = 0.0$ (LBCO) and 0.5 (hereafter referred to as Mg-LBCO) were measured at ambient temperature on the high-pressure neutron diffraction instrument PEARL. The sample with the greatest Mg-substitution level was chosen as the structure exhibits the largest structural difference from the LBCO sample and, as Mg-LBCO is known to exist in the LTO phase at 300 K, the aim was to observe a pressure-induced LTO→HTT phase transition.

4.6.1 $La_{1.875}Ba_{0.125}CuO_4$

The measured high-pressure diffraction patterns for LBCO are shown in Figure 4.29. The two most intense peaks ((111) and (200) reflections) arising from the lead pressure marker are indicated with asterisks. Sample peaks shift to lower *d*-spacing values, reflecting an increasingly compressed structure.

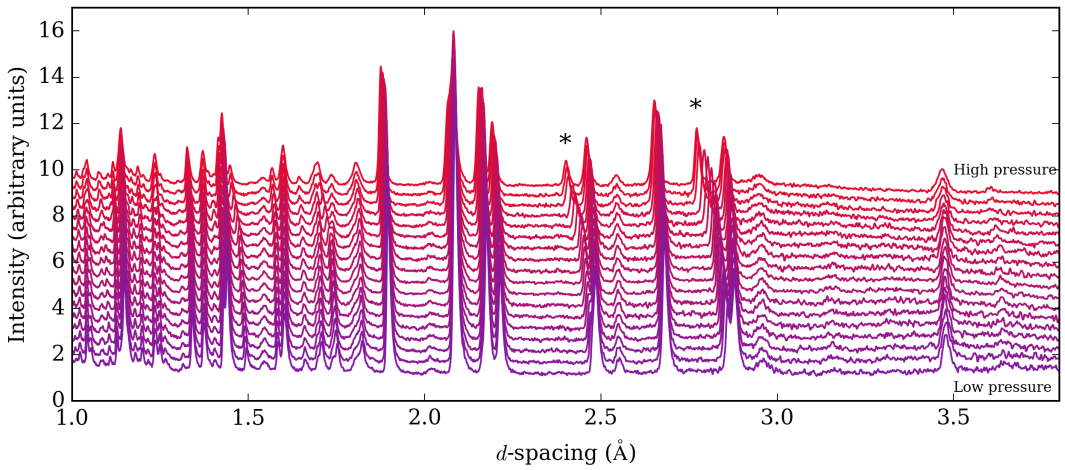

Figure 4.29: Neutron diffraction patterns of LBCO collected on the PEARL instrument, offset in the y-direction with increasing pressure. Reflections due to the lead pressure marker are indicated by asterisks.

At ambient temperature and pressure, LBCO is known to exist in the HTT phase, and this was confirmed in the lowest pressure measurement *via* Rietveld refinement, where modelling as described in Section 4.2.5 was performed. The HTT structure was fitted to the neutron diffraction pattern of the lowest pressure (0.037(6) GPa) measurement along with additional Al_2O_3 and ZrO_2 phases due to the ZTA anvil and a Pb pressure marker phase. The refinement resulted in an excellent fit, shown in Figure 4.34.

Sequential refinement of all diffraction patterns confirmed that there was no phase transition and, fitting to a HTT structure continued to provide excellent fits to the data up to 5.53 GPa (also shown in Figure 4.34).

4.6.2 Mg-substituted $La_{1.875}Ba_{0.125}CuO_4$

The high-pressure neutron diffraction patterns of Mg-LBCO from the first and second sample loading are shown in Figure 4.31. The difference in relative intensities between anvil and sample reflections between the first and second loading are due to differing microstructures and strains of the ZTA anvils used between the first and second loading experiments. The average structure study reported

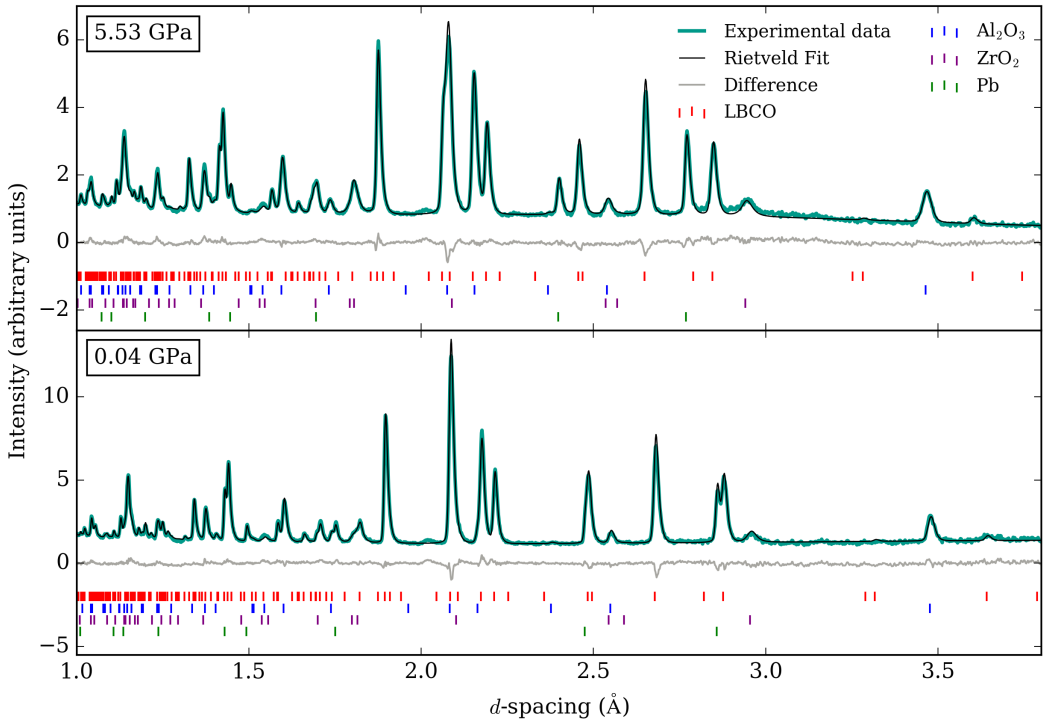

Figure 4.30: Rietveld fits of the lowest and highest pressure measurements of LBCO. The LBCO peaks were fitted using the HTT structure and all remaining peaks were fitted using Al_2O_3 and ZrO_2 phases to account for scattering from the anvils, or a Pb pressure marker phase.

earlier in this Chapter found that at 300 K, Mg-LBCO adopts the LTO structure with $a = 5.41270, b = 5.43003$ and $c = 13.02571$ Å. Peak splitting indicative of orthorhombic symmetry was not observed and therefore diffraction patterns, using peak shape parameters refined from standard CeO_2 measurements, were modelled to investigate the differences in Bragg peak shapes expected from an LTO compared to a HTT structure measured on PEARL.

The (200)/(020) peak splitting expected for the structure of Mg-LBCO at 300 K has been compared to the splitting expected for the variable temperature Mg-LBCO structure with the largest degree of orthorhombicity (using lattice parameters determined from variable temperature XRD measurements at 180 K), and to the (200) peak arising from a tetragonal (HTT) structure (using lattice parameters from the 380 K measurement). The peaks are plotted in Figure 4.32 and show that while the (200) and (020) reflections arising from the anticipated

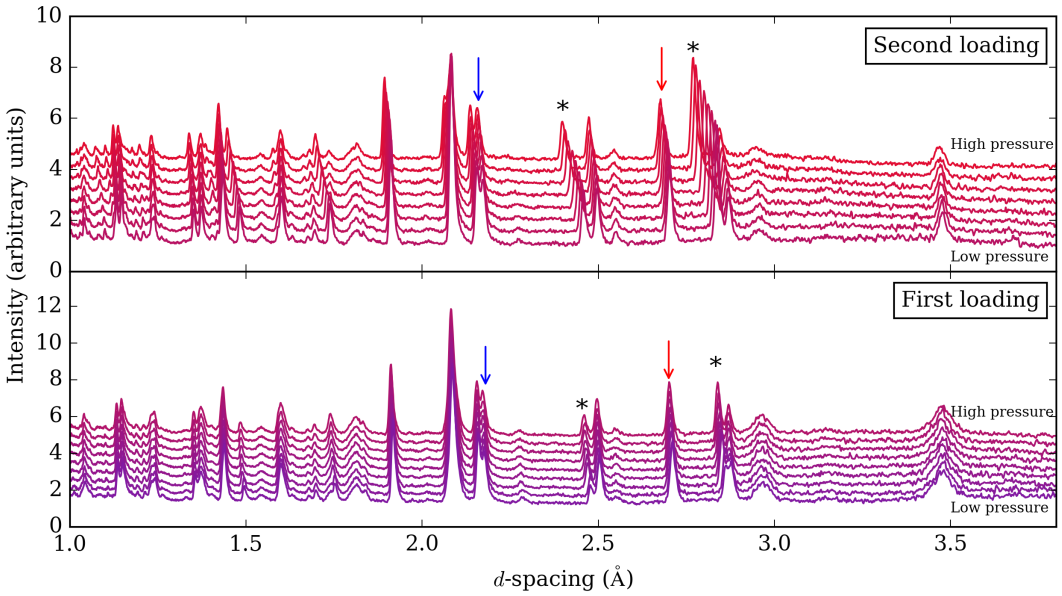

Figure 4.31: Neutron diffraction patterns of Mg-LBCO collected on the PEARL instrument, offset in the y-direction with increasing pressure. Reflections due to the lead pressure marker are indicated by asterisks, blue arrows point to the (006) peak, and red arrows point to the (200) peak.

orthorhombic structure at 300 K cannot readily be distinguished by eye, there is clear peak broadening that may originate from multiple peaks.

Assuming non-hkl dependent broadening, differences should be observed between the full width half maxima (FWHM) of (h00) peaks (of the HTT

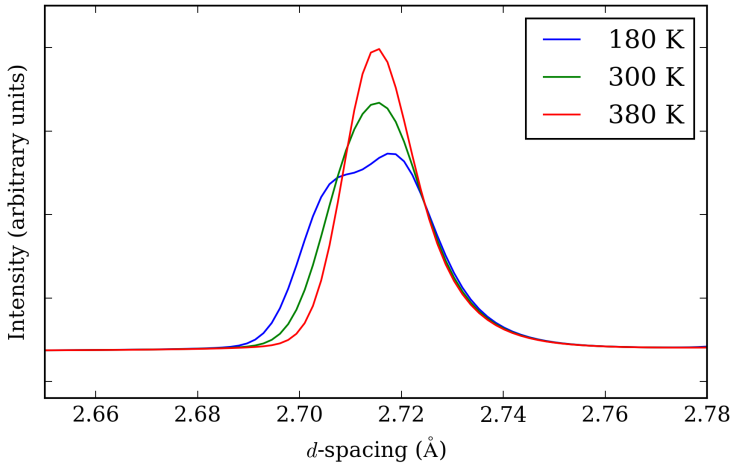

Figure 4.32: Simulated (200)/(020) peak shapes using a PEARL instrument resolution function and lattice parameters of Mg-LBCO with varying degrees of orthorhombicity ($\eta = 0.005$, 0.003 and 0.000 for measurements at 180, 300, and 380 K respectively).

structure)—where broadening due to orthorhombicity is expected—and (00l) peaks which are independent of changes to the a and b lattice parameters. Therefore, potential peak broadening—indicative of (200)/(020) peak splitting—was investigated by comparing the FWHM of pseudo-Voigt functions, implemented in TOPAS, fitted to the (200) reflection (indicated by the red arrow in Figure 4.31), to the FWHM of the (006) reflection (indicated by the blue arrow in Figure 4.31). It was necessary to fit both the (115) and (006) peaks due to peak overlap, but these are clearly distinct from each other.

The measured FWHM of the (200) and (006) peaks, as a function of pressure, are plotted in Figure 4.33. Although there are differences in the FWHM within the pressure region 0.1–1.5 GPa compared to the higher pressure values, there is no significant broadening of the (200) peak relative to the (006) peak at the pressures measured up to 5.752(7) GPa. More notably, the peak shape parameter values of the peaks measured at the lowest pressure, ca. 0.12 GPa are within error of each other. Analysis of the peak shape parameters found at the lowest measured pressure of the first loading (0.01(8) GPa) confirmed the same result. The low errors on the pressure values are likely underestimated due to

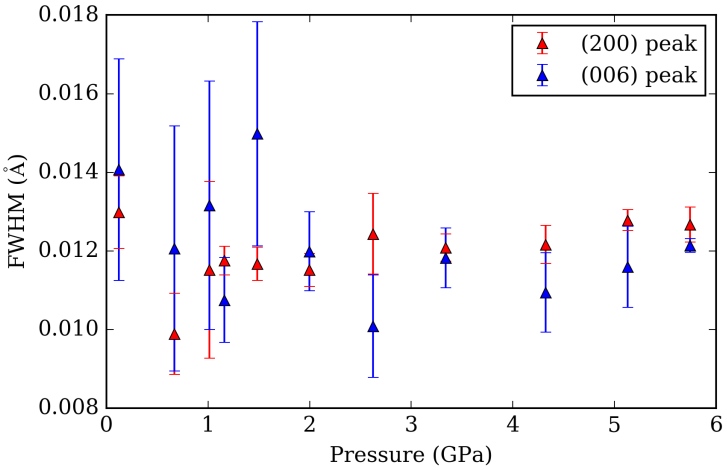

Figure 4.33: Plots of pressure-dependent FWHM of fitted pseudo-Voigt functions, implemented in TOPAS, to the (200) and (006) diffraction peaks.

unaccounted-for errors in alignment of the PE press and therefore it is possible the the pressures applied to the sample were in reality slightly higher. Nevertheless, these results suggest that the application of a small amount of pressure can be used to drive the LTO phase towards the HTT phase. In addition, the small differences in variable-temperature lattice parameters observed by the XRD experiment suggest that applying pressure can produce a more drastic effect on the unit cell and that the LTO phase observed at ambient temperature exists over a very small pressure region within the phase diagram.

The low pressure phase transition of Mg-LBCO means that the compressibility and structural behaviour in the high-pressure HTT phase can be compared directly to that of LBCO. The variable-pressure diffraction patterns were fitted with the HTT structure, which again provided good fits up to the highest pressure

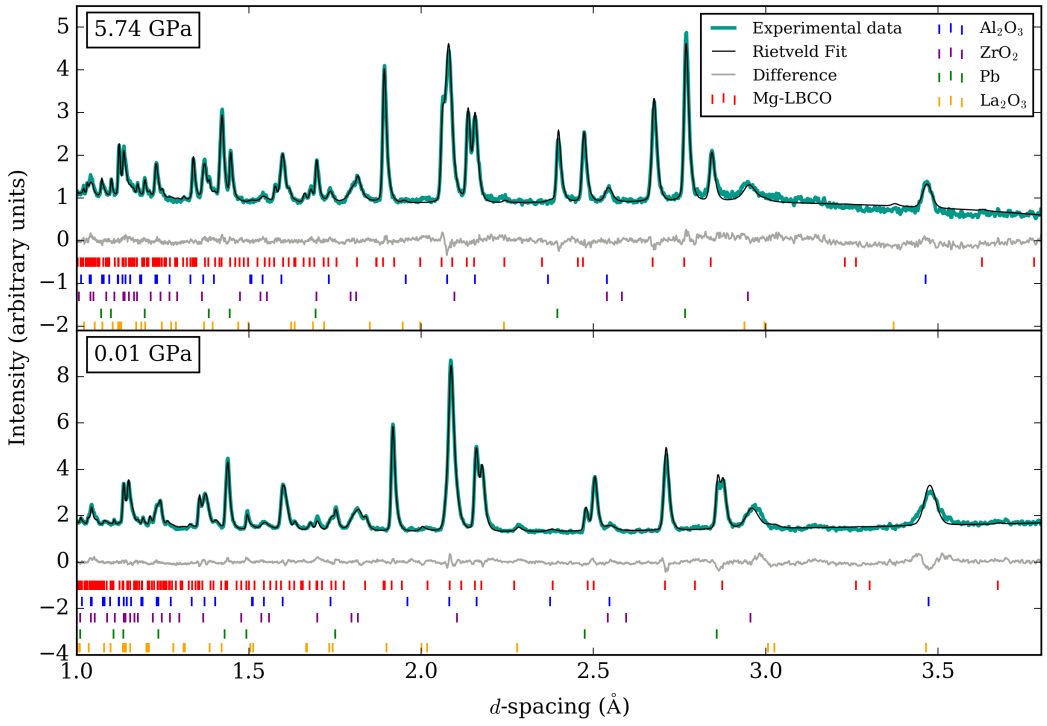

Figure 4.34: Rietveld fits of the lowest and highest pressure measurements of Mg-LBCO. The Mg-LBCO peaks were fitted using the HTT structure and all remaining peaks were fitted using Al_2O_3 and ZrO_2 phases to account for scattering from the anvils, or a Pb pressure marker phase. A small amount of La_2O_3 impurity was found.

measured (ca. 5.74 GPa). The Rietveld fits for the lowest and highest pressure measurements are shown in Figure 4.34. An additional peak at $d = 2.28$ Å, which was not attributed to sample or environment scattering, was found to be due to a small impurity phase of La_2O_3—a reactant material used in the solid-state synthesis of the sample.

4.6.3 Comparison of high-pressure behaviour

Figure 4.35 shows the unit cell volume (V) of LBCO and Mg-LBCO as a function of pressure. The volume compresses smoothly and the HTT structure is found to be stable up to pressures of at least ca. 6 GPa for both samples.

The EoS of ambient temperature LBCO and Mg-LBCO was determined, by fitting a third order BM EoS using the EoSfit software.[52,53] The resulting values are reported in Table 4.9. The bulk modulus B_0 of 142.2 GPa found for LBCO reflects a relatively incompressible structure (Ni and MgO with $K_0 = 177$ and 180 GPa were studied in Chapter 2 in part for their hardness). The linear compressibilites (κ) of the a and c lattice directions were calculated, using the program PASCal,[54] and determined to be $\kappa_a = 2.123(9)$ TPa^{-1} and $\kappa_c = 2.000(9)$ TPa^{-1}

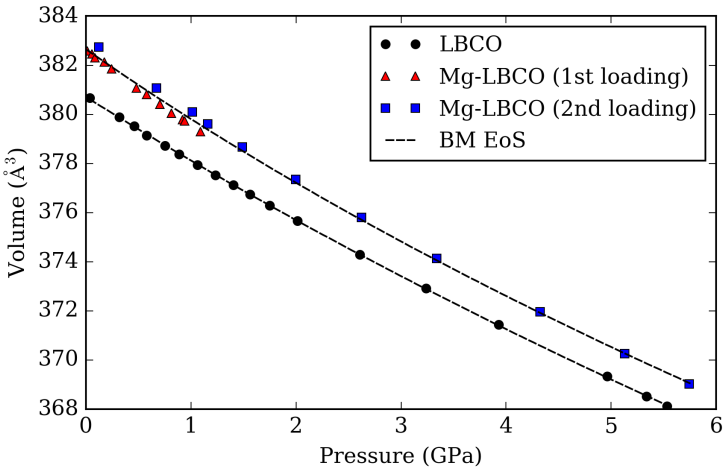

Figure 4.35: The unit cell volume of LBCO and Mg-LBCO as a function of pressure at ambient temperature. Dashed lines show the fits of the data to a third order BM equation of state. The calculated BM parameters for LBCO and Mg-LBCO are reported in Table 4.9.

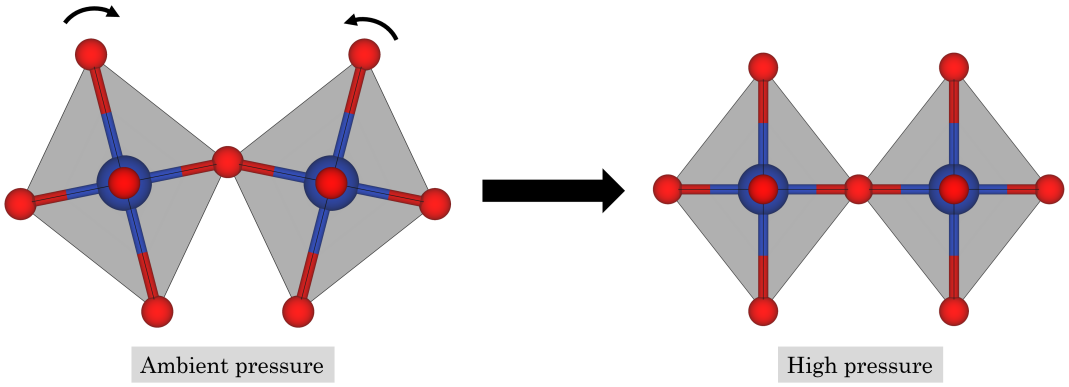

Figure 4.36: A schematic of the reduction of local octahedra rotation, induced by increased hydrostatic pressure.

showing that the *a*-axis is slightly more compressible than the *c*-axis. This is surprising since the JT distortion of the CuO_6 and longer Cu–O bonds along the *c*-direction might be expected to result in a higher compressibility. The increased compressibility in the *a*-direction is therefore rationalised by considering the potential disordered and dynamic arrangement of octahedra tilted away from the *c*-direction, observed by PDFs of the HTT LBCO structure. Increased pressure is expected to result in a reduction in a dynamic distortion (Figure 4.36), as electrostatic interactions increasingly favour aligned octahedra and the local and average structures become increasingly similar. The slight difference in *a*- and *c*-direction compressibilities is therefore thought to be due to the rotation of rigid octahedra—a similar effect has been observed in the isostructural system $La_{1.48}Nd_{0.4}Sr_{0.12}CuO_4$.[55]

Table 4.9: BM coefficients for LBCO and Mg-substituted LBCO.

Mg content (y)	B_0 (GPa)	B' (GPa)	V_0 (Å^3)
0.0	142.2076	9.0852	380.7106
0.5 (1st loading)	113.7439	18.978	382.6481
0.5 (2nd loading)	118.7138	14.4900	383.1270
0.5 (combined)	128.1451	12.4417	382.6514

For Mg-LBCO, measurements were carried out over two loadings so individual EoS's were calculated as well as a 'combined' EoS for all data. The calculated

bulk moduli vary quite significantly, highlighting the importance of measuring data over a wide range of pressures. The largest of the three calculated B_0 (the 'combined' value) is smaller than that of the value reported for LBCO, suggesting that Mg-LBCO is more compressible. The calculated linear compressibilities were calculated to be $\kappa_a = 2.74(12)$ KPa^{-1} and $\kappa_c = 1.71(6)$ KPa^{-1} showing that compared to LBCO, Mg-LBCO is more compressible in the a-direction and less compressible in the c-direction. The reduction in anisotropy of the a- and c-direction compressibilities between the LBCO and Mg-LBCO is due to the replacement of JT-distorted CuO_6 octahedra for MgO_6 octahedra with six equal Mg–O bond lengths, such that the average equatorial B–O bond length is longer and the apical length is shorter.

The smaller bulk modulus of Mg-LBCO in the HTT phase additionally supports a model of a dynamic soft mode of rotated Cu/MgO_6 octahedra with increased rotation magnitude compared to LBCO. In this model, the compressibility of Mg-LBCO is enhanced by a larger range in motion of the Cu/MgO_6 octahedra which can therefore be compressed more than LBCO, where the disordered rotation magnitude is found to be smaller.

More fundamentally, the EoS of the previously unreported Mg-LBCO structure would now allow high pressure measurements to be carried out without a pressure marker—a particularly important consideration for future local structure measurements. Such measurements would prove valuable in determining whether the compressibility of Mg-LBCO in the HTT phase can be ascribed to increased octahedral rotation over short correlation lengths.

4.7 Conclusions

Solid-state synthesis of a novel Mg-substituted LBCO series and subsequent structural analysis has provided insight into the appearance of the anomalous LTT phase in LBCO. Variable-temperature XRD analysis of the average structure of Mg-substituted LBCO revealed a stabilisation of the LTT and LTO phases with increased Mg-content. Rotation angles of the Cu/MgO_6 octahedra calculated from constrained oxygen distortions suggests that increased Mg content also results in a larger average rotation magnitude.

Systematic testing of two-phase LTT and LTO models over the first-order low temperature phase transition has shown that the pronounced phase coexistence observed for LBCO can be suppressed through the substitution of Cu for Mg. This holds significance for revealing the origin of the suppressed superconductivity in LBCO and suggests that there is an intrinsic coupling between the phase coexistence disorder and anomalous suppression of functionality.

Investigation of the local structure *via* X-ray PDF measurements has revealed a HTT phase of LBCO and Mg-substituted LBCO with dynamic rotation of Cu/MgO_6 octahedra, however its not clear if or how much these deviate from what would be expected of soft phonon modes of this character within the harmonic approximation. Small-box modelling of only the shortest atom–atom distances such that octahedral rotation correlations are not considered shows a slight preference for an LTO-type local structure. Further measurements using neutron instruments, capable of a larger Q_{max}, might enable distinct Mg–O and Cu–O distances to be resolved, and variable temperature experiments would reveal how the structure evolves throughout the phase transitions identified through average structure measurements.

High-pressure average structure measurements have shown that the LTO-to-HTT phase transition is driven by pressures of <0.1 GPa, showing that the LTO

phase is much more stable with respect to temperature than pressure. The comparison of LBCO and Mg-substituted LBCO compressibilities has revealed that Mg substitution results in a more compressible *a*-lattice direction and a less compressible *c*-direction (compared to LBCO). This is due to a hardening of the average apical Cu/Mg–O bond relative to the equatorial Cu/Mg–O bond, and reflects the type of structural properties that may be designed through cation substitution.

4.8 References

[1] D. van Delft and P. Kes, *Phys. Today*, 2010, **63**, 38–42.

[2] J. G. Bednorz and K. A. Müller, *Z. Phys. B. Con. Mat.*, 1986, **64**, 189–193.

[3] R. J. Cava, R. B. van Dover, B. Batlogg and E. A. Rietman, *Phys. Rev. Lett.*, 1987, **58**, 408–410.

[4] E. Takayama-Muromachi, Y. Uchida, M. Ishii, T. Tanaka and K. Kato, *Jpn. J. Appl. Phys.*, 1987, **26**, 1156–1158.

[5] A. Schilling, O. Jeandupeux, S. Büchi, H. R. Ott and C. Rossel, *Phys. C*, 1994, **235-240**, 229–232.

[6] B. Shen, Y. Öztürk, W. Wu, L. Lu, J. Sheng, Z. Huang, Y. Zhai, Y. Yuan, W. Wang, J. Yin, D. Menon, A. Ercole, A. Carpenter, T. Painter, C. Li, J. Gawith, J. Ma, J. Yang, M. Parizh and T. Coombs, *IEEE Trans. Appl. Supercond.*, 2020, **30**, 1–5.

[7] T. C. Cosmus and M. Parizh, *IEEE Trans. Appl. Supercond.*, 2011, **21**, 2104–2109.

[8] L. Bromberg, M. Tekula, L. A. El-Guebaly and R. Miller, *Fusion Eng. Des.*, 2001, **54**, 167–180.

[9] A. R. Moodenbaugh, Y. Xu, M. Suenaga, T. J. Folkerts and R. N. Shelton, *Phys. Rev. B*, 1988, **38**, 4596.

[10] M. Hücker, M. V. Zimmermann, G. D. Gu, Z. J. Xu, J. S. Wen, G. Xu, H. J. Kang, A. Zheludev and J. M. Tranquada, *Phys. Rev. B*, 2011, **83**, 41–50.

[11] J. M. Tranquada, *Adv. Phys.*, 2020, **69**, 437–509.

[12] J. M. Tranquada, M. P. Dean and Q. Li, *J. Phys. Soc. Japan*, 2021, **90**, 111002.

[13] J. D. Axe and M. K. Crawford, *J. Low Temp. Phys.*, 1994, **95**, 271–284.

[14] T. A. Assefa, Y. Cao, J. Diao, R. J. Harder, W. Cha, K. Kisslinger, G. D. Gu, J. M. Tranquada, M. P. Dean and I. K. Robinson, *Phys. Rev. B*, 2020, **101**, 054104.

[15] X. M. Chen, C. Mazzoli, Y. Cao, V. Thampy, A. M. Barbour, W. Hu, M. Lu, T. A. Assefa, H. Miao, G. Fabbris, G. D. Gu, J. M. Tranquada, M. P. Dean, S. B. Wilkins and I. K. Robinson, *Nat. Commun.*, 2019, **10**, 1435.

[16] J. D. Axe, A. H. Moudden, D. Hohlwein, D. E. Cox, K. M. Mohanty, A. R. Moodenbaugh and Y. Xu, *Phys. Rev. Lett.*, 1989, **62**, 2751–2754.

[17] J. M. Tranquada, B. J. Sternlieb, J. D. Axe, Y. Nakamura and S. Uchida, *Nature*, 1995, **375**, 561–563.

[18] M. Fujita, H. Goka, K. Yamada, J. M. Tranquada and L. P. Regnault, *Phys. Rev. B*, 2004, **70**, 104517.

[19] E. Berg, E. Fradkin, S. A. Kivelson and J. M. Tranquada, *New J. Phys.*, 2009, **11**, 115004.

[20] A. Himeda, T. Kato and M. Ogata, *Phys. Rev. Lett.*, 2002, **88**, 117001.

[21] M. Braden, M. Meven, W. Reichardt, L. Pintschovius, M. T. Fernandez-Diaz, G. Heger, F. Nakamura and T. Fujita, *Phys. Rev. B*, 2001, **63**, 140510.

[22] M. Hücker, M. V. Zimmermann, M. Debessai, J. S. Schilling, J. M. Tranquada and G. D. Gu, *Phys. Rev. Lett.*, 2010, **104**, 057004.

[23] E. S. Božin, S. J. Billinge, G. H. Kwei and H. Takagi, *Phys. Rev. B*, 1999, **59**, 4445–4454.

[24] S. J. Billinge, G. H. Kwei and H. Takagi, *Phys. Rev. Lett.*, 1994, **72**, 2282–2285.

[25] D. Haskel, E. Stern and F. Dogan, *Phys. Rev. B*, 2000, **61**, 7055–7076.

[26] M. K. Crawford, R. L. Harlow, E. M. McCarron, W. E. Farneth, J. D. Axe, H. Chou and Q. Huang, *Phys. Rev. B*, 1991, **44**, 7749–7752.

[27] T. Park, E. Park, H. Lee, T. Klimczuk, E. D. Bauer, F. Ronning and J. D. Thompson, *J. Phys. Condens. Matter*, 2008, **20**, 322204.

[28] T. Yamauchi, Y. Ueda and N. Môri, *Phys. Rev. Lett.*, 2002, **89**, 057002.

[29] A. Yamamoto, N. Takeshita, C. Terakura and Y. Tokura, *Nat. Commun.*, 2015, **6**, 8990.

[30] C. W. Chu, P. H. Hor, R. L. Meng, L. Gao, Z. J. Huang and Y. Q. Wang, *Phys. Rev. Lett.*, 1987, **58**, 405–407.

[31] N. Yamada and M. Ido, *Phys. C*, 1992, **203**, 240–246.

[32] M. Hücker, *Phys. C*, 2012, **481**, 3–14.

[33] J. P. Attfield, *Chem. Mater.*, 1998, **10**, 3239–3248.

[34] R. D. Shannon, *Acta Crystallogr. Sect. A*, 1976, **32**, 751–767.

[35] A. K. Soper and E. R. Barney, *J. Appl. Crystallogr.*, 2011, **44**, 714–726.

[36] A. A. Coelho, *J. Appl. Crystallogr.*, 2018, **51**, 210–218.

[37] M. G. Tucker, D. A. Keen, M. T. Dove, A. L. Goodwin and Q. Hui, *J. Phys. Condens. Matter*, 2007, **19**, 335218.

[38] C. L. Bull, N. P. Funnell, M. G. Tucker, S. Hull, D. J. Francis and W. G. Marshall, *High Press. Res.*, 2016, **36**, 493–511.

[39] W. G. Marshall and D. J. Francis, *J. Appl. Crystallogr.*, 2002, **35**, 122–125.

[40] S. Klotz, J. C. Chervin, P. Munsch and G. Le Marchand, *J. Phys. D. Appl. Phys.*, 2009, **42**, 075413.

[41] O. Arnold, J. C. Bilheux, J. M. Borreguero, A. Buts, S. I. Campbell, L. Chapon, M. Doucet, N. Draper, R. Ferraz Leal, M. A. Gigg, V. E. Lynch, A. Markvardsen, D. J. Mikkelson, R. L. Mikkelson, R. Miller, K. Palmen, P. Parker, G. Passos, T. G. Perring, P. F. Peterson, S. Ren, M. A. Reuter, A. T. Savici, J. W. Taylor, R. J. Taylor, R. Tolchenov, W. Zhou and J. Zikovsky, *Nucl. Instruments Methods Phys. Res. Sect. A Accel. Spectrometers, Detect. Assoc. Equip.*, 2014, **764**, 156–166.

[42] B. J. Campbell, H. T. Stokes, D. E. Tanner and D. M. Hatch, *J. Appl. Crystallogr.*, 2006, **39**, 607–614.

[43] P. W. Stephens, *J. Appl. Crystallogr.*, 1999, **32**, 281–289.

[44] M. T. Dove, *Am. Mineral.*, 1997, **82**, 213–244.

[45] S. J. Billinge and P. M. Duxbury, *Phys. Rev. B*, 2002, **66**, 064529.

[46] J. H. Van Vleck, *J. Chem. Phys.*, 1939, **7**, 72–84.

[47] S. Katano, J. A. Fernandez-Baca, S. Funahashi, N. Mori, Y. Ueda and K. Koga, *Phys. C*, 1993, **214**, 65–72.

[48] T. A. Bird, A. Herlihy and M. S. Senn, *J. Appl. Crystallogr.*, 2021, **54**, 1514–1520.

[49] E. S. Bozin, R. Zhong, K. R. Knox, G. Gu, J. P. Hill, J. M. Tranquada and S. J. L. Billinge, *Phys. Rev. B*, 2015, **91**, 054521.

[50] A. Herlihy, T. A. Bird, C. J. Ridley, C. L. Bull, N. P. Funnell and M. S. Senn, *PRB*, 2022, **105**, 094114.

[51] C. M. Culbertson, A. T. Flak, M. Yatskin, P. H. Cheong, D. P. Cann and M. R. Dolgos, *Sci. Rep.*, 2020, **10**, 3729.

[52] J. Gonzalez-Platas, M. Alvaro, F. Nestola and R. Angel, *J. Appl. Crystallogr.*, 2016, **49**, 1377–1382.

[53] R. J. Angel, J. Gonzalez-Platas and M. Alvaro, *Z. Kristallogr. Cryst. Mater.*, 2014, **229**, 405–419.

[54] M. J. Cliffe and A. L. Goodwin, *J. Appl. Crystallogr.*, 2012, **45**, 1321–1329.

[55] G. Fabbris, *Ph.D. thesis*, Tuning Electronic Correlation with Pressure, Washington University in St. Louis, 2014.

Chapter 5

Conclusions and future work

The work reported in this Thesis is focussed on tuning the atomic structure of functional solid oxide materials, where the average and local structures have been manipulated using temperature, pressure, and/or chemical composition. Exploration of the structures of functional crystalline materials has historically relied on conventional crystallographic measurements, which provide a useful, but also limited, time-averaged interpretation of the structure. The technique of total scattering provides a method of simultaneously accounting for correlations over short and long-range length scales, and its value for studying crystalline structures exhibiting disorder is increasingly appreciated within the solid-state community.[1–5] The structural studies of perovskite and Ruddlesden-Popper solid oxides presented in Chapters 3 and 4 exemplify the types of order-disorder and displacive phase transitions respectively that can be better understood by considering their local structures. The former Chapter reports a cross-over from order-disorder, to displacive behaviour in $BaTiO_3$ that has not yet been fully appreciated despite decades of study of the well-known perovskite material, and, highlights the contrasting behaviour of temperature *versus* pressure-induced phase behaviour.

A particularly useful tool for exploring the structure of functional materials is pressure, where small changes in pressure can induce significant structural change. For example, the pressure-induced volume difference of LBCO observed in Chapter 4 was 4.3× the change induced by temperatures of 10–400 K. This provides scope to tune materials across a broad range of previously unexplored phases and symmetries, and gives further insight into structure-property relationships. Combining neutron total scattering and high-pressure techniques of crystalline materials has previously been limited to non-hydrostatic conditions, where a pressure transmitting medium has been omitted. It is envisaged that the correction procedure described in Chapter 2 will allow future users of PEARL to perform high-pressure local structure measurements at *hydrostatic* pressure using

the commonly used medium, methanol:ethanol.

The Fortran routine for correcting PDFs requires minimal input from users such as measured pressure and fitting ranges. The routine is currently specific to a ME PTM although other types of media are often required where the solubility of the sample is incompatible with ME. The advantage of the approach outlined in Chapter 2 is that the methods by which the ME PDFs have been parameterised can, in principle, be straightforwardly applied to other systems. Therefore other PTMs such as pentane mixtures may be modelled using the same empirical function approach as applied to ME.

The study of α-quartz and the resulting reverse Monte Carlo models, refined against corrected PDFs, represents the first scientific results derived from hydrostatic local structure measurements on PEARL, where Si–O–Si bond angle compressibilities were extracted. The difference in angle distribution compared with previous work in a non-hydrostatic environment further highlights the importance of using a PTM for measuring the local structure of crystalline materials. Further work is required in order to extend this approach to more complex and compressible systems, but the study of α-quartz provides a representative example of the types of flexible structural systems that would be suited to this type of experiment.

Previous neutron total scattering measurements of $BaTiO_3$ have shown that the temperature-induced ferroelectric tetragonal-to-cubic phase transition at T_C is of the order-disorder type and can be attributed to correlated, local, rhombohedral distortions below T_C. The application of judicious constraints to symmetry-motivated distortions allowed the behaviour of high-pressure $BaTiO_3$ to be interrogated over multiple length-scales, extracting information that otherwise would not have been apparent using more simplistic models. A phase transition better described by the harmonic approximation was identified through comparison

of rhombohedral, tetragonal and cubic local distortions over different ranges of the PDF, and highlighted the importance of considering the information encoded within different lengths-scales of the PDF.

There is perhaps further insight to be gained by performing high pressure total scattering experiments on $BaTiO_3$ up to 10 GPa in order to explore the literature suggestion that a local distortion persists up to these pressures. The successes of the local structure measurements reported in Chapter 3 have shown that the limited Q_{max} available on the PEARL instrument is sufficient for probing the magnitude and direction of local distortions. Is is noteworthy that, despite decades of study, there are still novel discoveries to be made as experimental capabilities are developed.

The microscopically-driven order-disorder phase transition of $BaTiO_3$ where local distortions of Ti and O atoms are coupled with neighbouring atoms contrasts with the macroscopically-driven disorder found in LBCO. In this case, the study reported in Chapter 4 has identified that a phase coexistence of the LTT and LTO average structures below the low temperature first order phase transition can be suppressed through chemical substitution. The substitution of Mg^{2+} for JT-active Cu^{2+} additionally stabilises the low temperature phases; the introduction of MgO_6 octahedra with shorter apical bonds and longer equatorial bonds, compared with CuO_6, results in a structure predisposed toward the octahedral rotations present in the LTT and LTO phases. The disappearance of the low temperature phase coexistence—which is otherwise observed in the parent LBCO compound—when Cu is replaced by Mg, suggests that it plays an important role in the anomalous suppression of superconductivity in the LBCO material. It would be interesting to perform physical property measurements on LBCO and the Mg-LBCO series to see if the physical properties can be reconciled with structural observations.

X-ray PDFs measured from LBCO and Mg-substituted LBCO samples suggested that the local structure of the HTT phase is comprised of anharmonic, dynamic rotations of the Cu/MgO_6 octahedra. Although this type of structure with significant, apparently-uncorrelated disorder is challenging to model, carefully-constrained and symmetry-motivated modelling again can extract meaningful information about structures with significant disorder. In this case, modelling has revealed a mode softening of the X_3^+-type distortion as the HTT-to-LTO phase transition is approached.

A high-pressure study of the average structures of LBCO and Mg-substituted LBCO showed that the ambient temperature LTO-to-HTT phase transition of Mg-LBCO occurs at pressures as low as <0.1 GPa and that the transition is facilitated by pressure to a greater extent than temperature. Further investigation of the pressure-temperature phase diagram of Mg-substituted LBCO could be achieved by low-temperature, high-pressure measurements and allow for additional comparison of the structural behaviour of LBCO *versus* Mg-substituted LBCO.

It would be interesting to explore the influence of enhanced sensitivity to the oxygen positions using the scattering contrast offered by neutrons and instruments such as GEM or POLARIS at ISIS. The increased PDF resolution and peak intensity of the lighter atoms would perhaps allow the distinction of such atom–atom distances and more robust modelling. Variable temperature measurements across all LTT, LTO, and HTT phases would also show how the local environment evolves as the soft rotation mode becomes frozen in.

The structural investigation of the well-known and widely-studied $BaTiO_3$ and LBCO materials, over multiple length scales, using a variety of tools to alter their structure, has provided novel insight into these functional materials. It is clear that high pressure neutron scattering will form an important emerging area

in the local structure community, where neutron experiments can provide the necessary sensitivity to lighter elements that the equivalent X-ray measurements do not.

5.1 References

[1] C. A. Young and A. L. Goodwin, *J. Mater. Chem.*, 2011, **21**, 6464–6476.

[2] X. Hua, P. K. Allan, C. Gong, P. A. Chater, E. M. Schmidt, H. S. Geddes, A. W. Robertson, P. G. Bruce and A. L. Goodwin, *Nat. Commun.*, 2021, **12**, 561.

[3] M. S. Senn, D. A. Keen, T. C. Lucas, J. A. Hriljac and A. L. Goodwin, *Phys. Rev. Lett.*, 2016, **116**, 207602.

[4] M. Scavini, M. Coduri, M. Allieta, M. Brunelli and C. Ferrero, *Chem. Mater.*, 2012, **24**, 1338–1345.

[5] D. A. Keen and A. L. Goodwin, *Nature*, 2015, **521**, 303–309.

Chapter 6

Appendix

6.1 High-pressure total scattering on PEARL

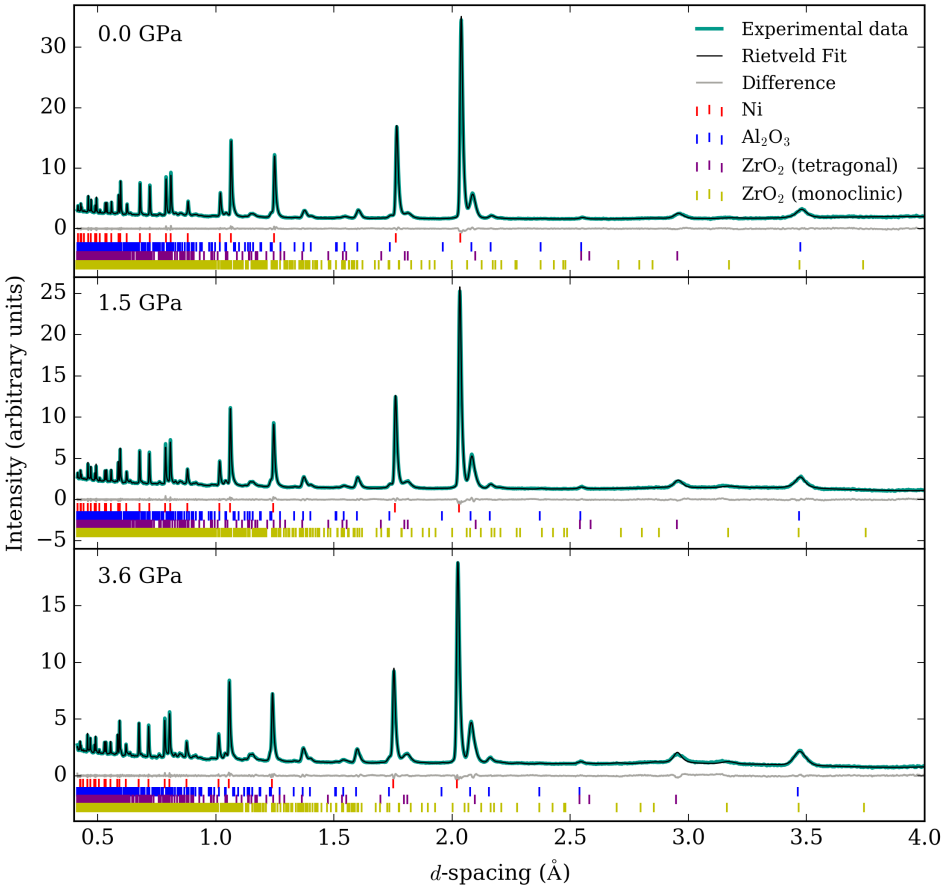

Figure 6.1: Rietveld fits to diffraction patterns of Ni measured in a Paris-Edinburgh press at pressures of 0.0, 1.5 and 3.6 GPa. Alumina and zirconia peaks are due to scattering from the ZTA anvils.

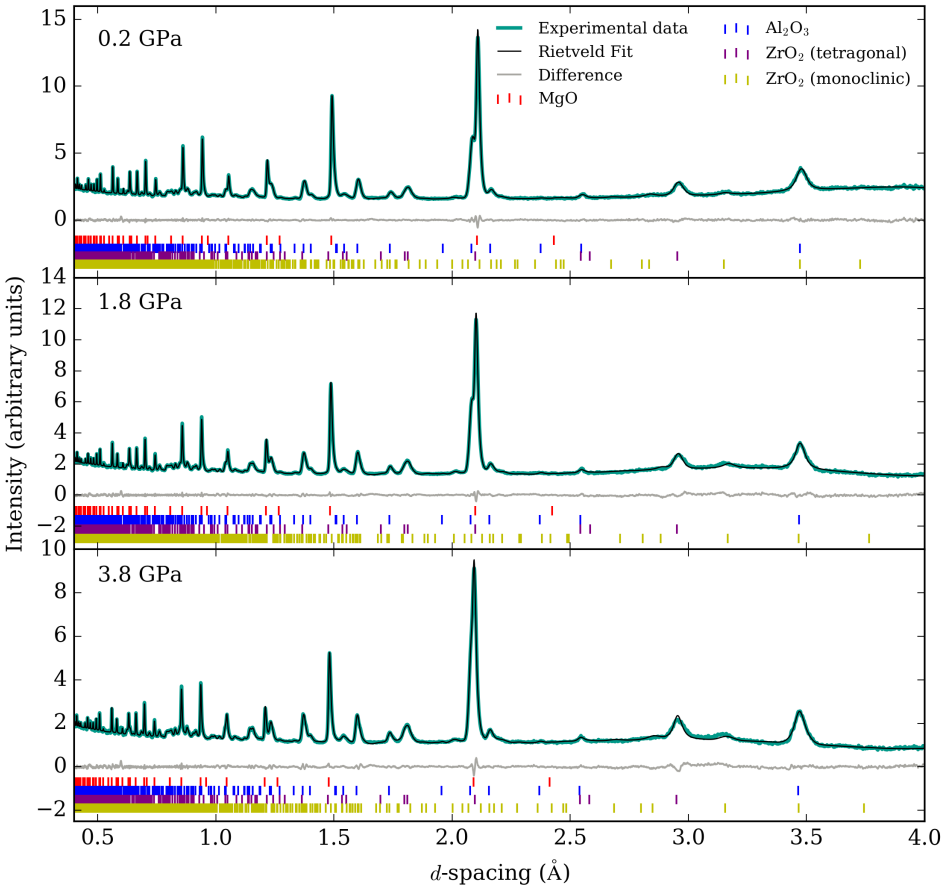

Figure 6.2: Rietveld fits to diffraction patterns of MgO measured in a Paris-Edinburgh press at pressures of 0.2, 1.8 and 3.8 GPa. Alumina and zirconia peaks are due to scattering from the ZTA anvils.

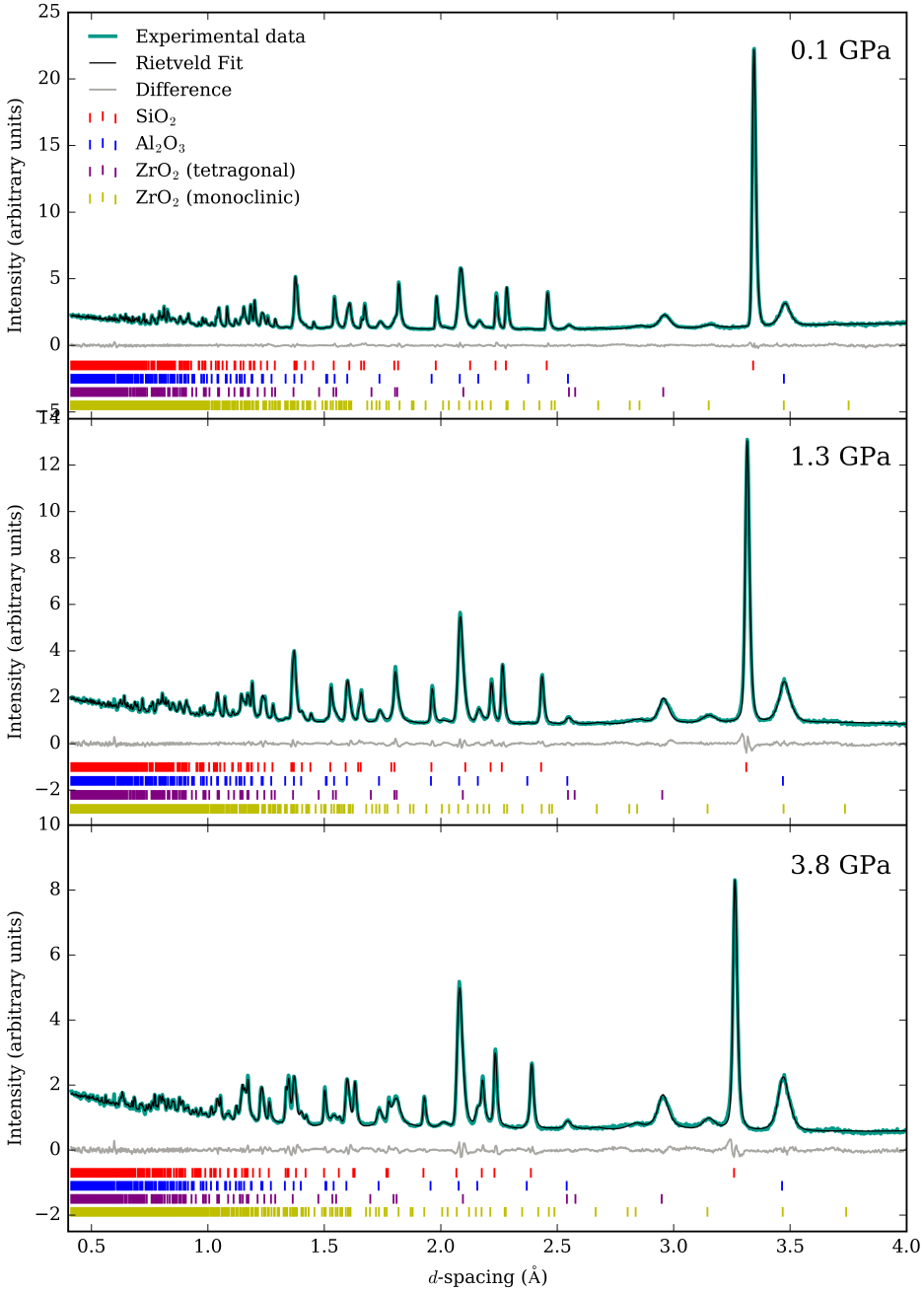

Figure 6.3: Rietveld fits to diffraction patterns of α-quartz (SiO_2) measured in a Paris-Edinburgh press at pressures of 0.1, 1.3 and 3.8 GPa. Alumina and zirconia peaks are due to scattering from the ZTA anvils.

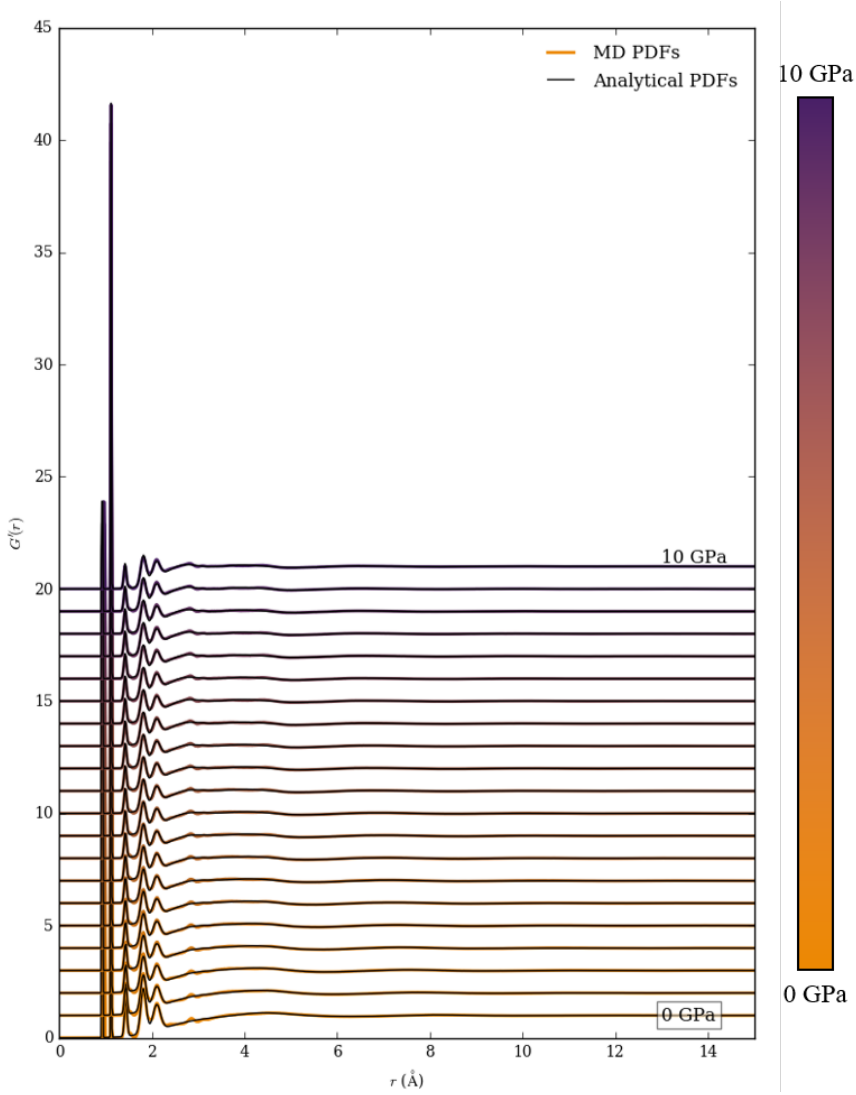

Figure 6.4: Calculated ME PDFs from each MD simulation and corresponding analytical PDFs, composed of 10 Gaussian peaks and an underlying shape function, at pressures from 0–10 GPa in steps of 0.5 GPa offset in the y-direction. The PDFs are free of any instrumental effects—particularly peak broadening which arises, primarily, because of limited instrumental Q_{max} values.

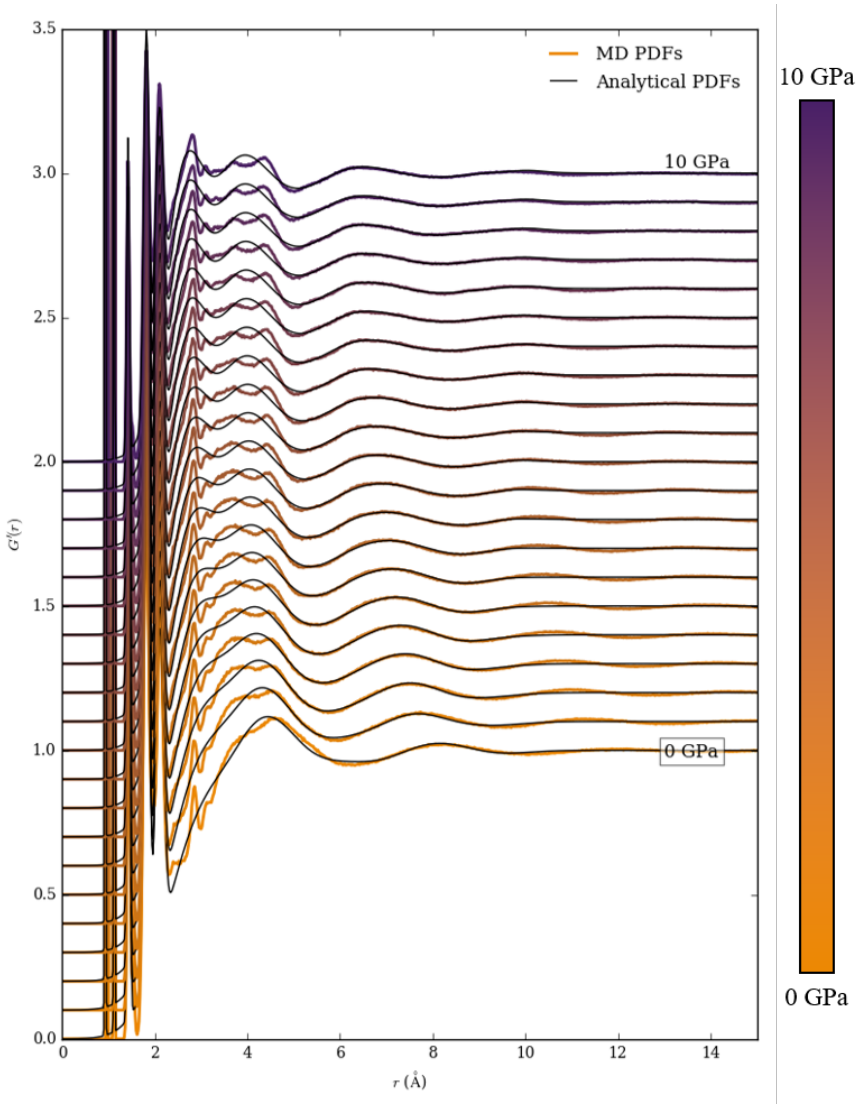

Figure 6.5: Zoomed comparison of variable pressure MD PDFs (0–10 GPa, as above).

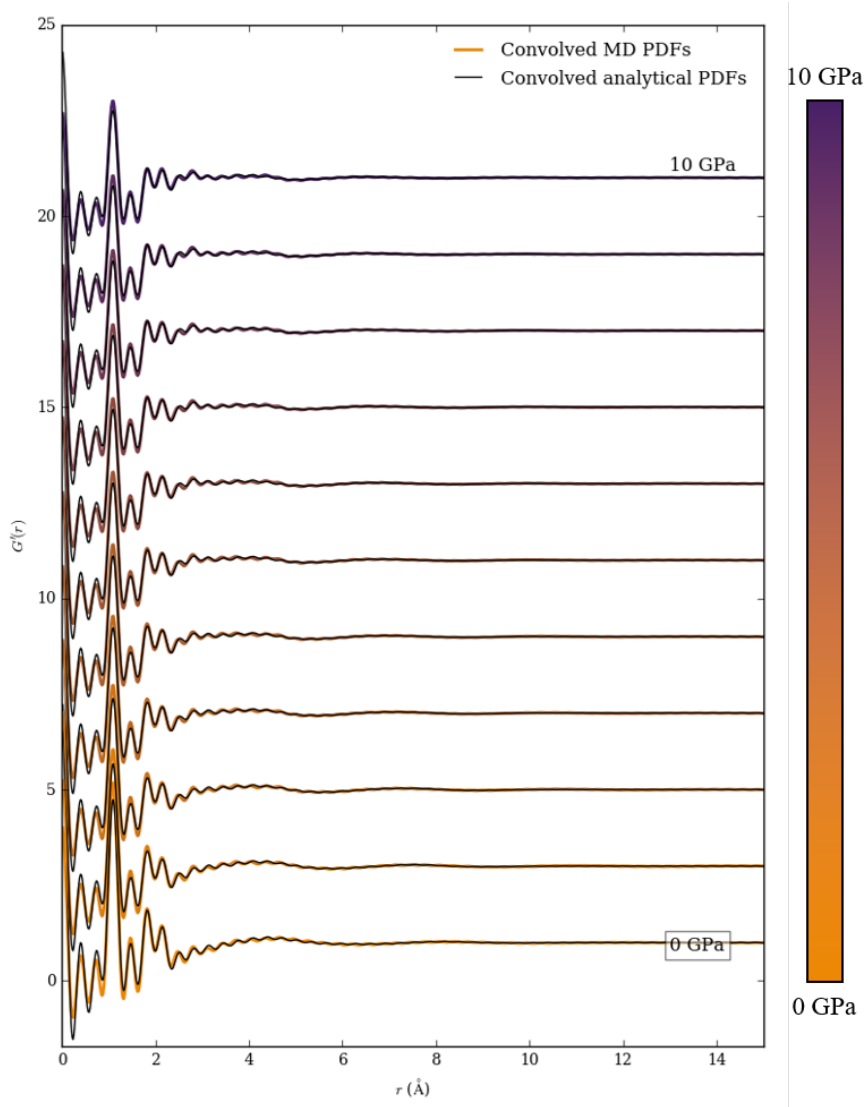

Figure 6.6: MD PDFs and analytical PDFs, convolved with $\sin(Q_{\max}/r)$, where $Q_{\max} = 20.32$ Å^{-1}. PDFs from 0–10 GPa in steps of 1 GPa are shown, offset in the y-direction.

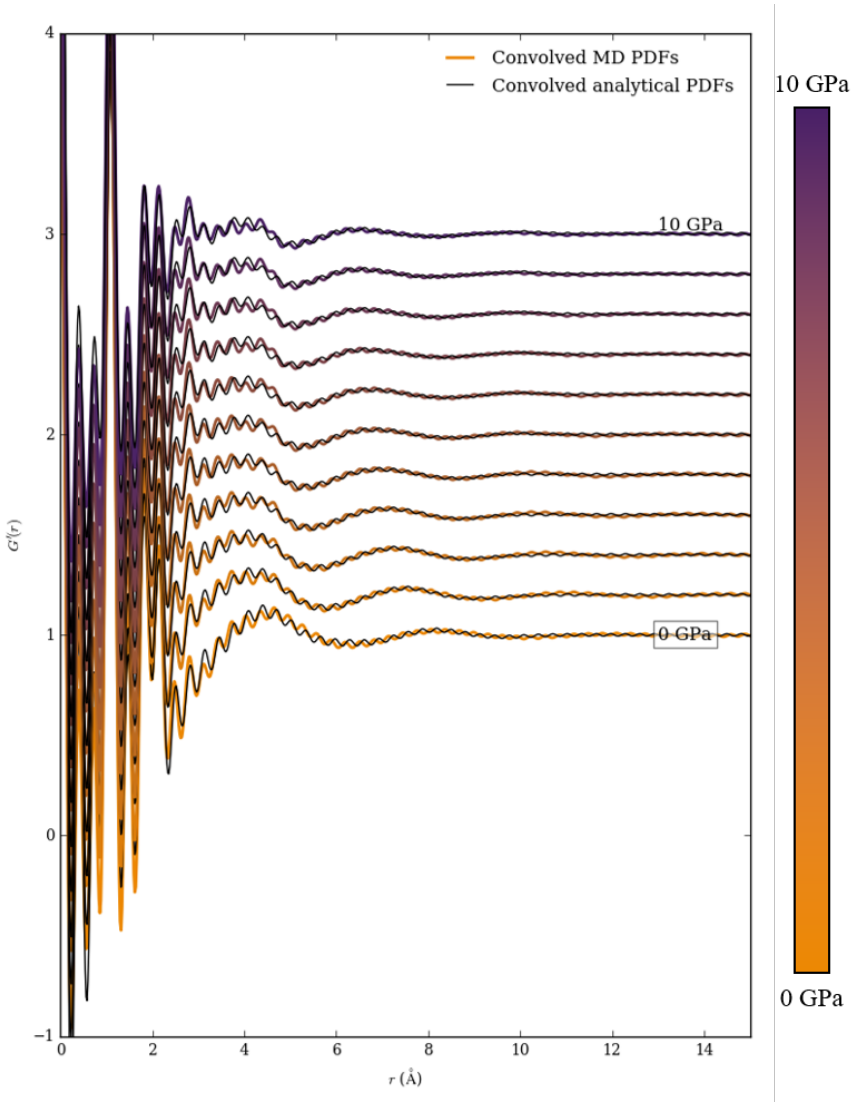

Figure 6.7: Zoomed comparison of convolved MD and analytical PDFs (0–10 GPa in steps of 1 GPa).

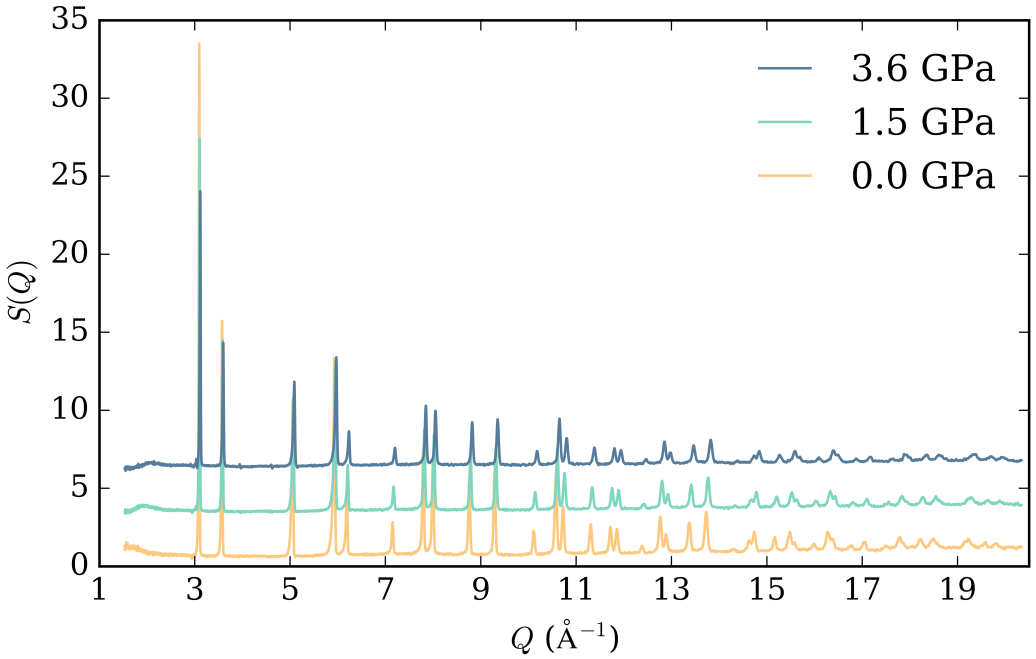

Figure 6.8: Neutron $S(Q)$ of Ni in ME at 0.0, 1.5 and 3.6 GPa offset in the y-direction.

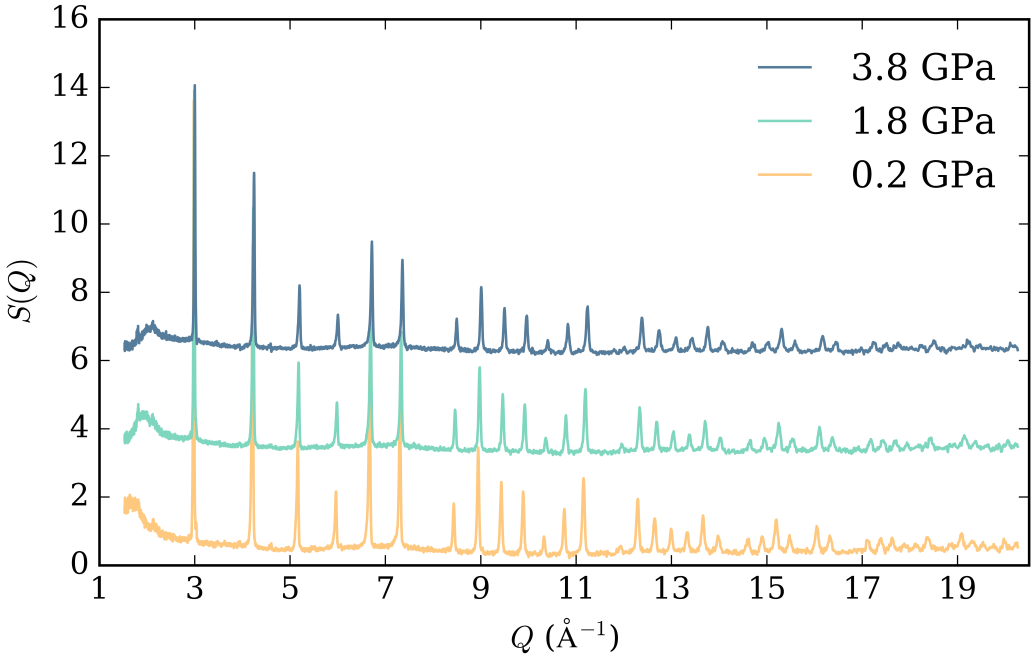

Figure 6.9: Neutron $S(Q)$ of MgO in ME at 0.2, 1.8 and 3.8 GPa offset in the y-direction.

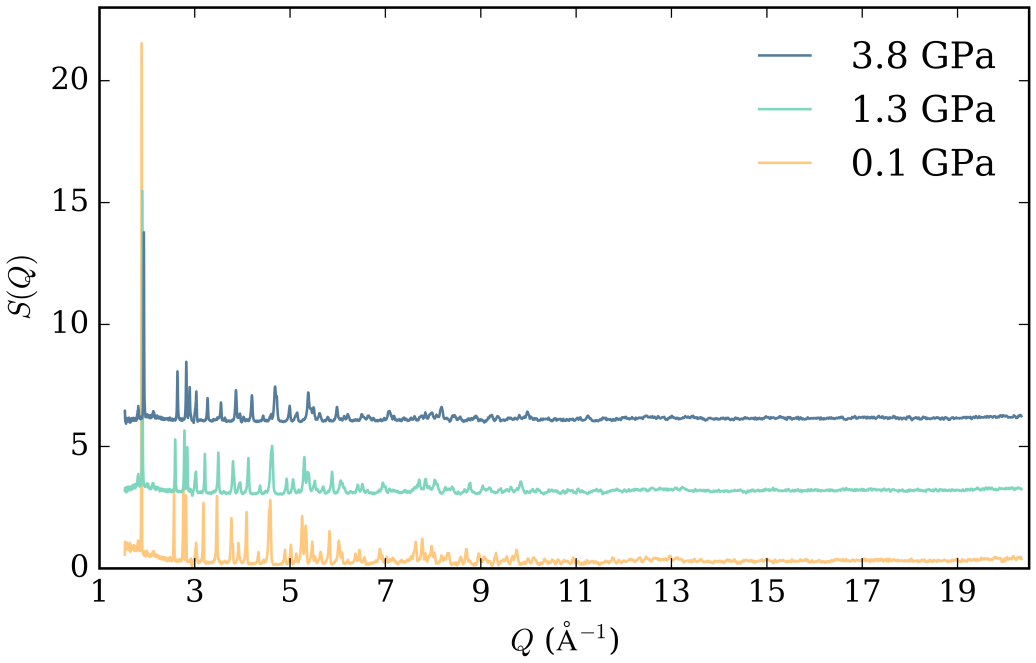

Figure 6.10: Neutron $S(Q)$ of α-quartz in ME at 0.1, 1.3 and 3.8 GPa offset in the y-direction.

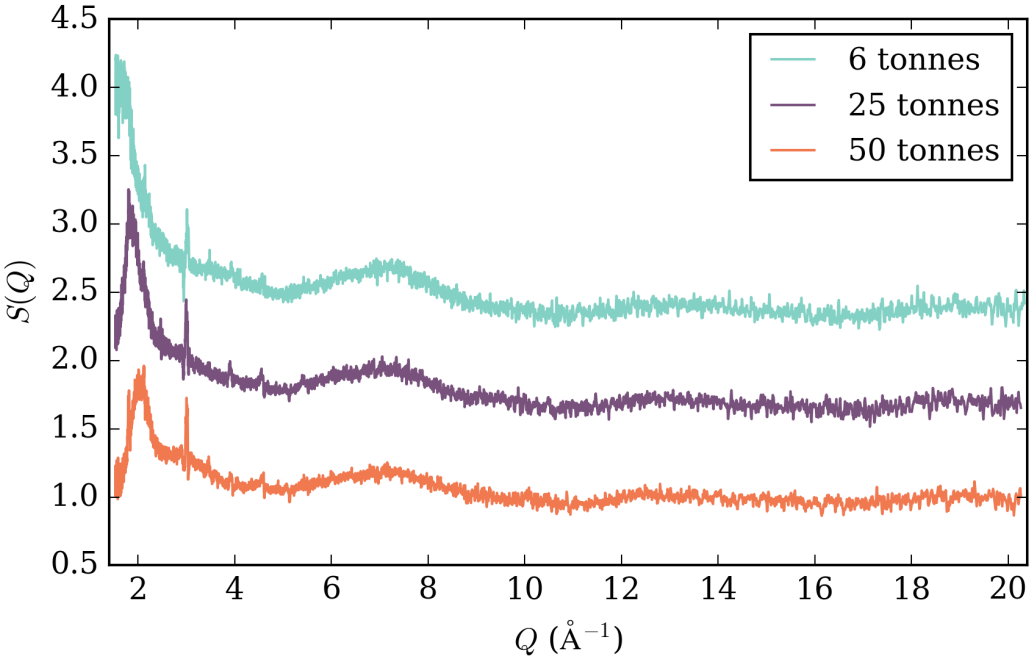

Figure 6.11: Neutron $S(Q)$ of a 4:1 deuterated methanol:ethanol mixture at applied loads of 6, 25 and 50 tonnes, offset in the y-direction.

6.1.1 RMCProfile settings

RMCProfile configurations for α-quartz were generated using $5 \times 9 \times 8$ supercells of the Rietveld-refined average structure unit cells. Eleven independent runs were performed for each pressure point, running for three days each, ensuring fit convergence. Closest approach (CA) constraints were applied between atom pairs; their respective values were informed by peak tails in the PDFs at each pressure. Additional potentials-based restraints (invariant with pressure) were used to preserve approximate tetrahedral connectivity of the SiO_4 units. The values used are given in Table 6.1 below. Angle and distance energies were unavailable for SiO_4 units in the RMCProfile manual; the values used here were informed by other similar, rigid, tetrahedral groups.

Table 6.1: Atom–atom constraints used in RMCProfile.

Atom pair	CA 0.1 GPa	CA 1.3 GPa	CA 3.8 GPa
Si–Si	2.00	2.00	2.00
Si–O	1.45	1.40	1.35
O–O	2.40	2.35	2.38
Atoms	Distance/Å	Angle/°	Energy/eV
Si–O	1.60	N/A	2.00
O–Si–O	N/A	109.5	7.60

6.1.2 Fortran90 routine

The code used for correcting for the presence of a ME PTM is reported here and can also be found online:

https://doi.org/10.1107/S1600576721009420

```
program metheth_nmf
implicit none

integer                                    :: i,j,k,l,m,n,s,nmoves,index1,index2,index3,iacc,iacc_total,cutoff,&
Acutoff,ncheck,nprm, ngaus,gauscomp,nbkgprm,nop,maxmoves,nprint,Fno
real, allocatable                          ::r(:)
real*8, allocatable                        :: D(:,:),C(:,:),H(:,:),A(:,:),A_diff(:,:),C_trial(:,:),H_trial(:,:),&
A_trial(:,:),A_diff_trial(:,:),G(:,:,:),Gpress(:,:),Gcurve(:,:),&
Gtot(:),bkgprm(:,:),bkgpress(:),bkg(:),pvalue(:),Ctot(:),z(:),dz(:),press(:),dtemp(:)
real*8                                     :: temperature,increment,incfac,tempfac,random,random2,random3,Fnorm,&
Fnorm_trial,Fdiff,prob,rmin,Crmin,dx,Armin,p0,bkgk,bkgj,rmax,Qmax,f,t,pi,temppress,Fcheck,Fcheckdiff
character (len=48)                         :: line
character (len=63)                         :: rundir,directory,datafile
character(len=8)                           :: cystring
character(len=255)                         :: cwd
character (len=1)                          :: MC,WV

call init_random_seed()

maxmoves=150000000
nprint=1000000
Fno=1000000
Fcheck=100

!------Experiment-dependent variables ------!
write(*,*) 'Enter number of pressure points:'
read(*,*)m
allocate(press(m))
```

```
do i=1,m
        write(6,'(a15,i2,a8)',advance='no') 'Enter pressure ',i, ' (GPa): '
        read(*,*) press(i)
        if (press(i)>10.0) write(*,*) '!!!ERROR!!! 10 GPa max.'
end do
write(6,'(a12)',advance='no')'Enter Qmax: '
read(*,*)Qmax
write(6,'(a12)',advance='no')'Enter rmax: '
read(*,*)rmax
write(6,'(a103)',advance='no')'Enter minimum r value to fit pure sample component to (value just '&
's below first expected sample peak): '
read(*,*)Crmin
write(*,*)'Fitting methanol:ethanol components to an rmin of 0.8 Angstroms.'
write(6,'(a37)',advance='no')'Allow individual weight values? (Y/N)'
read(*,*)WV
Armin=0.8
s=m*2
rmin=0.02
dx=0.02
cutoff=(((Crmin/dx)-(rmin/dx))+1)
Acutoff=(((Armin/dx)-(rmin/dx))+1)
n=rmax/dx

allocate(D(n,m))      !Measured PDF data
allocate(C(n,s))      !PTM + sample components
allocate(H(s,m))      !Weights
allocate(C_trial(n,s))   !Trial PTM + sample components
allocate(H_trial(s,m))   !Trial weights
allocate(A(n,m))      !Calculated fit
allocate(A_diff(n,m))    !Fit difference
allocate(A_trial(n,m))   !Trial calculated fit
allocate(A_diff_trial(n,m)) !Trial fit difference
allocate(r(n))   !x values of measured data
allocate(dtemp(n))
```

```
!------Info for building metheth PDFs------!
pi=3.14159265
ngaus=10
nprm=2
gauscomp=3
nbkgprm=2
nop=4

allocate(G(ngaus,nprm,gauscomp))
allocate(Gpress(ngaus,gauscomp))
allocate(Gcurve(ngaus,n))
allocate(bkgprm(nbkgprm,nprm))
allocate(bkgpress(nbkgprm))
allocate(bkg(n))
allocate(pvalue(nop))
allocate(Gtot(n))
allocate(Ctot(n))
allocate(z(n))
allocate(dz(n))
Gpress(:,:)=0
G(:,:,:)=0
C(:,:)=0
H(:,:)=0

!Prms for metheth build. G(ngaus,nprm,gauscomp)!
G(1,1,1)=13.3687    ; G(1,1,2)=0.93997    ; G(1,1,3)=0.00843
G(2,1,1)=38.7864    ; G(2,1,2)=1.12184    ; G(2,1,3)=0.00597
G(3,1,1)=1.69243    ; G(3,1,2)=1.43701    ; G(3,1,3)=0.02823
G(4,1,1)=1.98776    ; G(4,1,2)=1.82020    ; G(4,1,3)=0.059
G(5,1,1)=1.14016    ; G(5,1,2)=2.10307    ; G(5,1,3)=0.08247
G(6,1,1)=0.73789    ; G(6,1,2)=4.19965    ; G(6,1,3)=0.7789
G(7,1,1)=0.74228    ; G(7,1,2)=5.89068    ; G(7,1,3)=1.18849
G(8,1,1)=0.56305    ; G(8,1,2)=2.82531    ; G(8,1,3)=0.68215
```

```
G(9,1,1)=0.19607    ; G(9,1,2)=7.69561    ; G(9,1,3)=0.74348
G(10,1,1)=0.07021   ; G(10,1,2)=8.55338   ; G(10,1,3)=0.66596
G(1,2,1)=10.6467    ; G(1,2,2)=0.93999    ; G(1,2,3)=0.0069
G(2,2,1)=30.0013    ; G(2,2,2)=1.12432    ; G(2,2,3)=0.00502
G(3,2,1)=1.10191    ; G(3,2,2)=1.42307    ; G(3,2,3)=0.02694
G(4,2,1)=1.32051    ; G(4,2,2)=1.81945    ; G(4,2,3)=0.05761
G(5,2,1)=0.77506    ; G(5,2,2)=2.09224    ; G(5,2,3)=0.08667
G(6,2,1)=0.7761     ; G(6,2,2)=3.57569    ; G(6,2,3)=0.82707
G(7,2,1)=0.70076    ; G(7,2,2)=5.44504    ; G(7,2,3)=1.23998
G(8,2,1)=0.62872    ; G(8,2,2)=2.55983    ; G(8,2,3)=0.36258
G(9,2,1)=0.2857     ; G(9,2,2)=6.99541    ; G(9,2,3)=1.14765
G(10,2,1)=0.006     ; G(10,2,2)=10.2135   ; G(10,2,3)=0.28649

bkgprm(1,1)=7.97582       ;       pvalue(1)=4.84938
bkgprm(2,1)=6.17381  ;    pvalue(2)=0.55094
bkgprm(1,2)=7.74072  ;    pvalue(3)=3.85773
bkgprm(2,2)=6.54081       ;       pvalue(4)=4.25796

!------Generate methanol:ethanol PTM PDFs------!
do i=1,m
        Ctot=0
        temppress=press(i)
        call makemetheth(m,n,ngaus,nbkgprm,bkgprm,nprm,gauscomp,G,pvalue,temppress,Gtot,Ctot)
        do j=1,n
                C(j,i)=Ctot(j)
        end do
end do

!Output convolved PDF!
open(10, file='MEPDFs.txt', status='replace')
write(10,*) 'Analytical methanol:ethanol PTM PDFs', 'Qmax:', Qmax
write(10,*) 'r', (press(i), i=1,m)
do i=1,n
        write(10,*) i*dx, (C(i,j), j=1,m)
```

```
enddo
close(10)
write(*,*) 'Methanol:ethanol PTM PDFs have been generated.'

!------Setting the directory------!
call getcwd(cwd)
rundir =trim(cwd)//'\output'
call execute_command_line('mkdir '//trim(rundir)//'\samplecomponent')
call execute_command_line('mkdir '//trim(rundir)//'\weight')

!------Read in dataset------!
do j=1,m
        write(6,'(a38,f4.2,a6)',advance='no') 'Enter data file name for pressure at ', press(j), ' GPa: '
        read(*,*) datafile

        open(10, file=trim(datafile),status='old')
                read(10,*) ncheck
                if (ncheck<n) then
                        write(*,*) '!!! ERROR !!! Not enough data points.'
                endif
                read(10,*) line
                do i=1,n
                        read(10,*) r(i), D(i,j)
                enddo
                if(r(1)/=0.02) then
                        write(*,*) '!!! ERROR !!! First data point should be r = 0.02A.'
                endif
                if((r(2)-r(1))/=0.02) then
                        write(*,*) '!!! ERROR !!! Bin of 0.02 required.'
                endif
        close(10)
enddo
!------Initialising weights------!
!Assigning random initial values to MMF coefficients!
```

```
call random_number(random)
do j=1,m
        H(j,j)=random
        H(j+m,j)=1.0-random
end do

!Calculate initial fit!
A = matmul(C,H)
do i=Acutoff, n
        do j=1, m
                A_diff(i,j) = (D(i,j) - A(i,j))
        end do
end do
Fnorm = norm2(A_diff)

!Read out initial MMF configuration!
open(10,file=trim(rundir)//'\samplecomponent\'//'1'//'.txt', status='replace')
        do i = 1, n
                write(10,*) (C(i,j), j=m+1,s)
        enddo
close(10)
open(10,file=trim(rundir)//'\weight\'//'1'//'.txt', status='replace')
        do i = 1, s
                write(10,*) (H(i,j), j=1,m)
        enddo
close(10)

!------Monte Carlo parameters------!
write(*,*)'|----------Monte Carlo parameters----------|'
write(6,'(a54)',advance='no')'Would you like to use the default MC parameters? (Y/N)'
read(*,*) MC
if(MC=='Y') then
        temperature=0.01
        increment=0.01
```

```
        nmoves=10000
        incfac=1.0
        tempfac=0.99
elseif(MC=='N') then
        write(6,'(a19)',advance='no')'Enter temperature: '
        read(*,*)temperature
        write(6,'(a17)',advance='no')'Enter move size: '
        read(*,*)increment
        write(6,'(a66)',advance='no')'Enter number of moves before temperature and increment reduction: '
        read(*,*)nmoves
        write(6,'(a40)',advance='no')'Enter increment factor (1.0=no factor): '
        read(*,*)incfac
        write(6,'(a34)',advance='no')'Enter temperature product factor: '
        read(*,*)tempfac
end if

open(10,file=trim(rundir)//'\NMF_startingconfig.txt', status='replace')
        write(10,*)'Initial temp:', temperature
        write(10,*)'Initial move size:', increment
        write(10,*)'No. moves before temp. and inc. reduction:', nmoves
        write(10,*)'Increment factor:', incfac
        write(10,*)'Temperature factor:', tempfac
close(10)
open(10,file=trim(rundir)//'\NMF_charge_progress.txt', status='replace')
        write(10,'(A8,X,A8,X,A4,X,A9,X,A13)') 'Moves', 'Accepted', 'Temp', 'Increment', 'Energy(Fnorm)'
        write(10,*) 0, 0, temperature, increment, Fnorm
close(10)

do l = 1, maxmoves
!Terminal readout of parameters!
        if(mod(l,nmoves)==1)then
                temperature = tempfac*temperature        !Reducing 'temperature'
                increment = increment*incfac             !Reducing the amount by which elements can vary during each MC move
                write(*,*)'Cycle', l
```

```
                write(*,*) 'Changing temperature'
                write(*,*) 'New temperature: ',temperature
                write(*,*) 'New increment: ',increment
                write(*,*) 'Moves proposed, accepted: ',nmoves,iacc
                write(*,*) 'Current energy: ',Fnorm
                write(*,*)

                A_trial = matmul(C,H)

                do i=Acutoff, n
                        do j=1, m
                                A_diff_trial(i,j) = (D(i,j) - A_trial(i,j))
                        end do
                end do
                Fnorm_trial = norm2(A_diff_trial)

        iacc=0

        end if
!------Changing sample component------!
        if(mod(1,2)/=0) then
                C_trial(:,:) = C(:,:)
                H_trial(:,:) = H(:,:)
                !Selecting element to vary!
                call random_number(random)
                random = (random * n) + 1
                index1 = int(random)
                !Which component to vary!
                call random_number(random)
                random = (random * m) + (m+1)
                index2 = int(random)

                !if r value is lower than Crmin, then leave at 0!
                if(index1<cutoff) then
```

```
        do i=1,cutoff
                C_trial(i,index2)=0
        end do
endif
if(index1>=cutoff) then
!Selecting magnitude of MC move!
        call random_number(random2)
        random2 = random2 * increment
        call random_number(random3)
        if(random3<=0.5) then
                C_trial(index1,index2) = C_trial(index1,index2) + random2
        endif
        if(random3>0.5) then
                C_trial(index1,index2) = C_trial(index1,index2) - random2
        endif
        !Non-negative constraint!
        if(C_trial(index1,index2)<=0) then
                C_trial(index1,index2) = C_trial(index1,index2) + random2
        endif
end if

!Calculate fit!
A_trial = matmul(C_trial,H_trial)
do i=Acutoff, n
        do j=1, m
                A_diff_trial(i,j) = (D(i,j) - A_trial(i,j))
        end do
end do
Fnorm_trial = norm2(A_diff_trial)
Fdiff = Fnorm_trial - Fnorm

!Acceptance criteria!
if(Fdiff <= 0.0) then
        C = C_trial
```

```
            H = H_trial
            A = A_trial
            A_diff = A_diff_trial
            Fnorm = Fnorm_trial
            iacc=iacc+1
         endif
         if(Fdiff > 0.0) then
            prob = exp(-Fdiff/temperature)
            call random_number(random)
            if(prob > random) then
               C = C_trial
               H = H_trial
               A = A_trial
               A_diff = A_diff_trial
               Fnorm = Fnorm_trial
               iacc=iacc+1
            endif
            if(prob <= random) then
               C_trial = 0.0
               H_trial = 0.0
               A_trial = 0.0
               A_diff_trial = 0.0
               Fnorm_trial = 0.0
            endif
         endif
      endif
!-------Changing weights--------!
      if(mod(1,2)==0) then
         C_trial(:,:) = C(:,:)
         H_trial(:,:) = H(:,:)
         !Selecting weight to vary!
         call random_number(random)
         random = (random * m) + 1
```

```
index3 = int(random)
!Selecting magnitude of MC move!
call random_number(random)
random = random * increment

call random_number(random3)
if(random3<=0.5) then
        if(WV=='Y') then
                H_trial(index3,index3)=H_trial(index3,index3) + random
                H_trial(index3+m,index3)=1-H_trial(index3,index3)
                !Non-negative constraint on weights!
                if(H_trial(index3+m,index3)<0.0) then
                        H_trial(index3,index3) = H_trial(index3,index3) - random
                        H_trial(index3+m,index3)=1-H_trial(index3,index3)
                        cycle
                endif

        elseif(WV=='N') then
                do j=1,m
                        H_trial(j,j)=H_trial(j,j)+random
                        H_trial(j+m,j)=1-H_trial(j,j)
                        if(H_trial(j,j)<0.0) then
                                H_trial(j,j)=H_trial(j,j)-random
                                H_trial(j+m,j)=1-H_trial(j,j)
                                cycle
                        endif
                end do
        endif
endif

if(random3>0.5) then
        if(WV=='Y') then
                H_trial(index3,index3) = H_trial(index3,index3) - random
```

```
                H_trial(index3+m,index3)=1-H_trial(index3,index3)
                !Non-negative constraint on weights!
                if(H_trial(index3,index3)<0.0) then
                        H_trial(index3,index3) = H_trial(index3,index3) + random
                        H_trial(index3+m,index3)=1-H_trial(index3,index3)
                        cycle
                endif
        elseif(WV=='N') then
                do j=1,m
                        H_trial(j,j)=H_trial(j,j)-random
                        H_trial(j+m,j)=1-H_trial(j,j)
                        if(H_trial(j,j)<0.0) then
                                H_trial(j,j)=H_trial(j,j)+random
                                H_trial(j+m,j)=1-H_trial(j,j)
                                cycle
                        endif
                end do
        endif
endif

!Calculate fit!
A_trial = matmul(C_trial,H_trial)
do i=Acutoff, n
        do j=1, m
                A_diff_trial(i,j) = (D(i,j) - A_trial(i,j))
        end do
end do
Fnorm_trial = norm2(A_diff_trial)
Fdiff = Fnorm_trial - Fnorm

!Acceptance criteria!
if(Fdiff <= 0.0) then
        C = C_trial
        H = H_trial
```

```
                A = A_trial
                A_diff = A_diff_trial
                Fnorm = Fnorm_trial
                iacc=iacc+1
        endif
        if(Fdiff > 0.0) then
                prob = exp(-Fdiff/temperature)
                call random_number(random)
                if(prob > random) then
                        C = C_trial
                        H = H_trial
                        A = A_trial
                        A_diff = A_diff_trial
                        Fnorm = Fnorm_trial
                        iacc=iacc+1
                endif
                if(prob <= random) then
                        C_trial = 0.0
                        H_trial = 0.0
                        A_trial = 0.0
                        A_diff_trial = 0.0
                        Fnorm_trial = 0.0
                endif
        endif
endif

!Read-out current configuration to record progress of factorisation!
if(mod(l,nprint)==1) then
        write(cystring,'(i5)') (l+nprint)/nprint
        open(10,file=trim(rundir)//'\samplecomponent\'//trim(adjustl(cystring))//'.txt', status='replace')
        do i = 1, n
                write(10,*) (C(i,j), j=m+1,s)
        enddo
        close(10)
```

```
        endif
        if(mod(l,nprint)==1) then
                write(cystring,'(i5)') (l+nprint)/nprint
                open(10,file=trim(rundir)//'\weight\'//trim(adjustl(cystring))//'.txt', status='replace')
                do i = 1, s
                        write(10,*) (H(i,j), j=1,m)
                enddo
                close(10)
        endif

        !Write to charge progress!
        iacc_total=iacc_total+iacc

        if(mod(l,nprint)==1) then
                write(cystring,'(i5)') (l+nprint)/nprint
                open(10,file=trim(rundir)//'\NMF_charge_progress.txt', status='unknown', access='append')
                write(10,*) l, iacc_total, temperature, increment, Fnorm
                close(10)
        endif

        if(mod(l,Fno)==1) then
                Fcheckdiff=Fcheck-Fnorm
                write(*,*) Fcheck, Fnorm, Fcheckdiff
                if(abs(Fcheckdiff)<0.00000001) then
                exit
                elseif(abs(Fcheckdiff)>=0.00000001) then
                        Fcheck=Fnorm
                endif
        endif

end do

write(6,*) 'FINISHED!!! Final energy:', Fnorm
```

```
open(10,file=trim(rundir)//'\corrected_PDFs.txt', status='replace')
write(10,*) 'r', (press(i), i=1,m)
do i=1,n
        write(10,*)   r(i), ((D(i,j)-(C(i,j))*(H(j,j)))/H(j+m,j), j=1,m)
enddo
close(10)

!close(11)
deallocate(D)
deallocate(C)
deallocate(H)
deallocate(A)
deallocate(A_diff)
deallocate(C_trial)
deallocate(H_trial)
deallocate(A_trial)
deallocate(A_diff_trial)
deallocate(r)
deallocate(G)
deallocate(Gpress)
deallocate(Gcurve)
deallocate(Gtot)
deallocate(bkgprm)
deallocate(bkgpress)
deallocate(bkg)
deallocate(pvalue)
deallocate(press)
deallocate(Ctot)
deallocate(z)
deallocate(dz)
deallocate(dtemp)

contains
```

```
subroutine makemetheth(m,n,ngaus,nbkgprm,bkgprm,nprm,gauscomp,G,pvalue,press,Gtot,Ctot)
        implicit none
        integer          :: i,m,ngaus,gauscomp,n,nbkgprm,nprm
        real*8           :: Gpress(ngaus,gauscomp),Gcurve(ngaus,n),bkgprm(nbkgprm,nprm),G(ngaus,nprm,gauscomp),pvalue(nop)
        real*8           :: Gtot(n),bkgpress(nbkgprm),bkg(n),Ctot(n),z(n),dz(n),press
        real*8              f,t
        pi=3.14159265

        Gtot=0
        Ctot=0
        Gpress=0
        Gcurve=0
        bkgpress=0
        !Calculate Gaussian prms!
        do i=1,ngaus
                do k=1, gauscomp
                        if (k==1) then
                        Gpress(i,k)=(G(i,2,k) + ((G(i,1,k)-G(i,2,k))*Exp(-(temppress/(pvalue(2))))))
                        else if (k==2) then
                        Gpress(i,k)=(G(i,2,k) + ((G(i,1,k)-G(i,2,k))*Exp(-(temppress/(pvalue(3))))))
                        else if (k==3) then
                        Gpress(i,k)=(G(i,2,k) + ((G(i,1,k)-G(i,2,k))*Exp(-(temppress/(pvalue(4))))))
                        end if
                end do
        end do
        !Calculate individual Gaussians!
        do i=1, ngaus
                do j=1,n
                        Gcurve(i,j) = (Gpress(i,1))*Exp(-(((j*dx)-(Gpress(i,2)))**2)/(2*(Gpress(i,3))**2))
                        Gtot(j) = Gtot(j)+Gcurve(i,j)
                end do
        end do
        !Background!
        !Calculate background prms!
```

```
do i=1,nbkgprm
        bkgpress(i)=(bkgprm(i,2) + ((bkgprm(i,1)-bkgprm(i,2))*Exp(-(temppress/(pvalue(1))))))
end do
!Calculate background!
do i=1,n
        bkg(i)=(1-Exp(-(((i*dx)/bkgpress(1))**bkgpress(2))))
end do
!Gaussians+background!
do i=1, n
        Gtot(i) = Gtot(i)+bkg(i)
end do

!Convolution program from convol_norm_new!
do i=1,n
z(i)=i*dx
end do
dz(1)=z(2)-z(1)
dz(n)=z(n)-z(n-1)
do i=2,n-1
        dz(i)=(z(i+1)-z(i-1))*0.5
enddo

do i=1,n
        Ctot(i)=0.
        do j=1,n
                f=abs(z(j)-z(i))
                t=(z(j)+z(i))
                if (i.eq.j) then
                        Ctot(i)=Ctot(i)+z(j)*(Gtot(j))*(Qmax-sin(t*Qmax)/t)*dz(j)
                else
                        Ctot(i)=Ctot(i)+z(j)*(Gtot(j))*(sin(f*Qmax)/f-sin(t*Qmax)/t)*dz(j)
                endif
        enddo
        Ctot(i)=Ctot(i)/(z(i)*pi)
```

```
        enddo
end subroutine

!Random number generator!
subroutine init_random_seed()
        integer :: i, n, clock
        integer, dimension(:), allocatable :: seed

        call random_seed(size = n)
        allocate(seed(n))

        call system_clock(count=clock)

        seed = clock + 37 * (/ (i - 1, i = 1, n) /)
        call random_seed(put = seed)

        deallocate(seed)
end subroutine init_random_seed

end program metheth_nmf
```

6.2 Recovery of harmonic–like behaviour of the polar mode in $BaTiO_3$ at high pressures

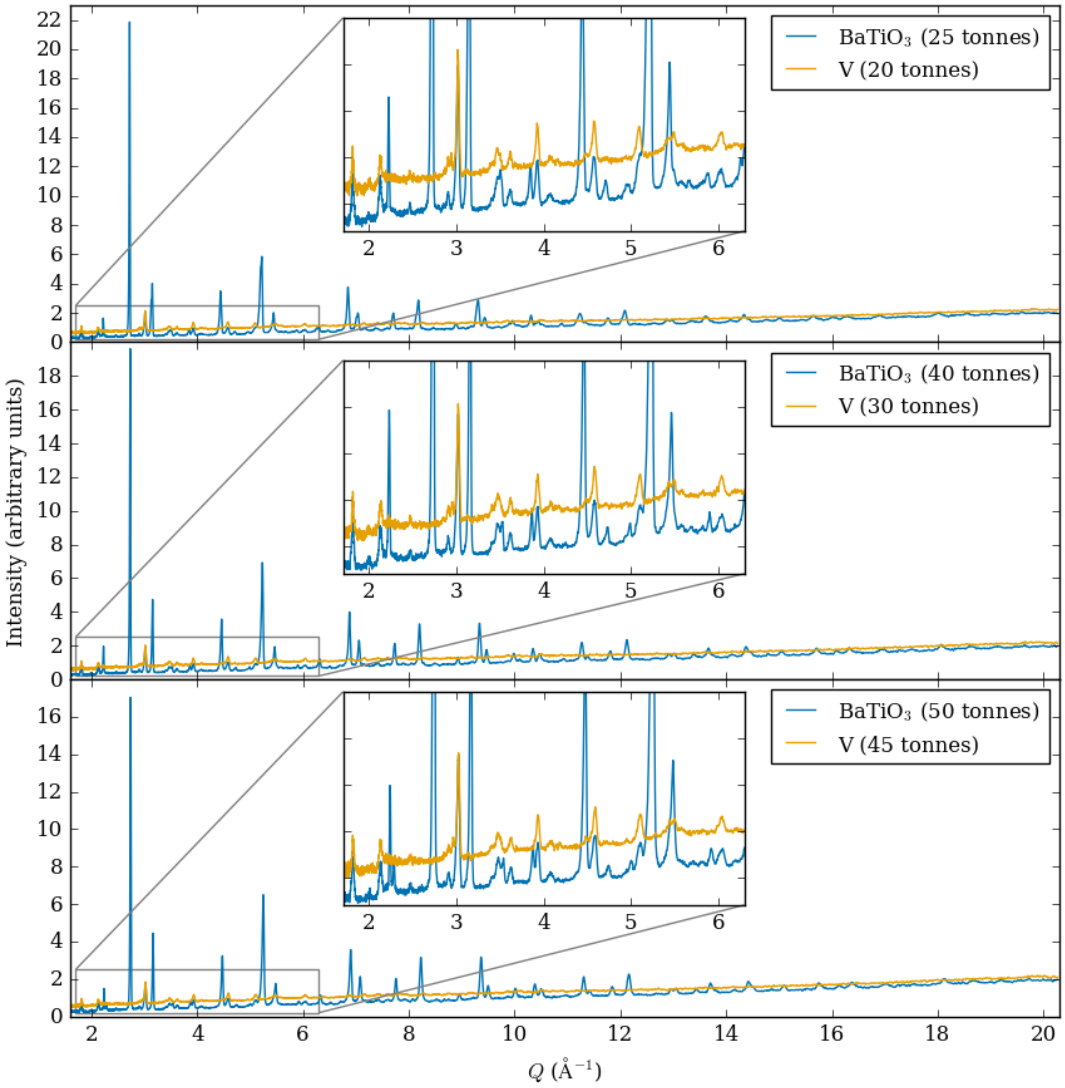

Figure 6.12: Neutron diffraction patterns of $BaTiO_3$ and vanadium measured on PEARL. The inset plots shows a comparison of the two diffraction patterns and the Bragg scattering from ZTA anvils more clearly.

Table 6.2: The irreps. modelled using the SAPA method and corresponding number of modes per irrep. which were tested against $BaTiO_3$ PDFs measured on GEM. R_{wp} values are for fits against a PDF processed with a Q_{max} of 40 Å^{-1}. Corresponding fits are shown in Figures 6.13 and 6.14.

Irrep.	R_{wp}	Number of modes per irrep.
R_5^+	6.475189	3
R_2^-	6.481642	1
X_1^+	6.498266	6
X_2^+	6.549475	3
R_3^-	6.393098	2
R_4^-	6.493399	6
M_1^+	6.5221	3
R_5^-	6.489462	3
M_4^+	6.329031	3
M_2^-	6.177942	6
M_3^-	6.493417	3
M_3^+	6.33423	3
M_5^+	6.850279	6
M_2^+	6.485019	3
M_5^-	6.097319	18
X_5^-	6.504651	12
X_5^+	6.013227	18
Γ_4^-	5.226887	12
Γ_5^-	5.886725	3
X_3^-	6.456776	6

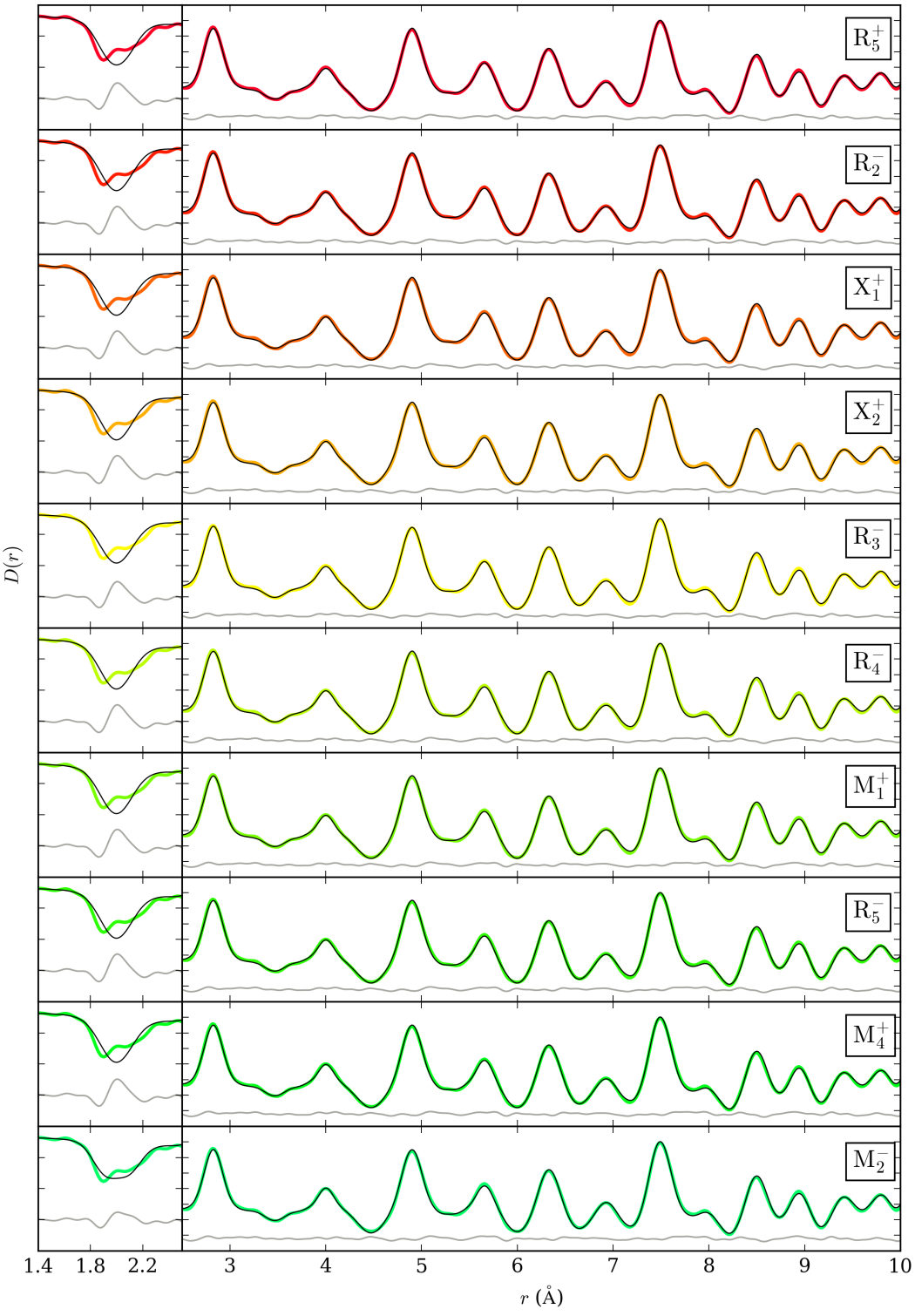

Figure 6.13: Fits to a $BaTiO_3$ PDF, measured at 300 K on GEM ($Q_{max} = 40$ Å^{-1}) against distortions described by the SAPA approach. The irreps. of the corresponding distortions of a cubic $Pm\bar{3}m$ structure are as indicated on the right. The low r-region (1.4–2.5 Å) is plotted on a separate x and y axis for clarity. *Continued...*

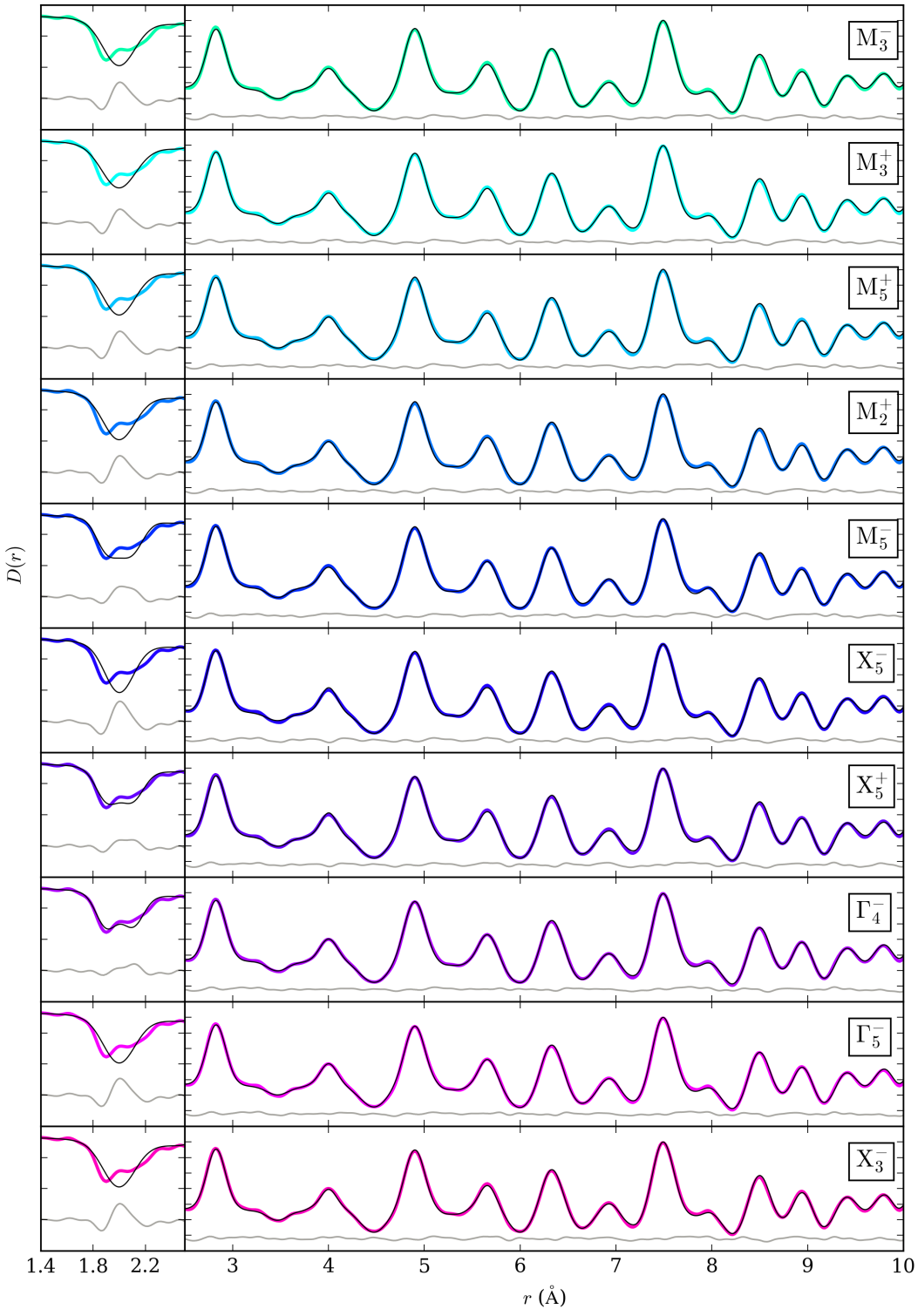

Figure 6.14: *Continued...* Fits to a $BaTiO_3$ PDF, measured at 300 K on GEM (Q_{max} = 40 Å^{-1}) against distortions described by the SAPA approach. The irreps. of the corresponding distortions of a cubic $Pm\bar{3}m$ structure are as indicated on the right. The low r-region (1.4–2.5 Å) is plotted on a separate x and y axis for clarity.

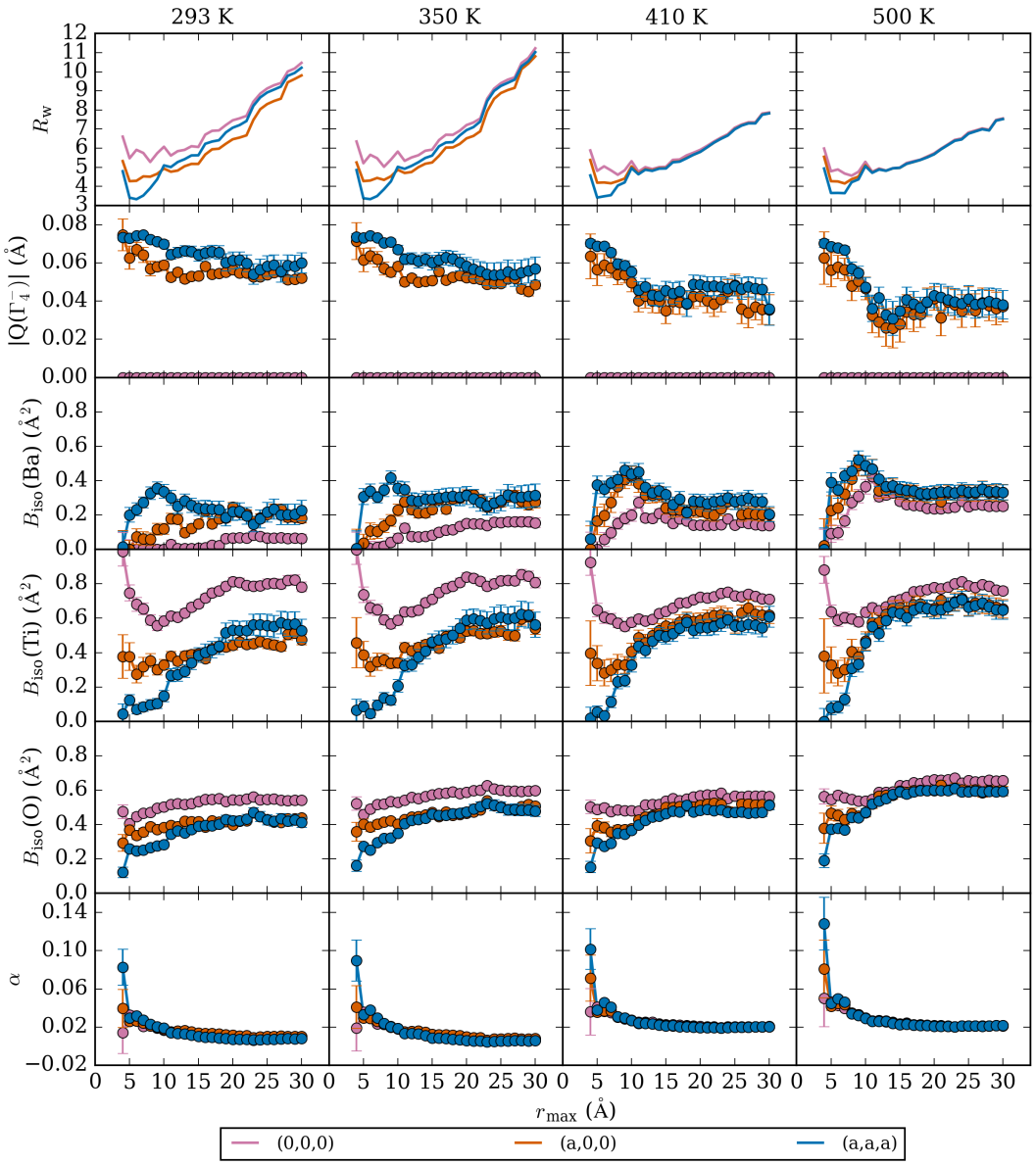

Figure 6.15: Fitting statistics (R_w), $|Q(\Gamma_4^-)|$ values and thermal parameters (B_{iso} and α, as described above) for constrained mode variable range refinements against variable temperature $BaTiO_3$ PDFs measured on GEM, and processed with a Q_{max} of 20 Å^{-1}.

6.2.1 Box-car modelling

An alternative approach to probing different lengths scales in a material is through 'box-car' fitting. Rather than increasing the r-range of the refinement to progressively model larger length-scales, the range is held constant and shifted along the PDF. In contrast to the variable-range fitting, sensitivity to the local Ti and O distortions is lost as longer length-scales are probed by the modelling range. Where variable-range refinements remain influenced by the shortest atom–atom correlations, the higher r refinements of box-car modelling are not, and beyond ca. 4 Å, already model the average of local Ti and O distortions.

A 10 Å-range box-car refinement was carried out on the variable pressure and temperature PDFs, such that the region modelled was progressed from 0–10 Å to 30–40 Å, in steps of 2 Å. Figure 6.16 shows the R_{w} and $|\mathrm{Q}(\Gamma_4^-)|$ values and r_{max} describes the uppermost r value fitted to but now, $r_{\mathrm{max}} = 30$ Å corresponds to a refinement over 20–30 Å, rather than 1.2–30 Å as described in the previous section. Note that the first data point at $r_{\mathrm{max}} = 10$ Å actually corresponds to a 9 Å range since the 0–1 Å region of the PDF is typically difficult to fit due to features introduced when modelling the effects of finite Q.

The variable pressure and temperature results are again comparable to each other in the tetragonal regime. At 0.24 and 1.19 GPa, low R_{w} values indicate that an (a, a, a) OPD is favoured below ca. 22 Å, and at 293 and 350 K the $(a, 0, 0)$ OPD is favoured (as seen in Figure 6.16), also up to ca. 22 Å. $|\mathrm{Q}(\Gamma_4^-)|$ tends to zero at $r_{\mathrm{max}} = 30$ Å in the tetragonal regime, supporting an order–disorder model, where for higher r_{max}, refined atom–atom distances will be a result of averaging rhombohedrally-displaced atoms.

In the cubic regime at 2.55 and 4.18 GPa, and 410 and 500 K, there is virtually no difference between the R_{w} values, in agreement with comparable variable-range results for $r_{\mathrm{max}} > 10$ Å. As previously seen, $|\mathrm{Q}(\Gamma_4^-)|$ at 4.18 GPa at the smallest

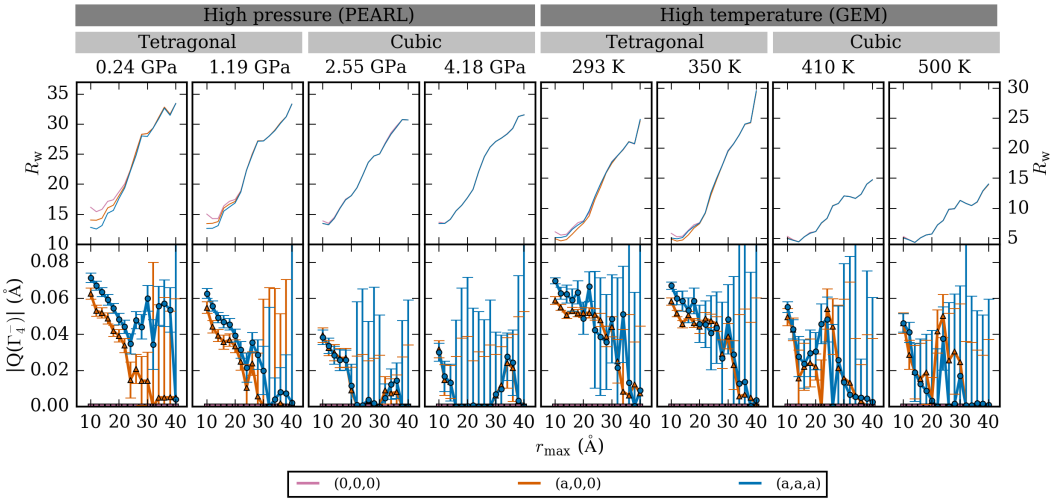

Figure 6.16: R_w and $|Q(\Gamma_4^-)|$ values for 10 Å box-car refinements for cubic (0,0,0), tetragonal $(a, 0, 0)$ and rhombohedral (a, a, a) OPDs against variable temperature and pressure PDFs. The data point indicates the maximum r-value encompassed by the box-car fitting range.

r_{max} is suppressed by ca. 1/2. At 500 K $|Q(\Gamma_4^-)|$ appears to decrease by ca. 0.65, although this is no different to the results found for the variable-range refinements where, for 1.2–10 Å, $|Q(\Gamma_4^-)|$ also decreases by ca. 0.68 between 293 and 500 K.

The loss of sensitivity to the distortion modes at relatively low r ($r_{max} = 14$ Å at both 500 K and 4.18 GPa) is surprising given the distinctly different results given by the variable-range refinements for the high pressure compared to high temperature refinements. This highlights a seemingly influential constraint placed on the model by the short-range data.

6.3 The average and local structure of Mg-substituted $La_{1.875}Ba_{0.125}CuO_4$

Table 6.3: Refined parameters from Rietveld refinements against variable temperature XRD patterns of $La_{1.875}Ba_{0.125}(Cu_{1-y}Mg_y)_{0.875}Cu_{0.125}O_4$ $y = 0.0$. Asterisks indicate data collected during a separate measurement.

Temperature (K)	Phase (Percentage %)	R_w	a (Å)	b (Å)	c (Å)	X_3^+	Γ_1^+	B_{iso}(A) (Å^2)	B_{iso}(B) (Å^2)	B_{iso}(O) (Å^2)
10	LTT* (57.6(5))	1.95976	5.35241(2)	5.35241(2)	13.22360(7)	0.0682	0.0819	0.252(5)	0.35(1)	0.73(3)
20	LTT* (53.5(5))	1.96859	5.35250(2)	5.35250(2)	13.22397(7)	0.1063	0.0834	0.221(6)	0.33(1)	0.54(3)
30	LTT* (52.3(4))	1.94264	5.35247(2)	5.35247(2)	13.22409(7)	0.0911	0.0925	0.216(6)	0.32(1)	0.62(3)
40	LTT* (46.5(4))	1.95124	5.35252(2)	5.35252(2)	13.22446(7)	0.0815	0.0713	0.231(6)	0.33(1)	0.68(3)
50	LTT* (37.4(14))	2.04000	5.35254(2)	5.35254(2)	13.22492(9)	0.1414	0.1229	0.225(5)	0.32(1)	0.64(3)
60	LTT* (21.4(3))	2.07692	5.35256(5)	5.35256(5)	13.22601(23)	0.1626	0.2027	0.232(6)	0.34(1)	0.65(3)
70	LTT* (12.9(3))	2.16112	5.35276(8)	5.35276(8)	13.22654(40)	0.2132	0.3466	0.257(6)	0.30(1)	0.68(3)
10	LTO* (42.4(5))	1.95976	5.33960(7)	5.36982(7)	13.22168(23)	0.1568	0.2672	0.252(5)	0.35(1)	0.73(3)
20	LTO* (46.5(5))	1.96859	5.33940(6)	5.36963(6)	13.22260(21)	0.1530	0.1968	0.221(6)	0.33(1)	0.54(3)
30	LTO* (47.7(4))	1.94264	5.33916(6)	5.36939(6)	13.22273(21)	0.1062	0.1208	0.216(6)	0.31(1)	0.62(3)
40	LTO* (53.5(4))	1.95124	5.33897(13)	5.36930(12)	13.22292(18)	0.0787	0.0683	0.231(6)	0.33(1)	0.68(3)
50	LTO* (62.6(14))	2.04000	5.33782(11)	5.36878(16)	13.22418(13)	0.0396	0.0280	0.225(5)	0.32(1)	0.64(3)
60	LTO* (78.6(3))	2.07692	5.33797(5)	5.36818(5)	13.22446(12)	0.0877	0.0198	0.232(6)	0.34(1)	0.65(3)
70	LTO* (87.1(3))	2.16112	5.33803(4)	5.36802(4)	13.22576(10)	0.0716	0.0249	0.257(6)	0.30(1)	0.68(3)
80	LTO* (100)	2.14300	5.33927(3)	5.36715(3)	13.22718(6)	0.1320	0.0061	0.276(6)	0.32(1)	0.67(3)
90	LTO* (100)	2.16755	5.33948(3)	5.36700(3)	13.22860(6)	0.1103	0.0238	0.274(6)	0.31(2)	0.59(3)
100	LTO* (100)	2.15813	5.33990(3)	5.36673(3)	13.22976(5)	0.1268	0.0220	0.276(6)	0.33(1)	0.66(3)
110	LTO* (100)	2.22336	5.34040(3)	5.36649(3)	13.23120(6)	0.1116	0.0157	0.332(6)	0.34(2)	0.68(3)
120	LTO* (100)	2.42108	5.34091(3)	5.36586(3)	13.23277(6)	0.1073	0.0398	0.314(7)	0.35(2)	0.62(3)
130	LTO* (100)	2.40985	5.34162(3)	5.36541(3)	13.23451(6)	0.1133	0.0564	0.327(6)	0.34(2)	0.62(3)

140	LTO (100)	8.25684	5.34218(2)	5.36389(2)	13.23543(4)	0.1202	0.0387	0.205(5)	0.11(1)	0.86(3)
150	LTO (100)	8.03037	5.34301(2)	5.36330(2)	13.23746(4)	0.1178	0.0452	0.225(4)	0.13(1)	0.86(3)
160	LTO (100)	8.04077	5.34388(2)	5.36265(2)	13.23946(4)	0.1146	0.0474	0.239(5)	0.14(1)	0.86(3)
170	LTO (100)	8.08836	5.34478(2)	5.36199(2)	13.24150(4)	0.1099	0.0483	0.252(5)	0.15(1)	0.87(3)
180	LTO (100)	8.32880	5.34572(2)	5.36130(2)	13.24351(4)	0.1084	0.0450	0.256(5)	0.16(1)	0.87(3)
190	LTO (100)	8.37890	5.34668(2)	5.36060(2)	13.24571(4)	0.1036	0.0449	0.267(5)	0.17(1)	0.87(3)
200	LTO (100)	8.29781	5.34776(2)	5.35981(2)	13.24822(4)	0.0974	0.0486	0.282(5)	0.18(1)	0.88(3)
210	LTO (100)	8.48350	5.34874(2)	5.35909(2)	13.25020(4)	0.0932	0.0457	0.286(5)	0.18(1)	0.88(3)
220	LTO (100)	8.54653	5.34997(2)	5.35816(3)	13.25250(4)	0.0849	0.0460	0.293(5)	0.19(1)	0.90(3)
230	LTO (100)	8.51310	5.35130(3)	5.35708(4)	13.25501(4)	0.0681	0.0555	0.310(5)	0.22(1)	0.92(3)
240	LTO (100)	8.68565	5.35233(3)	5.35628(4)	13.25745(4)	0.0501	0.0580	0.324(5)	0.23(1)	0.93(3)
250	LTO (100)	8.82940	5.35313(3)	5.35585(4)	13.25966(4)	0.0351	0.0604	0.333(5)	0.24(1)	0.94(3)
260	HTT (100)	8.79947	5.35433(1)	5.35433(1)	13.26137(4)	0	0.0573	0.345(5)	0.22(1)	0.93(3)
270	HTT (100)	8.52551	5.35476(1)	5.35476(1)	13.26342(4)	0	0.0602	0.353(5)	0.24(1)	0.92(3)
280	HTT (100)	8.44262	5.35519(1)	5.35519(1)	13.26516(4)	0	0.0634	0.36(4)	0.25(1)	0.91(3)
290	HTT (100)	8.22518	5.35574(1)	5.35574(1)	13.26735(4)	0	0.0690	0.380(4)	0.26(1)	0.92(3)
300	HTT (100)	8.23737	5.35627(1)	5.35627(1)	13.26923(4)	0	0.0700	0.386(4)	0.28(1)	0.92(3)

Table 6.4: Refined parameters from Rietveld refinements against variable temperature XRD patterns of $La_{1.875}Ba_{0.125}(Cu_{1-y}Mg_y)_{0.875}Cu_{0.125}O_4$ $y = 0.1$. Asterisks indicate data collected during a separate measurement.

Temperature (K)	Phase (Percentage %)	R_w	a (Å)	b (Å)	c (Å)	X_3^+	Γ_1^+	B_{iso}(A) (Å^2)	B_{iso}(B) (Å^2)	B_{iso}(O) (Å^2)
100	LTO (100)	3.83998	5.34991(3)	5.37775(3)	13.18482(6)	0.1366	0.0845	0.917(8)	0.80(2)	1.70(5)

110	LTO (100)	3.81494	5.35018(3)	5.37765(3)	13.18572(6)	0.1354	0.0796	0.928(8)	0.82(2)	1.75(5)	
120	LTO (100)	3.81601	5.35065(3)	5.37736(3)	13.18708(6)	0.1409	0.0828	0.936(8)	0.83(2)	1.70(5)	
130	LTO (100)	3.84731	5.35122(3)	5.37704(3)	13.18859(6)	0.1391	0.0810	0.953(8)	0.82(2)	1.67(5)	
140	LTO (100)	3.81961	5.35186(2)	5.37662(3)	13.19015(6)	0.1296	0.0836	0.971(8)	0.85(2)	1.70(5)	
150	LTO (100)	3.80601	5.35252(2)	5.37614(3)	13.19182(6)	0.1297	0.0878	0.995(8)	0.87(2)	1.67(5)	
160	LTO (100)	3.79134	5.35330(2)	5.37564(3)	13.19364(6)	0.1402	0.0892	1.006(8)	0.87(2)	1.73(5)	
170	LTO (100)	3.78507	5.35408(2)	5.37509(3)	13.19555(6)	0.1393	0.0871	1.020(8)	0.89(2)	1.68(5)	
180	LTO (100)	3.82853	5.35504(2)	5.37443(3)	13.19787(6)	0.1345	0.0918	1.040(8)	0.90(2)	1.61(5)	
190	LTO (100)	3.83692	5.35590(2)	5.37381(3)	13.19978(6)	0.1348	0.0751	1.048(8)	0.93(2)	1.60(5)	
200	LTO (100)	3.89863	5.35679(2)	5.37320(3)	13.20192(6)	0.1162	0.0779	1.063(8)	0.95(2)	1.69(5)	
210	LTO (100)	3.88782	5.35769(2)	5.37250(3)	13.20398(6)	0.1141	0.0847	1.078(8)	0.94(2)	1.71(5)	
220	LTO (100)	3.87393	5.35869(3)	5.37180(3)	13.20618(6)	0.1053	0.0907	1.095(8)	0.96(2)	1.69(5)	
230	LTO (100)	3.86662	5.35971(3)	5.37098(3)	13.20834(6)	0.1061	0.0999	1.101(8)	0.98(2)	1.66(5)	
240	LTO (100)	3.83101	5.36095(3)	5.37003(3)	13.21058(6)	0.0953	0.1009	1.109(8)	1.00(2)	1.66(5)	
250	LTO (100)	3.77937	5.36262(4)	5.36856(5)	13.21295(6)	0.1038	0.0943	1.102(8)	1.01(2)	1.69(5)	
260	LTO (100)	3.77786	5.36434(4)	5.36708(6)	13.21593(5)	0.1195	0.0896	1.111(8)	0.99(2)	1.65(5)	
270	LTO (100)	3.96457	5.36497(3)	5.36681(5)	13.21868(5)	0.1352	0.0883	1.103(8)	1.02(2)	1.62(5)	
280	HTT (100)	3.65581	5.36585(2)	5.36585(2)	13.22079(5)	0	0.0955	1.093(7)	0.98(2)	1.57(5)	
290	HTT (100)	3.65132	5.36626(2)	5.36626(2)	13.22284(5)	0	0.0991	1.096(7)	0.99(2)	1.53(5)	
300	HTT (100)	3.65079	5.36673(2)	5.36673(2)	13.22485(5)	0	0.0911	1.106(7)	1.01(2)	1.48(5)	
310	HTT (100)	3.62892	5.36723(2)	5.36723(2)	13.22675(5)	0	0.0930	1.120(7)	1.03(2)	1.48(4)	
320	HTT (100)	3.57512	5.36785(2)	5.36785(2)	13.22897(5)	0	0.0933	1.144(7)	1.05(2)	1.48(4)	
330	HTT (100)	3.60436	5.36831(2)	5.36831(2)	13.23054(5)	0	0.0983	1.154(7)	1.05(2)	1.49(4)	
340	HTT (100)	3.55584	5.36897(2)	5.36897(2)	13.23269(5)	0	0.0987	1.171(7)	1.07(2)	1.50(4)	

350	HTT (100)	3.56797	5.36957(2)	5.36957(2)	13.23458(5)	0	0.0935	1.175(7)	1.07(2)	1.50(4)
360	HTT (100)	3.58281	5.37021(2)	5.37021(2)	13.23644(5)	0	0.0799	1.193(7)	1.07(2)	1.48(4)
370	HTT (100)	3.59378	5.37080(2)	5.37080(2)	13.23830(5)	0	0.0970	1.201(7)	1.10(2)	1.45(4)
380	HTT (100)	3.5853	5.37141(2)	5.37141(2)	13.24011(5)	0	0.1062	1.222(7)	1.09(2)	1.45(4)
390	HTT (100)	3.59704	5.37204(2)	5.37204(2)	13.24195(5)	0	0.1083	1.230(7)	1.12(2)	1.47(4)
400	HTT (100)	3.57683	5.37266(2)	5.37266(2)	13.24375(5)	0	0.1143	1.251(7)	1.13(2)	1.49(4)

Table 6.5: Refined parameters from Rietveld refinements against variable temperature XRD patterns of $La_{1.875}Ba_{0.125}(Cu_{1-y}Mg_y)_{0.875}Cu_{0.125}O_4$ $y = 0.2$. Asterisks indicate data collected during a separate measurement.

Temperature (K)	Phase (Percentage %)	R_w	a (Å)	b (Å)	c (Å)	X_3^+	Γ_1^+	B_{iso}(A) (Å^2)	B_{iso}(B) (Å^2)	B_{iso}(O) (Å^2)
10	LTT* (100)	5.85478	5.37693(2)	5.37693(2)	13.14624(5)	0.1332	0.1392	0.56(1)	0.54(2)	0.83(3)
20	LTT* (100)	6.10810	5.37673(2)	5.37673(2)	13.14627(5)	0.1354	0.1116	0.46(1)	0.43(2)	0.83(3)
30	LTT* (100)	6.11095	5.37683(2)	5.37683(2)	13.14603(6)	0.1348	0.1349	0.44(1)	0.43(2)	0.80(3)
40	LTT* (100)	6.23487	5.37675(2)	5.37675(2)	13.14665(6)	0.1322	0.1295	0.49(2)	0.43(2)	0.73(3)
50	LTT* (100)	6.19523	5.37686(2)	5.37686(2)	13.14699(6)	0.1323	0.1251	0.47(2)	0.45(2)	0.80(3)
60	LTT* (100)	6.17270	5.37681(2)	5.37681(2)	13.14772(6)	0.1310	0.1077	0.49(2)	0.45(2)	0.79(3)
70	LTT* (84.8(4))	6.09920	5.37707(2)	5.37707(2)	13.14761(9)	0.1203	0.1555	0.387(4)	0.34(1)	0.72(3)
80	LTT* (80.6(4))	6.00719	5.37723(2)	5.37723(2)	13.14873(10)	0.1181	0.1866	0.384(4)	0.36(1)	0.68(3)
90	LTT* (63.6(3))	5.97528	5.37775(3)	5.37775(3)	13.14868(12)	0.1212	0.1638	0.396(4)	0.35(1)	0.72(3)
100	LTT* (27.4(9))	5.74642	5.37993(10)	5.37993(10)	13.14655(34)	0.2141	0.2766	0.398(4)	0.33(1)	0.75(3)
70	LTO* (15.2(4))	6.09920	5.36366(8)	5.39127(8)	13.15443(51)	0.2881	0.2348	0.387(4)	0.34(1)	0.72(3)
80	LTO* (19.4(4))	6.00719	5.36311(6)	5.39072(6)	13.15291(40)	0.2720	0.1723	0.384(4)	0.36(1)	0.68(3)
90	LTO* (36.4(3))	5.97528	5.36260(4)	5.39020(4)	13.15363(21)	0.1996	0.0530	0.396(4)	0.35(1)	0.72(3)

100	LTO* (72.6(9))	5.74642	5.36270(4)	5.39030(5)	13.15350(11)	0.1122	0.0535	0.398(4)	0.33(1)	0.75(3)
110	LTO (100)	3.01603	5.36178(1)	5.38819(1)	13.15081(3)	0.1422	0.0143	0.483(4)	0.22(1)	0.59(2)
120	LTO (100)	3.02293	5.36222(1)	5.38803(1)	13.15224(3)	0.1417	0.0177	0.495(4)	0.23(1)	0.59(2)
130	LTO (100)	3.02242	5.36275(1)	5.38771(1)	13.15383(3)	0.1397	0.0195	0.504(4)	0.24(1)	0.58(2)
140	LTO (100)	3.02696	5.36336(1)	5.38734(1)	13.15548(3)	0.1372	0.0208	0.517(4)	0.25(1)	0.58(2)
150	LTO (100)	3.04334	5.36410(1)	5.38697(1)	13.15715(3)	0.1306	0.0220	0.530(4)	0.26(1)	0.58(2)
160	LTO (100)	3.02729	5.36480(1)	5.38648(1)	13.15897(3)	0.1262	0.0216	0.541(4)	0.27(1)	0.59(2)
170	LTO (100)	3.02838	5.36559(1)	5.38600(1)	13.16085(3)	0.1214	0.0205	0.553(4)	0.28(1)	0.60(2)
180	LTO (100)	3.03291	5.36640(1)	5.38546(1)	13.16279(3)	0.1152	0.0164	0.567(4)	0.29(1)	0.61(2)
190	LTO (100)	3.03561	5.36724(1)	5.38490(1)	13.16485(3)	0.1110	0.0186	0.577(4)	0.30(1)	0.60(2)
200	LTO (100)	3.04432	5.36812(1)	5.38432(1)	13.16692(3)	0.1043	0.0164	0.590(4)	0.31(1)	0.61(2)
210	LTO (100)	3.05913	5.36904(1)	5.38371(1)	13.16904(3)	0.0989	0.0126	0.603(4)	0.31(1)	0.62(2)
220	LTO (100)	3.07525	5.36998(1)	5.38309(1)	13.17121(3)	0.0932	0.0110	0.614(4)	0.31(1)	0.63(2)
230	LTO (100)	3.07324	5.37095(1)	5.38236(1)	13.17348(3)	0.0864	0.0121	0.626(4)	0.31(1)	0.66(2)
240	LTO (100)	3.07141	5.37201(1)	5.38164(1)	13.17566(3)	0.0805	0.0130	0.638(4)	0.31(1)	0.68(2)
250	LTO (100)	3.07742	5.37319(1)	5.38082(1)	13.17785(3)	0.0691	0.0142	0.648(4)	0.30(1)	0.69(2)
260	LTO (100)	3.08235	5.37439(2)	5.37983(2)	13.17986(3)	0.0609	0.0175	0.654(3)	0.29(1)	0.70(2)
270	LTO (100)	3.22588	5.37572(2)	5.37868(3)	13.18284(3)	0.0548	0.0189	0.657(4)	0.30(1)	0.74(2)
280	LTO (100)	3.28001	5.37645(2)	5.37840(3)	13.18533(3)	0.0483	0.0155	0.671(4)	0.31(1)	0.78(2)
290	LTO (100)	3.27113	5.37698(2)	5.37840(3)	13.18720(3)	0.0486	0.0083	0.680(4)	0.31(1)	0.82(2)
300	HTT (100)	3.27030	5.37803(1)	5.37803(1)	13.18950(2)	0	0.0120	0.692(3)	0.310(10)	0.84(2)
310	HTT (100)	3.25503	5.37848(1)	5.37848(1)	13.19112(2)	0	0.0088	0.706(3)	0.314(10)	0.85(2)
320	HTT (100)	3.23028	5.37967(1)	5.37967(1)	13.19523(2)	0	0.0021	0.725(3)	0.322(10)	0.91(2)
330	HTT (100)	3.23502	5.38033(1)	5.38033(1)	13.19725(2)	0	0.0077	0.740(3)	0.335(10)	0.98(2)

340	HTT (100)	3.19404	5.38095(1)	5.38095(1)	13.19936(2)	0	0.0019	0.753(3)	0.358(10)	1.04(2)
350	HTT (100)	3.18783	5.38161(1)	5.38161(1)	13.20134(2)	0	0.0010	0.771(3)	0.375(10)	1.11(2)
360	HTT (100)	3.15229	5.38228(1)	5.38228(1)	13.20330(2)	0	0.0043	0.783(3)	0.376(9)	1.17(2)
370	HTT (100)	3.13272	5.38295(1)	5.38295(1)	13.20525(2)	0	0.0146	0.792(3)	0.402(10)	1.18(2)
380	HTT (100)	3.17784	5.38365(1)	5.38365(1)	13.20711(2)	0	0.0196	0.803(3)	0.412(10)	1.23(2)
390	HTT (100)	3.13873	5.38435(1)	5.38435(1)	13.20914(2)	0	0.0256	0.806(3)	0.437(10)	1.28(2)
400	HTT (100)	3.19015	5.38508(1)	5.38508(1)	13.21102(2)	0	0.0226	0.813(3)	0.451(10)	1.29(2)

Table 6.6: Refined parameters from Rietveld refinements against variable temperature XRD patterns of $La_{1.875}Ba_{0.125}(Cu_{1-y}Mg_y)_{0.875}Cu_{0.125}O_4$ $y = 0.3$. Asterisks indicate data collected during a separate measurement.

Temperature (K)	Phase (Percentage %)	R_w	a (Å)	b (Å)	c (Å)	X_3^+	Γ_1^+	B_{iso}(A) (Å^2)	B_{iso}(B) (Å^2)	B_{iso}(O) (Å^2)
20	LTT* (100)	6.08972	5.39038(2)	5.39038(2)	13.08578(5)	0.1409	0.2389	0.269(5)	0.24(2)	0.44(3)
30	LTT* (100)	6.0435	5.39039(2)	5.39039(2)	13.08603(5)	0.1416	0.2163	0.274(5)	0.26(2)	0.65(3)
40	LTT* (100)	6.05418	5.39051(2)	5.39051(2)	13.08628(5)	0.1408	0.1844	0.286(5)	0.23(2)	0.77(3)
50	LTT* (100)	6.03613	5.39046(2)	5.39046(2)	13.08672(5)	0.1376	0.1970	0.282(5)	0.22(2)	0.55(3)
60	LTT* (100)	5.99667	5.39052(2)	5.39052(2)	13.08761(5)	0.1351	0.2212	0.285(5)	0.24(2)	0.59(3)
70	LTT* (100)	5.94768	5.39068(2)	5.39068(2)	13.08835(5)	0.1359	0.2013	0.302(5)	0.26(2)	0.69(3)
80	LTT* (100)	6.06292	5.39078(2)	5.39078(2)	13.08917(6)	0.1319	0.1756	0.316(6)	0.26(2)	0.54(3)
90	LTT (76.2(6))	2.09654	5.39042(1)	5.39042(1)	13.08917(5)	0.1240	0.1291	0.990(3)	0.929(8)	1.39(2)
100	LTT (71.6(5))	2.18221	5.39053(1)	5.39053(1)	13.09032(5)	0.1321	0.1575	0.990(3)	0.957(8)	1.43(2)
110	LTT (46.7(4))	2.16076	5.39135(2)	5.39135(2)	13.08908(7)	0.1397	0.2123	1.006(3)	0.943(8)	1.42(2)
120	LTT (16.3(1))	2.22075	5.39266(4)	5.39266(4)	13.08675(17)	0.1986	0.4592	1.005(3)	0.954(8)	1.41(2)
90	LTO (23.8(6))	2.09654	5.37452(12)	5.40525(12)	13.09082(12)	0.2263	0.444	0.990(3)	0.929(8)	1.39(2)

100	LTO (28.4(5))	2.18221	5.37439(6)	5.40523(6)	13.09260(10)	0.1728	0.3400	0.990(3)	0.957(8)	1.43(2)
110	LTO (53.3(4))	2.16076	5.37536(3)	5.40415(2)	13.09507(5)	0.1724	0.1804	1.006(3)	0.943(8)	1.42(2)
120	LTO (83.7(1))	2.22075	5.37600(1)	5.40449(1)	13.09539(4)	0.1705	0.1458	1.005(3)	0.954(8)	1.41(2)
130	LTO (100)	2.65516	5.37690(1)	5.40418(1)	13.09606(3)	0.1679	0.1996	1.021(3)	0.92(1)	1.41(2)
140	LTO (100)	2.65524	5.37716(1)	5.40428(1)	13.09763(3)	0.1728	0.1971	1.022(3)	0.93(1)	1.41(2)
150	LTO (100)	2.59661	5.37755(1)	5.40408(1)	13.09949(3)	0.1721	0.1791	1.042(3)	0.92(1)	1.45(2)
160	LTO (100)	2.58097	5.37811(1)	5.40387(1)	13.10126(3)	0.1646	0.1439	1.063(3)	0.91(1)	1.51(2)
170	LTO (100)	2.56584	5.37872(1)	5.40353(1)	13.10322(3)	0.1572	0.1469	1.093(3)	0.93(1)	1.58(2)
180	LTO (100)	2.55542	5.37940(1)	5.40312(1)	13.10524(2)	0.1532	0.1507	1.123(3)	0.975(9)	1.56(2)
190	LTO (100)	2.55851	5.38014(1)	5.40273(1)	13.10722(2)	0.1547	0.1512	1.141(3)	0.956(9)	1.56(2)
200	LTO (100)	2.55439	5.38088(1)	5.40227(1)	13.10933(2)	0.1552	0.1538	1.151(3)	0.964(9)	1.53(2)
210	LTO (100)	2.52885	5.38168(1)	5.40183(1)	13.11142(2)	0.1529	0.1695	1.160(3)	0.978(9)	1.54(2)
220	LTO (100)	2.55959	5.38252(1)	5.40137(1)	13.11346(2)	0.1489	0.1702	1.169(3)	0.987(9)	1.57(2)
230	LTO (100)	2.59245	5.38336(1)	5.40085(1)	13.11567(2)	0.1417	0.1479	1.181(3)	0.997(9)	1.63(2)
240	LTO (100)	2.6634	5.38426(1)	5.40035(1)	13.11785(3)	0.1393	0.1685	1.197(3)	1.00(1)	1.57(2)
250	LTO (100)	2.67144	5.38515(1)	5.39975(1)	13.12025(3)	0.1349	0.1898	1.218(3)	0.99(1)	1.52(2)
260	LTO (100)	2.72223	5.38610(1)	5.39916(1)	13.12252(3)	0.1393	0.2165	1.231(3)	0.99(1)	1.52(2)
270	LTO (100)	2.6143	5.38708(1)	5.39847(1)	13.12492(2)	0.1316	0.2171	1.231(3)	1.023(9)	1.52(2)
280	LTO (100)	2.5217	5.38806(1)	5.39783(1)	13.12709(2)	0.1299	0.2406	1.231(3)	1.030(9)	1.59(2)
290	LTO (100)	2.53784	5.38942(1)	5.39692(1)	13.12970(2)	0.1234	0.2152	1.236(3)	1.028(9)	1.62(2)
300	LTO (100)	2.61058	5.39063(1)	5.39594(2)	13.13242(2)	0.1155	0.2013	1.255(3)	1.054(9)	1.58(2)
310	LTO (100)	2.7991	5.39157(1)	5.39531(2)	13.13517(3)	0.1101	0.2185	1.264(3)	1.03(1)	1.50(2)
320	LTO (100)	2.78957	5.39307(2)	5.39497(2)	13.14032(2)	0.1004	0.1900	1.307(3)	1.10(1)	1.50(2)
330	LTO (100)	2.84251	5.39365(2)	5.39538(2)	13.14233(2)	0.1032	0.1371	1.335(3)	1.14(1)	1.65(2)

340	HTT (100)	2.78602	5.39481(1)	5.39481(1)	13.14462(2)	0	0.1280	1.339(3)	1.14(1)	1.78(2)
350	HTT (100)	2.69071	5.39540(1)	5.39540(1)	13.14687(2)	0	0.1177	1.369(3)	1.133(9)	1.78(2)
360	HTT (100)	2.7226	5.39602(1)	5.39602(1)	13.14899(2)	0	0.0509	1.399(3)	1.155(9)	1.99(2)
370	HTT (100)	2.74573	5.39669(1)	5.39669(1)	13.15094(2)	0	0.0676	1.418(3)	1.17(1)	1.68(2)
380	HTT (100)	2.71254	5.39733(1)	5.39733(1)	13.15297(2)	0	0.0691	1.439(3)	1.179(9)	1.99(2)
390	HTT (100)	2.68224	5.39792(1)	5.39792(1)	13.15479(2)	0	0.0534	1.457(3)	1.222(9)	2.00(2)
400	HTT (100)	2.72633	5.39863(1)	5.39863(1)	13.15668(2)	0	0.0526	1.486(3)	1.24(1)	2.00(2)

Table 6.7: Refined parameters from Rietveld refinements against variable temperature XRD patterns of $La_{1.875}Ba_{0.125}(Cu_{1-y}Mg_y)_{0.875}Cu_{0.125}O_4$ $y = 0.4$.

Temperature (K)	Phase (Percentage %)	R_w	a (Å)	b (Å)	c (Å)	X_3^+	Γ_1^+	B_{iso}(A) (Å^2)	B_{iso}(B) (Å^2)	B_{iso}(O) (Å^2)
90	LTT (100)	2.18581	5.40642(1)	5.40642(1)	13.02699(3)	0.1487	0.3059	0.604(3)	0.639(9)	0.95(2)
100	LTT (100)	2.22328	5.40643(1)	5.40643(1)	13.02843(3)	0.1447	0.3127	0.609(3)	0.654(9)	0.94(2)
110	LTT (100)	2.25665	5.40649(1)	5.40649(1)	13.02997(3)	0.1418	0.3123	0.617(3)	0.665(9)	0.99(2)
120	LTT (67.5(8))	1.93993	5.40676(1)	5.40676(1)	13.03043(3)	0.1532	0.3059	0.643(2)	0.671(8)	1.03(2)
130	LTT (53.2(2))	1.92686	5.40706(1)	5.40706(1)	13.03127(4)	0.1602	0.3046	0.655(2)	0.682(8)	1.09(2)
140	LTT (29.5(3))	1.99017	5.40825(2)	5.40825(2)	13.02968(7)	0.1896	0.3729	0.658(2)	0.675(8)	1.08(2)
150	LTT (11.5(1))	2.06705	5.40903(5)	5.40903(5)	13.03188(19)	0.2617	0.4411	0.658(2)	0.667(8)	1.06(2)
120	LTO (32.5(2))	1.93993	5.39005(2)	5.42185(2)	13.03540(11)	0.1414	0.3061	0.643(2)	0.671(8)	1.03(2)
130	LTO (46.8(2))	1.92686	5.38999(2)	5.42179(2)	13.03684(7)	0.1370	0.2929	0.655(2)	0.682(8)	1.09(2)
140	LTO (70.5(3))	1.99017	5.39010(1)	5.42190(1)	13.03799(5)	0.1547	0.2703	0.658(2)	0.675(8)	1.08(2)
150	LTO (88.5(1))	2.06705	5.39067(1)	5.42248(1)	13.03801(3)	0.1618	0.2818	0.658(2)	0.667(8)	1.06(2)
160	LTO (100)	2.40568	5.39145(1)	5.42227(1)	13.03912(3)	0.1751	0.2899	0.663(3)	0.651(10)	1.09(2)

170	LTO (100)	2.34336	5.39174(1)	5.42221(1)	13.04116(3)	0.1756	0.2902	0.677(3)	0.663(9)	1.09(2)
180	LTO (100)	2.32485	5.39222(1)	5.42204(1)	13.04319(3)	0.1739	0.2857	0.690(3)	0.678(9)	1.08(2)
190	LTO (100)	2.32966	5.39279(1)	5.42182(1)	13.04517(3)	0.1710	0.2822	0.704(3)	0.684(9)	1.09(2)
200	LTO (100)	2.35117	5.39343(1)	5.42155(1)	13.04718(3)	0.1690	0.2853	0.717(3)	0.705(10)	1.10(2)
210	LTO (100)	2.33520	5.39410(1)	5.42120(1)	13.04934(3)	0.1677	0.2853	0.729(3)	0.714(9)	1.10(2)
220	LTO (100)	2.33614	5.39482(1)	5.42084(1)	13.05148(3)	0.1656	0.2877	0.741(3)	0.722(10)	1.13(2)
230	LTO (100)	2.33095	5.39557(1)	5.42045(1)	13.05368(3)	0.1614	0.2880	0.756(3)	0.728(9)	1.16(2)
240	LTO (100)	2.32928	5.39635(1)	5.42004(1)	13.05590(3)	0.1575	0.2880	0.772(3)	0.741(10)	1.17(2)
250	LTO (100)	2.35161	5.39704(1)	5.41969(1)	13.05777(3)	0.1523	0.2873	0.787(3)	0.753(10)	1.18(2)
260	LTO (100)	2.31731	5.39796(1)	5.41912(1)	13.06047(3)	0.1468	0.2866	0.805(3)	0.770(10)	1.20(2)
270	LTO (100)	2.29728	5.39879(1)	5.41858(1)	13.06295(3)	0.1428	0.2880	0.823(3)	0.794(9)	1.21(2)
280	LTO (100)	2.32523	5.39954(1)	5.41819(1)	13.06490(3)	0.1358	0.2832	0.839(3)	0.803(10)	1.24(2)
290	LTO (100)	2.34210	5.40056(1)	5.41757(1)	13.06767(3)	0.1318	0.2830	0.857(3)	0.819(10)	1.29(2)
300	LTO (100)	2.37484	5.40137(1)	5.41712(1)	13.06974(3)	0.1226	0.2785	0.871(3)	0.824(10)	1.35(2)
310	LTO (100)	2.40682	5.40187(1)	5.41683(1)	13.07103(3)	0.1169	0.2757	0.880(3)	0.821(10)	1.38(2)
320	LTO (100)	2.37907	5.40472(1)	5.41492(1)	13.07820(3)	0.0936	0.2485	0.920(3)	0.823(10)	1.41(2)
330	LTO (100)	2.37695	5.40601(1)	5.41404(2)	13.08082(3)	0.0805	0.2540	0.930(3)	0.837(10)	1.41(2)
340	LTO (100)	2.33667	5.40748(2)	5.41297(2)	13.08390(3)	0.1059	0.2885	0.937(3)	0.905(10)	1.44(2)
350	LTO (100)	2.39773	5.40858(2)	5.41205(2)	13.08697(2)	0.1103	0.2769	0.969(3)	0.982(10)	1.45(2)
360	LTO (100)	2.40479	5.40950(1)	5.41173(2)	13.08996(2)	0.0899	0.2413	1.012(3)	0.997(10)	1.34(2)
370	HTT (100)	2.69404	5.41071(1)	5.41071(1)	13.09232(3)	0	0.2249	1.036(3)	1.03(1)	1.46(2)
380	HTT (100)	2.71791	5.41123(1)	5.41123(1)	13.09454(3)	0	0.2095	1.047(3)	0.91(1)	1.49(2)
390	HTT (100)	2.57769	5.41176(1)	5.41176(1)	13.09686(2)	0	0.2217	1.078(3)	0.96(1)	1.38(2)
400	HTT (100)	2.49765	5.41237(1)	5.41237(1)	13.09893(2)	0	0.2135	1.110(3)	0.99(1)	1.41(2)

Table 6.8: Refined parameters from Rietveld refinements against variable temperature XRD patterns of $La_{1.875}Ba_{0.125}(Cu_{1-y}Mg_y)_{0.875}Cu_{0.125}O_4$ $y = 0.5$.

Temperature (K)	Phase (Percentage %)	R_w	a (Å)	b (Å)	c (Å)	X_3^+	Γ_1^+	B_{iso}(A) (Å^2)	B_{iso}(B) (Å^2)	B_{iso}(O) (Å^2)
90	LTT (100)	2.69611	5.41868(1)	5.41868(1)	12.98229(3)	0.1524	0.3101	0.933(3)	0.88(1)	1.04(2)
100	LTT (100)	2.72981	5.41868(1)	5.41868(1)	12.98382(3)	0.1513	0.3142	0.945(4)	0.90(1)	1.05(2)
110	LTT (100)	2.78070	5.41875(1)	5.41875(1)	12.98531(3)	0.1488	0.3139	0.950(4)	0.89(1)	1.03(2)
120	LTT (100)	2.83522	5.41879(1)	5.41879(1)	12.98695(4)	0.1473	0.3038	0.962(4)	0.90(1)	0.99(2)
130	LTT (100)	2.88907	5.41885(1)	5.41885(1)	12.98864(4)	0.1434	0.2927	0.970(4)	0.92(1)	1.01(2)
140	LTT (70.6(2))	2.22051	5.41948(1)	5.41948(1)	12.98796(3)	0.1340	0.3465	0.994(3)	0.92(1)	1.05(2)
150	LTT (53.3(1))	2.23945	5.41969(1)	5.41969(1)	12.98919(3)	0.1396	0.3464	1.014(3)	0.93(1)	1.08(2)
160	LTT (44.6(1))	2.11044	5.41971(1)	5.41971(1)	12.99107(5)	0.1608	0.3475	1.018(3)	0.96(1)	1.09(2)
170	LTT (22.1(1))	2.36544	5.42023(3)	5.42023(3)	12.99130(11)	0.1862	0.4117	1.031(3)	0.98(1)	1.11(2)
140	LTO (29.4(2))	2.22051	5.40205(4)	5.43104(4)	13.00723(19)	0.2780	0.1677	0.994(3)	0.92(1)	1.05(2)
150	LTO (46.7(1))	2.23945	5.40285(2)	5.43185(2)	13.00360(9)	0.2297	0.2145	1.014(3)	0.93(1)	1.08(2)
160	LTO (55.4(1))	2.11044	5.40286(3)	5.43238(3)	13.00249(8)	0.1832	0.2402	1.018(3)	0.96(1)	1.09(2)
170	LTO (77.9(1))	2.36544	5.40426(2)	5.43302(2)	12.99907(5)	0.1793	0.2272	1.031(3)	0.98(1)	1.11(2)
180	LTO (100)	2.73751	5.40552(1)	5.43294(2)	12.99872(3)	0.1889	0.2655	1.037(4)	0.98(1)	1.14(2)
190	LTO (100)	2.69526	5.40560(1)	5.43326(2)	13.00070(3)	0.1864	0.2585	1.056(3)	0.99(1)	1.16(2)
200	LTO (100)	2.72053	5.40591(1)	5.43319(2)	13.00303(3)	0.1850	0.2640	1.076(4)	1.00(1)	1.15(2)
210	LTO (100)	2.69908	5.40642(1)	5.43312(2)	13.00503(3)	0.1790	0.2625	1.094(4)	1.02(1)	1.17(2)
220	LTO (100)	2.71927	5.40695(1)	5.43285(2)	13.00736(3)	0.1754	0.2612	1.112(4)	1.04(1)	1.15(2)
230	LTO (100)	2.72489	5.40748(1)	5.43267(2)	13.00919(3)	0.1722	0.2621	1.127(4)	1.04(1)	1.15(2)

240	LTO (100)	2.71178	5.40822(1)	5.43233(2)	13.01172(3)	0.1701	0.2688	1.146(4)	1.05(1)	1.14(2)
250	LTO (100)	2.70724	5.40891(1)	5.43199(2)	13.01409(3)	0.1684	0.2753	1.157(4)	1.06(1)	1.16(2)
260	LTO (100)	2.69777	5.40965(1)	5.43165(2)	13.01633(3)	0.1662	0.2794	1.164(4)	1.07(1)	1.18(2)
270	LTO (100)	2.69502	5.41042(1)	5.43131(2)	13.01862(3)	0.1632	0.2766	1.175(4)	1.08(1)	1.22(2)
280	LTO (100)	2.71093	5.41116(1)	5.43082(2)	13.02124(3)	0.1597	0.2731	1.191(4)	1.08(1)	1.21(2)
290	LTO (100)	2.70317	5.41198(1)	5.43042(2)	13.02359(3)	0.1569	0.2681	1.210(4)	1.09(1)	1.27(2)
300	LTO (100)	2.72726	5.41270(1)	5.43003(2)	13.02571(3)	0.1552	0.2745	1.220(4)	1.11(1)	1.28(2)
310	LTO (100)	2.75832	5.41363(1)	5.42942(2)	13.02857(3)	0.1488	0.2882	1.240(4)	1.13(1)	1.29(2)
320	LTO (100)	2.73930	5.41543(1)	5.42828(2)	13.03394(3)	0.1386	0.3128	1.271(4)	1.15(1)	1.36(2)
330	LTO (100)	2.71494	5.41661(2)	5.42748(2)	13.03707(3)	0.1349	0.3246	1.290(4)	1.15(1)	1.31(2)
340	LTO (100)	2.74090	5.41784(2)	5.42660(2)	13.04010(3)	0.1336	0.2988	1.313(4)	1.22(1)	1.36(2)
350	LTO (100)	2.78520	5.41921(2)	5.42548(3)	13.04356(3)	0.1247	0.3097	1.313(4)	1.28(1)	1.28(2)
360	LTO (100)	2.77819	5.42058(2)	5.42454(3)	13.04673(3)	0.1232	0.2809	1.327(4)	1.29(1)	1.34(2)
370	LTO (100)	2.84937	5.42148(2)	5.42414(3)	13.04946(3)	0.1235	0.2607	1.356(4)	1.30(1)	1.33(2)
380	LTO (100)	2.91085	5.42223(2)	5.42422(3)	13.05190(3)	0.1191	0.2203	1.387(4)	1.31(1)	1.36(2)
390	HTT (100)	3.07255	5.42328(1)	5.42328(1)	13.05433(3)	0	0.2390	1.397(4)	1.31(1)	1.53(2)
400	HTT (100)	3.06088	5.42387(1)	5.42387(1)	13.05433(3)	0	0.2417	1.432(4)	1.28(1)	1.57(2)

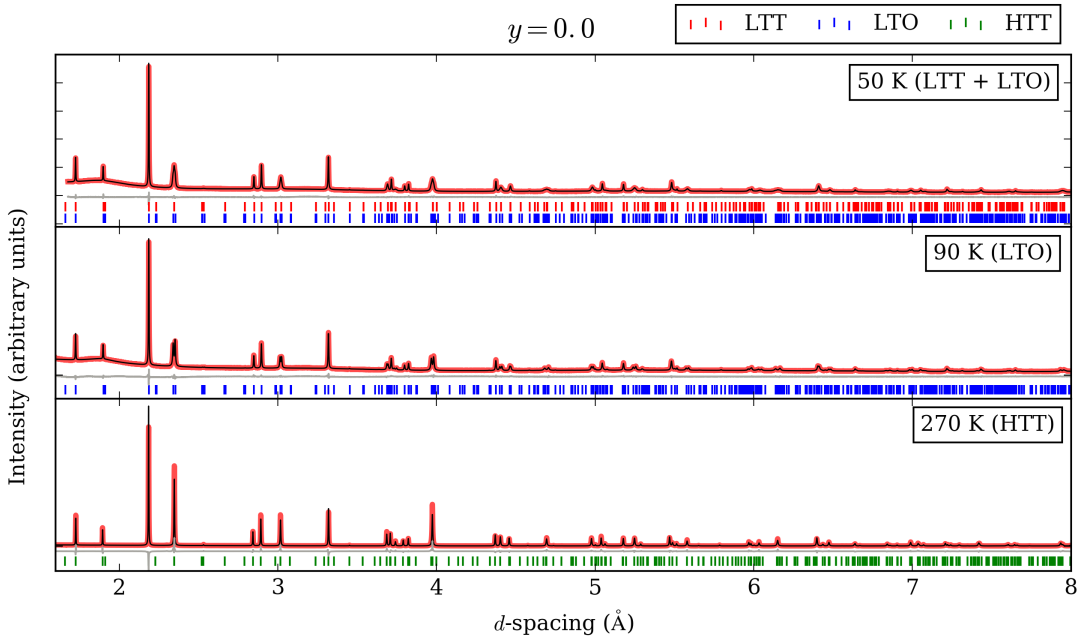

Figure 6.17: Representative Rietveld fits of $La_{1.875}Ba_{0.125}(Cu_{1-y}Mg_y)_{0.875}Cu_{0.125}O_4$, $y = 0.0$, at the labelled temperatures with the labelled phases.

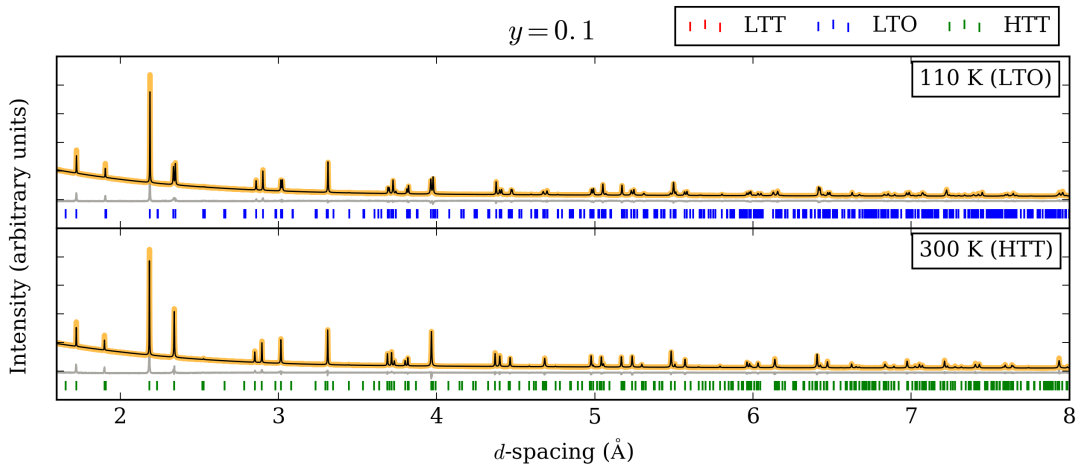

Figure 6.18: Representative Rietveld fits of $La_{1.875}Ba_{0.125}(Cu_{1-y}Mg_y)_{0.875}Cu_{0.125}O_4$, $y = 0.1$, at the labelled temperatures with the labelled phases.

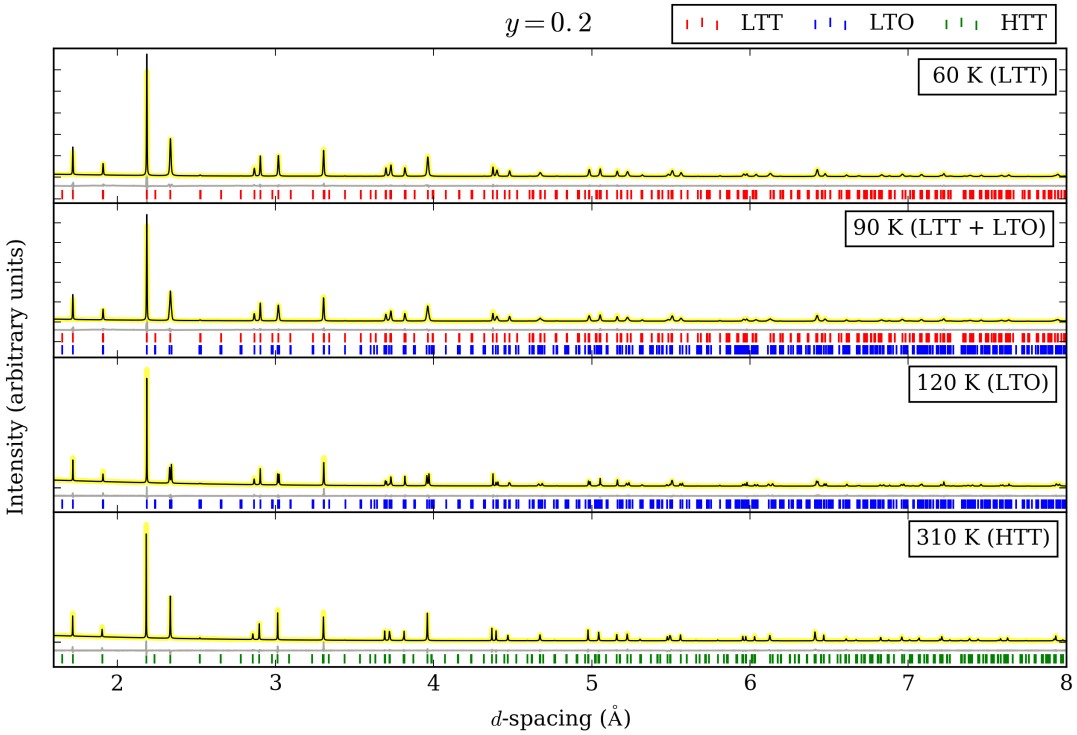

Figure 6.19: Representative Rietveld fits of $La_{1.875}Ba_{0.125}(Cu_{1-y}Mg_y)_{0.875}Cu_{0.125}O_4$, $y = 0.2$, at the labelled temperatures with the labelled phases.

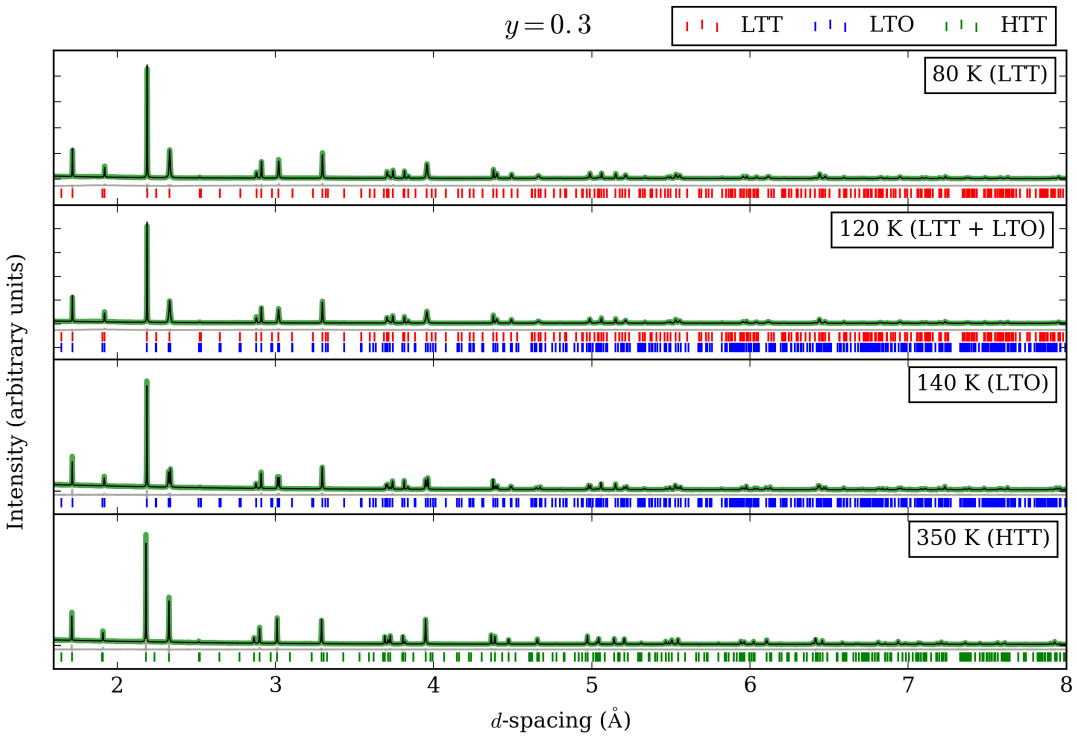

Figure 6.20: Representative Rietveld fits of $La_{1.875}Ba_{0.125}(Cu_{1-y}Mg_y)_{0.875}Cu_{0.125}O_4$, $y = 0.3$, at the labelled temperatures with the labelled phases.

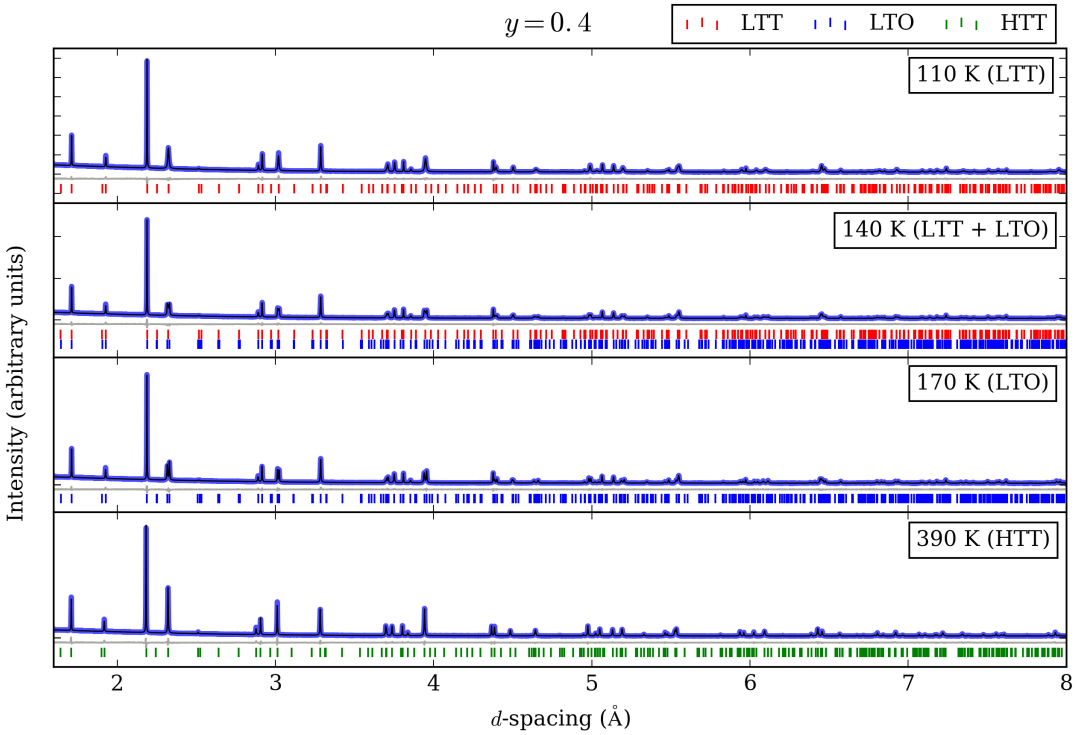

Figure 6.21: Representative Rietveld fits of $La_{1.875}Ba_{0.125}(Cu_{1-y}Mg_y)_{0.875}Cu_{0.125}O_4$, $y = 0.4$, at the labelled temperatures with the labelled phases.

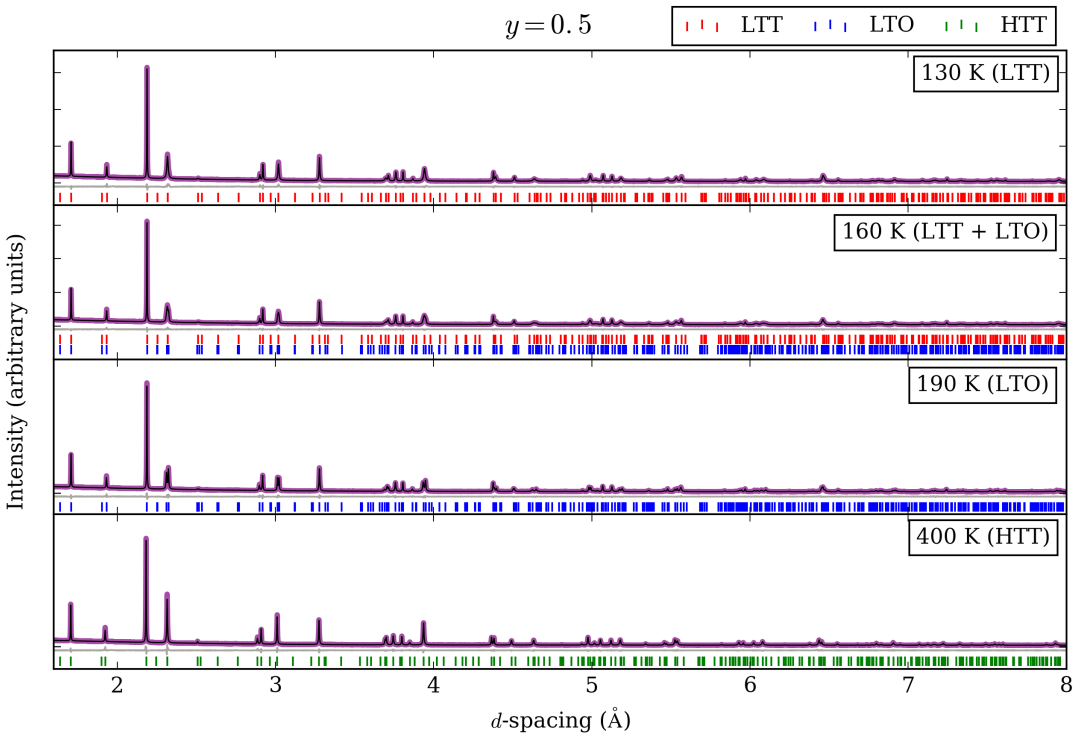

Figure 6.22: Representative Rietveld fits of $La_{1.875}Ba_{0.125}(Cu_{1-y}Mg_y)_{0.875}Cu_{0.125}O_4$, $y = 0.5$, at the labelled temperatures with the labelled phases.

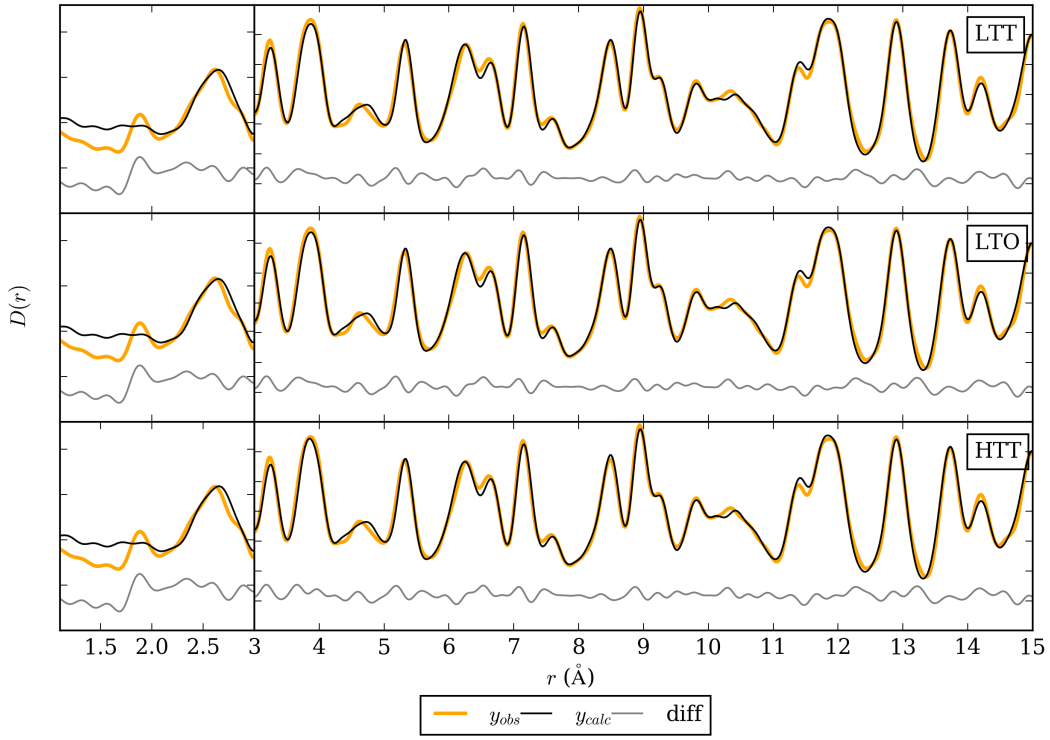

Figure 6.23: Small box fits to the X-ray PDF of $La_{1.875}Ba_{0.125}(Cu_{1-y}Mg_y)_{0.875}Cu_{0.125}O_4$, $y = 0.1$, using LTT, LTO and HTT models.

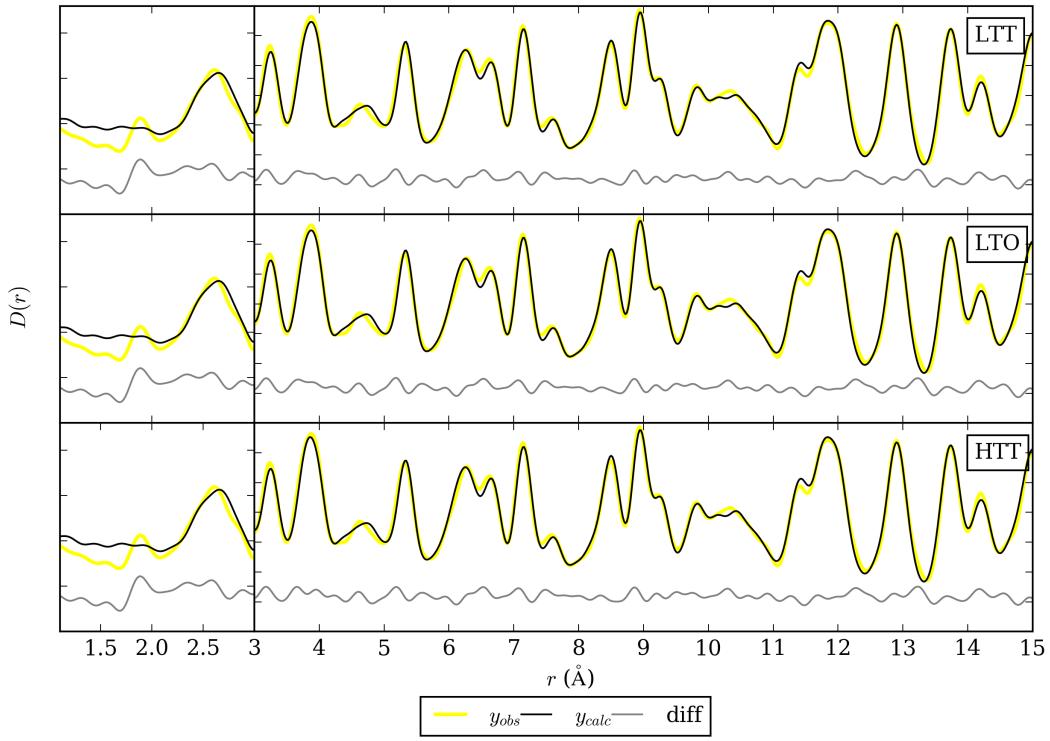

Figure 6.24: Small box fits to the X-ray PDF of $La_{1.875}Ba_{0.125}(Cu_{1-y}Mg_y)_{0.875}Cu_{0.125}O_4$, $y = 0.2$, using LTT, LTO and HTT models.

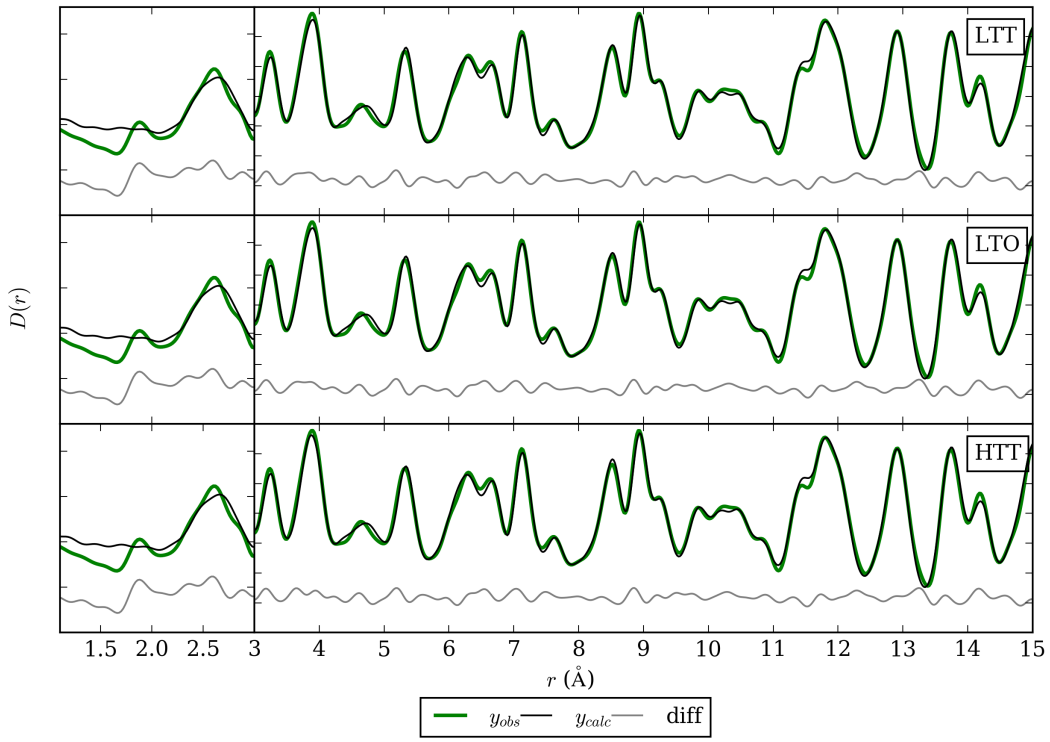

Figure 6.25: Small box fits to the X-ray PDF of $La_{1.875}Ba_{0.125}(Cu_{1-y}Mg_y)_{0.875}Cu_{0.125}O_4$, $y = 0.3$, using LTT, LTO and HTT models.

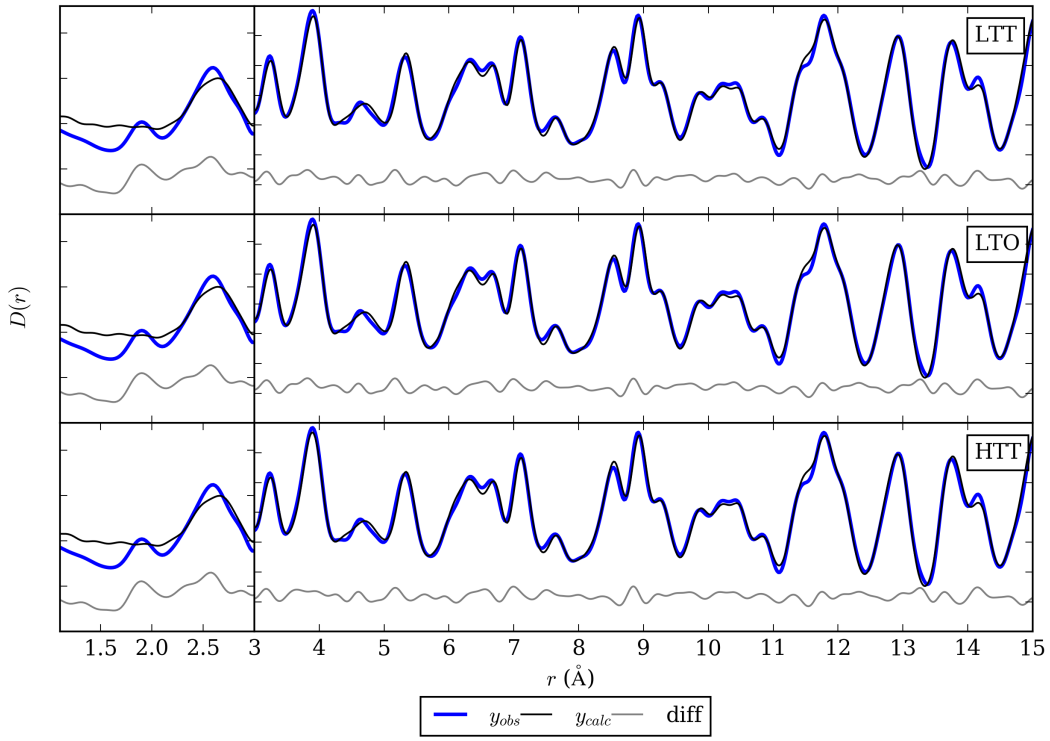

Figure 6.26: Small box fits to the X-ray PDF of $La_{1.875}Ba_{0.125}(Cu_{1-y}Mg_y)_{0.875}Cu_{0.125}O_4$, $y = 0.4$, using LTT, LTO and HTT models.

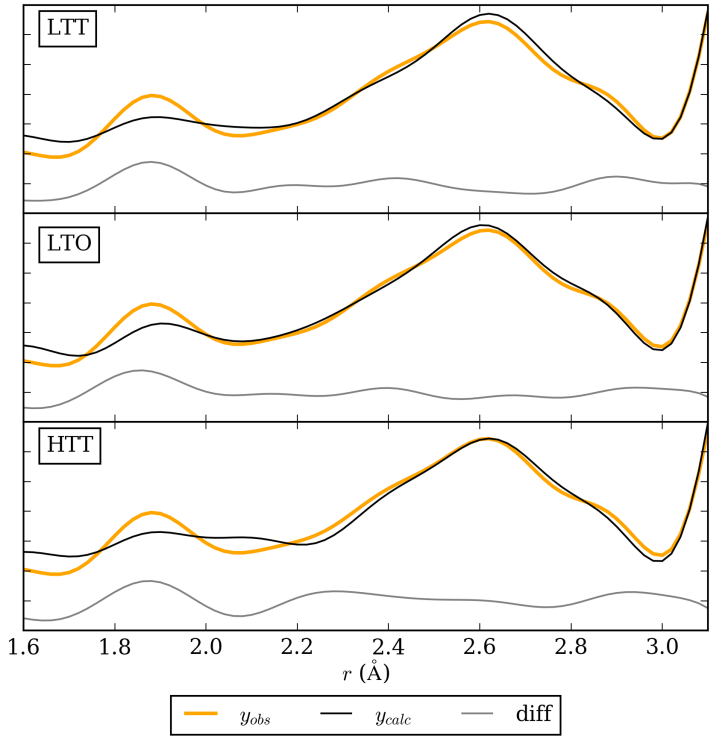

Figure 6.27: Small box fits to the X-ray PDF of $La_{1.875}Ba_{0.125}(Cu_{1-y}Mg_y)_{0.875}Cu_{0.125}O_4$, $y = 0.1$, using LTT, LTO and HTT models over the r-range 1.6–3.1 Å.

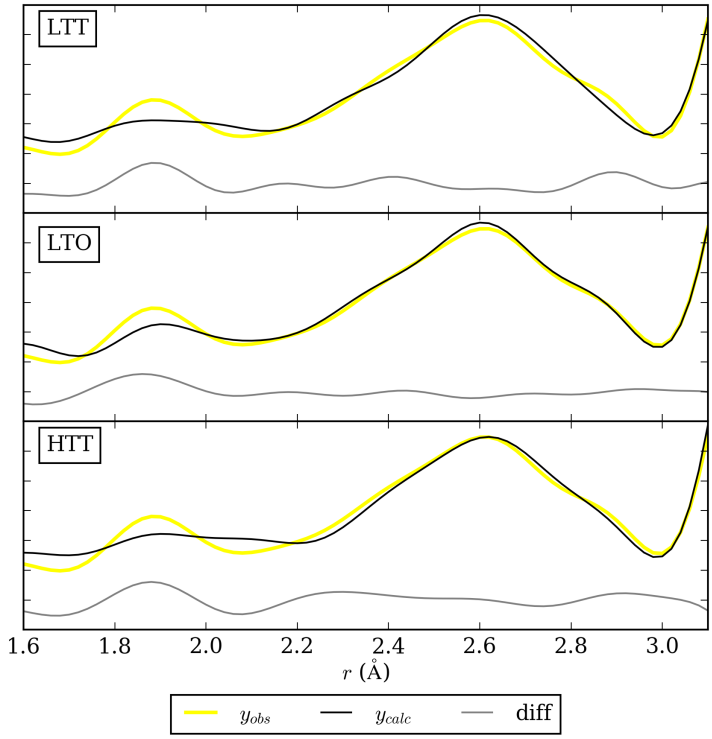

Figure 6.28: Small box fits to the X-ray PDF of $La_{1.875}Ba_{0.125}(Cu_{1-y}Mg_y)_{0.875}Cu_{0.125}O_4$, $y = 0.2$, using LTT, LTO and HTT models over the r-range 1.6–3.1 Å.

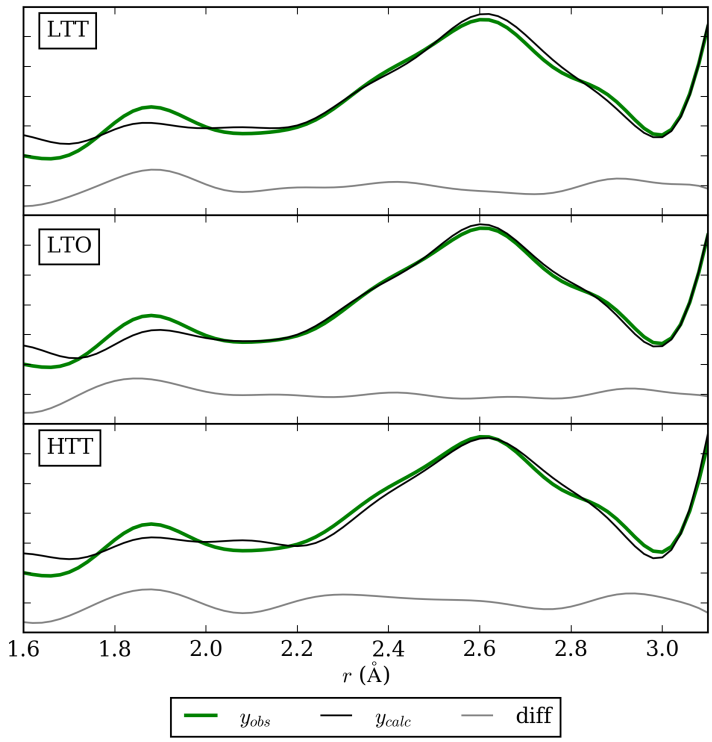

Figure 6.29: Small box fits to the X-ray PDF of $La_{1.875}Ba_{0.125}(Cu_{1-y}Mg_y)_{0.875}Cu_{0.125}O_4$, $y = 0.3$, using LTT, LTO and HTT models over the r-range 1.6–3.1 Å.

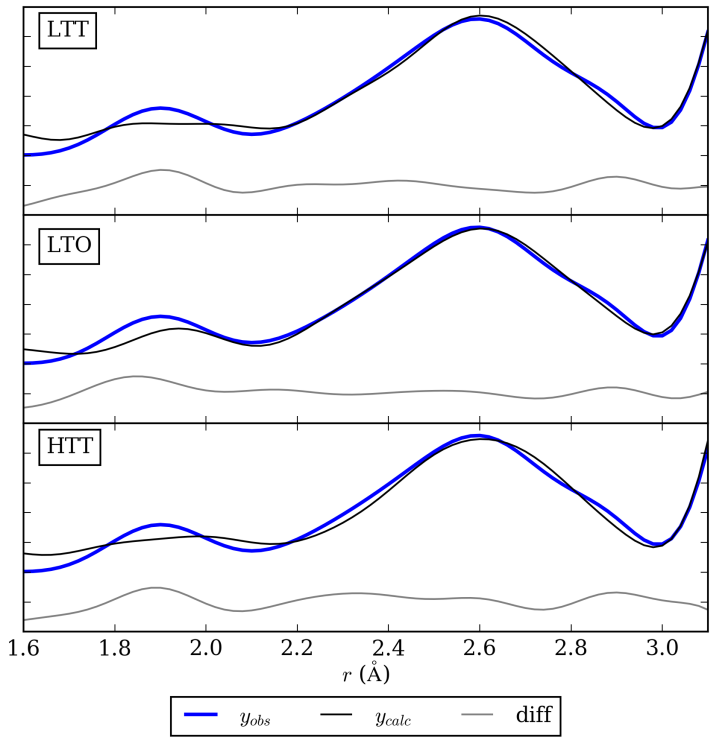

Figure 6.30: Small box fits to the X-ray PDF of $La_{1.875}Ba_{0.125}(Cu_{1-y}Mg_y)_{0.875}Cu_{0.125}O_4$, $y = 0.4$, using LTT, LTO and HTT models over the r-range 1.6–3.1 Å.

6.3.1 RMCProfile settings

Table 6.9: Minimum and maximum distance restraints used in RMCProfile for refinements against $La_{1.875}Ba_{0.125}(Cu_{1-y}Mg_y)_{0.875}Cu_{0.125}O_4$ PDFs.

	O–O	O–Cu	O–Mg	O–Ba	O–La
Minimum distance (Å)	2.2	1.6	1.6	2.1	2.1
Maximum distance (Å)	3.2	2.6	2.6	3.0	3.0

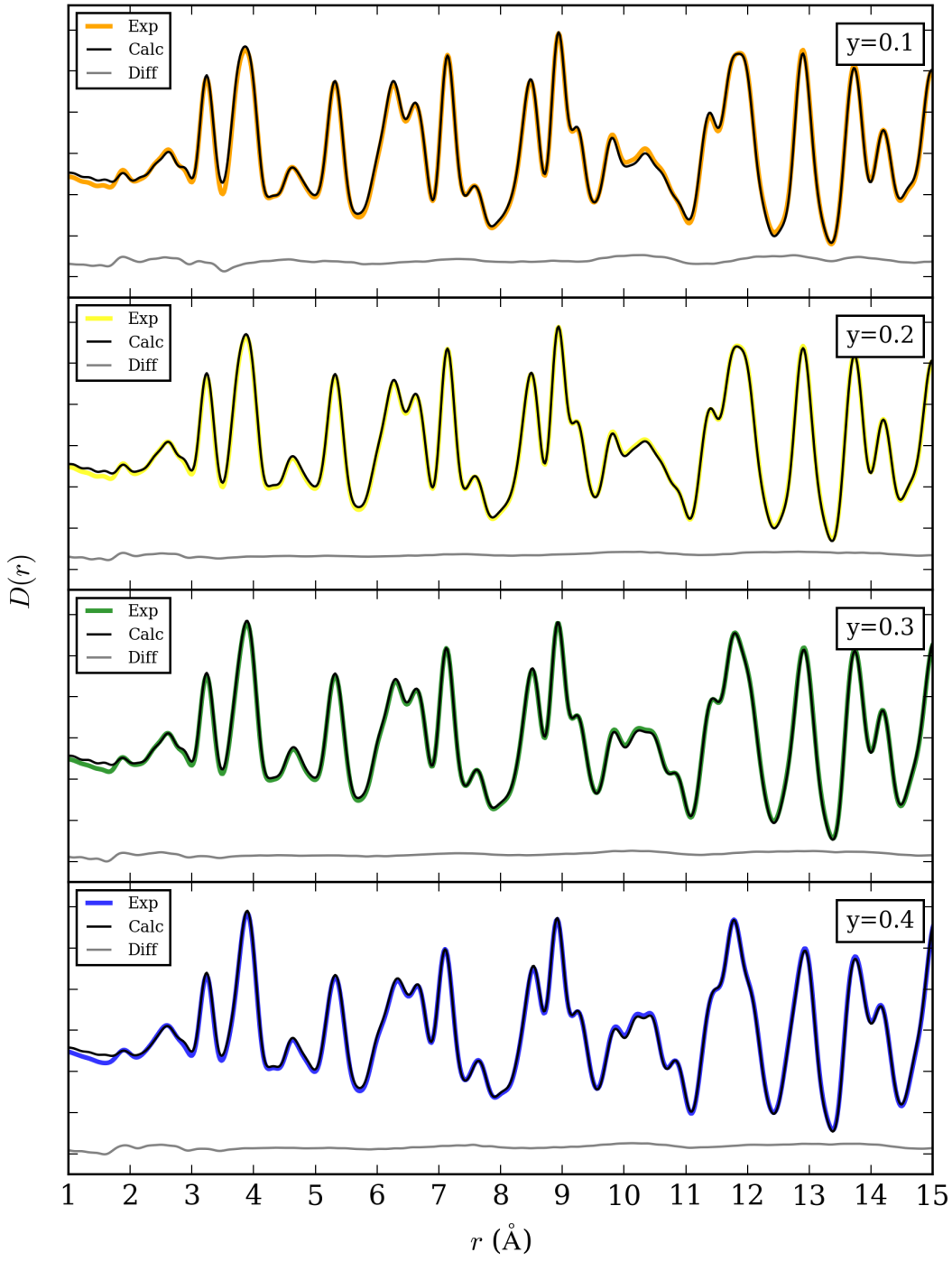

Figure 6.31: RMC fits of $La_{1.875}Ba_{0.125}(Cu_{1-y}Mg_y)_{0.875}Cu_{0.125}O_4$ X-ray PDFs measured at 400 K with y value labelled on the plots.